PHASE BEHAVIOR AND SHRINKING PARTICLE MODEL OF CELLULOSE

DISSOLUTION AND MODIFICATION IN SUB- AND SUPERCRITICAL

CARBON DIOXIDE SWITCHABLE SYSTEM: APPLICATIONS FOR

FABRICATION OF CASSAVA-BASED CELLULOSE TRANSPARENT FILM

AND POROUS CARBON ELECTRODE ON LITHIUM-AIR BATTERY
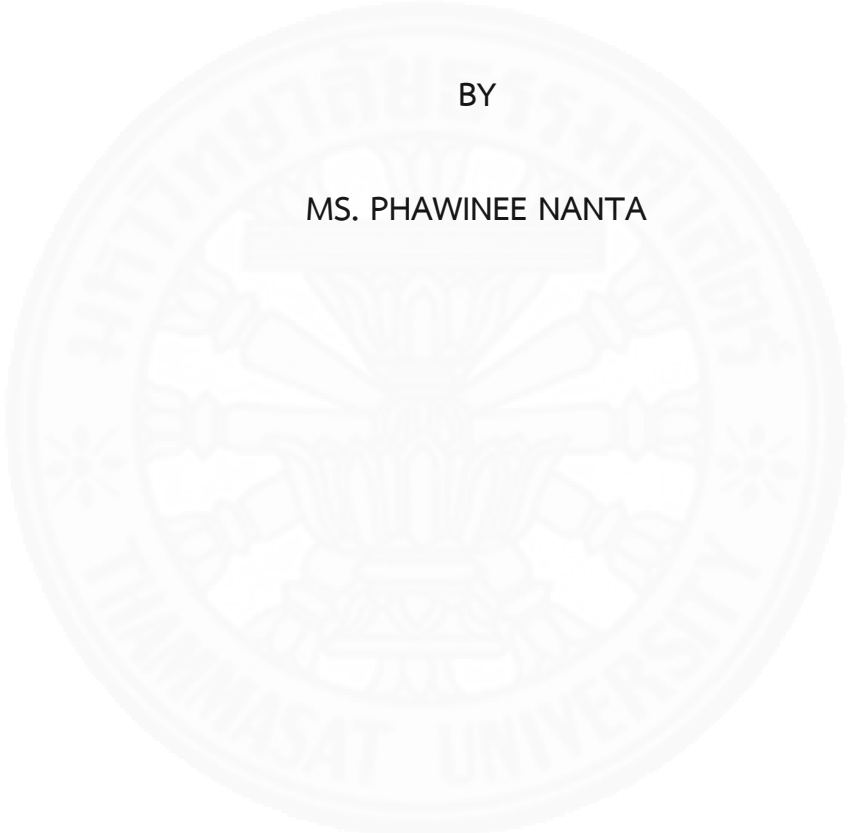

BY

MS. PHAWINEE NANTA

A DISSERTATION SUBMITTED IN PARTIAL

FULFILLMENT OF THE REQUIREMENTS FOR THE DEGREE OF

DOCTOR OF PHILOSOPHY PROGRAM IN ENGINEERING

FACULTY OF ENGINEERING

THAMMASAT UNIVERSITY

ACADEMIC YEAR 2017

COPYRIGHT OF THAMMASAT UNIVERSITY

PHASE BEHAVIOR AND SHRINKING PARTICLE MODEL OF CELLULOSE

DISSOLUTION AND MODIFICATION IN SUB- AND SUPERCRITICAL

CARBON DIOXIDE SWITCHABLE SYSTEM: APPLICATIONS FOR

FABRICATION OF CASSAVA-BASED CELLULOSE TRANSPARENT FILM

AND POROUS CARBON ELECTRODE ON LITHIUM-AIR BATTERY

BY

MS. PHAWINEE NANTA

A DISSERTATION SUBMITTED IN PARTIAL

FULFILLMENT OF THE REQUIREMENTS FOR THE DEGREE OF

DOCTOR OF PHILOSOPHY PROGRAM IN ENGINEERING

FACULTY OF ENGINEERING

THAMMASAT UNIVERSITY

ACADEMIC YEAR 2017

COPYRIGHT OF THAMMASAT UNIVERSITY

THAMMASAT UNIVERSITY

FACULTY OF ENGINEERING

DISSERTATION

BY

MS. PHAWINEE NANTA

ENTITLED

PHASE BEHAVIOR AND SHRINKING PARTICLE MODEL OF CELLULOSE DISSOLUTION AND

MODIFICATION IN SUB- AND SUPERCRITICAL CARBON DIOXIDE SWITCHABLE SYSTEM:

APPLICATIONS FOR FABRICATION OF CASSAVA-BASED CELLULOSE TRANSPARENT FILM AND

POROUS CARBON ELECTRODE ON LITHIUM-AIR BATTERY

was approved as partial fulfillment of the requirements for

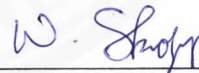the degree of Doctor of Philosophy in Engineering

on May 11, 2018

Chairman _____

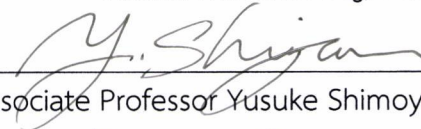(Associate Professor Cattaleeya Pattamaprom, Ph.D.)

Member and Advisor _____

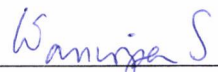(Associate Professor Wanwisa Skolpap, Ph.D.)

Member and Co-advisor _____

(Kittiwut Kasemwong, Ph.D.)

Member _____

(Associate Professor Yusuke Shimoyama, Ph.D.)

Member _____

(Assistance Professor Wanwipa Siriwatwechakul, Ph.D.)

Dean _____

(Associate Professor Thira Jearsiripongkul, Dr. -Ing.)

Dissertation Title	PHASE BEHAVIOR AND SHRINKING PARTICLE MODEL OF CELLULOSE DISSOLUTION AND MODIFICATION IN SUB- AND SUPERCRITICAL CARBON DIOXIDE SWITCHABLE SYSTEM: APPLICATIONS FOR FABRICATION OF CASSAVA-BASED CELLULOSE TRANSPARENT FILM AND POROUS CARBON ELECTRODE ON LITHIUM-AIR BATTERY
Author	Ms. Phawinee Nanta
Degree	Doctor of Philosophy in Engineering
Major Field/Faculty/University	Chemical Engineering
	Faculty of Engineering
	Thammasat University
Dissertation Advisor	Associate Professor Wanwisa Skolpap, Ph. D
Dissertation Co-Advisor	Kittiwut Kasemwong, Ph. D
Academic Years	2017

ABSTRACT

Cellulose is one of alternative sustainable raw materials for reducing petroleum-derived polymer dependency in the manufacturing of related industries. To widen the applications of cellulose, novel approaches for dissolution and modification of cellulose are considerable interest to improve processability of poorly soluble cellulose. Due to strong intra- and inter-molecular hydrogen bonding of cellulose, homogeneous cellulose form cannot be achieved by water and most conventional solvents.

This research aimed to dissolve cellulose using carbon dioxide switchable system (CO_2-SWS) and to investigate the phase behavior of cellulose during dissolving in this system. Cellulose derived from a cassava pulp waste was prepared and dissolved in the CO_2-SWS composed of 1,8-diazabicyclo [5.4.0] undec-7-ene (DBU), ethylene glycol (EG) and carbon dioxide (CO_2) mixture under various operating

pressures (p) and temperatures (T) where CO_2 exhibits properties of gaseous, sub-, and supercritical states. CO_2-SWS at super- and subcritical state was an effective solvent yielding transparent cellulose solution which was further used in preparing transparent film. Moreover, applying the homogeneous cellulose solution was used as preliminary study in preparing hybrid composite cellulose/carbon black electrode as a promising candidate binder solution for application in lithium-air rechargeable battery. After initial discharging the lithium-air battery, the specific energy density was about 10-fold higher than that of conventional lithium-ion battery. The cyclic performance was poor since the lithium-air battery failed after 10th cycles; however, it can potentially extend periods of cycling time of three-cycle results published on lithium-air battery. When the gaseous phase of CO_2 under lower p and T was applied, formation and precipitation of cellulose carbonate salts were observed in the CO_2-SWS as verified by Fourier transform infrared spectroscopy results. Based on the experiments of homogeneous cellulose dissolution, the correlation between initial CO_2 concentration and dissolving conditions was derived using regression analysis; which in turn, strongly relied on the pressure. The correlation allowed us to estimate CO_2 concentration representing the reactant concentration in CO_2-SWS for determining model-predicted diffusion coefficient of CO_2-SWS (D), completed cellulose dissolution time (τ), and cellulose dissolution conversion (X_c) by using the developed diffusion-limited shrinking particle model (SPM). The results showed that the D values range from 10^{-20} to 10^{-17} m^2 s^{-1} depending on the dissolution conditions. The R^2 value of 0.984 suggests that the predicted τ and X_c values were in good agreement with the observation. The influence of the CO_2-SWS operating conditions on the predicted numerical D, τ, and X_c values was investigated using analysis of Pearson's and Spearman's rho correlations. The estimated D and τ values were inversely related with p, whereas X_C showed a very strong positive relationship with p.

ACKNOWLEDGEMENTS

Shuhei, Sekiguchi, Nishioka, for their helpful suggestion about my research and my stay in Japan.

I acknowledge my friend, Dr. Weerinrada, Department of Statistics, Chiang Mai University, who expertly guided me about data analysis. Moreover, I also thank all of Thai Tokodai students especially, Sarocha, Thanataon, Kittisak, Chatri, for being my best friends in Japan.

Indispensably, my deep gratitude goes to my family, whose support has been valuable to me. They always work hard to support me for several years with willingness. They are my motivation helping me go to success in this Ph.D. study. I would like to express my appreciation to all of them.

Ms. Phawinee Nanta

TABLE OF CONTENTS

LIST OF TABLES

LIST OF FIGURES

LIST OF ABBREVIATIONS

Symbols/Abbreviations	Terms
ADF	Acid detergent fiber
ADL	Acid detergent lignin
AP	Alkaline treated pulp
$atmCO_2$	Atmospheric pressure carbon dioxide
BP	Bleached pulp
C.I.	Crystallinity index
CO_2-SWS	Carbon dioxide switchable system
CP	Cassava pulp
Cr	Crystallinity
DBU	1,8-diazabicyclo-[5.4.0]-undec-7-ene
DCP	Destarch cassava pulp
DMSO	Dimethyl sulfoxide
EG	Ethylene glycol
$HPCO_2$-SWS	High-pressure carbon dioxide switchable system
ILs	Ionic liquid
MC	Modified cellulose
NDF	Neutral detergent fiber
P	Pressure (MPa)
$ScCO_2$	Supercritical carbon dioxide
SHS	Switchable hydrophilicity solvent
SPM	Shrinking particle model
SPS	Switchable polarity solvent
T	Temperature (K)

LIST OF ABBREVIATIONS (Cont.)

Symbols/Abbreviations	Terms
T	Time
Tc	Conclusion temperature (K)
Td	Degradation temperature (K)
To	Onset temperature (K)
Tp	Peak temperature (K)
$C_{CO_2,l}$	Bulk concentration of carbon dioxide (kg m^{-3})
$C_{CO_2,s}$	Concentration of carbon dioxide at cellulose surface (kg m^{-3})
$C_{CO_2,e}$	Equilibrium concentration of carbon dioxide (kg m^{-3})
C_p	Specific heat capacity (J K^{-1} g^{-1})
D	Diffusion coefficient (m^2 s^{-1})
D_a	Diameter of the magnetic agitator (m)
d_p	Cellulose particle size (m)
k	Mass transfer coefficient (m^{-2} s^{-1})
N	Rotation speed (s^{-1})
N_C	Mass concentration of cellulose particle (kg m^{-3})
$\dot{Q}$	heat flux (J s^{-1})
R	Radius of cellulose particle (m)
R_0	Initial radius of cellulose particle (m)
r_s	Correlation coefficient
$-r_s''$	Diffusion flux of switchable solvent (kg m^{-3} s^{-1} m^{-2})
$-r_{CO_2}''$	Diffusion flux of carbon dioxide (kg m^{-3} s^{-1} m^{-2})

LIST OF ABBREVIATIONS (Cont.)

Symbols/Abbreviations	Terms
S_C	Surface area of cellulose particle (m^2)
ΔH	Enthalpy change ($J\ g^{-1}$)
υ	Heating rate ($K\ s^{-1}$)
ρ	Density ($kg\ m^{-3}$)
ρ_C	Mass concentration of cellulose particle in the system ($kg\ m^{-3}$)
μ	Dynamic viscosity ($kg\ m^{-1}\ s^{-1}$)
τ	Complete dissolution time (s)
σ	Conductivity ($S\ m^{-1}$)
ϕ	Porosity

CHAPTER 1

INTRODUCTION

This chapter describes background, motivation, and problem of this study. It includes hypotheses, purposes and expected outcomes.

1.1 Motivation

Polymers are large molecules used as raw materials for preparation of plastics. Nowadays, the polymer is derived from petroleum resources that are depleting, limited and unsustainable in the long-term. The Klass model reveals that oil and natural gas will have run out by 2042 (Singh & Singh, 2012). The fossil fuel and consumption data from CIA World Factbook were reported that oil and gas reserves would be available up to 2052 and 2060, respectively (Ecotricity, n.d.). In response to that issue, energy for sustainable development has been gained and increased attention. Renewable monomers such as carbon dioxide, terpenes, vegetable oils, and carbohydrates are possible substitute fossil raw materials (Zhu, Romain, & Williams, 2016). The Barbara group derived a new class of poly(esteralkenamer)s from the ferulic acid containing in lignocellulosic renewable biomass that shows their thermostable up to 556-643 K (Barbara, Flourat, & Allais, 2015). Poly(propylene carbonate) with a yield of 72% and the number average molecular weight (M_n) of 6498 gmol^{-1} were synthesized from soybean oil (Shaarani & Bou, 2017). Recently, the Luchese group has successfully developed biodegradable films from corn and cassava starch that showed similar mechanical properties as low-density polyethylene film (Luchese, Spada, & Tessaro, 2017).
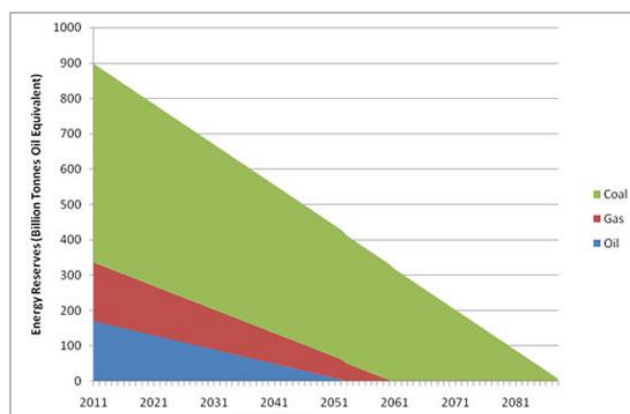
Figure 1.1 World estimated energy reserves for coal, gas and oil (Ecotricity, n.d.).

Cellulose, one of the most abundant bio-based materials, is nominated as renewable raw materials for plastic production replacing fossil-based raw materials due to its chemical structure and function of biopolymer found in nature. Additionally, strong hydrogen bonding both intra-sheets between neighboring cellulose polymer chain and inter-sheets between adjacent cellulose sheets gives cellulose, and its derivatives have a high melting point and glass transition temperature. The thermoplastic produced from cellulose was first invented by Alexander Parkes in 1850 and was patented as Parkesine in 1862. The Parkesine is a clothing waterproofer that generated from cellulose treated with nitric acid. In 1865, John Wesley Hyatt modified the Parkesine by adding camphor as a plasticizer and patented the modified Parkesine as Celluloid in 1872 (Gilbert, 2017). Celluloid was used in film industries before being replaced as cellulose acetate safety film in the 1950s.

1.2 Problems

A major concern in the application of cellulose derivatives is cellulose solubility in most conventional solvent. Cellulose processability can be improved by breaking the prevailing hydrogen bond network or preparing the homogeneous cellulose intermediate for subsequent chemical modification reaction. Some challenges in the cellulose dissolution using common solvents are the complicated dissolution reactions resulting from strong intra- and intermolecular hydrogen bonding

and a stable crystalline structure of the cellulose. Desirable chemical properties and functionalities of modified cellulose as homogeneous cellulose solution are critical factor for design of cellulose dissolution techniques (Song et al., 2015). The developed cellulose dissolution technologies such as aqueous system containing metal is effective (Saalwächter et al., 2000; Y. J. Yang et al., 2014); however, these dissolving cellulose do not promise for commercial cellulose solution due to their toxic byproducts released into the environment. Although ionic liquids (ILs), a potential solvent with high levels of product recovery and solvent recyclability (Mallakpour & Dinari, 2012), has been suggested as highly effective solvent for the homogeneous solution of cellulose (Pinkert et al., 2009). The halide anion based ILs are relatively high viscosity causing difficulty in cellulose processing. Moreover, the applications of ILs pertain to the serious drawbacks that ILs might chemically react with the cellulose or physically entrap the cellulose on the modification and regeneration processes. The reaction or entrapment of cellulose could give the undesirable effects on physical, chemical and biological properties of the final cellulose product (Gericke, Fardim, & Heinze, 2012).

Figure 1.2 Shifting conversion from a renewable resource to green plastics (Gilroy, 2017).

1.3 Hypotheses

Cellulose dissolution involving with deconstructing hydrogen bond network of cellulose is a great importance for expanding the application domains of cellulose. To achieve active soluble form of cellulose, high polar solvents were conventionally applied in breaking the hydrogen bond network. In meanwhile, Jessop and coworkers have reported a switchable polar solvent which is a high polar solvent reversely converting from its low polarity form by carbon dioxide (Jessop et al., 2005). Carbon dioxide, nontoxic, nonflammable and environmentally acceptable gas, has been recently gained more attractive on the development of the chemical or biochemical processes (Garcia-Gonzalez et al., 2007; Ngo et al., 2016; Park et al., 2002; Pasquini et al., 2010). The sub- and supercritical carbon dioxide perform admirable physical properties more than its typical liquid or gas form that they exhibit high diffusivity like a gas and high solubility like a liquid. Consequently, they can effectively penetrate into small solute pores causing swelling and dissolving cellulose at lower both viscosity and temperature.

Therefore, it was hypothesized that carbon dioxide switchable polarity system comprising either subcritical carbon dioxide or supercritical carbon dioxide was effectively dissolve cellulose by expectedly increasing solvent penetrability and accessibility in the cellulose structure.

1.4 Objective and scope of work

In this work, the switchable solution using sub- and supercritical carbon dioxide was employed in the dissolution and modification of cassava-based cellulose. The switchable solution in the presence of carbon dioxide was prepared using ethylene glycol and 1,8-Diazabicyclo [5.4.0] undec-7-ene which is a carbon dioxide capturing agent and strong base, correspondingly. The objectives of this work are listed below.

1. To study the phase behavior during the dissolution of the cellulose in the switchable solution under gaseous, sub- and supercritical states of carbon dioxide by varying temperatures and pressures.

2. To estimate diffusion coefficient of carbon dioxide and to predict cellulose conversion by a developed diffusion-controlled shrinking particle model (SPM) describing the effect of cellulose dissolution conditions in the switchable solution.

3. To use modified cellulose in fabrication of transparent film and application of cassava-based cellulose composite with carbon black for the fabricated cellulose/carbon lithium-air battery electrode.

CHAPTER 2

FUNDAMENTAL AND REVIEW OF LITERATURES

Relevant fundamentals and previous literature reviews are described in this chapter.

2.1 Cassava

Cassava is a tuber crop which is one of the most important crops in the tropical countries. During the past decade, the major producing countries are Nigeria, Thailand, Brazil and Indonesia. Since 2012, Thailand was the second largest cassava producer. In 2016, cassava root production in Thailand was 31.2 million tons annually that has been significantly increased by 41% from 2001 (FAO, 2016). The main utilizations of cassava are starch production for food, animal feed, and bioethanol production.
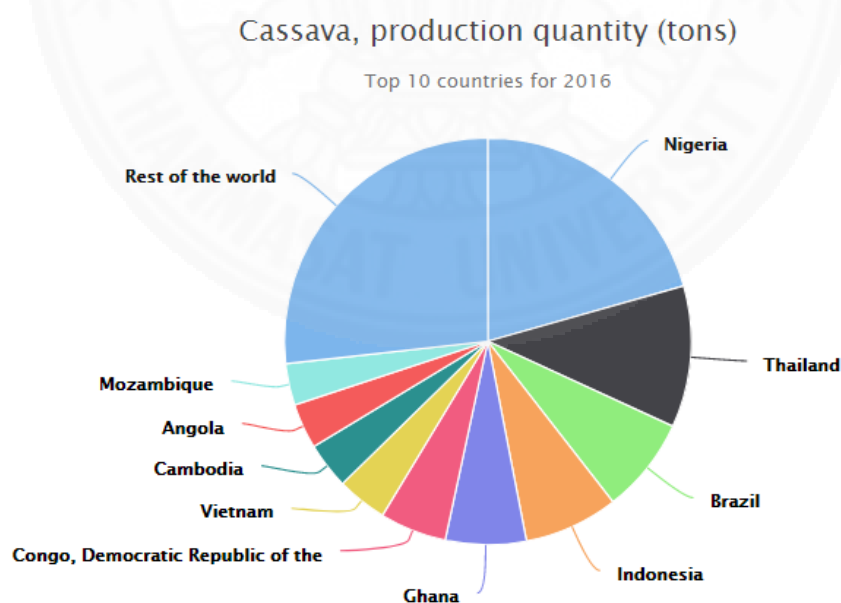
Figure 2.1 Global distribution of cassava production quantity in 2016 (FAO, 2016).

2.1.1 Cassava tuber structure and composition

Cassava tuber consists of three major components; periderm, phloem, and xylem. Figure 2.2 shows the cross-section of cassava tuber. Periderm is the outside tissue of the tuber which functions provides protection for the tissues. Phloem (cortex) is the living tissue that transports organic nutrients, especially sugar, to parts of the cassava plant. Xylem (starchy flesh), the central portion of the tuber functions as the transport tissue similar to phloem, but the main function of xylem is water transportation.

Xylem consists of short vessel elements that are connected together into long tubes. About 80-90 % of starch grains are packed with parenchyma cells which are food storage in xylem. Fiber cells including lignin, hemicellulose, and cellulose are the composition of the vessel cell wall in xylem.
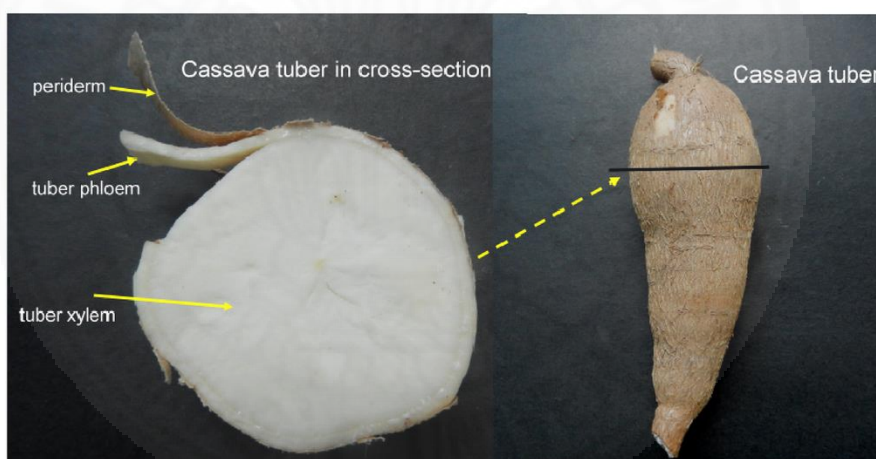
Figure 2.2 Cross-section of cassava tuber (Yao et al., 2014).

The variation of specific tissue (root or leaves), geographic location, variety, age of the plant and environmental conditions influence the composition of cassava (Morgan & Choct, 2016). Generally, it contains about 1% protein, 1% fiber, 3% fat, 30-35% of amyloses and amylopectins and 62% water, hence cassava is predominated as a starchy food. Starch manufacturing is playing an increasingly important role in the cassava industry. Figure 2.3 shows cassava starch process from cassava root. The total starch production of 25-30% is yielded.
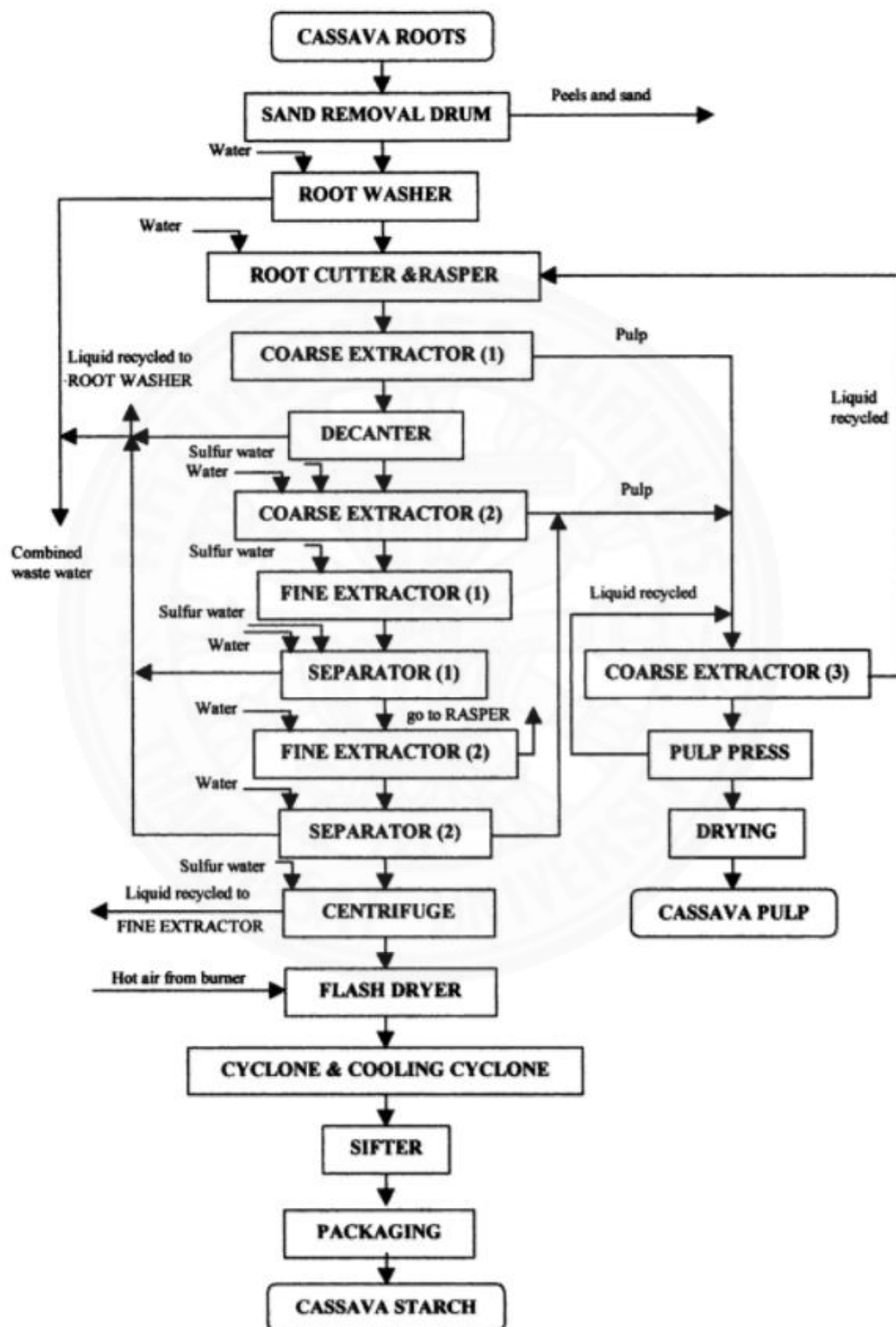
Figure 2.3 Cassava starch manufacturing process (Sriroth, 2000).

2.1.2 Cassava pulp

Cassava pulp, a by-product of cassava starch production, yields approximately 10-15% cassava fed as raw material. The pulp is separated from the starch in the screening process. Dried cassava pulp contains 5.3% protein, 56% starch, 0.1% fat, 2.7% ash and 35.9% fibre (FAO, 1977). Normally, cassava pulp is used for animal feed and biogas production (Piyachomkwan & Tanticharoen, 2011).

Fibre is a main component in cassava pulp. As previously discussed, plant cell walls are the primary source of fibre which structures with cellulose, hemicellulose, and lignin. Typical biomass resources contain 40-60% cellulose, 20-40% hemicellulose and 10-25% lignin.
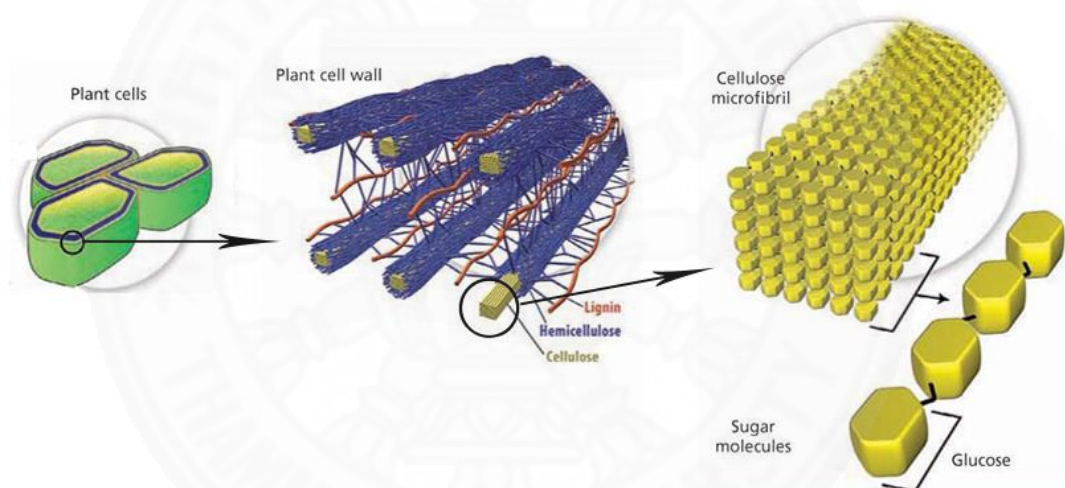
Figure 2.4 Plant cell wall structure (AKR, 2016).

2.1.2.1 Lignin

Lignin, the supporter and structure reinforcement of cell wall, is a large group of aromatic polymers resulting from the oxidative combinatorial coupling of three different hydroxyl-phenylpropanoid monomers; *p*-coumaryl (*p*-hydroxyphenyl; H), coniferyl (guaiacyl; G) and sinapyl (syringyl; S) alcohols (Brandt et al. 2013). Each monomer connects with various ether bonds and carbon-carbon bond (H. Chen, 2014). Lignin monomer composition differs among plant species. Lignin in gymnosperms or softwood consists mostly of G monomers with low levels of H monomers. Lignin in dicot angiosperm or hardwood consists mainly of G and S monomers with a few H

monomers. Lignin in monocot or grasses contains the comparable levels of G and S monomers with higher H monomers than lignin in dicot (Wertz et al., 2017).

The chemical deconstruction method such as alkaline hydrolysis modifies lignin by cleavage its ether bonds, but only some lignin can remove from the pulp. The combination of chemical fragmentation and the ability of the liquor to solvate the modified lignin fragments can enhance the lignin removal amount. Lignin can become water-soluble, as in the case of sulfite pulping and electrophilic substitution. An isolated lignin always contains a small amount of hemicellulose because lignin and hemicellulose are covalently cross-linked together.
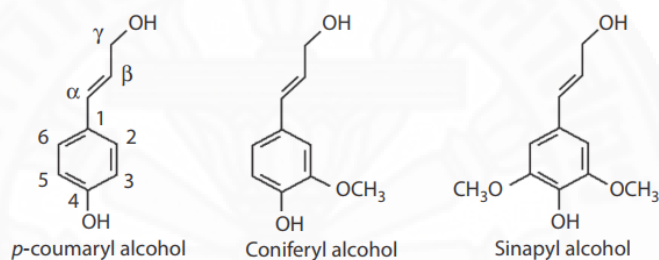
Figure 2.5 Monomers of lignin (Wertz et al., 2017).
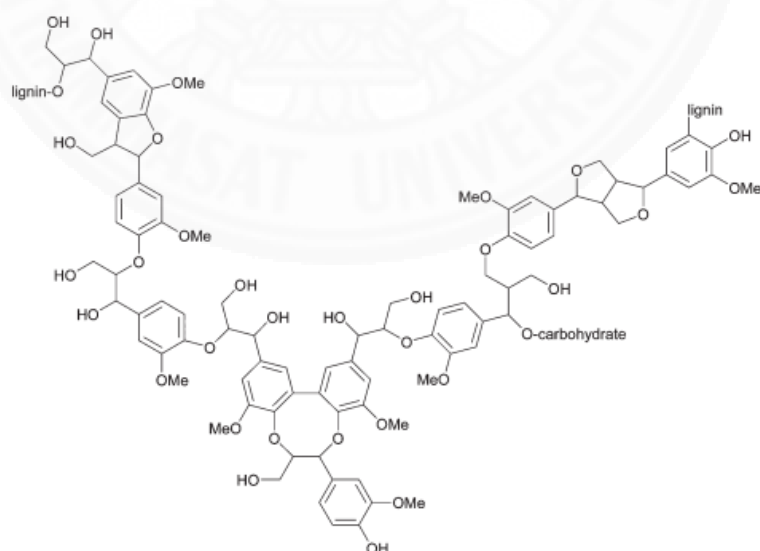
Figure 2.6 Lignin fragment with various C-O and C-C linkages typically present in native lignin (Brandt et al., 2013).

2.1.2.2 Hemicellulose

A hemicellulose is a group of branched polysaccharides that contain a variety of pentose (xylose and arabinose) and hexose (glucose, mannose, and galactose) sugars. The main chains of hemicellulose are formed from β-1,4-glycosidic bonds while side chains can be formed from β-1,2-, β-1,3-, and β-1,6-glycosidic bonds. The degree of polymerization of hemicellulose is less than 200 which is lower than cellulose and lignin. Hemicellulose is non-covalently bonded to the cellulose, but it binds to cellulose via hydrogen bonding.
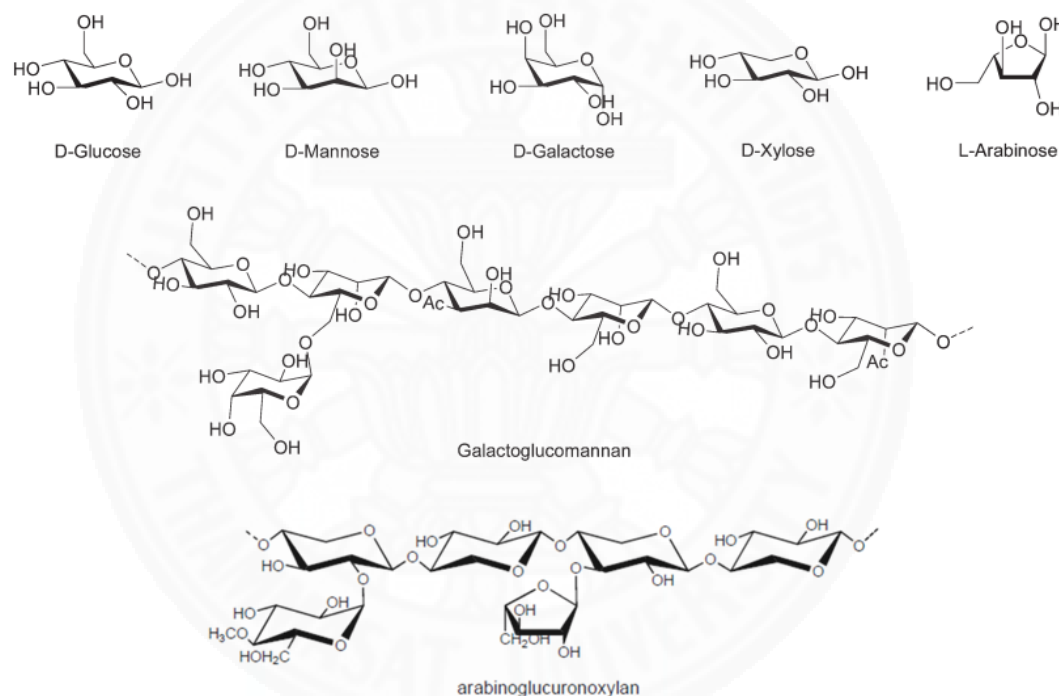
Figure 2.7 The hexoses and pentose typically found in hemicellulose and structure of two most common hemicelluloses found in softwood.

Hemicellulose is alkaline- and water-soluble polysaccharide. Due to its low molecular weight and amorphous structure, hemicellulose is more susceptible to hydrolysis or de-polymerization easily than cellulose. Many techniques have been applied to separate hemicellulose from pulp and cellulose. In 2008, Krawczyk and co-workers successfully separated and isolated arabinoxylan from barley husks using steam explosion (Krawczyk et al., 2008). Pressurized low-polarity water and pressurized

aqueous ethanol were also an effective system to remove hemicellulose (Buranov & Mazza, 2010) as well as the hydrothermal system combining with active alkaline (KOH) (Ma et al., 2014). Recently, ionic liquid/water system was developed to separate hemicellulose from the pulp. It was found that about 71-80% of hemicellulose was removed (Ma et al., 2017).

2.2 Cellulose

Cellulose is one of the most important components in plant and animal cell walls. Dissolution of cellulose is related to its physical and chemical structure which are described in detail below.

2.2.1 Chemical structure of cellulose

Cellulose is a linear homopolymer composition of D-glucopyranose units linked by β-1,4-glycosidic bonds. It is an organic compound with the formula $(C_6H_{10}O_5)_n$ where n is the degree of polymerization (DP) representing the number of D-glucopyranose unit. The degree of polymerization of a regular form of rayon, wood pulp and cotton are ranged between 250-450, 600-1500 and 9000-15000, respectively. Higher DP is associated with higher strengths. The behavior of microcrystalline cellulose with low and high DP is compared and shown in Table 2.1. The β-1,4-glycosidic linkage between the D-glucopyranose monomers results in the very straight polymeric chain. Subsequently, cellulose molecules closely pack together into crystalline fibrils, and that permits an intermolecular hydrogen bonding between the adjacent chains.
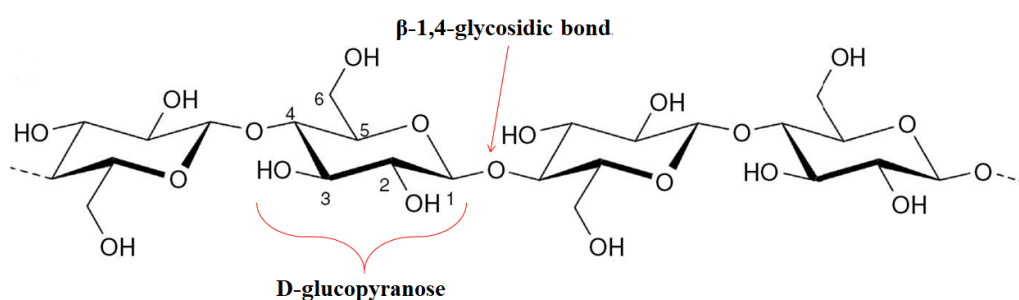
Figure 2.8 Chemical structure of cellulose adapted from Jedvert & Heinze (2017).

Table 2.1 Behavior comparison between cellulose with low and high DP (Kleinebudde, Jumaa, & El Saleh, 2000).

Low DP (Gel Model)	High DP (Sponge Model)
Marked reduction in the particle size	Small reduction in the particle size
Less water needed (immobilized water)	More water needed (absorbed water)
Deformation of microcrystalline cellulose (MCC) during the extrusion process	No deformation of MCC during the extrusion process
More shrinking during the drying process	Less shrinking during the drying the drying process
Low porosity of dried pellets	High porosity of dried pellets

    Each glucopyranose unit contains three hydroxyls (OH) groups (O2-H, O3-H, and O6-H) which can form hydrogen bond networks both intra-chain between neighboring glucopyranose unit and inter-chain between adjacent cellulose chains. The hydrogen bond linkages in cellulose are shown in Figure 2.9. The intra- and inter hydrogen bond linkage for various cellulose types will be detailedly discussed in a section 2.2.2.
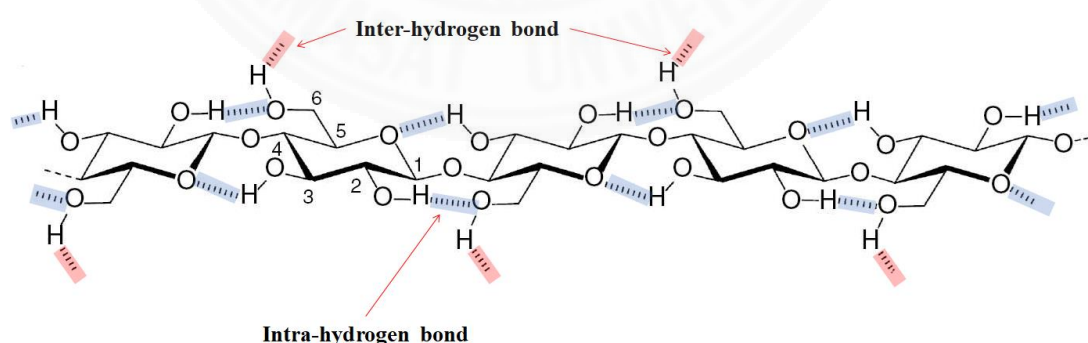
Figure 2.9 Intra- and inter- hydrogen bond linkages in cellulose adapted from Jedvert & Heinze (2017).

2.2.2 Physical structure and polymorphism of cellulose

Cellulose exists in several crystalline polymorphs (I, II, III and IV) with different packing arrangements in the unit cell (Zugenmaier, 2008). Cellulose found in nature is classified as cellulose I type which is a mixture of two crystalline forms, cellulose I_α and cellulose I_β. Cellulose I_α is a dominant form in bacterial cellulose which has a triclinic one-chain unit cell. The parallel cellulose I_α chains stack through van der Waals interactions, with progressive shear parallel to the chain axis. Cellulose I_β is a dominant form in higher plants (cotton, wood, ramie, *etc.*) which contains a monoclinic two-chain unit cell. The parallel cellulose I_β chains stack with alternating shear (Quiroz-Castañeda & Folch-Mallol, 2013). Cellulose I can be converted into cellulose II by mercerization (alkali treatment) and regeneration (solubilization and subsequent recrystallization). Cellulose II is the most stable form which has the monoclinic unit cell-like cellulose I_β whereas the chains arrangement is different. The chains of cellulose II are arranged in an anti-parallel orientation. Cellulose III and IV are derived by alkali or heat treatment from cellulose I and II, respectively
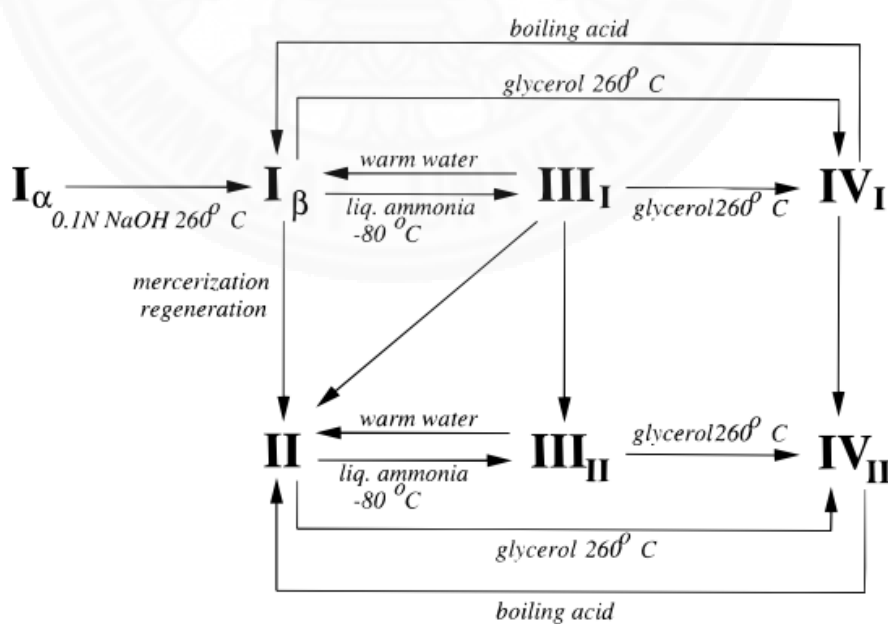
Figure 2.10 Polymorphs and conversions of cellulose (Kroon-Batenburg, Bouma, & Kroon, 1996).

The polymorphs of cellulose differ in conformation and packing arrangement which can be identified by the size of unit cells and hydrogen bonding arrangements. The unit cell is a geometrical unit that describes the structure of the crystallites. Figure 2.11 shows a unit cell composed of three axes dimensions with lengths a, b, c and angles between the axes given by α, β and γ.
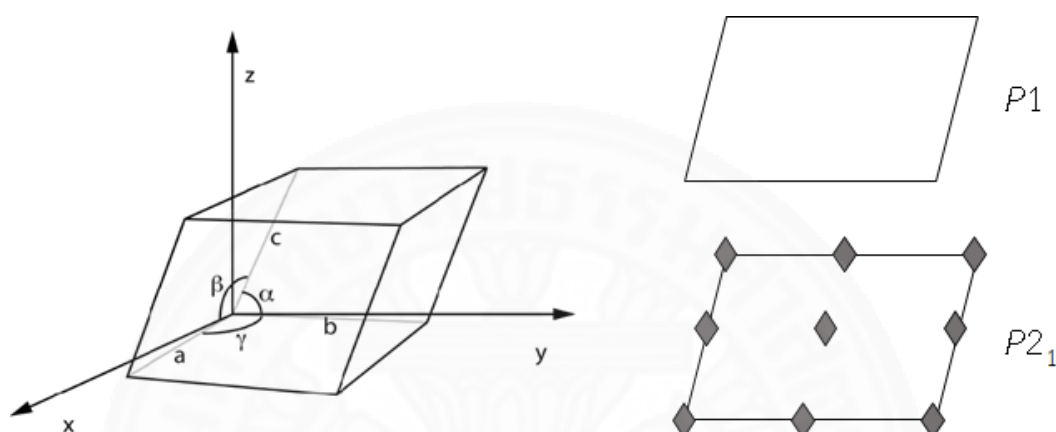
Figure 2.11 Unit cell definition with lengths a, b, c and angles between the sides given by α, β, γ and two-dimensional space groups $P1$, $P2_1$.

Each cellulose crystalline polymorph exhibits the different packing arrangements of the crystalline structure in the unit cell. The unit cell of cellulose is listed in Table 2.2. The space group is the symmetry group of a configuration in space. Cellulose polymorphs are classified as Triclinic and Monoclinic crystal systems with corresponding space group $P1$ and $P2_1$. The space group $P1$ is a primitive unit cell with the absence of any symmetry on the unit cell (no rotation axes) while the space group $P2_1$ is a primitive unit cell with twofold screw parallel to the b axis. The projection of various cellulose polymorphs in the [001] direction on the a-b plane are shown in Figure 2.12.

Table 2.2 Unit cells for polymorphs of cellulose.

Type	Space group	Number of chains	Unit cell					
			a (Å)	b (Å)	c (Å)	α (°)	β (°)	γ (°)
Cellulose I_α	$P1$	1	6.717	5.962	10.4	118.08	114.8	80.37
Cellulose I_β	$P2_1$	2	7.784	8.201	10.38	90	90	96.55
Cellulose II mercerized (flax)	$P2_1$	2	8.01	9.04	10.36	90	90	117.1
Cellulose II mercerized (ramie)	$P2_1$	2	8.1	9.03	10.31	90	90	117.1
Cellulose II regenerated (Fortisam)	$P2_1$	2	8.03	9.04	10.35	90	90	117.11
Cellulose III	$P2_1$	1	4.45	7.85	10.31	90	90	105.1
Cellulose IV_I	$P1$	2	8.03	8.13	10.34	90	90	90
Cellulose IV_{II}	$P1$	2	7.99	8.1	10.34	90	90	90

Note. Adapted from (Zugenmaier, 2008).
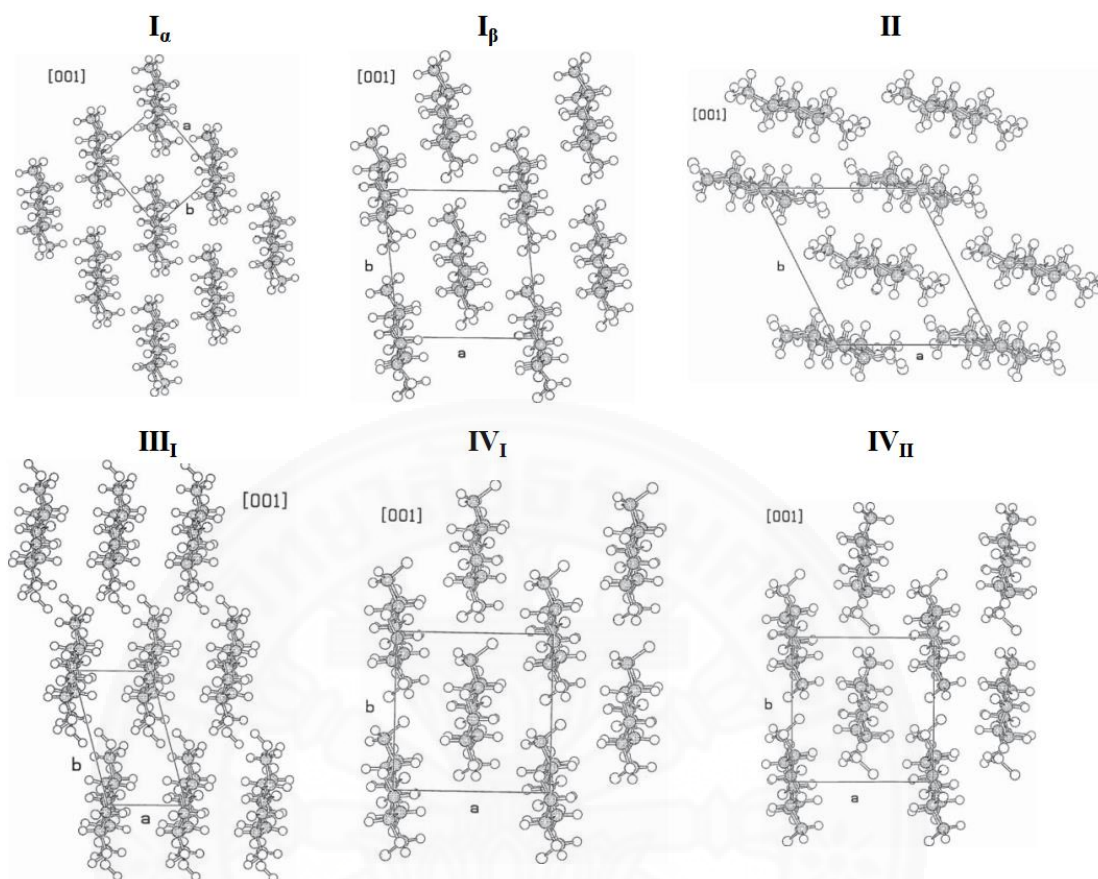
Figure 2.12 Projection of various cellulose chains in the [001] direction on the *a-b* plane adapted from Zugenmaier (2008).

2.2.2.1 Cellulose *I*

Cellulose *I* comprises the allomorphic mixture of cellulose I_α and cellulose I_β dividing by the conformation and packing arrangement. The polymorph system of cellulose I_α has one chain in an asymmetric triclinic unit cell with space group $P1$ while that of cellulose I_β has two chains in a monoclinic with space group $P2_1$. The unit cell dimensions *a, b, c* and the angles between the axes α, β, γ of cellulose I_α are approximately 6.717Å, 5.962Å, 10.4Å, 118.08°, 114.80° and 80.37°, respectively (Nishiyama et al., 2003). Those of cellulose I_β are 7.784Å, 8.201Å, 10.38Å, 90°, 90° and 96.55°, respectively (Nishiyama, Langan, & Chanzy, 2002).
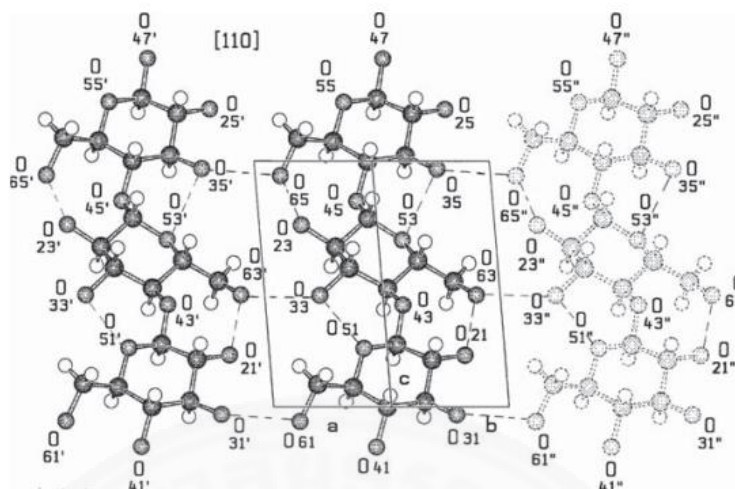
Figure 2.13 Projection of a sheet of cellulose I_α in the [110] direction. Dashed lines represent intramolecular hydrogen bonds on a diagonal plane. (Zugenmaier, 2008).

The projections of the crystal structure of cellulose I_α are presented in Figure 2.12. The structure of cellulose I_α and II comprise chains arranged in diagonal while those of cellulose III_I, IV_I and IV_{II} comprise chains arranged in parallel. The projection of the chains of cellulose I_α in [001] direction (Figure 2.12) suggests that each cellulose chain is arranged in sheet stacked in parallel-up pattern. The projection in [110] direction (Figure 2.13) suggests that the ribbon-like chains of cellulose I_α are connected by hydrogen bonds within only intra-sheets between O3...O6 and O6...O3.
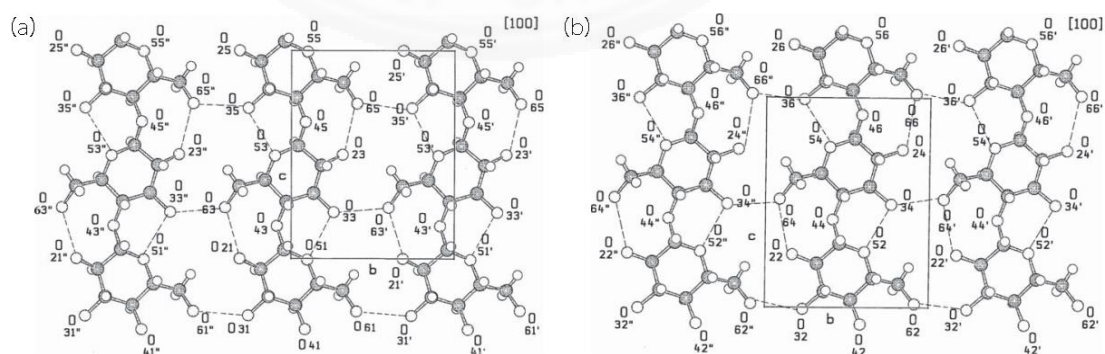
Figure 2.14 Projection of a sheet of cellulose I_β in the [100] direction (a) through the corner and (b) through the center of the unit cell, respectively (Zugenmaier, 2008).

The projection onto the [001] plane of cellulose I_β in Figure 2.12 suggests that the crystal structure is consisted of the parallel sheet arrangement with the unit cell axis *b*. Figure 2.14 compares two neighboring sheets through the corner and the center of the unit cell of cellulose I_β. It appears that one sheet is shifted relative to the adjacent one in the *c*-direction. Only intra-sheet hydrogen bonds have been detected in both cellulose I_β and I_α type edged on O3...O6 and O6...O3.

2.2.2.2 Cellulose II

Cellulose II results from mercerization of native cellulose in sodium hydroxide. The projection of the chains in *a-b* plane direction of cellulose II is shown in Figure 2.12. A sheet-like structure can be defined along both *a*-direction and diagonal direction through the corner and center of the unit cell. The polymorph system of cellulose II is monoclinic with space group $P2_1$ and two-chains repeating unit cell. The unit cell dimensions *a, b, c* are approximately 8Å, 9Å, and 10.3Å, respectively and the angles between the axes α, β, γ are approximately 90°, 90° and 117.1°, respectively. Some of the differences are observed depending on the source of cellulose (Langan et al., 1999, 2001, 2005).

In cellulose II, the packing arrangement occurs by both intra-sheet and inter-sheet hydrogen bonding to form an optimal hydrogen bonding network. The inter-sheet hydrogen bonds observed include O32...O63, O22...O21, and O64...O31. The intra-sheet hydrogen bonds through origin include O61...O21 and O23...O63 and that through the center are O22...O62 and O64...O24 (Figure 2.15) (Zugenmaier, 2001).
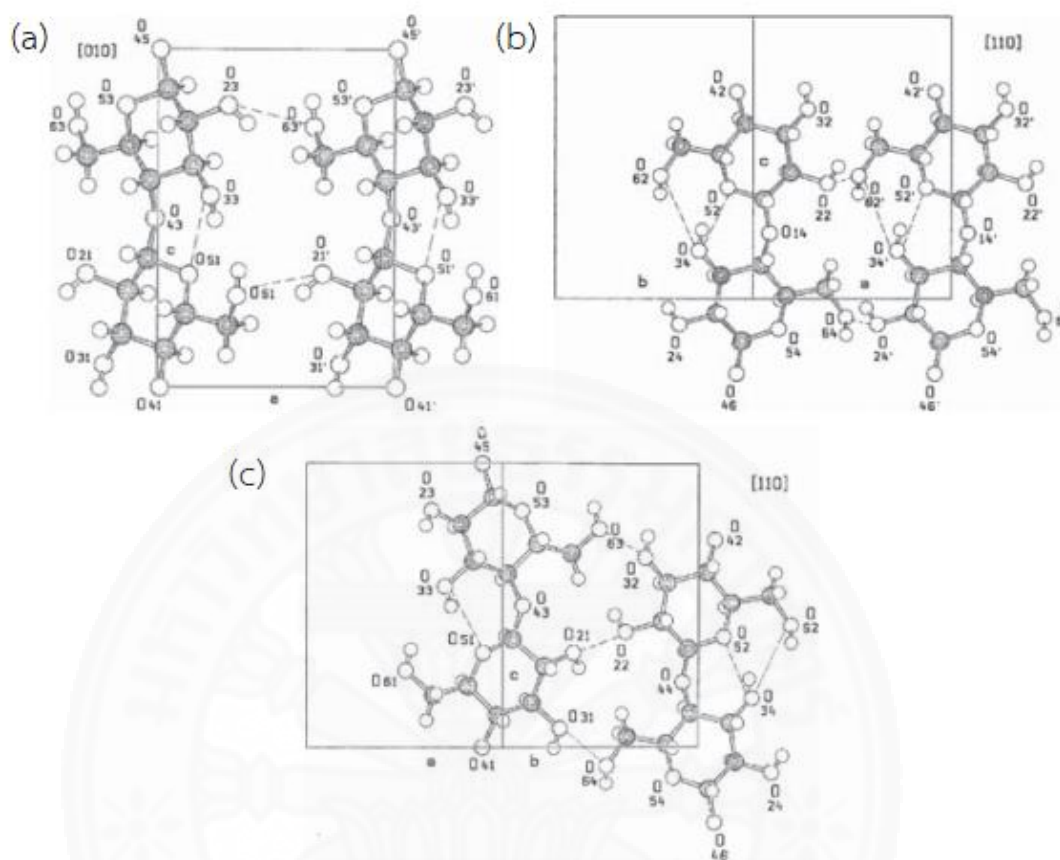
Figure 2.15 Sheet projection of cellulose *II* (a) through the corner along *a*-direction in the [010] plane, (b) through the center along *a*-direction in [110] plane and (c) the projection in the [110] direction of a sheet running through the corner and center of the unit cell (Zugenmaier, 2008).

2.2.2.3. Cellulose *III*

Cellulose *III* can be prepared by the treatment of native cellulose *I* and regenerated cellulose *II* in anhydrous liquid ammonia to form cellulose III_I and III_{II}, respectively. The unit cells for both cellulose III_I and III_{II} are very similar. The molecular and crystal structures of cellulose III_I were determined and proposed that cellulose III_I consists of a one-chain unit cell in monoclinic with space group $P2_1$ while the structure of cellulose III_{II} has not yet been definitely known. The packing parallel and antiparallel arrangements are oriented in unit cells of cellulose III_I, and those of cellulose III_{II}, respectively. The projection in the [001] direction on the *a-b*

plane for the chain structure of cellulose III_I is shown in Figure 2.12. The unit cell dimensions *a, b, c* for cellulose III_I are approximately 4.450 Å, 7.850 Å, 10.31 Å, respectively and angles between the axes α, β, γ are 90°, 90°, 105.1°, respectively (Wada et al., 2004). The similar results have been reported by Ford and co-workers (Ford et al., 2005).
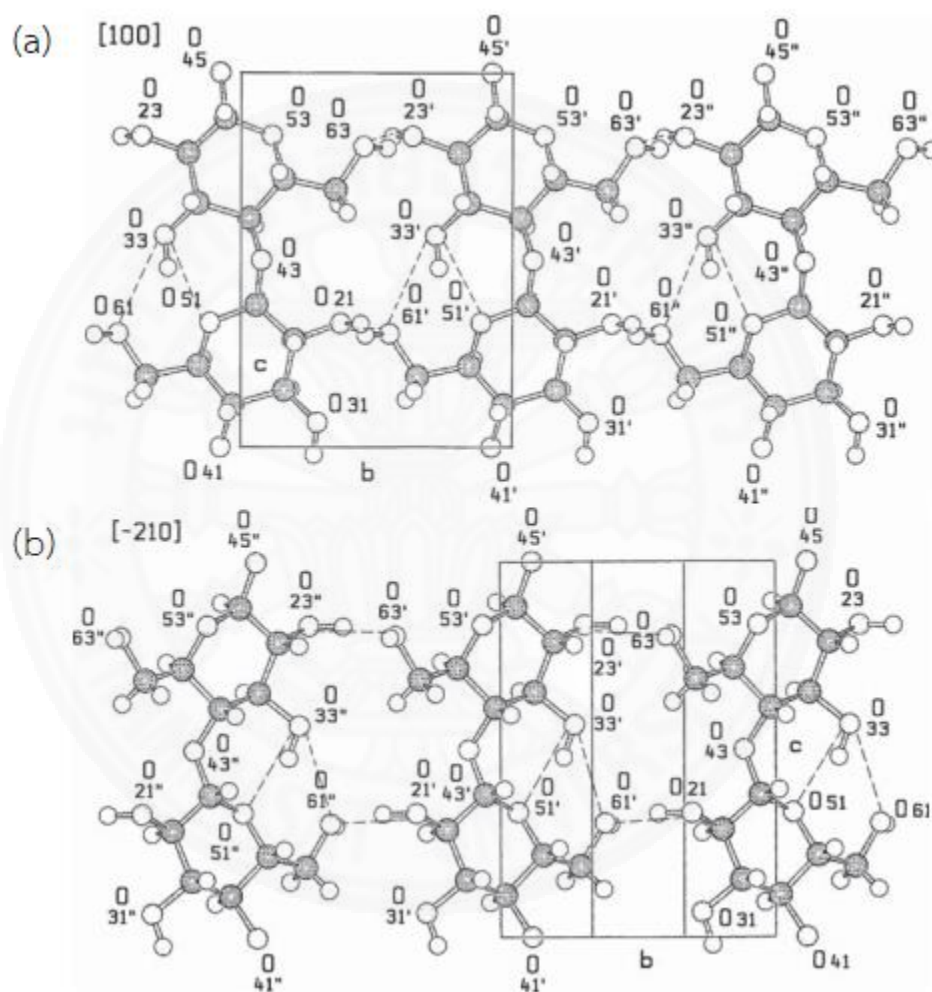
Figure 2.16 Projections of cellulose III_I through the corner along *b* (a) in [100] and (b) in [-210] directions (Zugenmaier, 2008).

Intra-sheets hydrogen bonding observed in cellulose III_I are shown in Figure 2.16. Two intra-sheets can be defined as one aligned along the *b*-axis of the unit cell, the other aligned in a diagonal direction. The same hydrogen bonding occurs between O6 and O2 of adjacent parallel neighboring chains. A bifurcated hydrogen

bond links a donating O3 atom to O5 atom and O6 atom of adjacent in the same chain. Figure 2.17 illustrates the chains stacking in cellulose III_I. The chains lie on top of each other stacking like pennies. The stacks are staggered by half a repeat distance so that hydrogen bonds between two chains in each neighboring stack through strong hydrogen bonds (O6...O2 hydrogen-bonded chains stacked through O2...O6 inter-sheet hydrogen bonds).
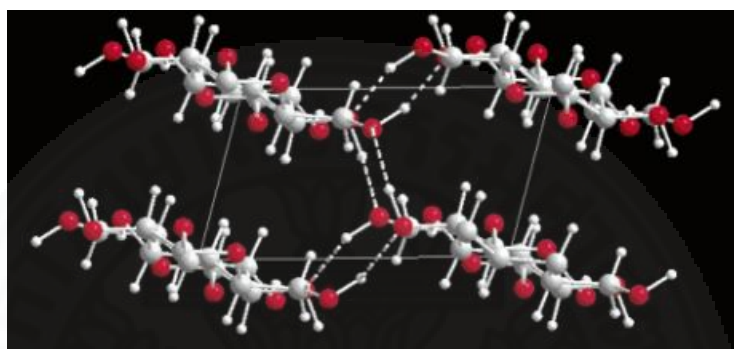
Figure 2.17 Projection of the crystal structure of cellulose III_I down the chain axes directions (Wada et al., 2004).

2.2.2.4 Cellulose IV

Cellulose IV is yielded by heating cellulose III in glycerol at 533 K. The two polymorphs are formed depending on the starting materials. Cellulose III starting from cellulose I is converted to cellulose IV_I polymorph while that starting from cellulose II is formed cellulose IV_{II} polymorph. The projections of the structure of the chain of cellulose IV are shown in Figure 2.12. The unit cell representation of both cellulose IV_I and IV_{II} are similar except for their sheets direction arrangement. The polymorph system of cellulose IV is orthorhombic with space group $P1$ and two chains of repeating unit cells. The unit cell dimensions a, b, c for cellulose IV_1 are 8.03 Å, 8.13 Å, 10.34 Å, respectively and those for cellulose IV_{II} are 7.99 Å, 8.10 Å, 10.34 Å, respectively (Gardiner & Sarko, 1985). The sheets of cellulose IV_I are arranged parallel packing while those of cellulose IV_{II} are arranged antiparallel packing.
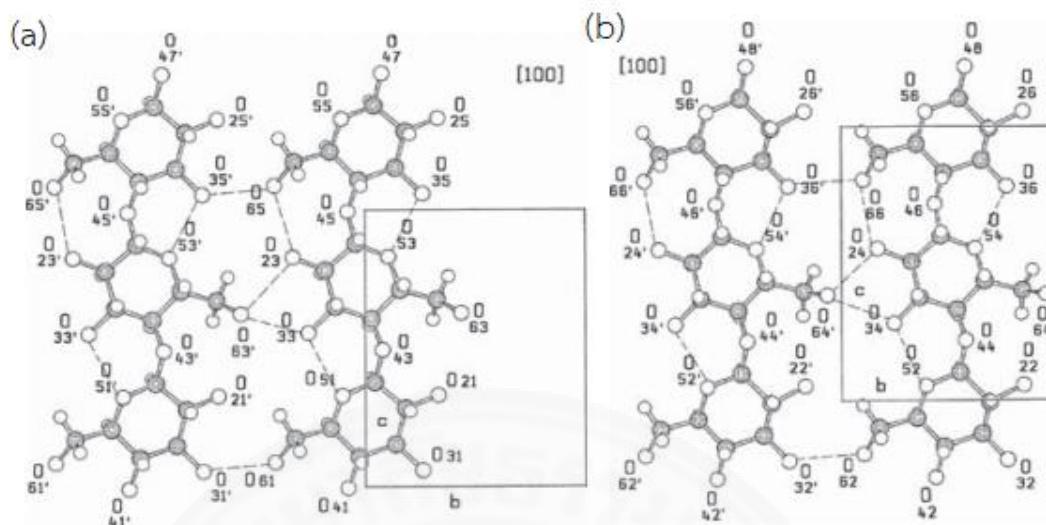
Figure 2.18 Projection in [100] direction of the parallel-running cellulose IV_I up chains in a sheet along b (a) through the origin and (b) through the center (Zugenmaier, 2008).
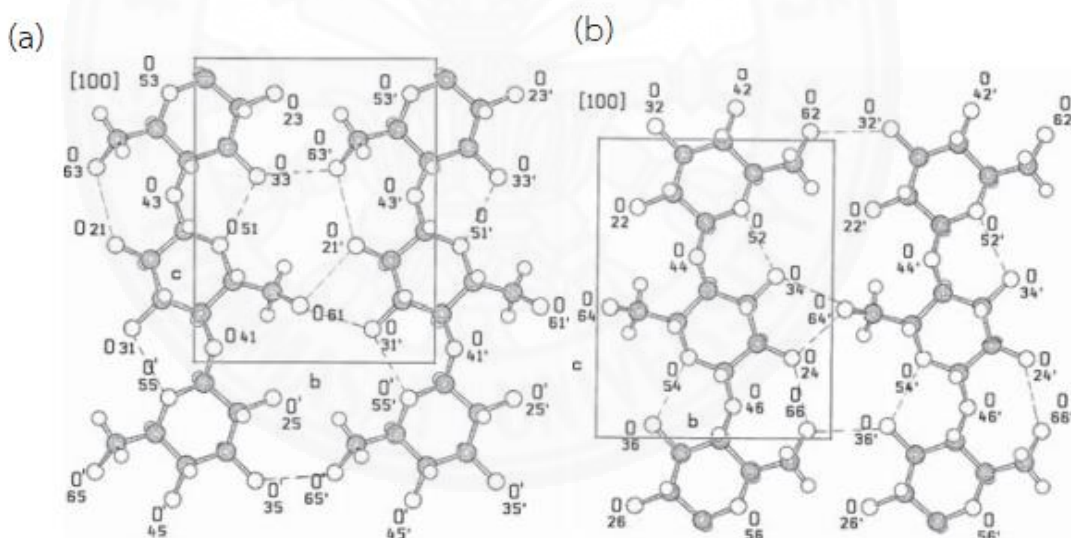
Figure 2.19 Projection in [100] direction of the parallel-running cellulose IV_{II} up chains in a sheet along b (a) through the corner and (b) through the center (Zugenmaier, 2008).

Only intra-sheet hydrogen bonds are presented in cellulose IV except for an inter-sheet hydrogen bond in cellulose IV_{II} positioned at O64 and O51. The intra-sheet hydrogen bonds through origin include O23...O63, O33...O63, O61...O21

and O61...O31 and that through center are O24...O64, O34...O64 and O62...O32 (Figure 2.18Figure 2.19).

2.2.3 Dissolution of cellulose

Cellulose cannot easily be processed homogeneously in conventional solvents owing to the stiffness of the molecules and the dense packing of its chains, due to intra-sheets hydrogen bond between neighboring cellulose polymer chain and inter-sheets hydrogen bond between adjacent cellulose sheets. Two basic solvent systems are used to dissolve cellulose as follows: (i) "Non-derivatizing solvent" dissolving cellulose without any chemical modification and (ii) "Derivatizing solvent" dissolving cellulose through a chemical reaction by covalent bond formation between cellulose and solvent.

2.2.3.1 Non-derivatizing solvent

In the non-derivatizing solvent system, cellulose dissolution results from physical interactions between cellulose and solvent yielding a homogeneous phase. The non-derivatizing solvent molecules dissolve cellulose by breaking the prevailing hydrogen bond network as illustrated in Figure 2.20. High polar solvents are capable of actively interacting with the hydroxyl groups of the cellulose and then the inter- and intramolecular hydrogen bonds are deconstructed. The physical properties of cellulose are changed after regeneration.
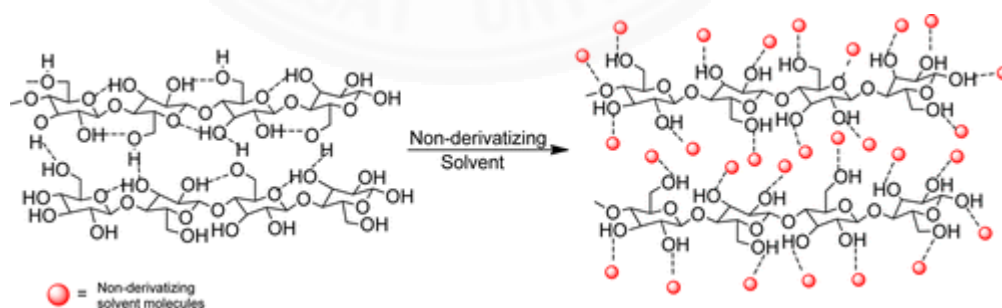
Figure 2.20 Deconstruction of inter- and intramolecular hydrogen bonds of cellulose during dissolution in non-derivatizing solvents (Sen, Martin, & Argyropoulos, 2013).

Cellulose can be dissolved by both aqueous and non-aqueous solvents such as aqueous sodium hydroxide (NaOH), molten salt hydrateds, N-methylmorphorine-N-oxide (NMMO), N,N-dimethylacetamide/lithium chloride (DMA/LiCl).

Isogai and co-worker reported that 5% (m/v) NaOH aqueous solution could dissolve 26-37% of MCC at low temperature of 253 K (-20°C) after swollen in 8-15% NaOH at 277 K (4 °C) (Isogai, Atalla, & Service, 1998). The cellulose dissolution efficiency of the aqueous NaOH was improved by adding urea or thiourea or urea/thiourea to the NaOH solution (Jin, Zha, & Gu, 2007; Ruan et al., 2004; S. Zhang et al., 2009, 2013).

Lyocell is the fibres regenerated from the concentrated solution of cellulose dissolution in an aqueous NMMO. The NMMO solution is the most attractive solvent for cellulose dissolution. Amine N-oxide group in NMMO can open the intrinsic hydrogen bonding between cellulose molecules and can form new hydrogen bonds with the hydroxyl groups of the cellulose. The water content in NMMO and reaction temperature are important factors affecting cellulose dissolution efficiency. Perepelkin proposed the regions of the reaction of the NMMO/water/cellulose system as shown in Figure 2.22 (Perepelkin, 2007). At the high concentration of water above 15 wt%, cellulose cannot be dissolved by NMMO since the hydrogen formation of NMMO with water is more favorable than with cellulose. Although the temperature has a positive effect on the degree of cellulose dissolution, safe processing temperature for cellulose dissolution is suggested in the range of 353-403 K (80-130°C). In 2009 microwave heating technique was applied to enhance the cellulose dissolution in NMMO with shorter time required than conventional heating (Dogan & Hilmioglu, 2009).
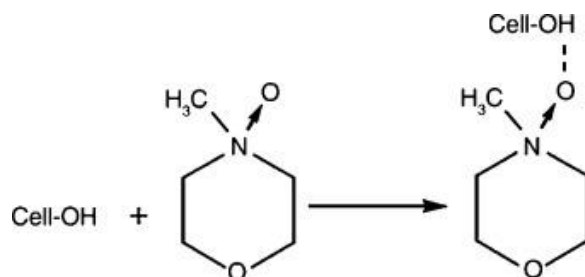
Figure 2.21 The mechanism of cellulose dissolution in NMMO (H. Li et al., 2006).
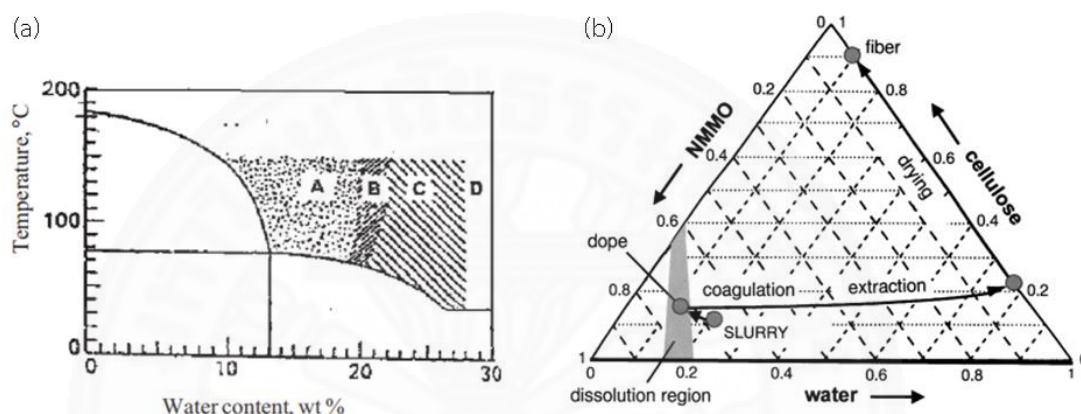
Figure 2.22 (a) Regions of the reaction of the NMMO/water/cellulose system: A) soluble, B and C) irreversible swelling, and D) no visible reaction (Perepelkin, 2007). (b) NMMO/water/cellulose phase diagram (Fink, et al., 2001).

DMA/LiCl is non-aqueous solvent system has been widely used to dissolve cellulose due to its high efficiency and ability to dissolve even high molecular weight cellulose. Figure 2.23 shows the proposed interaction between DMA/LiCl that the LiCl acts as a bridge between cellulose and DMA molecules. As shown in Figure 2.23 (a) the lithium cation interacts with the carbonyl oxygen of DMA via ion-dipole interaction while the chloride anion forms bridging hydrogen bond between hydroxyl groups of cellulose and a lithium-DMA macrocation (McCormick, Callais, & Hutchinson, 1985). Morgenstern and co-worker first suggested a different coordinated interaction between cellulose molecules (Morgenstern et al., 1992). The Morgenstern mechanism was extended by identifying a strong hydrogen formation between the hydroxyl protons of cellulose and the chloride anion with NMR observation as shown in Figure 2.23 (b) (C. Zhang et al., 2014).
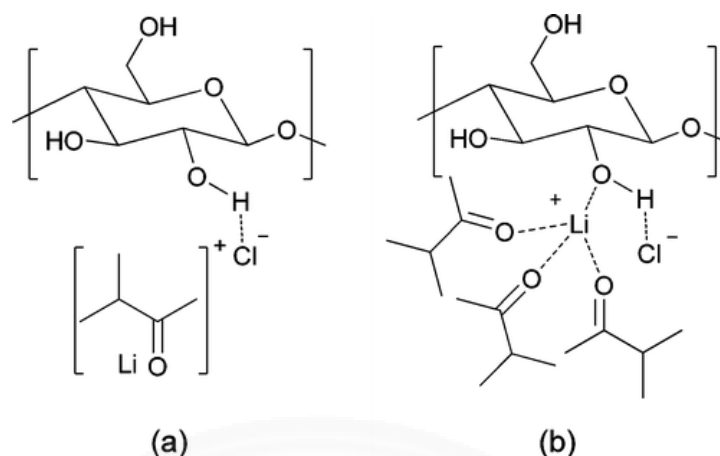
Figure 2.23 The mechanism of cellulose dissolution in DMA/LiCl proposed by (a) McCormick, Callais, & Hutchinson (1985) and (b) Morgenstern (C. Zhang et al., 2014).

Ionic liquids (ILs) are defined as molten salts consisting entirely of cations and anions with a melting point below 373 K (100°C) (Freemantle, 2010). In 1914 Paul Walden synthesized the first ILs, ethylammonium nitrate classified as protic ILs which is formed by the protonation of ethylamine. Molten N-ethylpyridinium chloride is the first IL suggested as solvent for cellulose dissolution (Graenacher, 1934); however, during that time period the definition of ILs was not given. In 2002, Roger and co-workers dissolved cellulose in ILs containing 1-butyl-3-methylimidazolium cation $[C_4mim]^+$ with various anions and also 1-hexyl-3-methylimidazolium cation $[C_6mim]^+$, 1-octyl-3-methylimidazolium cation $[C_8mim]^+$ with chloride salts. They found that 10 wt% of cellulose can be dissolved in $[C_4mim]Cl$ at 373 K (100 °C) and significantly improved to dissolve 25 wt% of cellulose by heating in a microwave oven. Although, cellulose dissolution in the longer-chain substituted ILs appears to be less efficient (Swatloski et al., 2002). Later on the shorter-chain substituted ILs with various anion have been employed to dissolve cellulose such as 1-allyl-3-methylimidazolium chloride [Amim]Cl (H. Zhang et al., 2005), 1-butyl-3-methylimidazolium acetate $[C_4mim]Ac$, 1-ethyl-3-methylimidazolium chloride $[C_2mim]Cl$, 1-ethyl-3-methylimidazolium acetate $[C_2mim]Ac$ (Kosan, Michels, & Meister, 2008).
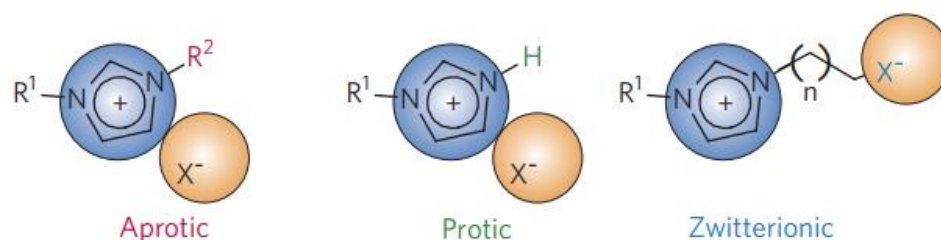
Figure 2.24 Types of ionic liquids: aprotic, protic and zwitterionic (Armand et al., 2009).

The dissolution of cellulose in ILs is achieved by the formation of electron donor-acceptor (EDA) complexes between the hydroxyl electrons and protons of cellulose and the cations and anions of ILs as illustrated in Figure 2.25. The oxygen and hydrogen atoms from hydroxyl groups are separated resulting in the opening of the inter- hydrogen bonds of the cellulose that causes dissolving of cellulose.
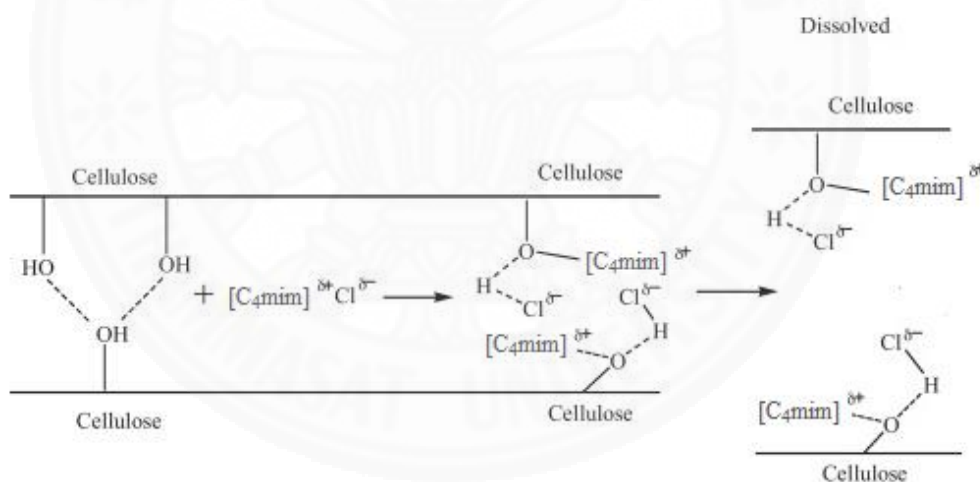
Figure 2.25 Dissolution mechanism of cellulose in ionic liquids adapted from Feng & Chen, (2008).

The dissolved cellulose in the non-derivatizing solvent can be regenerated by precipitation through the addition of anti-solvent. Water, methanol, ethanol, and acetone are excellent anti-solvents that efficiently precipitate cellulose from the solvent. After adding anti-solvent such as water to the solvent and cellulose

mixture, the ions of the solvent form hydrogen bonds with water molecules and they are displaced into the aqueous phase. The interactions between the cation, anion, and cellulose are shielded by the hydrodynamic shells built up by water molecules surrounding the ions of the solvent. Consequently, cellulose which previously interacted with the cation and anion is dissociated and rebuilt its intra and intermolecular hydrogen bonds and then precipitated (H. Tan & Lee, 2012).

2.2.3.2 Derivatizing solvent

The derivatizing solvent is a solvent which induces covalent modifications on the cellulose molecules backbone to form unstable ether, ester or acetal intermediate. Derivatizing cellulose was first accidentally discovered by Christian Friedrich Schoenbein, Swiss chemist in 1845 when he cleaned up some spills of the HNO_3/H_2SO_4 mixture with cotton apron (Liebert, 2010). Its derivative form was reported as cellulose nitrate. Cellulose nitrate or nitrocellulose was first officially synthesized by Alaxander Parkes in 1850 from cellulose treated with HNO_3 (Gilbert, 2017). It can be easily dissolved in alcohols and esters solvent to form a light yellow transparent viscous liquid.
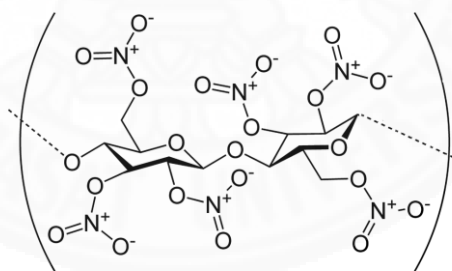
Figure 2.26 Structure of cellulose nitrate (Wikipedia, n.d.).

Dinitrogen tetroxide/N,N-dimethylformamide (N_2O_4/DMF) is one of the derivatizing solvents for cellulose. As the system is heated, N_2O_4 dissociates to NO_2 form which reacts with the hydroxyl group of cellulose. Consequently, an intermediate cellulose nitrite is formed (Schweiger, 1978). Although this homogeneous solution is highly toxic, it is suitable for subsequent acetylation and sulfation. The homogeneous cellulose nitrite was used to prepare cellulose sulfate as replacement of

heterogeneous sulfation of the hydroxyl groups of cellulose. The uniform distribution of the substituents was observed (Schweiger, 1979).

In 1981, the British chemists discovered that carbon disulfide (CS_2) could dissolve aqueous alkaline swollen cellulose to form an intermediate viscose cellulose xanthate. That intermediate can be regenerated in an ammonium sulfate or sulfuric acid and gives rayon or cellophane. Another derivatizing solvent for viscose process of cellulose is Urea/NaOH system. Cellulose reacts to urea and then give cellulose carbamate intermediate that is easily dissolved in dilute NaOH. The viscose cellulose carbamate can be regenerated in sulphuric acid or sodium carbonate solution to give fibers (Liebert, 2010). The derivatizing solvents discussed above are not only suitable for preparing the homogeneous cellulose solution, but also suitable for shaping of cellulose into the fiber and membranes. If the flammable or toxic reagents are used in that process, reactions will possibly produce the toxic by-products.
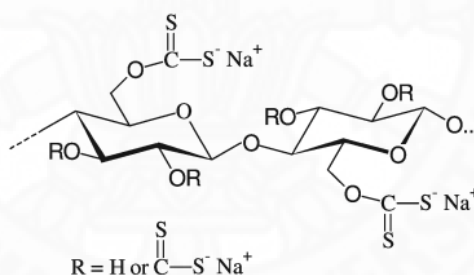
Figure 2.27 Cellulose xanthate, the intermediate formed during the viscose process (Liebert, 2010).

Hydrolytically carboxylic acid esters of the cellulose are investigated as potential derivatizing dissolution intermediate. Formic acid and trifloroacetic acid are main reagents employing for cellulose forming carboxylic acid ester intermediates. The rate of dissolution can be improved in the presence of sulfuric acid and catalyst. Schnabelrauch and co-workers dissolved cellulose in the mixture of formic acid, phosphoric acid, and water within several hours and, then they found that a very short reaction could be observed after addition of sulfuric acid to the system (Schnabelrauch et al., 1992). However, formic acid has been recently reported as hydrolysis reagent

for breaking down the structure of cellulose to monosaccharides and cellulose nanocrystals (B. Li et al., 2015; Sun et al., 2007). Trifloroacetic acid is capable of dissolving cellulose to trifluoroacetyl cellulose intermediate form at room temperature. Using ^{13}C-NMR analysis of cellulose film cast prepared from its trifluoroacetic acid solution, trifluoroacetyl esters are formed selectively at C6-hydroxyl groups of cellulose (Hasegawa et al., 1992).
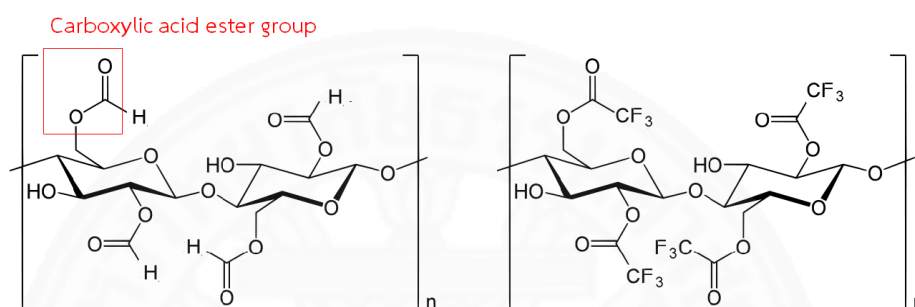
Figure 2.28 Hydrolytically unstable carboxylic acid esters of cellulose; cellulose formate and trifluoroacetyl cellulose.

The mixture of dimethyl sulfoxide/paraformaldehyde (DMSO/PF) has been proposed as a derivatizing solvent for cellulose (Hammer et al., 1979; Johnson, Nicholson, & Haigh, 1976). This solvent is capable of dissolving cellulose containing DP ranging from 16 to 8,000 without degrading α-glycosidic bonds. The optimum temperature for the dissolution is 368-373 K. The cellulose films and fibers are easily regenerated by solidification in methanol or water.

Dimethyl sulfoxide/tetrabutylammonium fluoride trihydrate (DMSO/TBMF) has been used as derivatizing solvent preparing the homogeneous cellulose intermediate which is used as reactant of subsequent reaction yielding cellulose acetate (Ass, Frollini, & Heinze, 2004; Ciacco et al., 2003). The degree of substitution (DS) of the cellulose acetates obtained can be controlled by reaction time, temperature and molar ratio between DMSO and TBMF. A solution of tetraallylammonium fluoride (TAAF) in DMSO has also been reported as a convenient solvent system for cellulose dissolution and derivatization (Casarano et al., 2011).

2.3 Carbon dioxide switchable solvent system

The switchable solvent system is a solvent that could be switched reversibly between one property and another different property by applying a trigger. Carbon dioxide acts as a trigger in the CO_2 switchable system. The process is easily reversed by removal of the CO_2 from the system. The CO_2 switchable solvents also are promising as a green solvents in a perspective of recyclable solvent (Blasucci et al., 2010; Kumar et al., 2017; Memon, Yilmaz, & Soylak, 2017). There are three main classes of switchable solvent system, such as switchable polarity solvent (SPS), switchable hydrophilicity solvent (SHS), and switchable water.

2.3.1 Switchable polarity solvents

The CO_2 switchable solvent was first developed by the Jessop group (Jessop et al., 2005). An ionic liquid (high polarity) was conversed from a molecular liquid (low polarity) by exposure of carbon dioxide and could be reversed back to its non-ionic form when purged with a non-acidic gas, e.g., nitrogen or argon. They reported that system as switchable polarity solvents (SPS). The SPS was prepared as mixtures of two liquid components containing a strong base in conjunction with a proton donor such as alcohol and primary amine and CO_2 gas as a trigger. In addition, only primary and secondary amine also can be switched into SPS after chemically react with CO_2 gas, since the amine is simultaneously both the nucleophile and the proton donor. In 2008, SPS prepared with only a single liquid component was developed and reported (Phan, Andreatta et al., 2008). The reaction between CO_2 and liquid secondary amines including butylmethylamine, benzylmethylamine, dipropylamine, butylethylamine, and butylethylamine forms SPS (molten carbamate salts). The examples of SPS are shown in Figure 2.29.
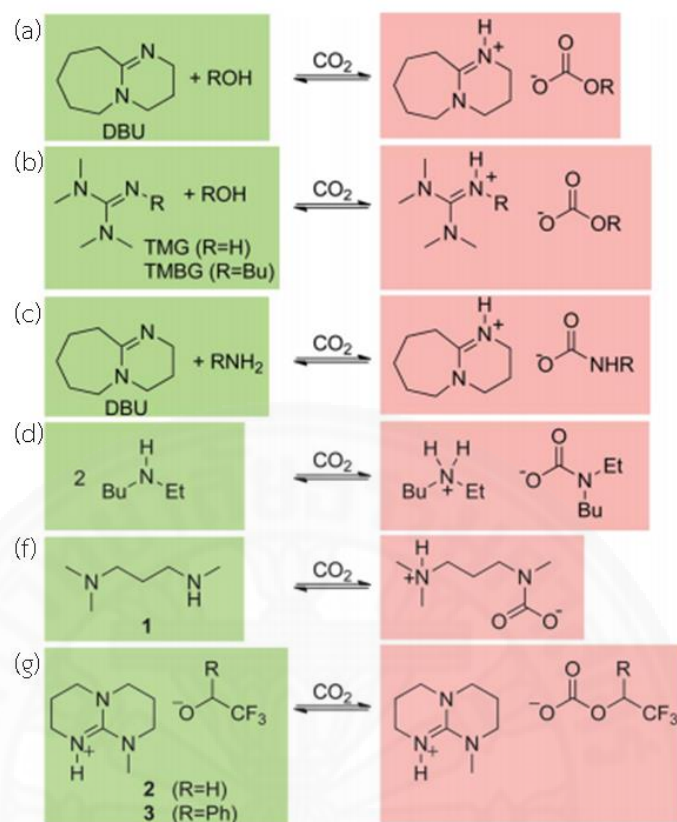
Figure 2.29 The example of SPS (Jessop, Mercer, & Heldebrant, 2012).

The SPS is useful as extracting media like hexane in solvent extraction. Phan and co-worker studied the polymerization of styrene in the mixture of 1,8-diazabicyclo-[5.4.0]-undec-7-ene (DBU) and 1-propanol with $K_2S_2O_8$ as initiator. After CO_2 was bubbled through the solution, the solution conversed into an ionic form, and polystyrene precipitated out of the solution (Phan, Andreatta et al., 2008). Since alcohol and oil have similar adequate polarities, the mixtures of DBU/alcohol or secondary amines/alcohol are miscible with oil resulting in molecular liquid (low-polarity) form. To induce immiscibility with the oil, the solvent decanting method can be carried out by switching the solvent to its high polarity form (Phan et al., 2009)

2.3.2 Switchable hydrophilicity solvents

The switchable hydrophilicity solvents (SHS) was developed later than SPS to improve product-solvent separation efficiency. The variety of SHS has been designed and reported by Vanderveen and co-workers (Vanderveen, Durelle, & Jessop, 2014).

SHS are a solvent capable of reversing its properties between a poorly water-miscible hydrophobic form to a completely water-miscible hydrophilic form (Vanderveen et al., 2014). Water was added to extract solvent from low-polarity organic products, i.e., oil. Consequently, solvent/water mixtures were separated by atmospheric CO_2 bubbling as shown in Figure 2.30 (a). However, the separation of solvent from water remains difficult due to the polar property of water (Phan et al., 2009). The SHS was then developed by adding carbonic water to the product/molecular solvent mixture rather than adding water alone as shown in Figure 2.30 (b). The product was separated from the solvent by switching the solvent hydrophobicity from hydrophobic to a hydrophilic form of the solvent. After decanting the product, solvent/water mixtures could be easily separated by removal of CO_2.
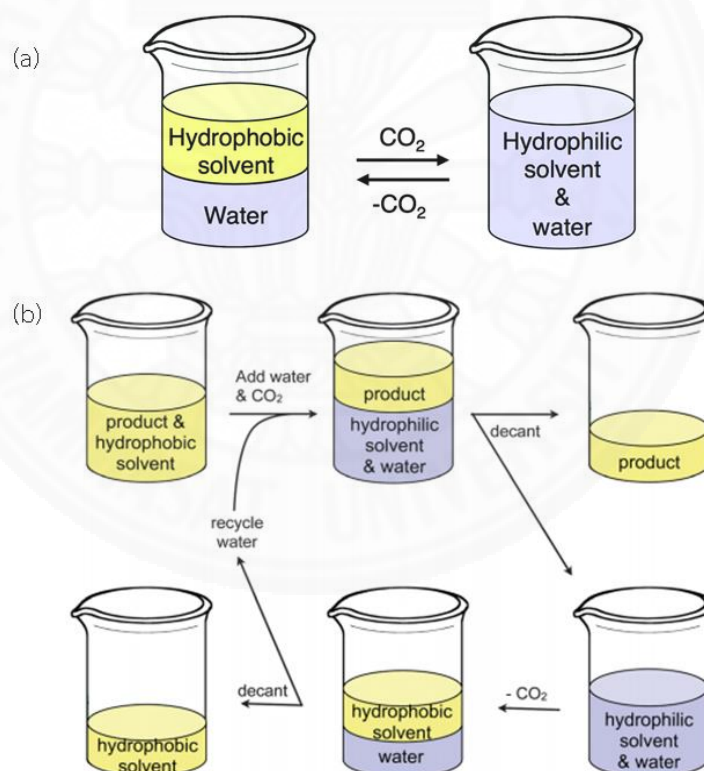
Figure 2.30 (a) SHS changes from hydrophobic to hydrophilic upon addition of CO_2 and removal of CO_2 (Durelle, Vanderveen, & Jessop, 2014) and (b) the application of SHS in separation the extracted product from hydrophobic solvent (Jessop et al., 2012).

2.3.3 Switchable water

Switchable water is an aqueous solution which can be reversibly converted between low-ionic strength and high-ionic-strength form. The aqueous solution consists of very low ionic strengths of base and water. After CO_2 is bubbled, the base is converted to a bicarbonate salt raising the ionic strength of the solution. Moreover, the salt solution can be converted back to its low-ionic strength by CO_2 removal. Applying switchable water for removal organic contaminants from wastewater is greener alternative than traditional salting-out extraction.
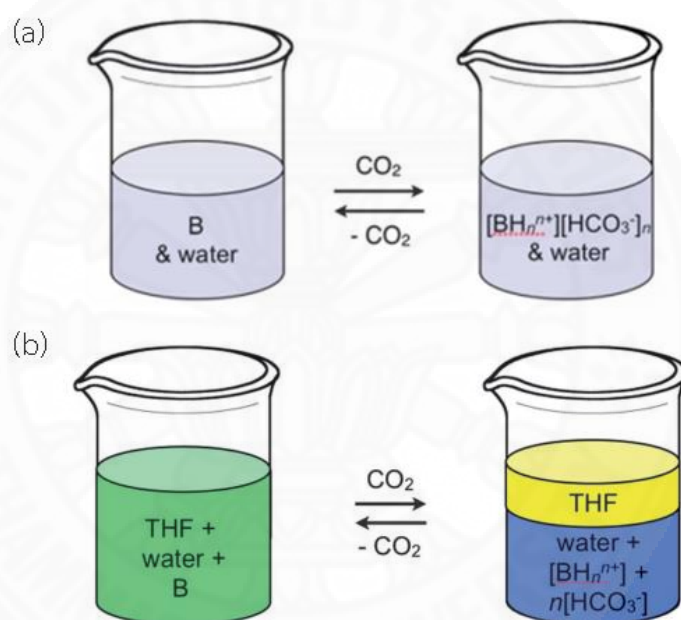
Figure 2.31 Switchable water. (a) The change of base to a bicarbonate salt raising the ionic strength and (b) the use of switchable water to salt-out an organic contaminant THF (Jessop et al., 2012).

2.3.4 Application of switchable solvent system for cellulosic materials

The CO_2 switchable solvents have been applied to cellulose dissolution techniques, such as the application for activation of microcrystalline cellulose (MCC) prior to cellulose hydrolysis yielding glucose. In 2013, the CO_2 switchable systems composed of a strong non-ionic base and CO_2 could completely dissolve the MCC in

dimethylsulfoxide (DMSO). After regeneration, decreasing in the crystallinity index of MCC caused the increase of glucose yield in acid-hydrolysis step (Q. Zhang et al., 2013). Later, the CO_2 switchable systems using 1,1,3,4-tetramethyl guanidine (TMG) in conjunction with various alcohols in DMSO have been designed for dissolution of cellulose. The decreasing crystallinity index of regenerated cellulose corresponds to the decreasing length of the aliphatic chain of alcohol (Xie et al., 2014).
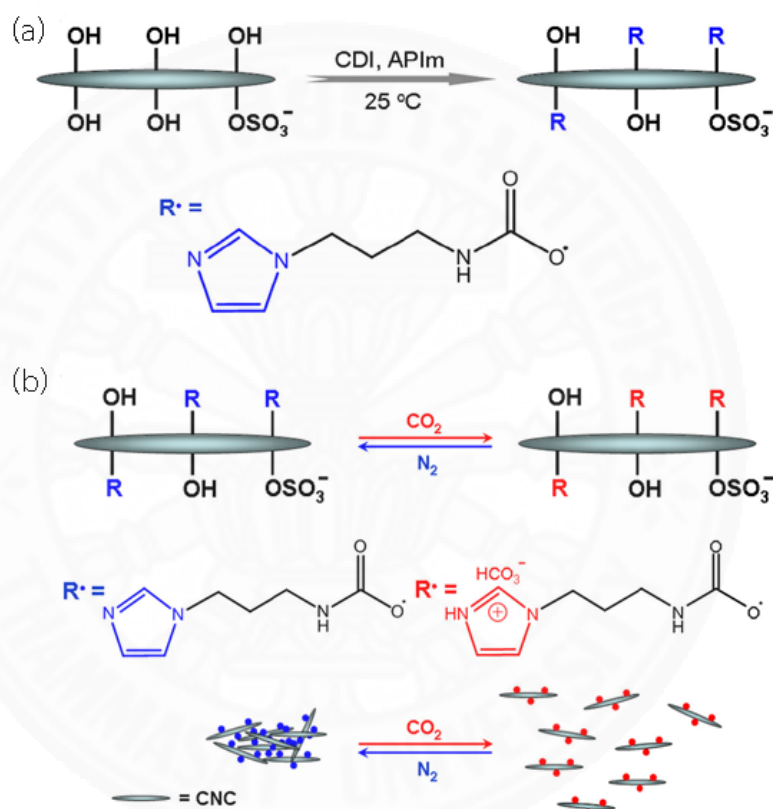
Figure 2.32 (a) Surface modification of CNCs with APIm and (b) Reversible dispersion and aggregation of CNC-APIm in the presence and in the absence of CO_2 (H. Wang et al., 2015).

The CO_2 switchable solvents were applied to the dispersion-gelation conversion of cellulose nanocrystals (CNCs) by surface modification with 1-(3-aminopropyl)imidazole (APIm). The dispersion and aggregation form of CNCs could be conversed by addition or removal of CO_2 (H. Wang et al., 2015). Yang and co-workers employed the CO_2 switchable solvent as a reaction media for in situ syntheses of

cellulose acetate (Y. Yang et al., 2015). Similarly, Song and co-workers employed the CO_2 switchable solvents as an effective media for in *situ* grafting L-lactide (LLA) to cellulose (Song et al., 2015).
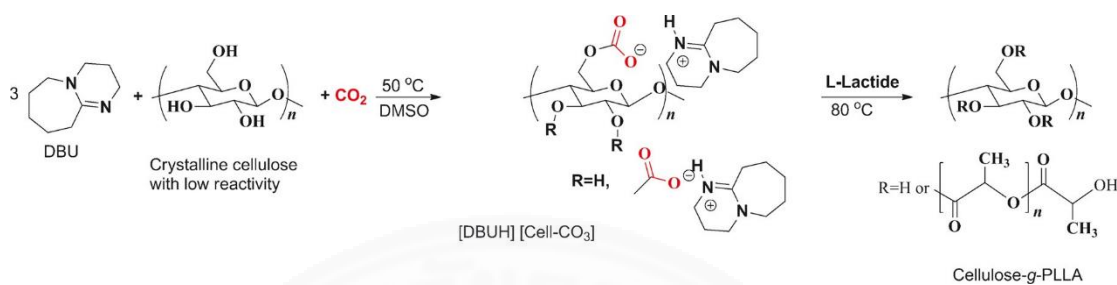
Figure 2.33 In *situ* synthesis of cellulose-g-PLLA in the CO_2 switchable solvent (Song et al., 2015).

2.4 Subcritical and supercritical Fluids

The solvency power of CO_2 can be changeable by varying pressures and/or temperatures including supercritical and subcritical regions.

2.4.1 Fundamentals and physical properties

Phase diagram is a type of chart used to show the preferred physical states of the substances and thermodynamic states of the system at different conditions (pressure, temperature, volume, etc.). Figure 2.34 (a) and (b) show the phase diagrams for a pure substance projection on the *p-T* and *p-V* planes, respectively. If the liquid is heated at a constant *p* or depressurized at a constant *T* across the vapor pressure curve, it will expand and reach to gas state. On the other hand, gas can be turned back into liquid state by cooling or pressurizing across the vapor pressure curve at constant *p* and *T*, respectively. The critical isotherm is represented as $T = T_c$ and the critical isobar is represented as $p = p_c$.

The T_c is the highest temperature where the coexistence of two phases (liquid and gas) of the substance is observed under corresponding combination of the *p-T* point is called the critical point (T_c, p_c) as shown in Figure 2.34 (a). The end of vapor

pressure curve (Figure 2.34 (b)) is a critical point of any substances at specific p and T. At p below p_c and T above T_c, the regime is called "subcritical-compressed gas" while, at T below T_c and p above p_c, the regime is called "subcritical-compressed liquid" as shown in Figure 2.34 (a). If the liquid is heated at constant p above the p_c, it expands and reaches a vapor-like state without undergoing a phase transition. This phenomenon is called "the continuity of states" and the vapor-like state beyond T_c and p_c point is called "the supercritical state". In a supercritical regime, a liquid and vapor phase cannot be distinguished.
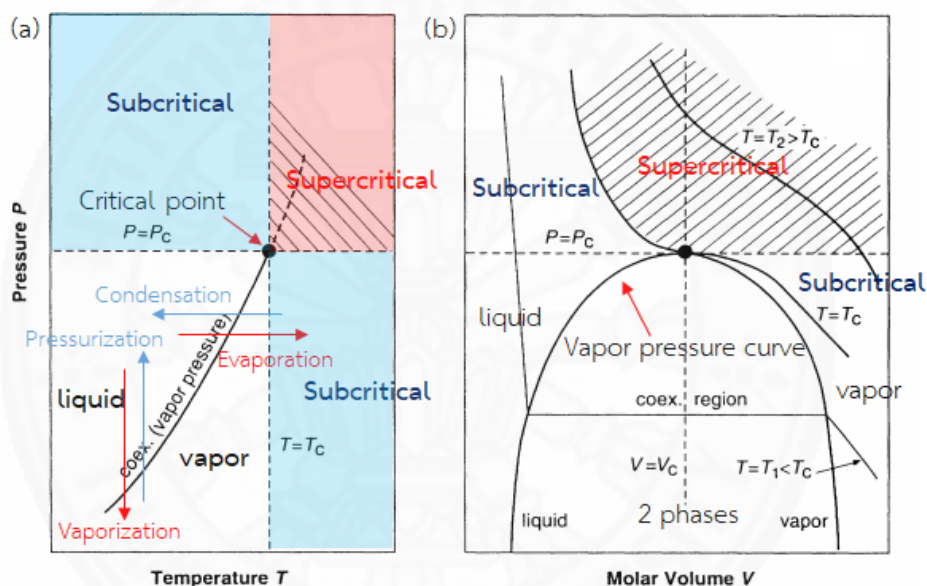
Figure 2.34 (a) The p-T phase diagram and (b) the p-V phase diagram of a one-component fluid with critical point adapted from Sengers (2000).

In Figure 2.34 (b), the two branches for vapor pressure curve and the critical isochore, $V = V_c$ are provided. The liquid and vapor phases coexist in the area under the vapor pressure curve (two-phase region). At two-phase region, the liquid-gas coexistence have the same pressure but different molar volume, so the isothermal compressibility (κ_T), the change in volume due to change in pressure under constant temperature, is infinite. At the critical point, the κ_T is also infinite unless the critical point is located at one-phase region. At the supercritical state, the isotherm ($T=T_2>T_c$) have finite slope and the κ_T is very high. The supercritical fluid (SCF) is neither liquid

nor gas; however, they perform an intermediate behavior between that of a liquid and a gas. SCFs exhibit liquid-like solvating characteristics of high density and gas-like mass transfer properties of low viscosity and high diffusivity that provide tunable properties of SCFs for various uses in materials preparation and processing technology.

Table 2.3 Physical properties for general gases, SCFs, and liquids.

Physical property	Gases	SCFs	Liquids
Density ($kg\,m^{-3}$)	0.6 – 2	200 – 500	600 – 1600
Dynamic Viscosity ($10^3\,kg\,m^{-1}\,s^{-1}$)	0.01 – 0.3	0.01 – 0.03	0.2 – 3
Kinematic viscosity ($10^6\,m^2\,s^{-1}$)	5 – 500	0.02 – 0.1	0.1 – 5
Diffusivity ($10^6\,m^2\,s^{-1}$)	10 – 40	0.07	0.0002 – 0.002

Table 2.3 lists typical values of the physical properties for each fluid state. Evidently, SCFs have physical properties both those of a gas and a liquid. As seen in Table 2.3, the physical properties show large gradients between gas and SCFs states; nevertheless, that large gradients present only at the pressure and temperature near the critical point. At above T_c, a gas cannot be liquefied, regardless of the pressure applied; however, a gas can be liquefied by applying pressure alone at temperature below its T_c as shown in Figure 2.35. At small increase of pressure, it gives rise to the density of SCFs. Moreover, a variation of pressure near the critical point causes large changes in several other physical properties such as viscosity and solubility. Therefore, SCFs is pressure-dependent change in the characteristic, especially density.

2.4.2 Applications

The SCFs typically have a viscosity ten times lower than water, a gas-like diffusivity and a liquid-like density, so it would be expected to have high penetrability into complex geometries better than normal liquids (Beckman, 2004). In addition, SCFs, especially $ScCO_2$, are non-toxic, non-flammable and naturally abundant sources material that can be withdrawn from the environment thus they are the promising

green and sustainable substance. Due to those unique physical and chemical properties of SCFs, supercritical fluid technologies have been exploited for a wide variety of industrial applications such as food, cosmetics, pharmaceutical, polymer and plastics, chemical, and materials industries.
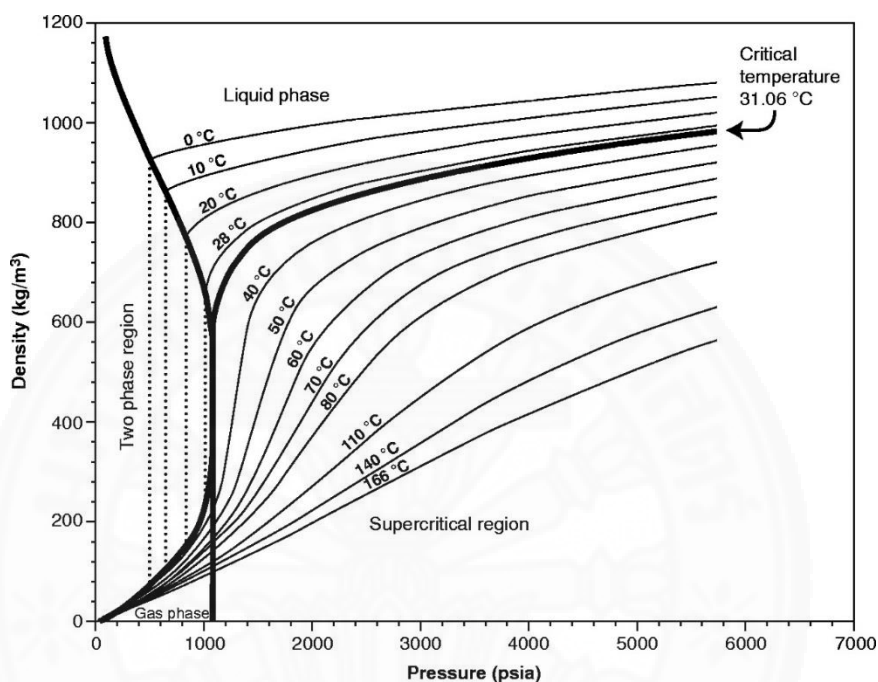
Figure 2.35 Density-pressure phase diagram for carbon dioxide (DeSimone, 2002).

2.4.2.1 Extractions

In food, cosmetics and pharmaceutical industries, SCFs have been employed as an extraction solvent for natural products such as herbs and essential oils to prevent the damage caused by high-temperature extraction process and organic solvent left in conventional extraction. Moreover, many literatures have recently reported that SCFs have the potential for extraction of fish oil and other bioactive compounds from animal sources to obtain high-quality products. The examples of the extract obtained using SCFs technology are listed in Table 2.4.

Table 2.4 Natural extracts obtained from natural sources by using SCFs as the extracting solvent.

Raw material	Extract	Media	Ref.
Thymus vulgaris leaves	Thymol and Carvacrol essential oils	$ScCO_2$	Vieira De Melo et al. 2000
Rosemary leaves	Carnosol, Rosmanol, Carnosic, Cirsimaritin, Genkwanin	Subcritical water	Ibañez et al. 2003
Shiitake	Shiitake oil	$ScCO_2$ or $ScCO_2$ + co-solvent	Kitzberger et al. 2009
Pomegranate seed	Phenolic compounds	Subcritical water	He et al. 2012
Fish	Fish oil	$ScCO_2$	Rubio-Rodríguez et al. 2012
Kabosu peel	Citrus	$ScCO_2$ + water	Suetsugu et al. 2013
Sunflower seed	Sunflower oil	$ScCO_2$ + ethanol	Rai, Mohanty, and Bhargava 2016
Hemp waste	Waxes and Cannabidiol	$ScCO_2$	Attard et al. 2018

2.4.2.2 Polymer processing

In plastics industry, SCFs are employed to swell polymer materials and change their physicochemical properties. Several literatures reveal the melting point of crystalline polymeric materials changes by applying SCFs-based processing. Lian and coworkers studied the depression of the biodegradable polymers melting temperature (T_m) using compressed carbon dioxide and they found that T_m of the polymers with a linear fashion decreases significantly as pressure of carbon dioxide increase (Lian et al., 2006). That indicates the SCFs are plasticizing agent in polymeric process since; they can reduce the system viscosity by sorption and swelling the polymer. Consequently, the system allows processing at lower temperature (decreasing T_m) (Kelly et al., 2012). Additionally, the literature also reveals that the SCFs absorption into the polymer results in the decreasing glass transition temperature (T_g) of the polymer (Kazarian, 2000).

The $ScCO_2$ is capable of dissolving the polymers with low molecular-weight and slightly polar. Carbon dioxide interacts with the basic site in polymer molecules, such as the interaction between the carbon dioxide and the carbonyl group in PMMA. The carbon dioxide acts as a Lewis acid and incorporates with carbonyl groups which served Lewis base causing PMMA miscible in $ScCO_2$ (Shieh & Liu, 2002). On the other hand, the high-polar or water soluble polymers cannot dissolve in $ScCO_2$ even at high temperature and pressure. It is pronounced that the dissolubility of the polymers in $ScCO_2$ depend on the polymer architecture, chain end groups and co-solvent using in the process (McHugh, Mandel, & Wang, 2002).

2.4.2.3 Materials drying

Drying gels by evaporation induce xerogels (dry gel) which exhibit significant shrinkage and cracking since capillary effects occurring as liquid is removed from the gels. SCFs, which have no existing liquid/gas phase boundary has been applied to dry the gels instead. Initially, the supercritical drying achieved by the transformation of the pore liquid (unbound) into a supercritical fluid by heating and pressuring the gel, resulting in removal of the pore fluid by depressurization to produce an aerogel (a porous dry gel).

Table 2.5 exemplifies the common single-component solvents and their critical values. However, in practice, several solvents have so high critical temperature and pressure that seriously affect the structure or destroy the crystal network of the gel. Additionally, safety issue arising from the usage of organic solvents at elevated temperature and pressure in industrial-scale production must take into consideration due to their hazardous and inflammability properties.

Table 2.5 Critical constants for solvents.

	T_c (K)	p_c (MPa)
Methanol	512.55	7.99
Ethanol	516.15	6.3
1-Propanol	536.65	5.1
2-Propanol	508.25	4.7
1-Hexanol	609.95	4.0
Tetrahydrofuran	540.15	5.12
Acetonitrile	548.15	4.77
Dichloromethane	510.15	6.0
Chloroform	536.35	5.42
Water	647.25	21.7
Carbon dioxide	304.15	7.3

Supercritical carbon dioxide ($ScCO_2$) which has a low critical temperature and pressure has been proposed and extensively applied for supercritical drying. Param and co-workers proposed the low-temperature supercritical drying by substituting liquid CO_2 for the alcohol in the alcogel (gel in ethanol) and pressurizing it to its supercritical state. They found that the time required for drying is shorter than conventional drying (Tewari, Hunt, & Lofftus, 1985). Figure 2.36 shows the protocols for different drying method using $ScCO_2$. In Figure 2.36 (a), the pore liquids that are miscible in CO_2 are washed and replaced first by liquid CO_2 following by elevating pressure to

its supercritical state. In the case of CO_2 immiscible pore liquid, the pore liquid has to be replaced by alcohol or acetone first. Alternatively, the mixture of pore liquid and CO_2 is pressurized to supercritical state together as shown in Figure 2.36 (b). That means the washing step is performed by supercritical CO_2; however; the critical constant for the binary system (the mixture of pore liquid and CO_2) should be considered. Figure 2.37 shows a binary critical curve of CO_2 and ethanol system. Above the binary critical curve, CO_2 and ethanol are miscible under a supercritical state. Below the binary curve, liquid ethanol coexists with gaseous CO_2.
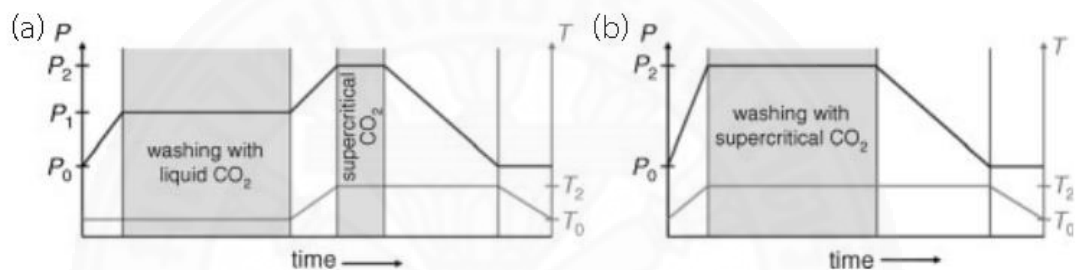
Figure 2.36 Protocols for drying methods with $ScCO_2$ (Tsotsas & Mujumdar, 2014).
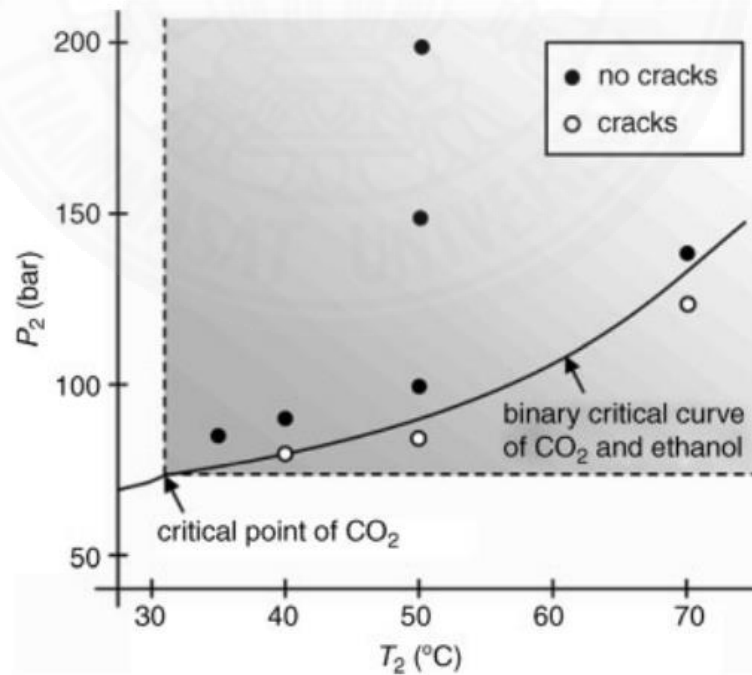
Figure 2.37 Binary phase diagram of ethanol/CO_2 mixture above the critical point of CO_2 (Tsotsas & Mujumdar, 2014).

ScCO$_2$ drying technique has been used to remove water from Berau coal (Iwai et al., 2002). Due to high critical pressure of water, it took more than 40 h and 30 h to dry the coal at 313.15 K under ScCO$_2$ at 9.8 and 14.7 MPa, respectively. The solvents with low critical constant such as methanol has been added as an entrainer. After adding 10.4 mol % methanol with CO$_2$, the drying time reduces about four times.

2.5 Shrinking unreacted-core model

A shrinking unreacted-core model is a rate expression model describing the heterogeneous reaction that the solid particle contacts with surrounding gas or liquid. The reaction occurs first at the outer surface of the particle and then moves into the particle. During the reaction, the solid reactant in the reaction zone is converted to product or inert solid (ash) while that in the non-reaction zone (unreacted core) shrinks in size by time.

The shrinking unreacted-core model has been widely studied in the literature. For example, the shrinking particle–shrinking core model has improved predictions of the leaching of zinc from zinc ore containing silica by incorporation of the mass transfer resistance of a thin gelatinous layer into the model (Safari et al., 2009). Dokoumetzidis et al. (2008) developed a kinetically limited model for drug dissolution under the assumption of the rate controlling step. A developed numerical predictive model of the pyrolysis of shrinking cellulose particles for bio-oil production illustrated that intraparticle heat transfer was the dominant step in cellulose pyrolysis (Lin et al., 2012). Chen et al. (2017) recently modified a shrinking core model for the combustion of gaseous fuel via heterogeneous reactions with granular metal oxide and achieved better prediction of the conversion rate under varying gaseous reactant diffusion rate and particle shape conditions.

The present work involves with the reaction between a porous solid and a gaseous reactant, thus unreacted shrinking core model and shrinking particle model are commonly applied.

2.5.1 Unreacted shrinking core model

An unreacted shrinking core model describing the progressive conversion with reaction time as shown in Figure 2.38. The converted substance or "ash" is referred as porous and inert solid so that it allows diffusion of gas reactant from the outer particle surface to the surface of the unreacted core. As a result, the size of unreacted core shrinks during progress of the reaction whereas the particle size of the reactant remains unchanged. The shrinking core model is the most adequate to the majority of reacting gas-solid interface by which a combustion of coal is the best example. During the combustion, oxygen gas diffuses through the gas boundary and reacts with coal at its external surface. During conversion of the reacted coal to the ash layer around unreacted coal region, carbon dioxide is generated as gas product.
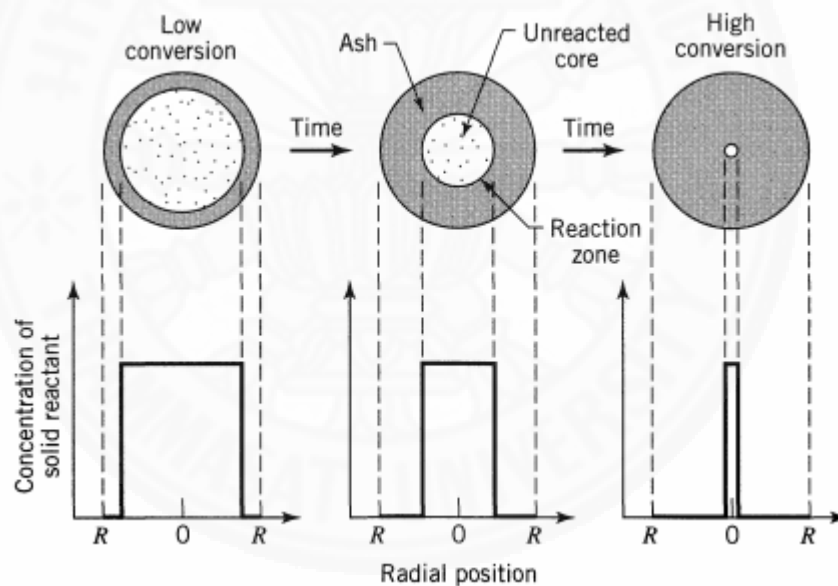
Figure 2.38 Schematic diagram of unreacted shrinking core model. The reaction initially takes place at the external particle surface and proceeds toward the center of the particle (Levenspiel, 1972).

The unreacted core model was first developed by Yagi and Kunii (Yagi & Kunii, 1955) who studied combustion rate of single carbon particle in flames and fluidized bed. Yagi and Kunii proposed five steps that proceed during the reaction as shown in Figure 2.39. Firstly, the gaseous reactant A diffuses to the surface of the solid

particle B through the gas film covering the particle. Secondly, the gaseous reactant A then pass through the ash layer to the unreacted core surface. Thirdly, the reaction between gaseous A and solid B reactants takes place at the surface of the unreacted core. Next, gaseous products diffuse through the ash layer back to the outer surface of the solid particle. Finally, the gaseous products at the particle surface then diffuse through the gas film back into the main body of fluid.

The step with the highest resistance (slowest step) that is considered as rate-controlling step is used to simplify the overall rate of reaction. However, the diffusion of gaseous product through the ash layer and gas film do not contribute directly to the resistance to the reaction if no gaseous products are formed or if the reaction is irreversible. Therefore, only the conversion equations in steps 1, 2 and 3 are developed and considered as rate-controlling steps.
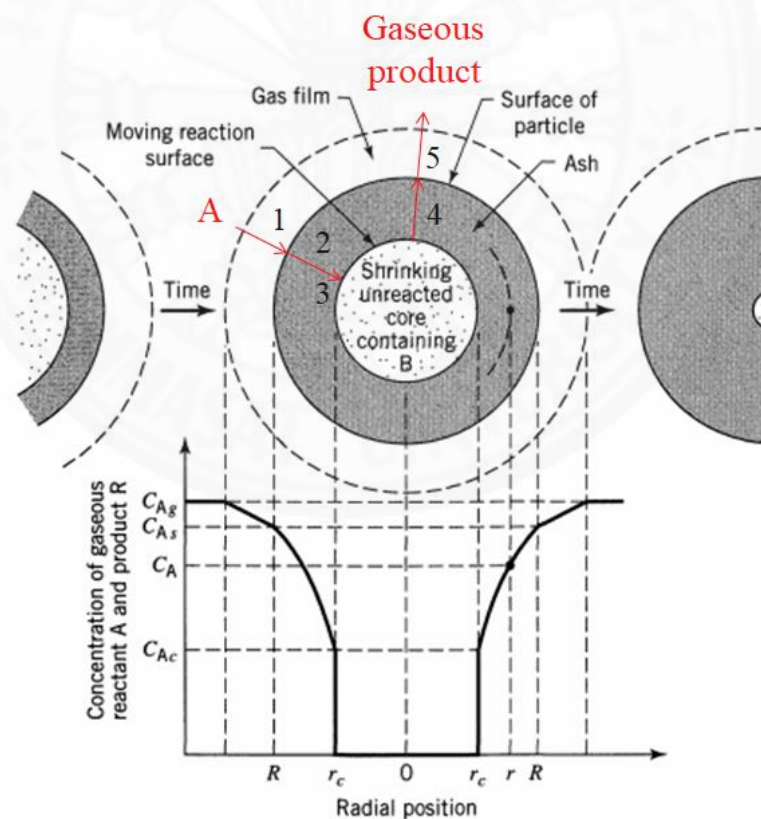
Figure 2.39 According to the unreacted shrinking core model, mass transfer and reaction steps occurring in series, and concentration profile of gaseous reactant A and product for the reaction $A(g) + bB(s) \rightarrow product$ adapted from Levenspiel (1972).

2.5.1.1 Gas film diffusion controls

The concentration profile for gaseous reactant A when the resistance of the gas film controls the overall rate of reaction as illustrated in Figure 2.40. C_{Ag}, C_{As} and C_{Ac} represent the concentration of gaseous A at the main body of the fluid, particle surface and unreacted core surface, respectively. In addition, R and r_c are the radius of the solid particle and unreacted core, respectively. At the surface of the particle $C_{As} = C_{Ac} = 0$; therefore, the concentration driving force, represented by ($C_{Ag} - C_{As}$) is constant as reaction of the particle proceeds.
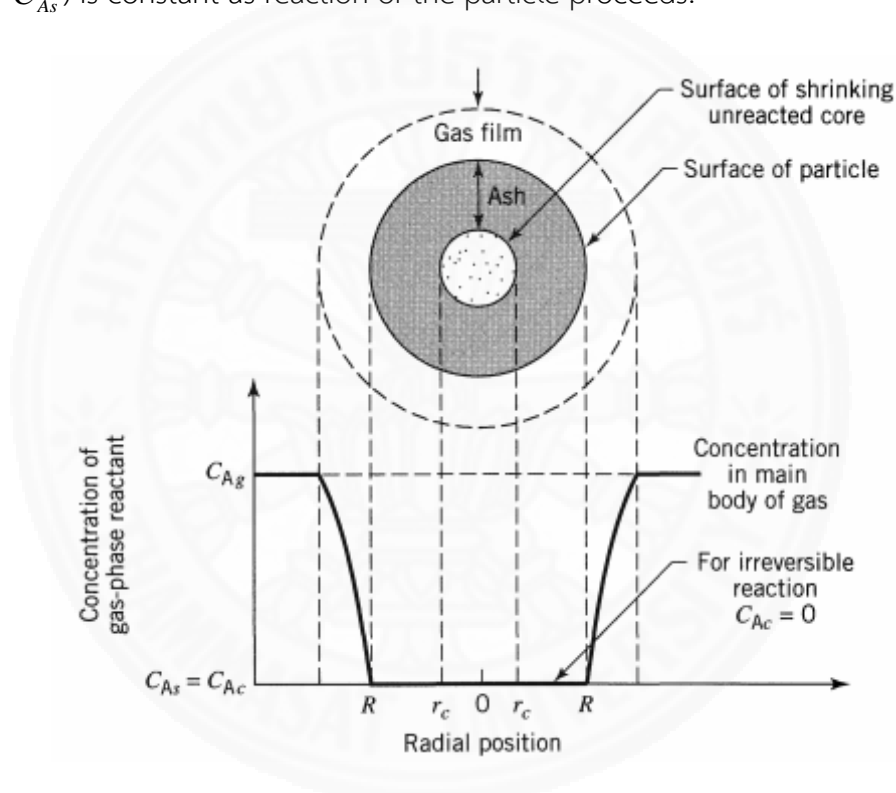
Figure 2.40 Schematic diagram and concentration profile of a reacting particle when diffusion through the gas film is the controlling resistance (Levenspiel, 1972).

The reaction between gaseous A reactant and solid B reactant gives

$$A(g) + bB(s) \rightarrow product \qquad\qquad 2\text{-}1$$

Hence, the stoichiometry of Eq. (2-1) is $dN_B = bdN_A$, where N_A and N_B are the moles of reactant A and B, respectively.

The kinetic equation based on the particle surface (S_{ex}) is given by

$$-\frac{1}{S_{ex}}\frac{dN_B}{dt} = -\frac{1}{4\pi R^2}\frac{dN_B}{dt} = -\frac{b}{4\pi R^2}\frac{dN_A}{dt} = bk_g\left(C_{Ag} - C_{As}\right) = bk_g C_{Ag} = \text{constant} \quad \text{2-2}$$

The amount of B present in the particle (N_B) is expressed in Eq. (2-3)

$$N_B = \rho_B V = \left(\frac{\text{moles B}}{\text{m}^3 \text{solid}}\right)\left(\text{m}^3 \text{solid}\right) \quad \text{2-3}$$

where ρ_B is the molar density of B in the solid

and V is the volume of a particle.

The decrease in volume or radius of unreacted core associated with the disappearance of the moles of solid reactant (dN_B) is then given by

$$-dN_B = -b\, dN_A = -\rho_B dV = -\rho_B d\left(\frac{4}{3}\pi r_c^3\right) = -4\pi\rho_B r_c^2 dr_c \quad \text{2-4}$$

Substituting Eq. (2-4) into Eq. (2-2) gives the rate of reaction in terms of the shrinking radius of the unreacted core as the following

$$-\frac{1}{S_{ex}}\frac{dN_B}{dt} = -\frac{\rho_B r_c^2}{R^2}\frac{dr_c}{dt} = bk_g C_{Ag} \quad \text{2-5}$$

where k_g is the mass transfer coefficient between fluid and particle.
Rearranging and integrating, thus

$$-\frac{\rho_B}{R^2}\int_R^{r_c} r_c^2 dr_c = bk_g C_{Ag}\int_0^t dt \quad \text{2-6}$$

$$t = \frac{\rho_B R}{3bk_g C_{Ag}}\left[1 - \left(\frac{r_c}{R}\right)^3\right] \quad \text{2-7}$$

Set $r_c = 0$ for complete conversion of a particle in Eq. (2-7), then the time required (τ) is given by

$$\tau = \frac{\rho_B R}{3 b k_g C_{Ag}}$$ 2-8

The fraction of radius of the unreacted core existing between dimensionless residence time and time for complete conversion is obtained by combining Eqs. (2-7) and (2-8) yielding

$$\frac{t}{\tau} = 1 - \left(\frac{r_c}{R}\right)^3$$ 2-9

Writing in terms of fractional conversion obtains

$$1 - X_B = \left(\frac{volume\ of\ unreacted\ core}{total\ volume\ of\ particle}\right) = \frac{\frac{4}{3}\pi r_c^3}{\frac{4}{3}\pi R^3} = \left(\frac{r_c}{R}\right)^3$$ 2-10

Therefore, the time-radius and time-conversion relationships can be expressed as

$$\frac{t}{\tau} = 1 - \left(\frac{r_c}{R}\right)^3 = X_B$$ 2-11

2.5.1.2 Ash layer diffusion controls

When the resistance of diffusion through the ash is a rate-controlling step, the rate expression is developed and analyzed in two steps. Initially, a typical partially reacted particle is examined by writing the flux relationships for diffusion of gaseous reactant A into the particle at any r. Subsequently, a fully reacted particle is determined by integrating the function of the first step between R and 0. The concentration profile for gaseous reactant A during diffusion through the ash layer controls the overall rate of reaction as shown in Figure 2.41. The boundary of the unreacted core moves radially inward from R to r_c position similar to the moving direction of reactant A. In modeling of gas/solid system, the steady-state approximation of the stationary unreacted core is justified because the shrinkage rate of the unreacted core is about 1000-fold slower than the flow rate of A toward the unreacted core.
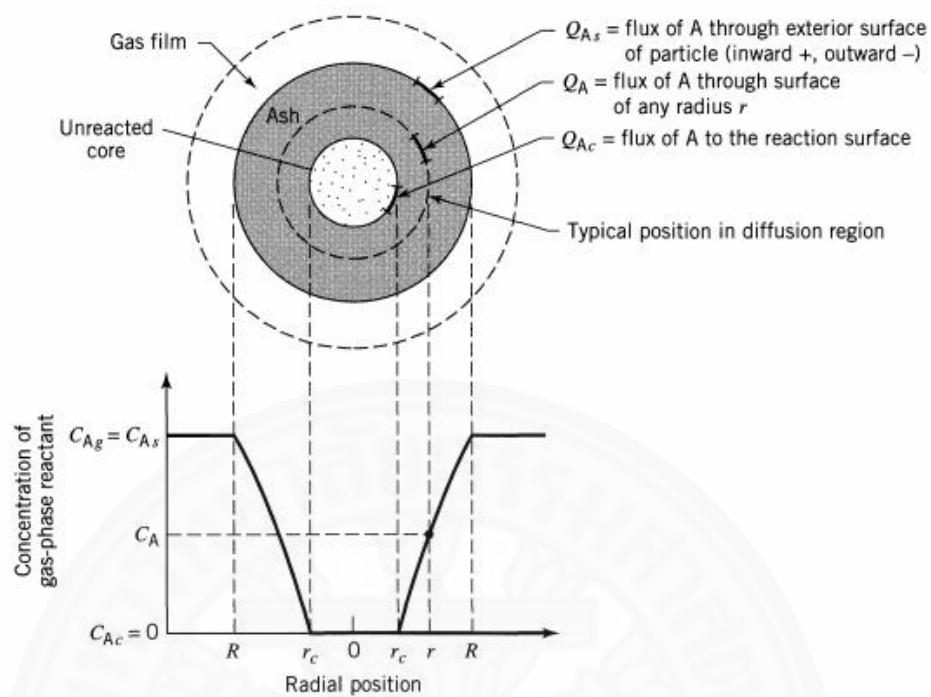
Figure 2.41 Schematic diagram and concentration profile of a reacting particle when diffusion through the ash layer is the controlling resistance (Levenspiel, 1972).

For gas/solid system, the rate of diffusion of A to the reaction surface is constant due to the steady-state assumption. Considering the rate diffusion of A in the ash layer to the reaction surface at any time gives

$$-\frac{dN_A}{dt} = 4\pi r^2 Q_A = 4\pi R^2 Q_{As} = 4\pi r_c^2 Q_{Ac} = \text{constant} \qquad \text{2-12}$$

For facilitating problem-solving procedure, let the flux of A within the ash layer be expressed by Fick's law for equimolar counter-diffusion, though other forms of this diffusion equation will give similar result. It is noted that both Q_A and dC_A / dr are positive, then

$$Q_A = D_e \frac{dC_A}{dr} \qquad \text{2-13}$$

where D_e is the effective diffusion coefficient of gaseous reactant A in the ash layer. Combining Eqs. (2-12) and (2-13), then the rate of reaction of A for any r is obtained as

$$-\frac{dN_A}{dt} = 4\pi R^2 D_e \frac{dC_A}{dr} = \text{constant} \qquad \text{2-14}$$

Integrating across the ash layer from R to r_c obtains

$$-\frac{dN_A}{dt} \int_{r=R}^{r=r_c} \frac{dr}{r^2} = 4\pi R^2 D_e \int_{C_{Ag}=C_{As}}^{C_{Ac}=0} dC_A \qquad \text{2-15}$$

or

$$-\frac{dN_A}{dt}\left(\frac{1}{r_c} - \frac{1}{R}\right) = 4\pi D_e C_{Ag} \qquad \text{2-16}$$

Eq. (2-16) represents the conditions of a reacting particle at any time.

In the second step of analysis, the size of unreacted core changes with time. As the unreacted core shrinks, the ash layer becomes thicker resulting in the decreasing rate of diffusion of A (dN_A/dt is no longer constant).

Writing N_A in Eq. (2-16) in terms of r_c by replacing dN_A with $\frac{4\pi\rho_B r_c^2}{b} dr_c$ (Eq. (2-4)) then rearranging and integrating across the moving unreacted core from R to r_c obtains

$$-\rho_B \int_{r_c=R}^{r_c}\left(\frac{1}{r_c} - \frac{1}{R}\right) r_c^2 dr_c = bD_e C_{Ag} \int_0^t dt \qquad \text{2-17}$$

or

$$t = \frac{\rho_B R^2}{6bD_e C_{Ag}}\left[1 - 3\left(\frac{r_c}{R}\right)^2 + 2\left(\frac{r_c}{R}\right)^3\right] \qquad \text{2-18}$$

Then, the time required for complete conversion ($r_c = 0$) of a particle is

$$\tau = \frac{\rho_B R^2}{6bD_e C_{Ag}}$$
2-19

Dividing Eq. (2-18) by Eq. (2-19) yields the progression of reaction in terms of the time dimensionless residence time and time for complete conversion (Eq. (2-20)) and fractional conversion (Eq. (2-21)).

$$\frac{t}{\tau} = 1 - 3\left(\frac{r_c}{R}\right)^2 + 2\left(\frac{r_c}{R}\right)^3$$
2-20

and

$$\frac{t}{\tau} = 1 - 3(1 - X_b)^{2/3} + 2(1 - X_b)$$
2-21

2.5.1.3 Chemical reaction controls

Figure 2.42 illustrates concentration profile of the gaseous reactant A under chemical reaction control. When the mass transfer rate through the gas film around the particle is assumed to be very fast, the concentration of A at unreacted core surface equals to that at outer particle surface and that in the bulk gas.
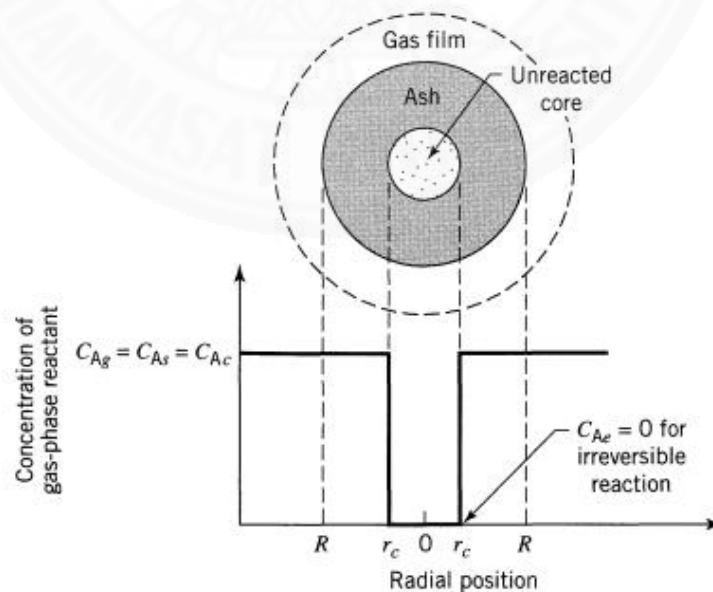
Figure 2.42 Schematic diagram and concentration profile of a reacting particle when the chemical reaction is the controlling resistance (Levenspiel, 1972).

The reaction occurs at the surface of unreacted core regardless of existing ash layer; thus, the rate of reaction is written based on the unit surface of unreacted core as

$$-\frac{1}{4\pi r^2_c}\frac{dN_B}{dt}=-\frac{b}{4\pi r^2_c}\frac{dN_A}{dt}=bk''C_{Ag} \qquad \text{2-22}$$

where k'' is the first-order rate constant for the surface reaction. Writing N_B in terms of the shrinking radius by substituting Eq. (2-4) in to Eq. (2-22) gives

$$-\frac{1}{4\pi r^2_c}\rho_B 4\pi r^2_c\frac{dr_c}{dt}=-\rho_B\frac{dr_c}{dt}=bk''C_{Ag} \qquad \text{2-23}$$

Rearranging and integrating yields

$$-\rho_B\int_R^{r_c}dr_c=bk''C_{Ag}\int_0^t dt \qquad \text{2-24}$$

or

$$t=\frac{\rho_B}{bk''C_{Ag}}\left(R-r_c\right) \qquad \text{2-25}$$

Finding the time for complete conversion by setting r_c equal to zero, then yields

$$\tau=\frac{\rho_B R}{bk''C_{Ag}} \qquad \text{2-26}$$

Writing the progression of reaction time in terms of fractional conversion gives

$$\frac{t}{\tau}=1-\frac{r_c}{R}=1-\left(1-X_B\right)^{1/3} \qquad \text{2-27}$$

2.5.2 Shrinking spherical particle model

Unlike the shrinking-core model, shrinking particle model is applied to the reaction that the reacted solid particle shrinks during the reaction. Consequently, no ash layer surrounding the solid reactant particle is observed. For the shrinking particle model, there is a series of three step reaction including diffusion of gaseous reactant

A to the surface of the solid reactant, the reaction between A and solid on the surface and diffusion of the product back into the body of gas as shown in Figure 2.43.
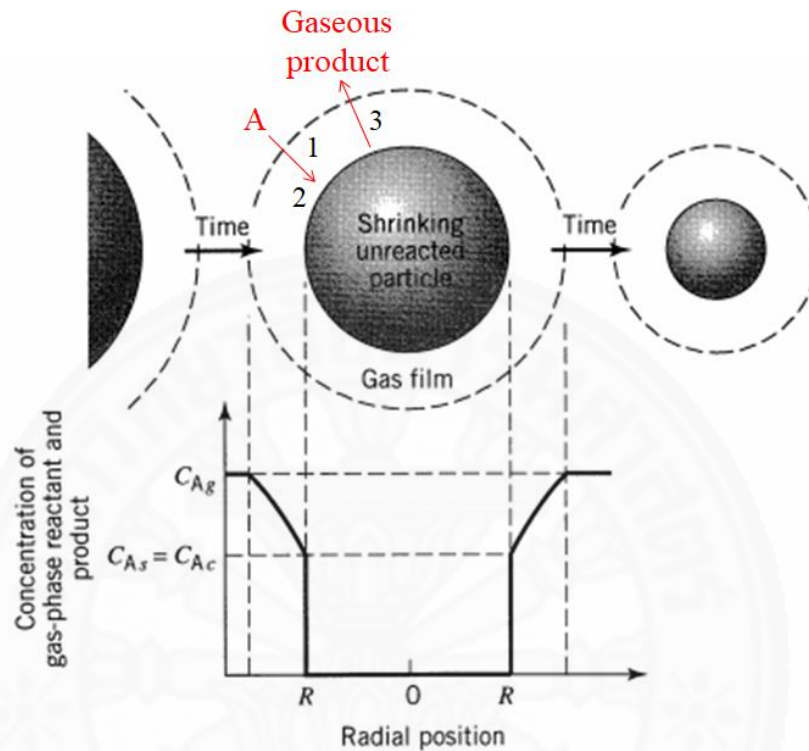
Figure 2.43 According to the shrinking particle model, mass transfer and reaction steps occurring in series, and product for the reaction $A(g) + bB(s) \rightarrow product$ adapted from Levenspiel (1972).

2.5.2.1 Gas-film diffusion controls

Film resistance in shrinking particle model differs from shrinking core model, especially considering the size of the solid particle change with time. In that case, mass transfer coefficient k_g is not constant but varies within a particular range depending on various factors, such as the relative velocity between particle and fluid, size of the particle, fluid properties and method of contacting fluid with solid. For example of contacting fluid with solid in free fall system, a mass transfer of a solid component of mole fraction y in a fluid is given by

$$\frac{k_g d_p y}{D} = 2 + 0.6(Sc)^{1/3}(\mathbf{Re})^{1/2} = 2 + 0.6\left(\frac{\mu}{\rho D}\right)^{1/3}\left(\frac{d_p u \rho}{\mu}\right)^{1/2} \qquad \text{2-28}$$

If diffusion is a limiting factor, changing particle size during reaction causes change in k_g. Generally, k_g rises for an increase in gas velocity and for smaller particles.

$$k_g \sim \frac{1}{d_p} \text{ for small } d_p \text{ and } u$$

$$k_g \sim \frac{u^{1/2}}{d_p^{1/2}} \text{ for large } d_p \text{ and } u$$

The decrease in volume as the radius of a particle reducing from R_0 to R is then given by

$$dN_B = \rho_B dV = 4\pi \rho_B R^2 dR \qquad \text{2-29}$$

Thus, the rate of reaction in terms of the shrinking particle radius based on the particle surface is then given by

$$-\frac{1}{S_{ex}}\frac{dN_B}{dt} = -\frac{\rho_B 4\pi R^2}{4\pi R^2}\frac{dR}{dt} = -\rho_B \frac{dR}{dt} = bk_g C_{Ag} \qquad \text{2-30}$$

As example for small particle (particle in the Stokes law regime $k_g \sim \frac{1}{d_p}$) Eq. (2-28) reduces to

$$k_g = \frac{2D}{d_p} = \frac{D}{R} \qquad \text{2-31}$$

Combining and integrating

$$\int_{R_0}^{R} RdR = \frac{bC_{Ag}D}{\rho_B}\int_0^t dt \qquad \text{2-32}$$

$$t = \frac{\rho_B R_0^2 bC_{Ag}D}{2bC_{Ag}D}\left[1 - \left(\frac{R}{R_0}\right)^2\right] \qquad \text{2-33}$$

Thus, the time required for complete disappearance of a particle is

$$\tau = \frac{\rho_B R_0^2 b C_{Ag} D}{2 b C_{Ag} D}$$ 2-34

Writing the progression of reaction time in terms of fractional conversion gives

$$\frac{t}{\tau} = 1 - \left(\frac{R}{R_0}\right)^2 = 1 - \left(1 - X_B\right)^{2/3}$$ 2-35

2.5.2.2 Chemical reaction controls

The rate expression of shrinking particle model when chemical reaction controls is identical to that of the shrinking-core model as described in section 2.5.1.3.

2.6 Lithium-air battery

The lithium-air battery which is the second highest theoretical energy density battery of an anode and cathode couple, is assembled with the combination of lithium metal and air electrodes couple (Imanishi, Luntz, & Bruce, 2014). It is a rechargeable battery that gains increasing attention in its development as possible power sources for electric vehicles (EVs). Toyota Motors, the world's biggest car company has been researching on development of lithium-air battery as the next generation vehicle battery which can store more energy than the lithium-ion battery (Casey, 2017). Abraham and Jiang proposed the concept of the lithium-air rechargeable battery as the battery consisting of a lithium metal anode, an electrolyte conducting lithium ion, and a composite cathode made up of high surface area carbon (Abraham & Jiang, 1996). Cathode is separated from anode by a separator filled with electrolyte containing lithium salts in organic solvents or ionic liquids. The electrolyte is responsible for the separation of ionic transport and electronic transport by the diffusion of lithium ions from cathode to anode during the charging and the reverse discharging process. For carbon-composite electrode oxygen, an electroactive cathode material with air accessed from the environment is reduced at the air cathode during battery discharge to generate electric power.

$$2Li + O_2 \leftrightarrow Li_2O_2 \qquad\qquad\qquad 2\text{-}36$$

$$4Li + O_2 \leftrightarrow 2Li_2O \qquad\qquad\qquad 2\text{-}37$$

$$4Li + 6H_2O + O_2 \leftrightarrow 4\left(LiOH \cdot H_2O\right) \qquad\qquad 2\text{-}38$$

There are two types of reversible lithium-air battery depending on the electrolyte type such as non-aqueous and aqueous systems. The redox reactions at the air cathode in the non-aqueous system are given in Eqs. (2-36) and (2-37) while the reaction in the aqueous system is given in Eq. (2-38). Recently, hybrid non-aqueous/aqueous and solid-state lithium-air batteries have been proposed as newly developed lithium-air batteries (Tan et al., 2017). However, it is technically challenging to develop the non-aqueous lithium-air battery towards improving environmental performance.
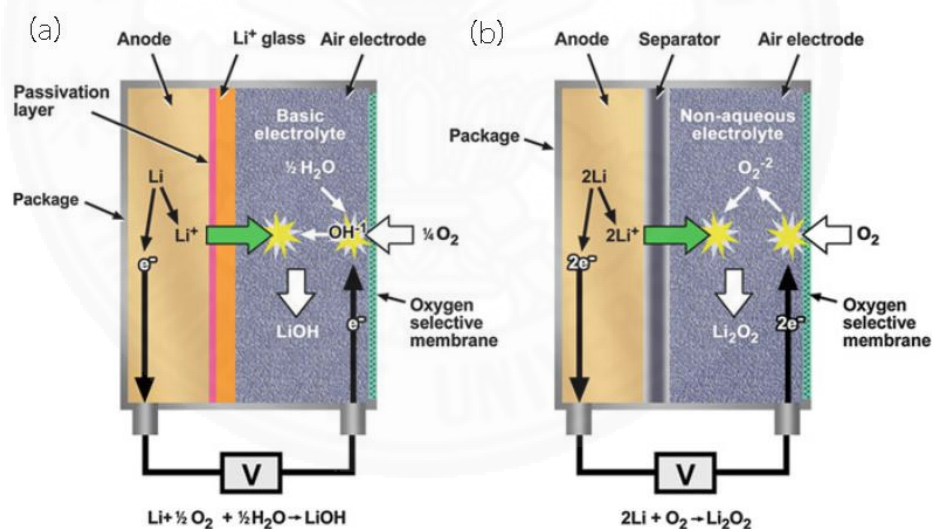
Figure 2.44 Schematics of reaction processes in the lithium-air battery during battery discharge. (a) Aqueous lithium-air battery and (b) non-aqueous lithium-air battery (Imanishi et al., 2014).

2.6.1 Electrochemistry mechanism

Electricity results from the flow of electrons from one atom to another. The electrons transfer from anode to cathode due to the electrochemical potential

force during battery discharge and move in the opposite direction due to the electric rechargeable. The reactions at anode and cathode site are shown in Eqs. (2-39) to (2-41).

$$Li \leftrightarrow Li^+ + e^- \qquad \text{(Anode)} \qquad \text{2-39}$$

$$2Li^+ + 2e^- + O_2 \leftrightarrow Li_2O_2 \qquad \text{(Cathode)} \qquad \text{2-40}$$

$$4Li + 4e^- + O_2 \leftrightarrow 2Li_2O \qquad \text{(Cathode)} \qquad \text{2-41}$$
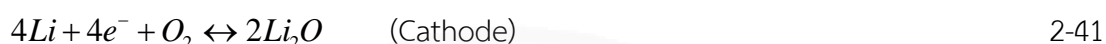
Lithium metal is such a powerful reducing agent that it tends to lose electrons as readily as possible during battery recharge as written in Eq. (2-39). Moreover, lithium is one of favorable candidates for anode material due to its light weight, lowest anode potential and high specific capacity of all. To achieve high reversible capacity, improved power capacity, good ionic and electrical conductivity, and long cycle stability, composite active material is developed by selecting suitable porous material to host the lithium metal.

The anode is reduced upon charge and oxidized during discharge as shown in Figure 2.45 (a) and (b). On the other hand, the cathode is a sink for the lithium ions, is oxidized during charge as shown in Eqs. (2-40) and (2-41). After oxygen enters cathode, it is reduced and accepts the electron from anode during discharge. Subsequently, forming lithium- and oxygen-containing species, namely Li_2O_2 and Li_2O, are adsorbed on the cathode surface associated with electrolyte film decomposition and impurities adsorption resulting in the air-diffusion path blocking. In case of the air-breathing cathode, Li_2O_2 is the major discharge product produced (Tan et al., 2017).
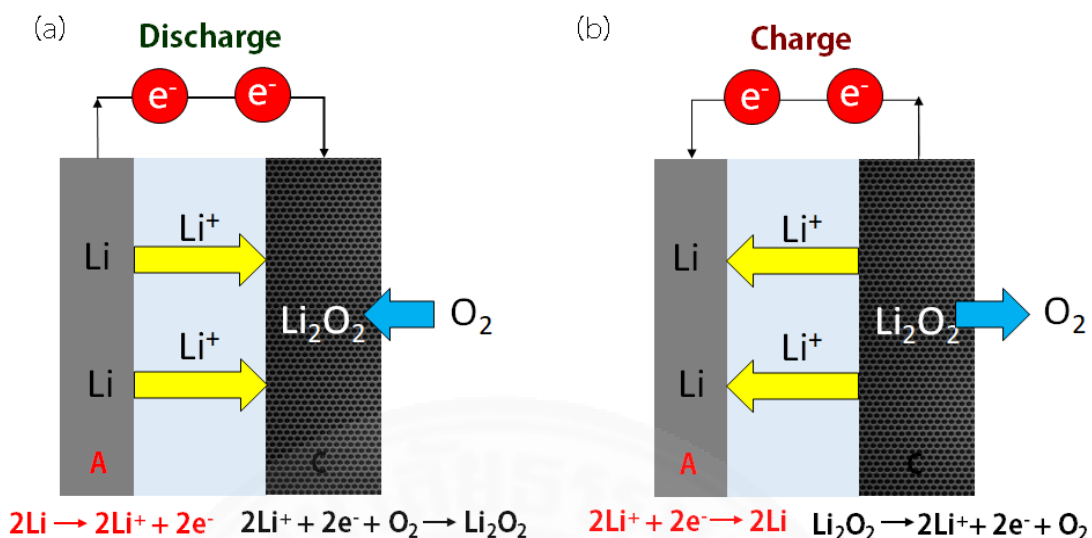
Figure 2.45 Schematics of the non-aqueous lithium-air battery (a) during battery discharge and (b) during battery charge.

2.6.2 Carbon as an air cathode

The carbon materials are used to improve performances of the air cathode due to its high capacity, high surface area, and high porosity. Example of various benefits arising from the use of carbon electrode which the porous carbon electrode supplies electrons continuously for the electrochemical process resulting in enhancement of energy storage. Additionally, the carbon with large surface area gives high lithium-air battery performance due to more active sites for electrochemical reactions and catalyst loading. Unfortunately, the product formed from the reaction between carbon and Li_2O_2 can block the oxygen-diffusion path by the decomposition of carbon materials as shown in Eqs. (2-42) and (2-43) (Tan et al., 2017).

$$Li_2O_2 + C + \frac{1}{2}O_2 \rightarrow Li_2CO_3 \qquad\qquad 2\text{-}42$$

$$2Li_2O_2 + C \rightarrow Li_2O + Li_2CO_3 \qquad\qquad 2\text{-}43$$

The carbon air cathode usually composites with a small amount of a binder such as a polytetrafluoroethylene (PTFE) and polyvinylidene fluoride (PVDF) for

long-term stability (Kunanusont & Shimoyama, 2018; Y. Wang & Zhou, 2010). Wang and Zhou (2010) developed the carbon cathode that composed of the Mn_3O_4/carbon composite catalytic layer and acetylene black/PTFE gas diffusion layer for an aqueous lithium-air battery. They found the battery performs very high discharge capacity of 50,000 mAhg^{-1}. Kunanusont and Shimoyama (2018) fabricated the porous acetylene carbon black/PVDF electrode and applied in the lithium-air battery. They found that the battery can perform discharge-charge capability more than 3 cycles. This is a further challenge to improve the carbon air cathode to be stable for the long term and to practically work in the lithium-air battery.
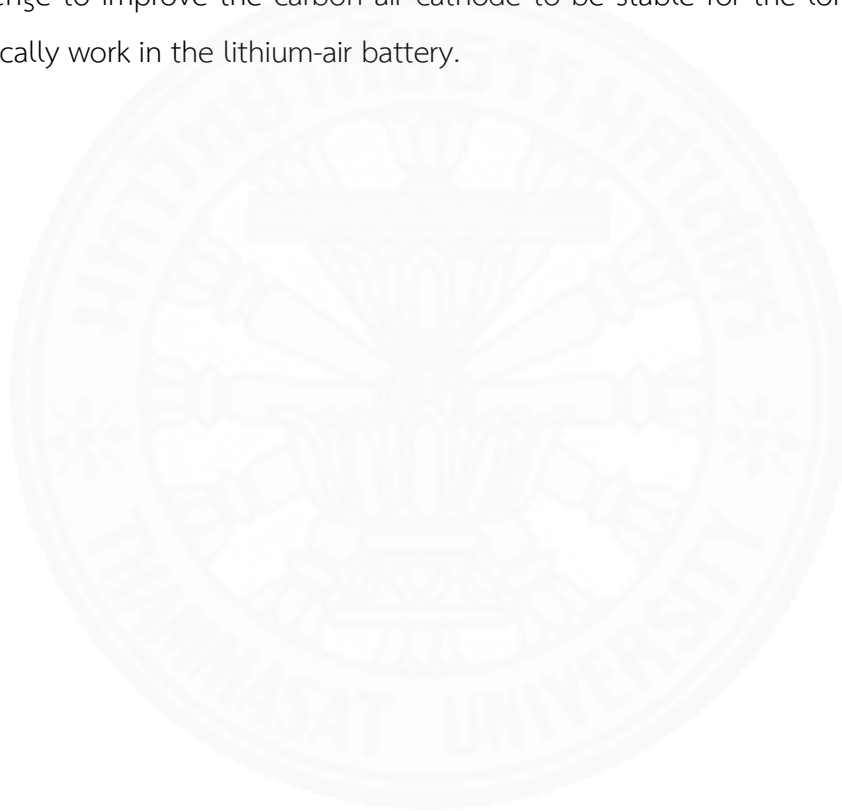
CHAPTER 3
RESEARCH METHODOLOGY

This chapter provides a detailed explanation of the methodology and data analysis used in this research. Figure 3.1 summarizes the steps of cellulose processing beginning from the extraction of cellulose from cassava solid waste to the final products; transparent cellulose film and cellulose/carbon black composite electrode. The detailed explanation for each step describes below.
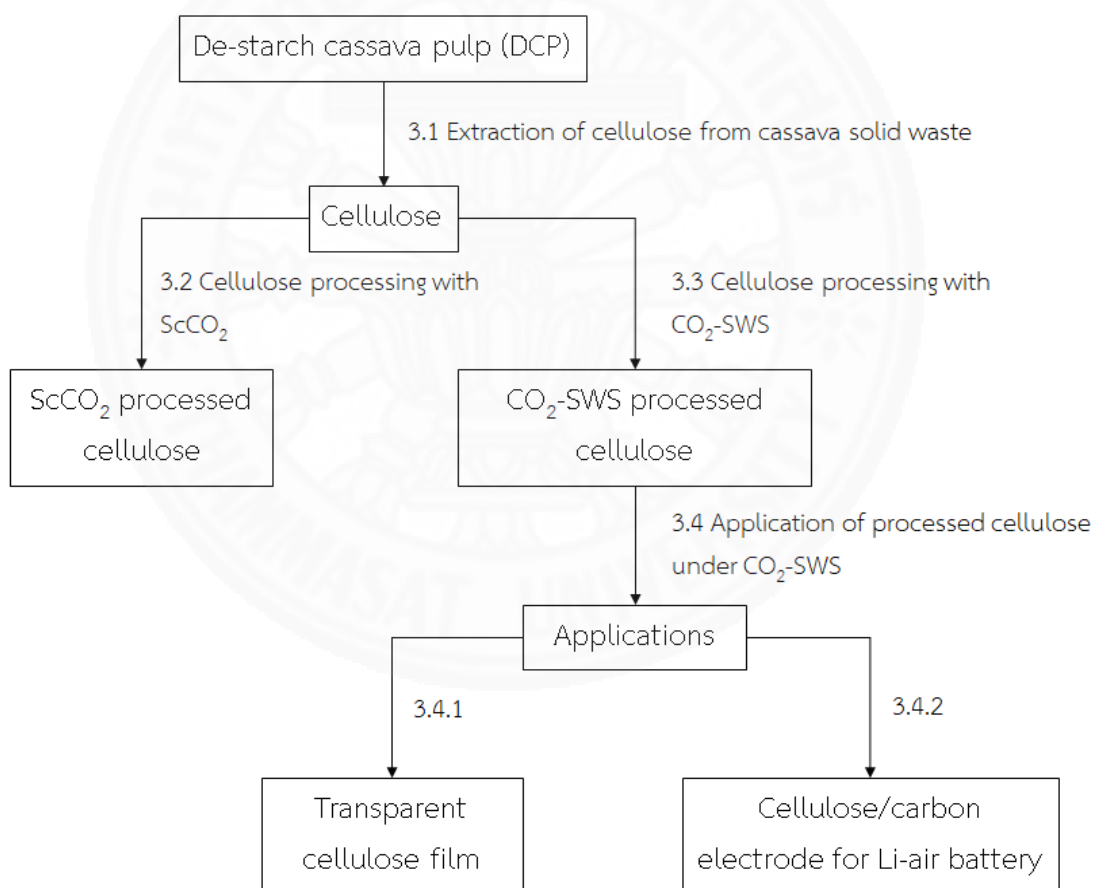
Figure 3.1 Flow-chart of the cellulose processing steps. Numbers shown in the flow chart refer to corresponding subsections.

3.1 Extraction of cellulose from cassava pulp waste

In this work cellulose was prepared by extraction of cassava pulp waste (CP) provided by CHOLCHAROEN GROUP, Chonburi, Thailand. Additionally, the CP was de-starch treated yielding De-starch cassava pulp (DCP) which was employed as raw material in this research. Sodium hydroxide solution was employed to remove hemicellulose and lignin from the pulp in the *Alkaline treatment* process as described in subsection 3.1.1 Alkaline treatment. Remained lignin was then removed via sodium chlorite in *Bleaching* process as described in subsection 3.1.2 Bleaching. The sample was further dried using *Spray drying*. The spray drying process is described in subsection 3.1.3 Spray drying

3.1.1 Alkaline treatment

Materials

1. De-starch cassava pulp (DCP)

2. Sodium hydroxide (NaOH) analytical grade purchased from CARLO ERBA.

3. Tap water

4. Deionized water (DI water)

Method

1. Every 15 g of DCP was weighed in 250-mL Erlenmeyer flask.

2. 375 mL of 4% (w/v) NaOH was poured into each flask, and the mixture was then stirred until DCP completely wet.

3. Each mouth flask is plugged with an aluminum foil covered cotton.

4. The flasks were then placed in an autoclave (TOMY SX-700, Japan) with sterile liquid mode which was set at the temperature of 393.15 K for 1 h.

5. After the brown solution mixture was cooled down, the brown precipitates were filtrated using No. 4 of filter paper.

6. The precipitates were washed with tap water until neutral and were then stored in a refrigerator for further experiment. After alkaline treatment, the pulp is called alkaline treated pulp (AP).

3.1.2 Bleaching

Materials

1. Sodium chlorite ($NaClO_2$) technical grade (80%) purchased from Sigma-Aldrich.

2. Acetic acid analytical grade purchased from CARLO ERBA.

3. Tap water

4. Deionized water (DI water)

Method

1. AP extracted from 30 g of DCP was mixed with 375 mL of 1% (v/v) $NaClO_2$ and then pH was adjusted to 5 with 4% (v/v) acetic acid.

2. The mixture was transferred to a screw capped bottle and then was placed in a shaking water bath at 353.15 K for 24 h.

3. After cooling the solution, the white precipitates were filtered and washed with tap water until neutral. The neutral white precipitate was kept in a refrigerator for further experiment. The neutral white is called bleached pulp (BP).

3.1.3 Spray drying

1. 750 mL of DI water was added to the BP.

2. The mixture was stirred by magnetic stirrer following by homogenization (ULTRA-TURRAX T25 Digital High-Speed Homogenizer, IKA) at 8,000 rpm for 5 minutes.

3. Spray drying was performed using a Niro MOBILE MINOR™ 2000 model (pilot-scale) spray dryer with an inlet temperature of 403.15 K, 0.5 MPa air pressure and 20 mL min^{-1} spray rate.

4. White cellulose powder collected for further experiments is called "cellulose".

Figure 3.2 Appearances of (a) DCP, (b) AP, (c) BP, and (d) cellulose extracted from cassava solid waste.

3.1.4 Characterization of derived cellulose

3.1.4.1 Proximate analysis

(1) Moisture content

The moisture content of cellulose powder was determined by measuring the mass of cellulose before and after the removal of water via evaporation at 408.15 K for 2 h.

$$\%\text{Moisture} = \frac{m_{wet} - m_{dried}}{m_{wet}} \times 100 \qquad \text{3-1}$$

where m_{wet} is the mass of cellulose sample before drying,

m_{dried} is the mass of cellulose sample after drying.

The moisture content measurement is described below.

1. Clean weighing bottles with glass lids were dried at 408.15 K for 2 h. After that the bottles were cooled in a desiccator and weighed. Weight of the bottles and lids were recorded.

2. About 2 g of cellulose sample was weighed in weighing bottle. The actual amount of each sample was recorded.

3. During drying the samples containing in weighing bottles in an oven at 408.15 K for 2 h, the lids were open. The oven-dried samples containing in bottles were cooled in a desiccator.

4. The total dried weight of the sample containing in the bottle covered with the lid was measured. The actual amount of each dried cellulose sample was calculated by subtracting the weight of the bottle and covered with the lid from weight of the total dried weight.

(2) Crude protein

Crude protein (CP) is derived through the measurement of nitrogen content (N) in the sample. Commonly, the average nitrogen content of proteins contains about 16% for all food sources except wheat grains; therefore, the factor for converting nitrogen content into crude protein containing cellulose is 6.25 (1/0.16). Crude protein content was calculated using Eq. (3-2).

$$\%CP = \%N \times 6.25 \hspace{4cm} \text{3-2}$$

Nitrogen content was determined by using CHNS analyzer (628 Series, LECO Instruments Co. Ltd, Thailand) which is designed to measure nitrogen by combustion at high temperature in of pure oxygen. The detection system was calibrated using ethylenediaminetetraacetic acid (EDTA) as a standard. The samples were weighed in an aluminium foil and burned at 1,223.15 K in pure oxygen. Nitrogen compounds (weight/weight) were then detected with thermal conductivity detection.

(3) Crude fat

The dried sample containing crude fat is extracted with organic solvent by following AOAC (1995). The sample was weighed in a thimble and then dried at 378.15 K for 3 h. The thimble with adapter and thimble support were placed in the extraction unit. Petroleum ether was employed to boil and extract the sample for 30 min and 60 min, respectively. After petroleum ether evaporation, the extracted sample was dried in an oven for 30 min and then was weighed. The crude fat is calculated using Eq. (3-3).

$$\%\text{Crude fat} = \frac{W_2}{W_1} \times 100 \hspace{3cm} \text{3-3}$$

where W_1 is the sample weight (g),

W_2 is the fat weight after extraction (g).

(4) Ash

The ash content of cellulose powder was carried out following APPITA P3 M-69 standard method.

1. Porcelain crucibles with lids were dried at 373.15 K for 1 h and then were cooled in a desiccator. The dried weight of each crucible was recorded.

2. About 2 g of the cellulose sample was weighed in the crucible with lid, and an actual amount of the sample was recorded.

3. All crucibles were then placed in a muffle furnace (P-320, Nabertherm) with the program control below.

heat up from room temperature to 378.15 K

hold at 378.15 K for 12 min

heat up from 378.15 K to 523.15 K at the rate of 10 K min^{-1}

hold at 523.15 K for 30 min

heat up from 523.15 K to 848.15 K at the rate of 20 K min^{-1}

hold at 848.15 K for 180 min

cool down from 848.15 K to 378.15 K

4. After the hot crucibles were cooled down in a desiccator, they were weighed. The ash content was calculated as follows:

$$\%\text{Ash} = \frac{m_2 - m_1}{m_{sample}} \times 100 \qquad\qquad 3\text{-}4$$

where m_{sample} is the mass of the sample before burning (g),

m_1 is the mass of crucible (g)

and m_2 is the mass of crucible with sample after burning (g).

(5) Crude fiber

The amount of crude fiber content was determined by the digestion in sulfuric acid and sodium hydroxide solution following AOAC (1995). The defatted sample was weighed about 2.5 g and then was mixed with 200 mL of boiling 0.255N H_2SO_4 solution. The mixture was boiled for 30 min under reflux and at the end of the boiling period, the residue was collected via filtration. The residue was washed

with boiling water and then was mixed with 200 mL of 0.313N NaOH solution. The boiling step was repeated. After the filtered residuals were washed with boiling water and HCl solution, they were washed three times with petroleum ether. The residue was dried at 378.15 K for 12 h. The weight of dried residue was recorded.

$$\%\text{Crude fiber} = \frac{m_1 - m_2}{m_{sample}} \times 100 \qquad\qquad 3\text{-}5$$

The crude fiber was calculated using Eq. (3-5)

where m_{sample} is the mass of sample before digestion (g),

   m_1 is the mass of dried sample after digestion (g)

and m_2 is and the mass of ash (g).

3.1.4.2 Cellulose, hemicellulose, and lignin determination using detergent technique

The detergent techniques including neutral detergent fiber (NDF), acid detergent fiber (ADF), and acid detergent lignin (ADL) are common measurement for fiber. After digesting in neutral detergent solution, the fiber residues are predominantly cellulose, hemicellulose and lignin. The fiber residues after digesting in acid detergent in ADF method contain predominantly cellulose and a part of lignin while those of in ADL method contain predominantly lignin. The detergent procedure is shown in Figure 3.3. NDF, ADF and ADL were determined according to the methods of Van Soest (Van Soest, Robertson, & Lewis, 1991) and AOAC (1995).

$$\%\text{Cellulose} = \%\text{ADF} - \%\text{ADL} \qquad\qquad 3\text{-}6$$

$$\%\text{Hemicellulose} = \%\text{NDF} - \%\text{ADF} \qquad\qquad 3\text{-}7$$
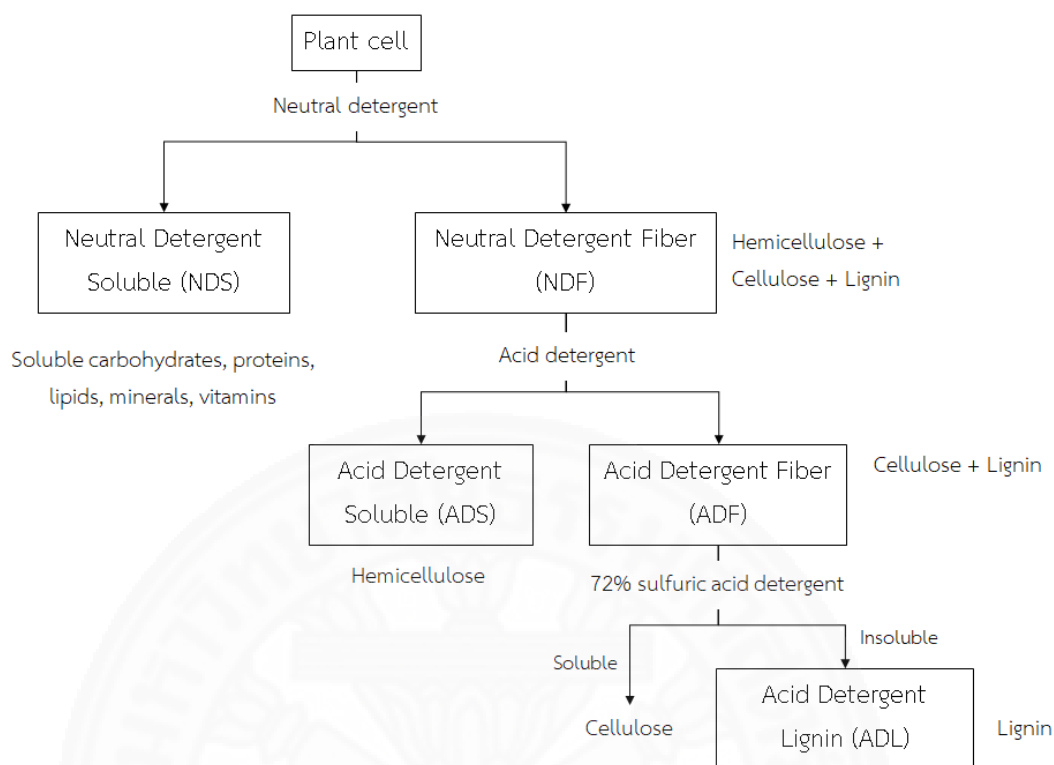
Figure 3.3 Detergent procedure of the fiber.

(1) Neutral detergent fiber (NDF)

Neutral detergent solution was prepared by dissolving 30 g of sodium lauryl sulfate, 18.61 g of disodium EDTA, 6.81 g of sodium tetraborate decahydrate, 4.56 g of disodium phosphate anhydrous and 10 mL of triethylene glycol in 1000 mL of DI water (pH 6.9 – 7.1). The NDF determination was performed following procedure below.

1. The sample was weighed (m_{sample}) and mixed with 100 mL of neutral detergent solution with 0.5 g of sodium sulfite and *n*-octanol.

2. The mixture was then heated and refluxed for 60 min.

3. The residue was filtered and washed with boiling water and cold acetone and then was dried at 378.15 K for 8 h.

4. The weight of dried residue was recorded as m_1.

$$\%NDF = \frac{m_1}{m_{sample}} \times 100 \qquad\qquad 3\text{-}8$$

(2) Acid detergent fiber (ADF)

Acid detergent solution was prepared by dissolving 20 g of cetyltrimethylammonium bromide in 1000 mL of 1N of sulfuric acid. Tensioactive was added to promote dissolution. The ADF determination was performed following procedure below.

1. NDF residue was mixed with 100 mL of acid detergent solution and n-octanol at room temperature.

2. The mixture was heated and then refluxed for 60 min.

3. The residue was filtered and washed with boiling water and cold acetone and then was dried at 378.15 K for 8 h.

4. The weight of dried residue was recorded as m_2.

$$\%\text{ADF} = \frac{m_2}{m_{sample}} \times 100 \qquad\qquad 3\text{-}9$$

(3) Acid detergent lignin (ADL)

1. ADF residue was mixed with a cold 72% sulfuric acid and stirred for 3 h over the temperature range 293.15-296.15 K.

2. The residue after the digestion was filtered with vacuum and washed with boiling water until free form acid.

3. The acid free residue was then dried in an oven for 24 h at 378.15 K.

4. The weight of dried residue was recorded as m_3.

$$\%\text{ADL} = \frac{m_3}{m_{sample}} \times 100 = \%\text{Lignin} \qquad\qquad 3\text{-}10$$

3.1.4.3 Cellulose, hemicellulose, and lignin determination using pyrolysis technique

Cellulose, hemicellulose, and lignin show a great difference in pyrolysis behavior. Hemicellulose is easily decomposed and that yields the maximun mass loss at the temperature around 541.15 K and following by decomposition of cellulose at the temperature around 628.15 K while lignin is hardly decomposed (H.

Yang et al., 2007). Thermogravimetric analysis (TGA) was applied to investigate three main components in the sample (cellulose, hemicellulose and lignin). The TGA measurement was carried out with SDTA851^e model (Mettler Toledo, Ohio, USA). 5 mg of cellulose sample was weighed in 70 μL alumina oxide crucible and then was heated from 298.15 to 1,073.15 K at a heating rate of 25 K min^{-1} under nitrogen gas flow.

3.1.4.4 Alpha-, beta-, and gamma-cellulose analysis

TAPPI T 203 cm-99 standard method was employed to determine the content of alpha-, beta-, and gamma-cellulose in the cellulose sample. The method can be applied to a bleached or de-lignified pulp only.

Materials

1. Sodium hydroxide (NaOH) solution, 5.21 $\pm$ 0.005N, carbonate-free was prepared by completely dissolving NaOH in in a certain amount of DI water in the concentration about 50% w/v. The concentrated NaOH was let stand until the suspended carbonates have settled. The clear solution was decanted and diluted with CO_2-free DI water following by normality adjusting to 5.21N.

2. 0.5N potassium dichromate solution was prepared by completely dissolving 24.52 g of $K_2Cr_2O_7$ in a certain amount of DI water. Then the solution was made up with DI water to 1000 mL.

3. 0.1N ferrous ammonium sulfate solution was prepared by completely dissolving 40.5 g of $Fe(NH_4)_2(SO_4)_2.6H_2O$ in a certain amount of DI water. After adding 10 mL of concentrated H_2SO_4 to the solution, DI water was added to bring the final voulume of solution up to 1000 mL. Due to the instability of the solution, the exact normality of the solution should be determined daily by titration with 0.1N of potassium dichromate standard solution.

4. In preparation of phenanthroline-ferrous sulfate indicator (Ferroin), 1.5 g of 1,10-phenanthroline monohydrate ($C_{12}H_8N_2 \cdot H_2O$) and 0.7 g of ferrous sulfate haptahydrate ($FeSO_4 \cdot 7H_2O$) were dissolved in 100 mL of DI water.

5. In preparation of 3N sulfuric acid, 83.5 mL of concentrated H_2SO_4 was added to an excess of DI water and then the solution was made up with DI water to 1000 mL.

Method

1. 1.5 g of cellulose sample was gradually added to a 300 mL beaker containing 100 mL of 17.5% NaOH (w/v) at room temperature (298.15 K). The time at which the reagent added was noted.

2. The suspension was stirred until completely dispersed with avoidance drawing air into the suspension at 298.15 K for 30 min.

3. 100 mL of DI water was then added to the suspension and stirred at 298.15 K for 30 minutes.

4. The suspension was transferred to a filter funnel. The first 10 to 20 mL of filtrate was discarded, then about 100 mL of the filtrate was collected.

5. Alpha-cellulose was determined as follows:

10 mL of the filtrate (a solution of analyzate) and 10 mL of 0.5N $K_2Cr_2O_7$ solution were pipetted into a 250 mL flask. 30 mL of concentrated H_2SO_4 was cautiously added to the solution while swirling the flask gently. After about 15 min, the solution was cooled, then 50 mL of DI water was added. 2 to 4 drops of Ferroin indicator were added and the solution was titrated with 0.1N ferrous ammonium sulfate solution (a titrant) until purple colour was observed. A blank titration was performed by replacing the filtrate with the mixture containing 5 mL of 17.5% NaOH and 5 mL of DI water. Alpha-cellulose was calculated using the Eq. (3-11)

$$\%\text{Alpha cellulose} = 100 - \frac{6.85(V_2 - V_1) \times N \times 20}{V \times W}$$ 3-11

where V_1 is volume of titrant used during titration of the solution containing the filtrate (mL),

        V_2 is volume of titrant used during titration of the blank solution (mL),

        N is exact normality of the ferrous ammonium sulfate solution,

        V is the volume of the filtrate (10 mL),

and W is dried weight of pulp sample (g).

6. Beta- and gamma-cellulose were determined follows;

50 mL of the filtrate (a solution of analyzate) was pipetted into a 100 mL graduated cylinder with ground glass stopper, and then 50 mL of 3N H$_2$SO$_4$ was added and thoroughly mixed by inversion. The cylinder was heated to about 343.15-363.15 K in a hot water bath for a few minutes to coagulate the beta-cellulose. The precipitate was settled overnight; then the clear solution was obtained by filtration. 50 mL of the clear solution was pipetted into 300 mL flask following by addition of 10.0 mL of 0.5N K$_2$Cr$_2$O$_7$ solution. 90 mL of concentrated H$_2$SO$_4$ was cautiously added while swirling the flask gently. After about 15 min, the solution was cooled, then 50.0 mL of DI water was added. 2 to 4 drops of Ferroin indicator were added and the solution was titrated with 0.1N ferrous ammonium sulfate solution (a titrant) until the purple colour was observed. It is usually to perform a blank titration by which the procedure was repeated with replacement of the filtrate with a mixture containing 12.5 mL of 17.5% NaOH, 12.5 mL of DI water, and 25 mL of 3N H$_2$SO$_4$. Beta- and gamma-cellulose were calculated using Eqs. (3-12) and (3-13), respectively.

$$\%\text{Gamma cellulose} = \frac{6.85(V_4 - V_3) \times N \times 20}{25 \times W} \qquad \text{3-12}$$

where V_3 is volume of titrant used during titration of the solution after beta cellulose precipitation (mL)

V_4 is volume of titrant used during titration of the blank solution (mL).

$$\%\text{Beta cellulose} = 100 - (\%\text{alpha} + \%\text{gamma}) \qquad \text{3-13}$$

3.2 Cellulose processing with supercritical carbon dioxide (ScCO$_2$)

Supercritical carbon dioxide (ScCO$_2$) technology has been applied as an alternative to a traditional organic solvent method for cellulosic materials processing. However, the observance of cellulosic materials in contact with ScCO$_2$ has not been extensively studied. In this study we examined the properties of cassava cellulose after processing in ScCO$_2$ without additional of co-solvent that was compared with the

properties of unprocessed and atmCO$_2$-processed cellulose. Cellulose preparing in section 3.1 was processed in ScCO$_2$ with various processing pressures (p), temperatures (T) and times (t). The surface morphology, thermal and crystalline properties of the ScCO$_2$-processed sample were characterized.

3.2.1 Processing of cellulose in ScCO$_2$

Figure 3.4 shows the experimental apparatus for ScCO$_2$ processing. The processing temperature and pressure controlled using TharSCF software were in the range of 313.15 to 353.15 K and 8 to 20 MPa, respectively. About one gram of the prepared cellulose powder was loaded into a sample holder as shown in Figure 3.4(a), which is a component of a high-pressure vessel 1. Carbon dioxide from the gas cylinder flowed through the flow instrument (SITRANS F C MASS 2100, SIEMENS, Denmark) after that it was cooled in heat exchanger 1 and pressurized by a high-pressure pump (model P2004, Thar Instrument Inc., USA). The pressurized carbon dioxide was heated by heat exchanger 2 and introduced into the high-pressure vessel 1. The processing was conducted for 60 and 120 min. The sample was then removed after the depressurizing of the system to atmospheric pressure by controlling the valve (No. 9). The experiment of atmCO$_2$ processing was carried out at the pressure of 0.1 MPa.

3.2.2 Characterization
3.2.2.1 Surface morphological analysis

The surface morphology of the cellulose sample was analyzed by a field emission scanning electron microscopy (FE-SEM) technique on FEI Versa 3D model (Thermo Fisher Scientific Inc., USA) operating at 5 kV. The samples were sputter coated with a 7 nm layer of silver using a high vacuum sputter coater Leica EM ACE600 model (Leica Microsystems Ltd., Singapore) before measurement. The fiber diameters of the sample were determined using ImageJ Java software.
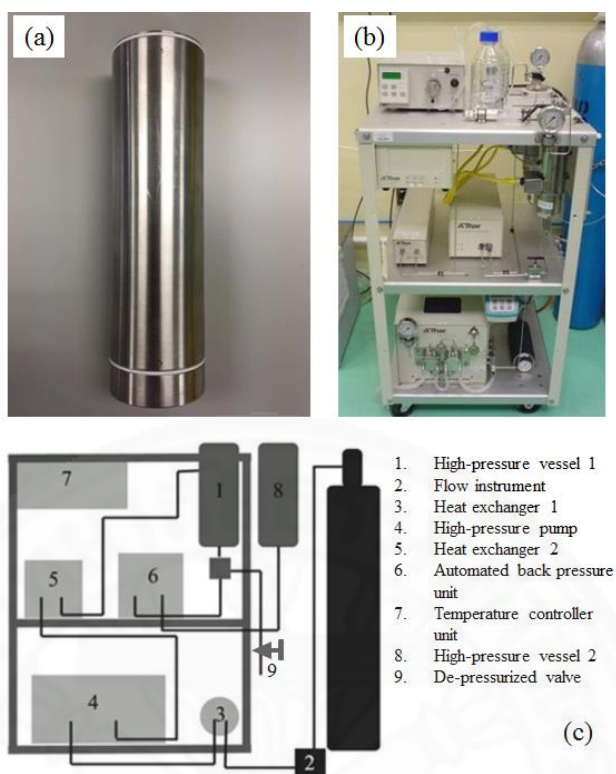
Figure 3.4 (a) Sample holder, (b) apparatus appearance, and (c) schematic of supercritical carbon dioxide processing apparatus.

3.2.2.2 Thermal properties analysis

Thermal properties of cellulose samples were characterized using thermogravimetric analysis (TGA) and a differential scanning calorimetry (DSC) techniques. The TGA measurement was conducted using TGA2 model (Mettler Toledo, USA). Actual amount (about 10 mg) of the dried cellulose sample was kept in a 70 μL alumina crucible and then was heated from 303.15 to 873.15 K at a heating rate of 10 K min^{-1} under N_2 flow. The DSC measurement was carried out using DSC823^e model (Mettler Toledo, USA) at a heating rate of 10 K min^{-1} in the range of 298.15 to 873.15 K under an N_2 atmosphere at the flow rate of 10 mL min^{-1}. The actual amount of the dried sample was weighed in a standard 40 μL aluminum crucible and then twice the of mass of DI water was added to each sample. After each crucible was closed with lid, it was then homogenized in an ultrasonic bath for 15 min and kept in a refrigerator for 24 h before the measurement.

3.2.2.3 Crystallinity analysis

Several methods are acceptable for the determination of crystallinity of cellulose, e.g., XRD, FTIR, and solid-state ^{13}C NMR (S. Park et al., 2010). X-ray diffraction (XRD) of all samples were performed on Bruker D8 Advance Diffractometer model (Massachusetts, USA) using CuKα radiation with a coupled mode between 4° and 30° at 0.05° step size and 2 s of a count time. To calculate crystallinity index and degree of crystallinity of the sample, Segal's equation (peak height method) (Segal et al., 1959) and Herman's equation (amorphous subtraction and peak deconvolution method) (Hermans & Weidinger, 1948) were applied as expressed in Eqs. (3-14) and (3-15), respectively.

$$C.I. = (I_{002} - I_{AM})/I_{002} = 1 - (I_{AM}/I_{002}) \qquad 3\text{-}14$$

$$Cr = A_{crystalline}/A_{total} \qquad 3\text{-}15$$

where I_{200} is the maximum intensity of the (200) lattice diffraction
and I_{AM} is the intensity of amorphous diffraction.
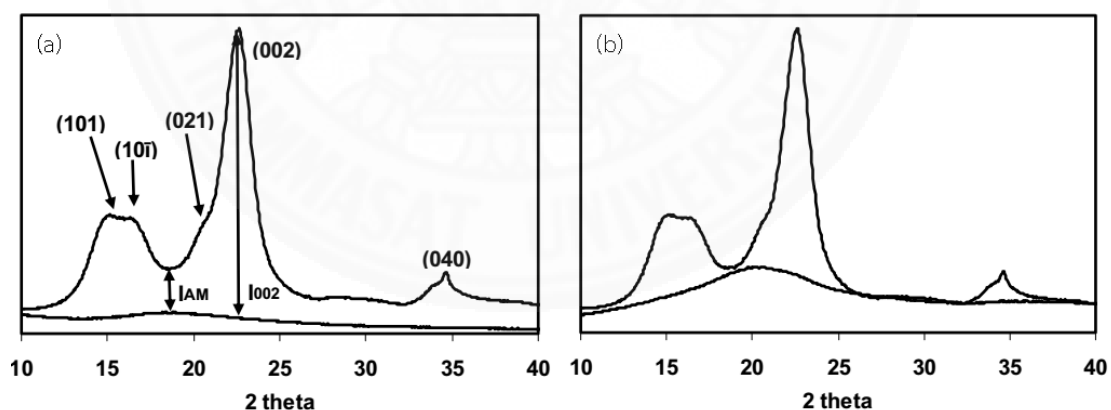
Figure 3.5 X-ray diffraction spectra of Avicel PH-101 illustrating the methods for calculating crystallinity. (a) Segal's method and (b) Herman's method. (S. Park et al., 2010)

Fourier transform spectroscopy (FTIR) has been used for characterizing the crystallinity of cellulose (C. Chen et al., 2014; Ciolacu, Ciolacu, & Popa, 2011; Parida,

Dash, & Pradhan, 2015). The dried cellulose sample was mixed with KBr powder at the concentration of 1% w/w. In a preparation of the KBr pellet, an adequate amount of fine powder of the cellulose/KBr mixture was placed to cover bottom in a stainless steel pellet die. The IR spectra of all samples were measured on Nicolet 6700 model FT-IR microscope (Thermo Fisher Scitific Inc., USA) in the range of 4000-400 cm^{-1} in transmission mode. The crystallinity index was determined by calculating relative peak intensities of the IR spectra at the position between 1372 cm^{-1} and 2900 cm^{-1} as expressed in Eq. (3-16) and those of the IR spectra at the position between 1430 cm^{-1}, and 893 cm^{-1} as expressed in Eq. (3-17).

$$C.I. = I_{1372} / I_{2900} \qquad\qquad 3\text{-}16$$

$$C.I. = I_{1430} / I_{893} \qquad\qquad 3\text{-}17$$

Solid state ^{13}C NMR was used to evaluate the crystallinity of unprocessed and processed cellulose sample by employing Newman method (Newman & Hemmingson, 1990). The NMR measurement was performed using a Bruker Ascend 400 WB spectrometer model (USA). To estimate the degree of crystallinity, the crystalline peak area integrating peak between 87 and 93 ppm was normalized by the total area assigned to C4 peaks integrating between 80 and 93 ppm.
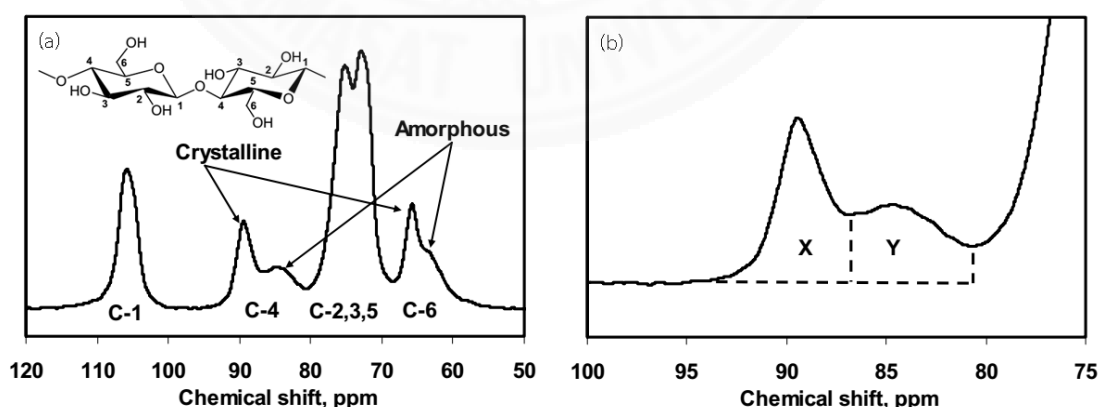
Figure 3.6 Solid state ^{13}C NMR spectrum of Avicel PH-101. (a) Whole spectrum showing the assignment of peaks to the carbon in a glucopyranose repeat unit and (b) sub-

spectrum showing peaks assigned to the C4 in cellulose. The CI is calculated by x/(x+y). (S. Park et al., 2010)

3.2.3 Data analysis

The analysis of variance was employed to determine the statistically significant results of the difference among three estimates form the processing groups, which were unprocessed, atmospheric pressure-processed (atmCO$_2$-processed), and supercritical pressure-processed (ScCO$_2$-processed) cellulose. Normality test is applied to evaluate the distribution of the estimates within groups. One-way ANOVA, a parametric test, is employed to determine the variance of normal distribution estimates using F-test while Kruskal-Wallis One-way ANOVA, a rank-based nonparametric test, is employed to determine the variance of non-normal distribution estimates using H-test. A significance level of 0.05 was used.

Pearson's correlation and Spearman's rho correlation test were carried out to investigate the strength and direction of the relationship among processing conditions (*T, p,* and *t*) of atmCO$_2$ and ScCO$_2$ cellulose treatment. Pearson's and Spearman's rho correlation coefficients were the measurement for the corresponding normally distributed and non-normally distributed data, respectively. The correlation coefficient (r) has a value between -1 and +1 ($-1 \leq r \leq 1$) where positive values suggest direct correlation while negative values suggest an inverse correlation. The higher the absolute value of r indicates a higher degree of strength of association among model variables. An indication of the correlation strength is the following: 0.00 – 0.19 very weak; 0.20 – 0.39 weak; 0.40 – 0.59 moderate; 0.60 – 0.79 strong; and 0.80 – 1.00 very strong.

Table 3.1 Summary of data analysis.

	Parametric statistics	Non-parametric statistics
Data distribution	Normal	Non-normal
Analysis of variance	One-Way ANOVA	Kruskal Wallis One-Way ANOVA
Correlation test	Pearson's correlation	Spearman's correlation

3.3 Cellulose processing with carbon dioxide switchable system (CO_2-SWS)

In this section, carbon dioxide switchable system (CO_2-SWS) is employed as a solvent of the cellulose. The CO_2-SWS in the presence of carbon dioxide is prepared using ethylene glycol and 1,8-diazabicyclo [5.4.0] undec-7-ene which are a carbon dioxide capturing agent and strong base, correspondingly. Cellulose preparing in section 3.1 is processed in the system performed under a pressure range of 0.1 to 10.0 MPa and a temperature of 298.15 and 333.15 K. The phase behavior and chemical structure of the cellulose in CO_2-SWS are studied under gaseous, sub- and supercritical phases of carbon dioxide. Additionally, the behavior of cellulose dissolution in CO_2-SWS at any conditions is described by a developed diffusion-controlled shrinking particle model (SPM).

3.3.1 Dissolution of cellulose in CO_2-SWS

Materials

Cellulose was prepared in section 3.1. 1,8-diazabicyclo [5.4.0] undec-7-ene (DBU), ethylene glycol (EG) and dimethyl sulfoxide (DMSO) were purchased from Wako Pure Chemical Industries, Ltd. Carbon dioxide (99.95%) was supplied from Fujii Bussan Co.Ltd.

Method

Cellulose powder was added to the solution of DBU and EG with a molar ratio of 2:1 to give the cellulose concentration in the solution of 4 mg mL^{-1}. The cellulose suspension was diluted by mixing with DMSO in the twice volume of the suspension. The suspension was used for the dissolution and modification of the cellulose by CO_2-SWS that was carried out by the apparatus as shown in Figure 3.7. The set up was very similar to the titanium sol-gel reaction in supercritical carbon dioxide as given in the literature (Kinoshita & Shimoyama, 2016). The glass cell with 1.5 mL of the cellulose suspension was put into a high-pressure vessel with view window in advance. Carbon dioxide from the gas cylinder was flowed through a ball check valve (6136G4Y, HOKE, Tokyo, Japan), cooled by the chiller and got to liquid state. The

liquefied carbon dioxide was pressurized by double plunger pump (NP-D-321, Nihon Seimitsu Co. Ltd., Saitama, Japan). The pressure of the system was controlled by a backpressure regulator (26-1700 Series, TESCOM^{TM}, Shinagawa-ku, Japan). The pressurized carbon dioxide was heated by flowing through a preheating coil and installed into the high-pressure vessel heated by several cartridge heaters. The phase behaviour during the dissolution and modification of the cellulose was observed through the view window with microscope digital camera with 32 modifications (SPACE Inc., Tokyo, Japan). The dissolution and modification of the cellulose were conducted for 2 h at 0.1 to 10.0 MPa and 298.15 to 333.15 K. The system was depressurized up to atmospheric pressure after the dissolution and modification operations controlling by a needle valve (RK1200 Series, Kojima Instruments Inc., Kyoto, Japan). After the high-pressure vessel had been depressurized, the modified cellulose in the CO_2-SWS was removed.
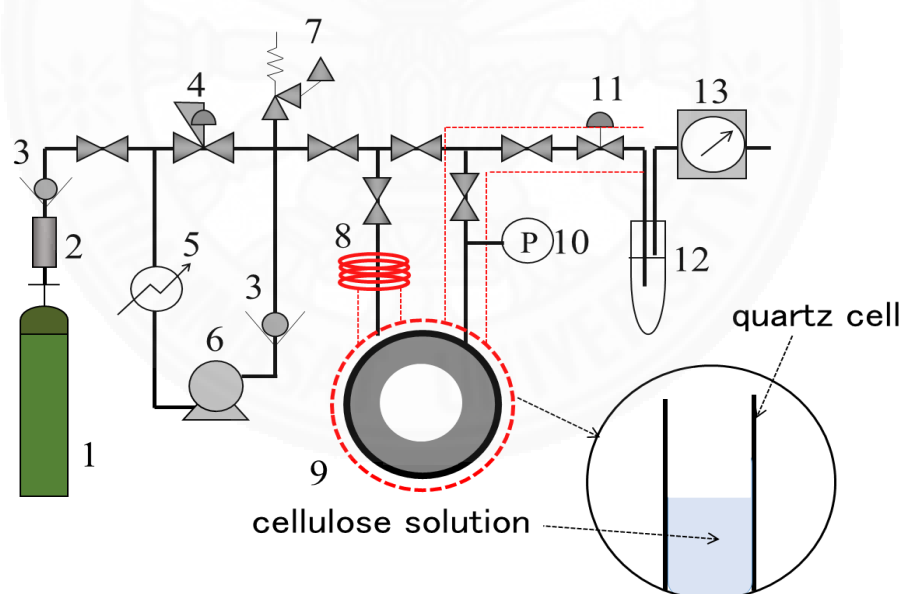
Figure 3.7 Schematic diagram of the setup for phase behavior study of switchable solution during cellulose dissolution. 1; CO_2 cylinder, 2; silica gel cell,3; check valve, 4; back pressure regulator, 5; chiller, 6; double plunger pump,7; safety valve, 8; pre-heating coil, 9; high-pressure vessel, 10; pressure gauge, 11; needle valve, 12; solvent trap, 13; wet type gas flow meter.

3.3.2 Determination of the phase boundary of cellulose in CO_2-SWS

The cellulose suspension was used for determination of the phase boundary on the dissolution of the cellulose in a CO_2-SWS using the setup in Figure 3.7. The cellulose suspension was installed into the high-pressure vessel before heating and pressuring the system. The temperature or the pressure in the system was gradually elevated until completion of the cellulose dissolution and was then recorded as the phase boundary condition at the cellulose/CO_2-SWS. The system was depressurized after the complete dissolution of the cellulose in the solution.

3.3.3 Investigation of chemical structure of cellulose in CO_2-SWS

Fourier transform spectroscopy (FT-IR) (FT-IR-4100, JASCO, Tokyo, Japan) was employed in the investigation of the chemical structure of cellulose modified in the switchable solution under the high-pressure carbon dioxide. A curve fitting technique from the literature (Wojdyr, 2010) was applied for qualitative analysis of the IR spectra with a Gaussian function.

3.3.4 Shrinking particle model for cellulose dissolution in CO_2-SWS

Cellulose powder, with approximately 19-μ m diameter particles, was suspended in a mixture of DBU, EG, and DMSO to give a 4 mg mL^{-1} (0.04 %w/v) concentration of cellulose. After CO_2 was pressurized into the mixture to produce CO_2 switchable solvent, the cellulose dissolved as shown in Figure 3.8.
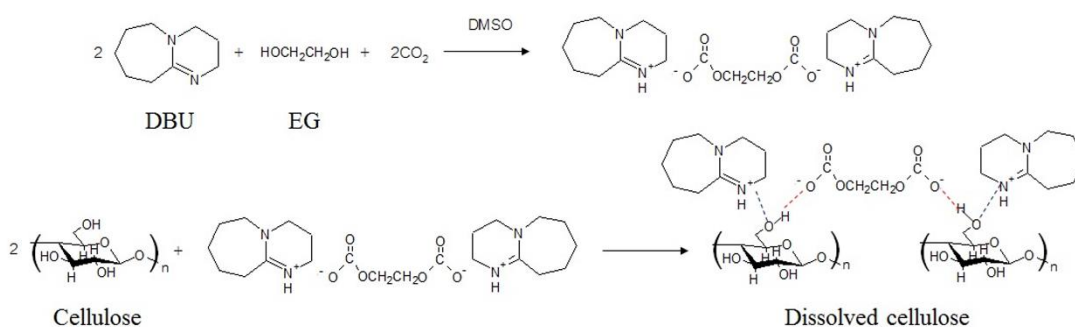
Figure 3.8 Cellulose dissolution reaction.

The cellulose particles were consumed by dissolution in the CO_2-SWS. Subsequently, the consumed cellulose particles were reduced in size. The reaction takes place on the exposed surface of the particle, and the product completely dissolves in the liquid. The cellulose dissolution in this work could be explained using the shrinking particle model (SPM), which describes similar work relating to leaching phenomena. According to the SPM, cellulose dissolution progressed according to the following four steps (Figure 3.9):

1. CO_2 switchable solvent production by reaction between CO_2 and DBU + EG in the liquid mixture,

2. diffusion of CO_2 switchable solvent through the liquid film to the surface of cellulose,

3. reaction of CO_2 switchable solvent on the cellulose surface, and

4. diffusion of cellulose dissolved from the surface through the liquid film and back into the main body of the solvent.
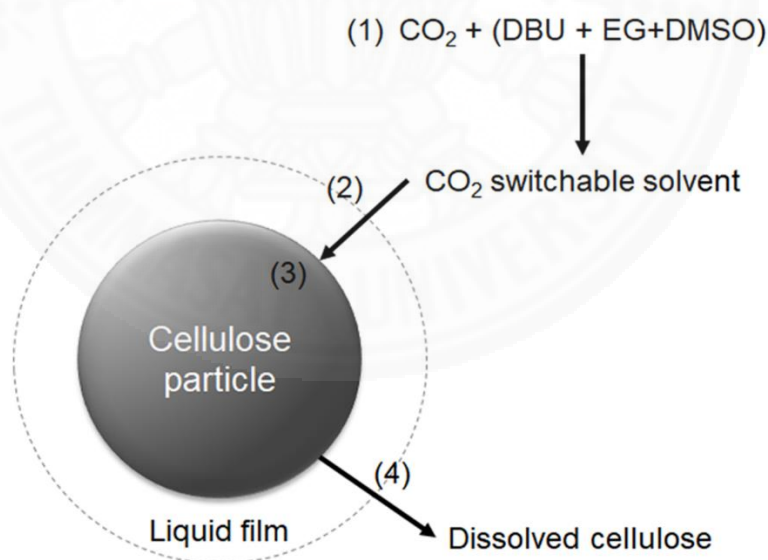
Figure 3.9 Steps in cellulose dissolution.

3.3.4.1 Model assumptions and limitations

The reaction mechanism of DBU and CO_2 in alkanol solution was studied by the Öztürk group (Öztürk, Ume, & Alper, 2012). The literature reveals the

high value of the pseudo-first-order reaction rate constant (k_o = 96–610 s^{-1}) of CO_2 absorption in the DBU/alkanol system which is indicative of the rapid reaction occurring in Step (1) in Figure 3.9. A small particle size has a positive effect on reaction rate (Shen et al., 2016; Mehra, 1996). This is justified to assume fast reaction rate through the liquid film around the particle (Step (3) in Figure 3.9). In addition, the characteristic length scale for diffusion which is much larger than the size of solute particles, is established by substantial diffusional gradient of the particles due to fast reaction. The formed driving force for such dissolution is considerable since difference between cellulose solubility in the CO_2-SWS and the local concentration of cellulose in the "near solid-liquid interface" region (Step (4) in Figure 3.9) (Mehra, 1996). Therefore, diffusion of the CO_2-SWS through the liquid film to the surface of cellulose (Step (2) in Figure 3.9) dictated the overall rate of cellulose dissolution and was considered as the rate limiting step. Related assumptions are as follows:

1. The cellulose particles are spherical.

2. All CO_2 is absorbed in the liquid system and the equilibrium concentration of CO_2 depends on the pressure and temperature of the system.

3. The time required to produce a transparent solution is the complete consumption time for cellulose particles.

4. Owing to the equimolar amounts of DBU and EG under all dissolving conditions, the molar consumption rate of CO_2 controls the reaction of the CO_2-SWS as shown in Step (1) in Figure 3.9.

5. The flux of CO_2 in the ionic liquid mixture represents the diffusion flux of the CO_2-SWS to the cellulose surface.

6. The properties of DMSO represent liquid mixture properties, i.e., density and viscosity.

3.3.4.2 Liquid film resistance diffusion modeling

The CO_2-SWS diffuses through the liquid film to the cellulose surface where it reacts to produce dissolved cellulose, which subsequently diffuses back into the main body of the liquid phase. The relevant reaction expression for the liquid/solid reaction that takes place on the cellulose surface and the concentration profile of CO_2

(which represents the concentration of the CO_2-SWS) are shown in Eq. (3-18) and Figure 3.10, respectively.

$$\text{cellulose (C)} + CO_2 \text{ - SWS(S)} \rightarrow \text{dissolved cellulose (DC)} \qquad \text{3-18}$$
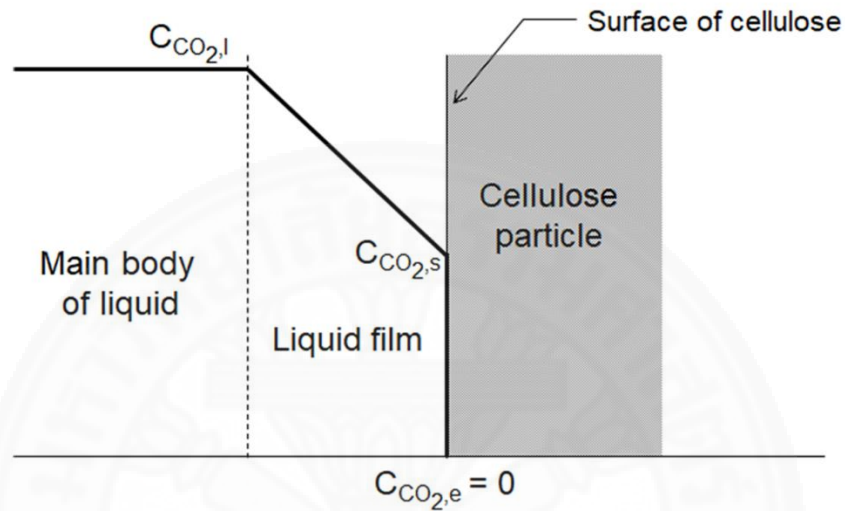
Figure 3.10 Representation of reactant concentrations in the liquid mixture.

The flux of switchable solvent diffusion to the cellulose surface ($-r_S''$) equals the flux of CO_2 diffusion ($-r_{CO_2}''$), according to the model assumption

$$-r_S'' = -r_{CO_2}'' = k(C_{CO_2,l} - C_{CO_2,s}) \qquad \text{3-19}$$

where r_S'' is the diffusion flux of switchable solvent (kg m^{-3} s^{-1} m^{-2}),

r_{CO_2}'' is the diffusion flux of CO_2 (kg m^{-3} s^{-1} m^{-2}),

k is the mass transfer coefficient of the CO_2-SWS through the liquid mixture film to the cellulose particle (m^{-2} s^{-1}),

$C_{CO_2,l}$ is the bulk concentration of CO_2 (kg m^{-3}),

and $C_{CO_2,s}$ is the concentration of CO_2 at the cellulose surface (kg m^{-3}).

Because the instantaneous reaction of the CO_2-SWS and cellulose, $C_{CO_2,s}$, reaches equilibrium ($C_{CO_2,e}$) rapidly ($C_{CO_2,s} = C_{CO_2,e} = 0$) then Eq. (3-19) reduces to

$$-r_S'' = -r_{CO_2}'' = kC_{CO_2,l} \qquad \text{3-20}$$

The Frössling correlation (Frössling, 1938) proposes a convection mass transfer correlation for fluid flow around a spherical particle as shown in Eq. (3-21); this can be applied to the present work because of the occurrence of similar phenomena:

$$\frac{kd_p}{D} = Sh = 2 + 0.6(\mathbf{Re})^{1/2}(\mathbf{Sc})^{1/3}$$
3-21

Rearranging Eq. (3-21),

$$k = \frac{2D}{d_p} + \frac{0.6D}{d_p}(\mathbf{Re})^{1/2}(\mathbf{Sc})^{1/3} = \frac{D + 0.3D(\mathbf{Re})^{1/2}(\mathbf{Sc})^{1/3}}{R}$$
3-22 (a)

when

$$\mathbf{Re} = \frac{\rho N D_a^2}{\mu}$$
3-23 (b)

$$\mathbf{Sc} = \frac{\mu}{\rho D}$$
3-24 (c)

where d_p is cellulose particle size (m),

D is the diffusion coefficient of CO_2-SWS into the liquid mixture film (m^2 s^{-1}),

ρ is the density of the liquid mixture (kg m^{-3}),

μ is dynamic viscosity of the liquid mixture (kg m^{-1} s^{-1}),

N is the rotation speed (s^{-1}),

D_a is the diameter of the magnetic agitator (m),

and R is the radius of the unreacted cellulose particle (m).

Then, the flux of cellulose consumption is obtained by

$$-r_C'' = -\frac{1}{S_C}\frac{dN_C}{dt}$$
3-25

where S_C is the surface area of the cellulose particle (m^2)

and N_C is the mass of the cellulose particle (kg).

The disappearance of cellulose, written in terms of the decrease in volume or radius is then given by

$$-dN_C = -\rho_c dV = -\rho_c d\left(\frac{4}{3}\pi R^3\right) = -4\pi\rho_c R^2 dR$$

3-26

where ρ_c is the mass concentration of the cellulose particle in the system (kg m^{-3}).

Substituting Eq. (3-24) into Eq. (3-23) gives the flux of cellulose dissolution in terms of the decreasing radius of a cellulose particle as

$$-\frac{1}{S_C}\frac{dN_C}{dt} = -\frac{1}{4\pi R^2}\frac{4\pi\rho_c R^2 dR}{dt} = -\rho_c\frac{dR}{dt}$$

3-27

Considering the stoichiometry of Eq. (3-18), every one mole of CO_2-SWS reacts with one mole of cellulose particles as express in Eq. (3-18). The flux of cellulose dissolution is controlled by the flux of CO_2-SWS diffusion to the cellulose surface; hence, $-r_C'' = -r_S''$.

$$-\rho_c\frac{dR}{dt} = kC_{CO_2,l} = \frac{C_{CO_2,l}\left(D + 0.3D(\text{Re})^{1/2}(\text{Sc})^{1/3}\right)}{R}$$

3-28

Integrating Eq. (3-26) gives

$$\int_{R_0}^{R}-RdR = \int_{0}^{t}\frac{C_{CO_2,l}\left(D + 0.3D(\text{Re})^{1/2}(\text{Sc})^{1/3}\right)}{\rho_c}dt$$

$$R_0^2\left[1-\left(\frac{R}{R_0}\right)^2\right] = \frac{C_{CO_2,l}\left(D + 0.3D(\text{Re})^{1/2}(\text{Sc})^{1/3}\right)}{\rho_c}t$$

$$t = \frac{R_0^2\rho_c}{C_{CO_2,l}(D + 0.3D(\textbf{Re})^{1/2}(\text{Sc})^{1/3})}\left[1-\left(\frac{R}{R_0}\right)^2\right]$$

3-29

The time for complete dissolution of the cellulose particle (τ, s) is

$$\tau = \frac{R_0^2 \rho_C}{C_{CO_2,l}(D + 0.3D(\mathbf{Re})^{1/2}(\mathbf{Sc})^{1/3})}$$

<div align="right">3-30</div>

Dividing Eq. (3-27) by Eq. (3-28) yields

$$\frac{t}{\tau} = 1 - \left(\frac{R}{R_0}\right)^2 = 1 - (1 - X_C)^{2/3}$$

<div align="right">3-31</div>

where

$$X_C = 1 - \left(\frac{R}{R_0}\right)^3$$

<div align="right">3-32</div>

3.3.4.3 Data analysis

Pearson's and Spearman's rho correlation coefficients were the measurement for the corresponding normally distributed and non-normally distributed data, respectively. The correlation coefficient (r_s) has a value between -1 and +1 ($-1 \leq r_s \leq 1$) where positive values suggest direct correlation while negative values suggest an inverse correlation. The higher the absolute value of r_s indicates a higher degree of strength of association among model variables. An indication of the correlation strength is the following: 0.00 – 0.19 very weak; 0.20 – 0.39 weak; 0.40 – 0.59 moderate; 0.60 – 0.79 strong; and 0.80 – 1.00 very strong. However, in the case of high dataset variance and low sample size, the p-value is a relatively poor indicator of whether the correlation is statistically significant. Therefore, the r_s value is used as the main statistical term for examining the relationship between variables in this work.

3.4 Application of processed cellulose under CO_2-SWS

3.4.1 Cassava cellulose transparent film

The treated cellulose in CO_2-SWS at any conditions prepared in section 3.3 is employed to fabricate a transparent film. The properties of the film including surface

morphology, chemical functionality, thermal and crystalline properties are characterized.

3.4.1.1 Transparent film preparation

The solution with the cellulose modified in the CO_2-SWS in section 3.3 was heated at 313.15 K with stirring for 6 h to remove the carbon dioxide dissolved in the solution. And then, the solution was cast on a glass substrate. Ethanol was added, and the gel-like cellulose was formed in the ethanol solution. To remove DMSO, EG and remaining DBU the gel-like cellulose was repeatedly soaked and washed with ethanol until neutral. The gel-like cellulose was dried at 313.15 K in the air bath to fabricate the film of the modified cellulose as the final product.
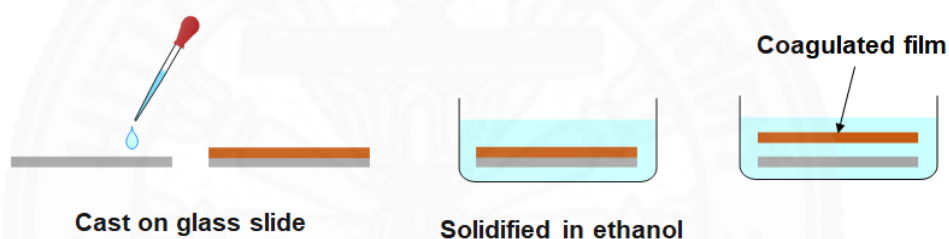
Figure 3.11 Cellulose film casting.

3.4.1.2 Characterization

(1) Scanning electron microscopy

Scanning electron microscopy (SEM) (JCM-6000 Plus, JEOL, Tokyo, Japan) was used for the observation of the surface morphologies of the cellulose tfilm after a sputter coating with Pt-Pd (MINI QUICK COATER SC-701MkII ECO, Sanyu Electron Co., Ltd, Tokyo, Japan).

(2) Fourier transform spectroscopy

Fourier transform spectroscopy (FT-IR) (FT-IR-4100, JASCO, Tokyo, Japan) was employed in the investigation of the chemical structure of the cellulose modified in the switchable solution under the high-pressure carbon dioxide.

(3) Thermogravimetric analysis

Thermal property of the modified cellulose sample was analyzed using a thermogravimetric analyzer (TG) (TGA-50, SHIMADZU, Tokyo, Japan).

The TG analysis was conducted by heating from 298.15 to 823.15 K at the rate of 5 K min^{-1} under a nitrogen stream.

(4) X-ray diffraction

Crystal structure of the modified cellulose was analyzed by an X-ray diffraction method (XRD) (D8 Advance Diffractometer, Bruker, Bangkok, Thailand) using CuKα radiation. The operating condition on the XRD analysis was a couple of 2θ mode between 4° and 40° at 0.05° step size with a count time of 2 s.

3.4.2 Cellulose/carbon electrode for lithium-air battery

The treated cellulose in CO_2-SWS was applied for the fabrication of the composite with carbon black electrode on lithium-air battery application. The influences of the phase of the treated cellulose, the composite preparing method and drying method on the surface morphology, porosity and conductivity of the composite electrode were studied. An appropriate electrode was chosen for lithium-air battery fabrication. Additionally, the electric capacity of the battery was measured.

3.4.2.1 Treatment of cellulose in CO_2-SWS

Materials

Cellulose was prepared according to the procedure outlined in section 3.1. 1,8-diazabicyclo [5.4.0] undec-7-ene (DBU), ethylene glycol (EG) and dimethyl sulfoxide (DMSO) were supplied from Wako Pure Chemical Co. Ltd. Carbon dioxide (99.95%) was bought from Fujii Bussan Co.Ltd.

Method

The cellulose was treated in CO_2-SWS by the method outlined in section 3.3.1. The solution of DBU and EG with a molar ratio of 2:1 was prepared. The cellulose in the concentration 4 mg mL^{-1} was suspended in the solution of DBU and EG followed by the twice volume of DMSO. The glass cell with 1.5 mL of the cellulose suspension was put into a high-pressure vessel for the CO_2-SWS treatment. Carbon dioxide gas was pressurized to 5.8 MPa or 10.0 MPa to obtain the soluble and precipitated cellulose, respectively. The system was then heated to 313.15 K and

conducted for 2 h. The system was depressurized to atmospheric pressure and the treated cellulose was removed.

3.4.2.2 Fabrication of porous cellulose/carbon electrode

Materials

Treated cellulose in CO_2-SWS prepared according to the procedure outlined in section 3.4.2.1. Acetylene carbon black (CB) with average particle size of 0.042 μ m (99.99%) and ethanol (99.5%) were supplied from Wako Pure Chemical Co. Ltd. Carbon dioxide (99.95%) was bought from Fujii Bussan Co.Ltd.

Method

Prior to drying, the treated cellulose in CO_2-SWS was pretreated by the following two routes: (A) with carbon dioxide removal from the CO_2-SWS by heating and stirring at 313.15 K for 6 h and (B) without carbon dioxide removal as shown in Figure 3.12. Known amount of CB 0.04 g mL^{-1} was added into the treated cellulose in CO_2-SWS after the pre-treatment. The mass ratio of CB and the cellulose in the suspension was 1:1 or 2:1. The suspension of CB and treated cellulose was treated in an ultrasonic bath at 313.15 K for 3 h to obtain the uniform dispersion. After the sonication, the suspension was poured into a petri dish at room temperature. The gel-like form of cellulose/CB composite electrode was obtained after the immersion of the petri dish into an ethanol bath. The supercritical drying was conducted at 313.15 K and 20.0 MPa by the procedure in the literature (Kunanusont & Shimoyama, 2018). The composite of cellulose and CB was used as the cathode of the lithium air battery.
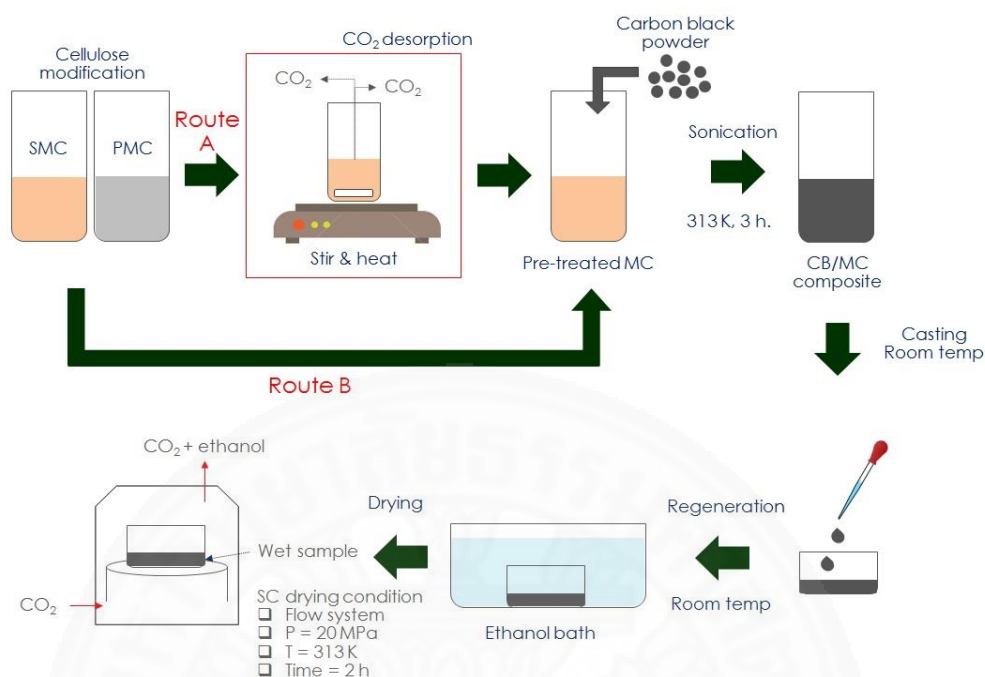
Figure 3.12 Schematic for the fabrication of cellulose/CB composite electrode.

3.4.2.3 Fabrication of lithium air battery

Materials

The porous electrode was prepared by the procedure outlined in section 3.4.2.2. Lithium Bis(trifluoromethane sulfonyl)imide (LiTFSI) and 1-Butyl-3-methylimidazolium bis(trifluoromethyl sulfonyl)imide (bmim[TFSI]) were supplied from Wako Pure Chemical Co. Ltd. Argon (99.99%) were bought from Fujii Bussan Co.Ltd.

Method

A coin-typed cell (Meshed CR2032) of lithium-air battery was constructed using the carbon electrode with the cellulose binder in argon-filled glovebox. The cell structure is shown in Figure 3.13 referred in the literature (Kunanusont & Shimoyama, 2018). The carbon electrode with the cellulose binder was assembled with lithium metal as anode, electolyte with the solution of [Li][Tf2N] in [bmim][Tf2N], carbon paper in diameter 12 mm, and the two stainless steel spacers. Finally, the assembled coin-type cell was compressed and sealed using an MSK110 hydraulic crimper (MTI Co.)
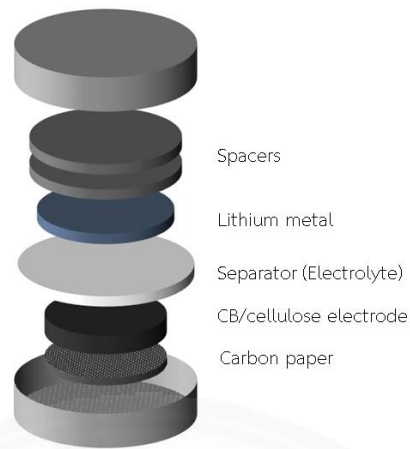
Figure 3.13 Coin cell assembly of the Lithium air battery.

3.4.2.4 Characterization

(1) Surface morphology

The surface morphology and thickness of the carbon electrode with the cellulose binder were observed by Scanning Electron Microscope (SEM) using JSM5610LV (JELO). The samples were sputter coated with Au-Pd period to the measurement.

(2) Porosity analysis

The porosity ϕ was calculated using a fraction of the void volume (V_{void}) over the total volume of the composite electrode (V_{total}) that given by the Eq. (3-31).

$$\varphi = \frac{V_{void}}{V_{total}} \qquad \qquad 3\text{-}33$$

where V_{void} and V_{total} were calculated by the following equation

$$V_{void} = V_{total} - \sum \frac{W_{solid}}{\rho_{solid}} \qquad \qquad 3\text{-}34$$

$$V_{total} = A_{surface} \times w \qquad \qquad 3\text{-}35$$

where W_{solidl} is the weight of CB in the composite (mg)

and ρ_{solidl} is the weight of cellulose in the composite (mg).

The densities of the solid materials were experimentally measured using Archimedes' principle defined in the literature (Kunanusont & Shimoyama, 2018).

(3) Conductivity analysis

The electric conductivity, σ (S m^{-1}) of the composite electrode, was defined as the inverse of resistivity which was calculated using the Eq. (3-34)

$$\sigma = \frac{1}{r} \qquad\qquad 3\text{-}36$$

where r is a body resistivity measured by a four-point probe method.

Figure 3.14 (a) illustrates an arrangement the four probes that located on the surface of the composite with thickness (w). The length between each probe (S) was fixed at 0.5 cm. A Potentiostat/Galvanostat (VersaSTAT 3-200, Princeton Applied Research) was employed to measure a voltage (V) that correlates to an applied electric current (I). The resistance (R) was calculated from the slope of linear relation between I and V as shown in Figure 3.14 (b). For the sample with a thickness less than half of the probe spacing ($w < S/2$), the simple formula for calculating r is in the Eq. (3-35).

$$r = \frac{\pi w R}{\ln 2} \qquad\qquad 3\text{-}37$$

Substituting Eq. (3-35) in Eq. (3-34) gives the equation for the electric conductivity calculation as the following equation.

$$\sigma = \frac{\ln 2}{\pi w R} \qquad\qquad 3\text{-}38$$
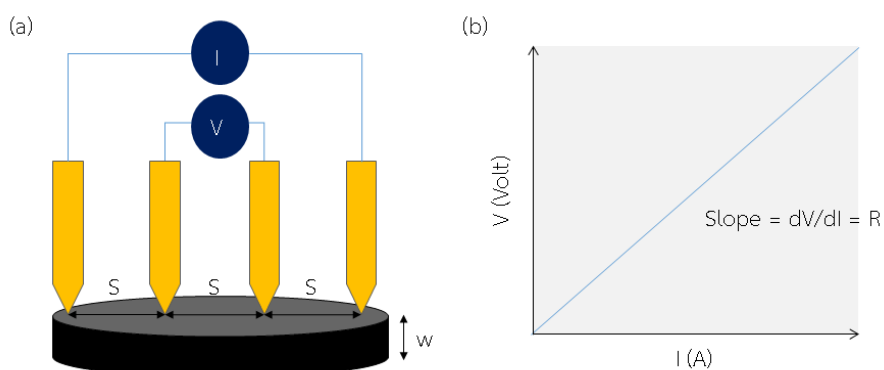
Figure 3.14 (a) Arrangement of a four-point probe on a thin sample with thickness w and (b) Current and voltage plot measured using a four-point probe technique.

(4) Electric capacity measurement

The assembled coin-type cell was put into the closed aluminium cell with air flowing at 50 mL min^{-1} and at the room temperature. The schematic of apparatus for capacity measurement is presented in Figure 3.15. The coin cell was connected to Potentiostat/Galvanostat (VersaSTAT 3-200, Princeton Applied Research) for the measurement of the discharge and charge electric capacity. The electric capacity was measured in the range from 1.5 to 4.5 V at constant current density of 0.075 mA cm^{-2}. The specific electric capacity value is based on the weight of CB.
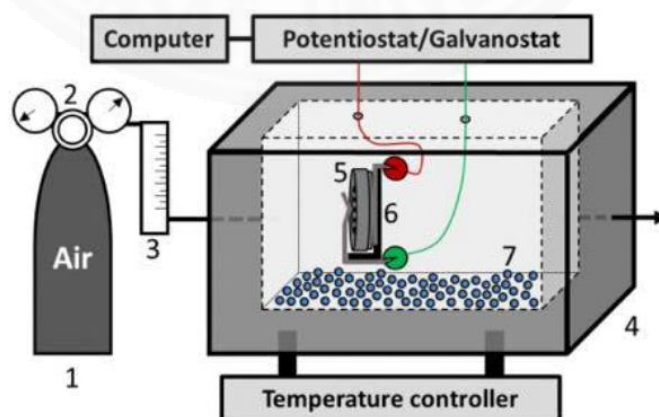
Figure 3.15 Schematic apparatus for capacity measurement: (1) Air cylinder; (2) regulator; (3) flowmeter; (4) aluminium cell box; (5) coin cell; (6) coin cell holder; (7) silica gel beads (Kunanusont, 2017).

CHAPTER 4
RESULTS AND DISCUSSION

In this chapter, the experimental results are discussed using statistical analysis. It also elaborates a shrinking particle modeling of cellulose dissolution and modification in CO_2-SWS.

4.1 The composition of derived cellulose

Average 40 grams of extracted cellulose can be derived from 100 grams of DCP; however, in this study, 25 %(w/w) were lost by spray drying. The extracted cellulose sample, treated pulps, and raw pulp were determined the composition and the results are listed in Table 4.1. The result shows the increasing in fiber content (purity) after the treatments as well as crude fiber increased to 39% and 77% after de-starch and chemical treatment, respectively.

Table 4.1 Products yield and proximate composition of cassava pulp, de-starch cassava pulp, alkaline treated pulp, bleached pulp, and cellulose.

Proximate composition (%)	CP[a]	DCP	AP	BP	Cellulose
Yield	n/a	n/a	50 [b]	40[b]	15
Moisture	n/a	11.87 ± 0.11	13.14 ± 0.08	n/a	12.29 ± 0.02
Crude protein	2.65 ± 0.05	3.20 ± 0.20	1.85 ± 0.10	0.72 ± 0.02	
Crude fat	0.20 ± 0.11	0.18[a] ± 0.02	n/a	0.50 ± 0.05	
Starch	55.07 ± 0.82	0.39[a] ± 0.10	n/a	n/a	
Crude fiber	19.45 ± 0.05	39.21[a] ± 0.14	n/a	77.00 ± 0.46	
Ash	1.98 ± 0.00	3.01 ± 0.09	2.36 ± 0.06	2.12 ±0.02	

[a] Punyanunt 2017, [b] the weight after air drying

The fiber components of derived cellulose were analyzed and identified as listed in Table 4.2. The fiber is classified into cellulose, hemicellulose and lignin using detergent and pyrolysis techniques. The detergent results show that the extracted cellulose composes of 86.10, 7.18, and 0.16 % of cellulose, hemicellulose and lignin, respectively, while DCP composes of 60.87% of cellulose, 11.62% of hemicellulose, and 24.96 % of lignin (Punyanunt, 2017). Using the pyrolysis technique gives only 70.21 % purity of cellulose. The method for determination of alpha-, beta- and gamma-cellulose is T203 cm-99 which can only be applied to bleached or delignified pulps. The alpha-cellulose consisting mainly of cellulose pulp is the most stable (un-degraded) component with the highest degree of polymerization while the beta- and gamma-cellulose are known as a degraded cellulose and hemicellulose, respectively (TAPPI T 203 cm-99, 1999). The result reveals that the derived cellulose composes of 93.17 % cellulose (72.25 % undegraded form and 20.92 % degraded form) and 4.71 % hemicellulose. As seen in Table 4.2, the T203 cm-99 method could not be used to define the lignin content in the sample because of limitation of the technique.

Table 4.2 Influence of composition analysis on fiber composition and on content of cellulose class.

Fiber type	Composition analyzed (wt%)		Cellulose content (T203 cm-99) (wt%)		
	Using detergent	Using pyrolysis	Alpha-	Beta-	Gamma-
Cellulose	86.10 ± 0.29	70.21	72.25 ± 0.36	20.92 ± 0.26	n/a
Hemicellulose	7.18 ± 0.31	4.26	n/a	n/a	4.71 ± 0.11
Lignin	0.16 ± 0.02	0.98			n/a

4.2 Influences of supercritical carbon dioxide processing on cellulose properties

4.2.1 Thermal properties

A change in the thermal behavior of the cellulose after the processing was evaluated by DSC analysis based on measurement of peak temperature (T_p), the range between conclusion temperature and onset temperature (T_c-T_o), specific heat capacity (C_p), and enthalpy change (ΔH). The DSC results for all samples are listed in Table 4.3. Figure 4.1 shows DSC patterns for unprocessed cellulose (Figure 4.1 (a)), processed cellulose under atmCO$_2$ (Figures 4.1 (b) and (c)) and processed cellulose under ScCO$_2$ (Figures 4.1 (d) – 4.4 (i)), respectively. For all samples, an exothermic peak responsible for heat release during the cellulose decomposition was observed. It was attributed that the breakdown product of ether cleavage was released and then reacted with each other to form solid char in vapor phase (Jahirul et al., 2012) resulting in heat released to the environment. The maximum temperature of the exothermic peaks (T_p) was located in 610-640 K interval. The statistical analysis suggests that no significant differences in Tp position between unprocessed cellulose and the cellulose processing in atmCO$_2$ and ScCO$_2$ (p-value 0.057). The difference in T_c-T_o represents the degree of heterogeneity of the crystals within the cellulose structure (Arns et al., 2015). Figure 4.1 shows the increase of the T_c-T_o values after the processing; however, those increasing values are also insignificant. The terms of C_p and ΔH were evaluated using the fundamental thermodynamic relationship as expressed in Eqs. (4-1) and (4-2), respectively.

$$C_p = \frac{\dot{Q}}{m\upsilon} \qquad\qquad 4\text{-}1$$

$$\Delta H = \int C_p dT \qquad\qquad 4\text{-}2$$

where C_p is specific heat capacity (J K^{-1} g^{-1}),

$\dot{Q}$ is heat flux (J s^{-1}),

m is mass (g),

υ is the heating rate (K s^{-1})

and ΔH is the change of enthalpy between two states (J g^{-1}).

As a result, it was evident that both atmCO$_2$ and ScCO$_2$ processing did not cause any significant change in C_p and ΔH values of the processed cellulose.

Table 4.3 Thermal behavior of the cellulose from DSC analysis.

p (MPa)	T (K)	t (min)	T_o (K)	T_c (K)	T_p (K)	ΔH (J g^{-1})	C_p (JK^{-1} g^{-1})	ΔC_p (W g^{-1})
Unprocessed		0	594.23	631.06	614.83	53.52	1.70588	1.41176
0.1	313.15	60	604.56	652.70	629.11	51.09	1.29412	3.64706
8	313.15	60	596.04	642.55	620.98	63.59	1.58824	3.41176
8	333.15	60	613.67	670.27	635.54	82.87	1.58824	2.76471
8	353.15	60	617.33	667.68	635.59	62.58	1.17647	1.11765
15	313.15	60	614.78	670.57	635.60	60.84	1.52941	2.64706
15	333.15	60	613.28	658.80	634.52	45.15	1.41176	2.64706
15	353.15	60	615.91	673.46	634.79	51.08	1.23529	3.05882
20	313.15	60	628.22	729.53	636.38	101.23	1.52941	2.58824
20	333.15	60	616.01	662.34	636.42	68.30	1.52941	3.94118
20	353.15	60	616.17	668.56	636.40	54.21	1.47059	3.76471
0.1	313.15	120	614.41	655.69	633.93	34.82	1.23529	2.41176
8	313.15	120	614.19	665.41	634.19	56.79	1.11765	1.76471
8	353.15	120	614.55	658.99	634.26	31.67	1.05882	2.64706
15	353.15	120	616.89	658.98	635.61	39.08	1.35294	2.52941
20	333.15	120	617.11	658.89	635.73	34.98	1.23529	2.05882
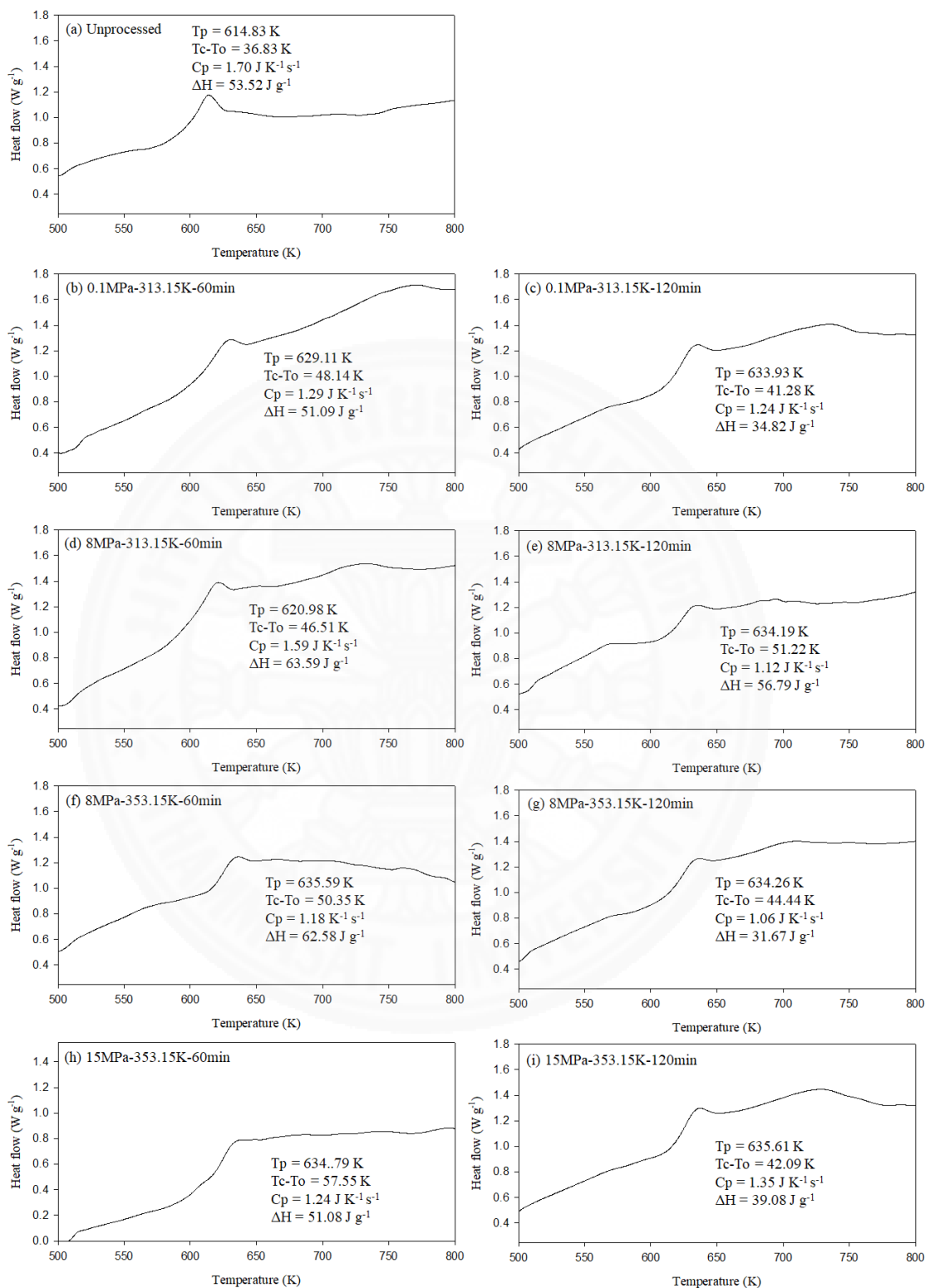
Figure 4.1 DSC illustrating heat flow patterns of unprocessed and processed cellulose samples.

TGA analysis is suggested to evaluate the thermal stability of cellulose rather than DSC analysis. The estimation of thermal stability of the cellulose after the processing was based on the beginning of the decomposition temperature (T_o), decomposition temperature (T_d), and mass change (%loss). Table 4.4 shows the thermal properties of unprocessed and processed cellulose analyzed by comparing the TGA/DTG curves for unprocessed and processed cellulose under atmCO$_2$ and ScCO$_2$ processing as shown in Figure 4.2. The significant mass loss appeared in the temperature range between 580 K and 630 K due to the decomposition of cellulose sample. The unprocessed cellulose starts decomposed at the temperature around 583.9 K while the cellulose after the processing under atmCO$_2$ and ScCO$_2$ processing starts to decompose at the temperature around 582.6 and 584.6 K, respectively. Comparing the decomposition behavior with unprocessed cellulose, it appears that T_d value significantly increases after the processing. Statistical analysis indicated the statistically significant difference of T_d values among three treatments (p-value 0.001) and those between atmCO$_2$ and ScCO$_2$ processing (p-value 0.003). Similarly, the significant difference between %loss values before the processing and those after the processing was observed (p-value 0.041). The value of %loss significantly decreases after the processing under atmCO$_2$ and more decrease of %loss observed for the processing under ScCO$_2$. It was attributed that the ScCO$_2$ processing enhanced the thermal resistance of cellulose.

Table 4.4 Thermal properties of the unprocessed and processed cellulose using TGA analysis.

p (MPa)	T (K)	t (min)	Loss of moisture				Loss of cellulose			
			T_o (K)	T_c (K)	T_P (K)	%Loss	T_o (K)	T_c (K)	T_P (K)	%Loss
Unprocessed			339.37	392.68	365.49	4.4265	583.88	624.00	612.33	87.5641
0.1	313.15	60	341.32	409.73	373.99	4.2839	582.05	631.04	613.99	76.8796
0.1	313.15	60	342.75	409.63	378.83	4.1157	582.89	631.50	614.66	76.9065
8	313.15	60	343.07	401.60	374.33	4.1327	583.17	630.45	614.66	78.0805
8	333.15	60	343.54	399.30	369.49	3.8839	583.88	631.95	615.83	78.5005
8	353.15	60	341.07	394.55	370.99	3.7630	584.60	632.62	616.66	78.8730
15	313.15	60	342.16	405.48	372.83	4.1807	585.14	632.63	617.33	80.0956
15	333.15	60	341.21	399.36	371.33	3.9442	584.45	631.70	616.16	77.3107
15	353.15	60	341.66	405.24	368.83	4.4499	583.65	631.78	614.99	77.7696

Table 4.4 (Cont.)

p (MPa)	T (K)	t (min)	Loss of moisture				Loss of cellulose			
			T_o (K)	T_c (K)	T_P (K)	%Loss	T_o (K)	T_c (K)	T_P (K)	%Loss
20	313.15	60	T_{Onset}	T_{Endset}	T_{Peak}	%Loss	T_{Onset}	T_{Endset}	T_{Peak}	%Loss
20	333.15	60	338.97	401.20	368.33	4.0401	585.49	633.26	617.99	77.9367
20	353.15	60	341.28	406.54	376.83	4.4640	586.22	633.57	618.16	78.9776
0.1	313.15	120	349.86	405.97	381.99	3.3211	581.69	630.45	613.16	78.2017
0.1	313.15	120	342.44	404.49	373.83	3.8563	583.62	632.05	615.83	77.7011
8	313.15	120	340.69	399.05	373.66	3.6801	584.78	633.18	617.66	77.2437
8	353.15	120	340.66	396.58	366.99	3.9163	583.58	632.20	615.99	79.2643
15	353.15	120	340.29	393.89	363.16	3.9155	585.02	632.41	617.66	78.6049
20	333.15	120	340.85	394.30	366.49	4.2630	585.01	632.43	616.83	78.4669
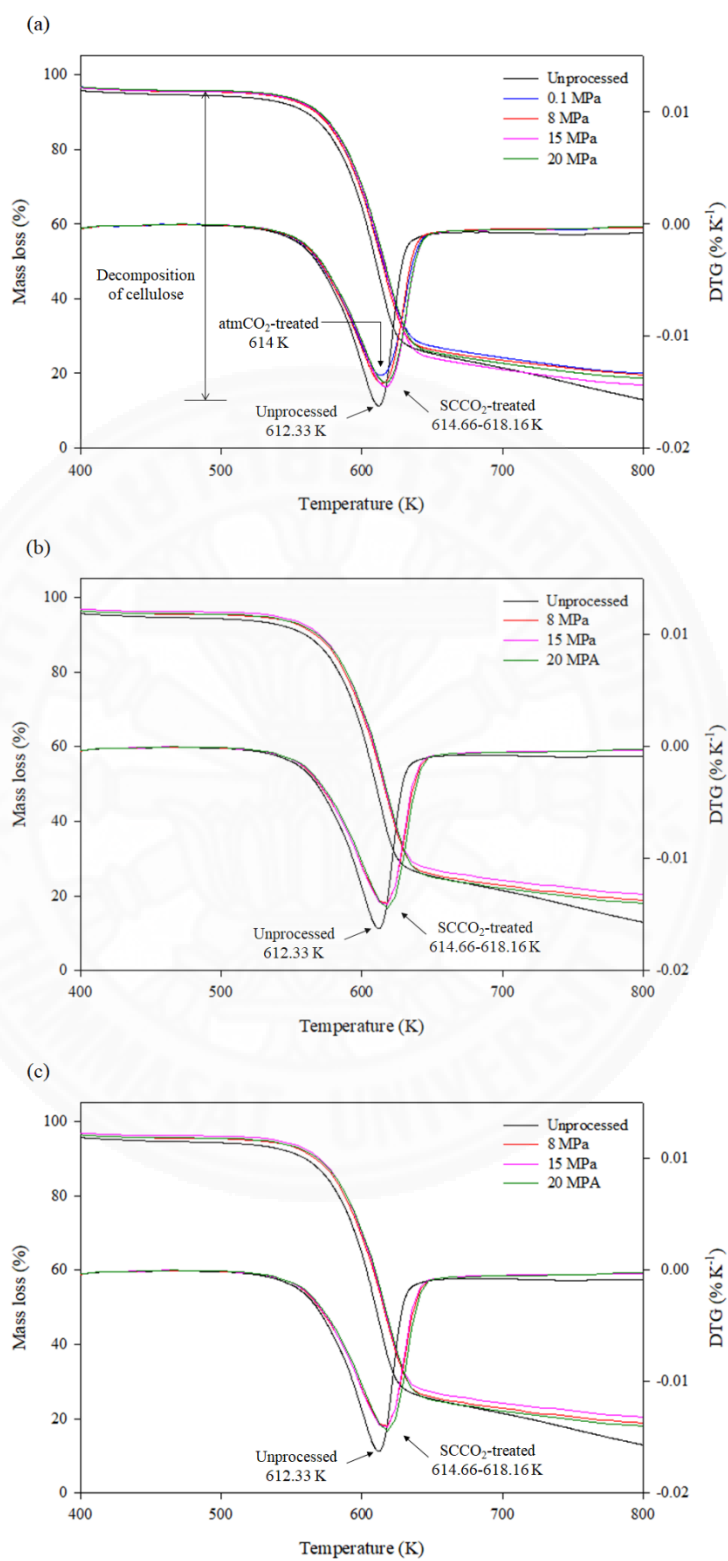
Figure 4.2 TGA and DTG thermograms of unprocessed and processed cellulose under the temperature of (a) 313.15 K, (b) 333.15 K and (c) 353.15 K for 60 min.

4.2.3 Crystallinity

XRD results show the same crystalline diffraction pattern for both unprocessed and processed cellulose. Four main peaks were found around 15, 16.5, 20 and 22° corresponding to the scattering of the 101, 10 $\overline{1}$, 021 and 002 reflection planes in cellulose I type. The XRD results for all samples are shown in Appendix D. The crystallinity of cellulose before and after the processing was evaluated via the degree of crystallinity (Cr) and crystallinity index (C.I.). The Cr is the fractional amount of crystalline in the polymer sample while the C.I. is an empirical measure of the relative amount of crystalline material in cellulose (crystal and amorphous). Figure 4.3 (a) illustrates peak separations of X-ray diffraction after the subtraction of amorphous region. The Gaussian model fitting was performed using the Origin software yielding area under the amorphous and crystalline peaks. The Cr was calculated using Eq. (3-15) and, calculated Cr under various treatment levels are shown in Table 4.5. The Cr of unprocessed cellulose is 49.7 %, and the means Cr of processed cellulose under atmCO$_2$ and ScCO$_2$ are 49.7 % and 50.9 %, respectively. It was observed that the Cr insignificantly changes after the processing both under atmCO$_2$ and ScCO$_2$ (p-value 0.659). Solid state ^{13}C NMR was applied to determine the Cr of cellulose before and after processing under ScCO$_2$. Figure 4.3 (d) shows ^{13}C NMR spectrum of cellulose. The focusing signals for the determination of Cr are C-4 carbons of cellulose that located between 80 and 93 ppm. The signals between 87 and 93 ppm correspond to crystalline form whereas the signals between 80 and 87 ppm correspond to amorphous form. After the ScCO$_2$ processing proceeds, the Cr slightly increases from 42.4 % to 43.1 % (Calculation is shown in appendix E). That is consistent with the Cr result from X-ray diffraction analysis.
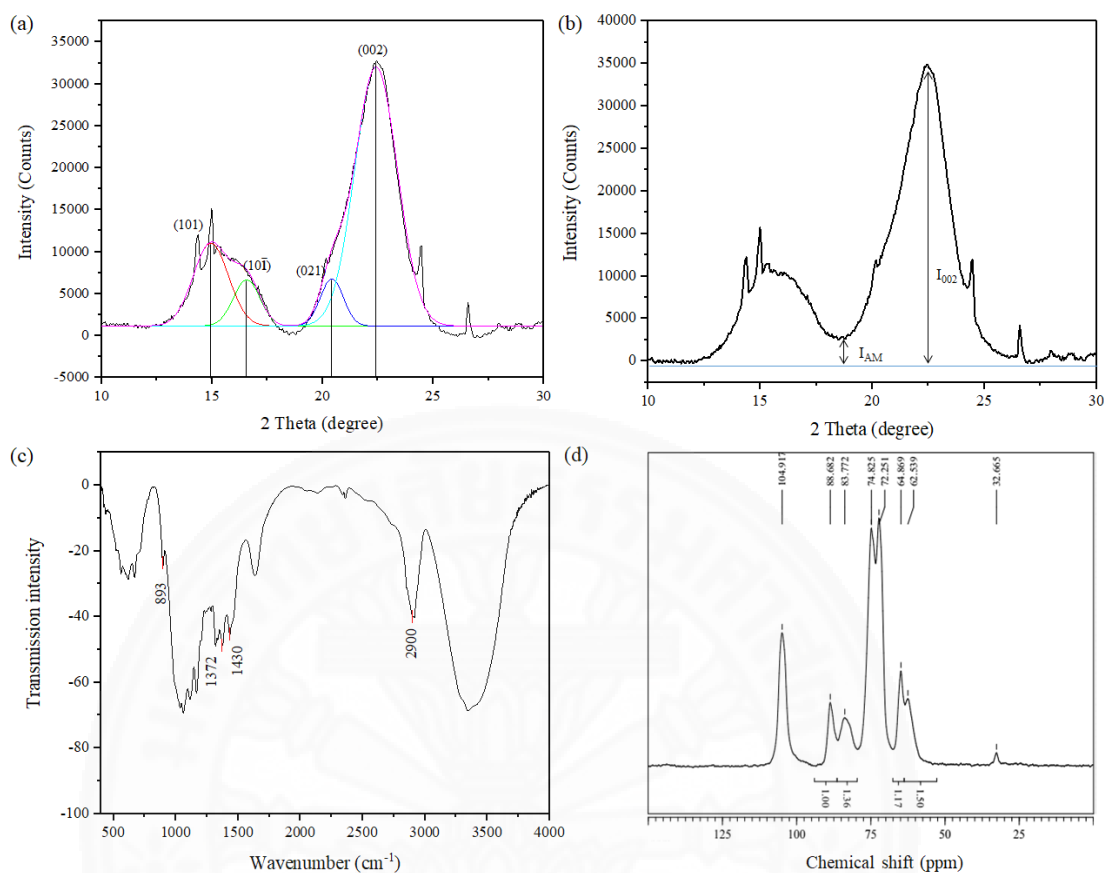
Figure 4.3 Illustration of the four methods for evaluating the crystallinity of cellulose. (a) Amorphous subtraction and peak deconvolution method (Herman's equation), (b) peak height method (Segal's equation), (c) FTIR method, and (d) Solid-state ^{13}C NMR method (Newman method).

Figure 4.3 (b) and (c) illustrate the evaluation of C.I. using peak height method and FTIR method, respectively. The C.I. was calculated from X-ray diffraction results using peak height method that considers the relative intensity between the crystalline peak at 22.4° (I_{002}) and the amorphous region at 18.6° (I_{AM}) as shown in Eq. (3-14). There was no statistically significant difference in C.I. between unprocessed cellulose and processed cellulose samples (p-value 0.165). Similarly, the FTIR results obtained from unprocessed cellulose and processed cellulose samples (p-value 0.163) were not found significant difference.

Table 4.5 The calculated degree of crystallinity (*Cr*) and crystallinity index (C.I.) of cellulose before and after processing.

p (MPa)	*T* (K)	*t* (min)	*Cr* Herman's equation	C.I.	
				Segal's equation	FTIR technique
Unprocessed		0	0.4966	0.7944	0.7917
0.1	313.15	60	0.4943	0.7898	0.6819
0.1	313.15	60	0.4454	0.7435	0.7010
8	313.15	60	0.5017	0.7940	0.7215
8	333.15	60	0.5393	0.8191	0.7542
8	353.15	60	0.5049	0.7783	0.7182
15	313.15	60	0.5060	0.7943	0.7274
15	333.15	60	0.5125	0.8026	0.7111
15	353.15	60	0.4900	0.7891	0.6774
20	313.15	60	0.4696	0.7793	0.7735
20	333.15	60	0.4802	0.7879	0.7350
20	353.15	60	0.5252	0.8174	0.7981
0.1	313.15	120	0.5092	0.7824	0.7650
0.1	313.15	120	0.5385	0.8029	0.6993
8	313.15	120	0.5209	0.7979	0.7475
8	353.15	120	0.5153	0.8024	0.7433
15	353.15	120	0.5216	0.8067	0.7605
20	333.15	120	0.5282	0.8131	0.6904

4.2.1 Surface morphology and fibril size

The high-resolution organization of the cellulose fibril was observed using FE-SEM. Figure 4.4 shows FE-SEM images of the cellulose sample before and after the treatment under $atmCO_2$, and $ScCO_2$ at 313.15 K. The aggregation and strong reciprocal packing of fibrils were observed in unprocessed cellulose while more fibrillated fibrils were observed after the treatment under $ScCO_2$ for 120 min. This result is consistent with the study of Zheng that reported the disruption of the cellulosic structure by supercritical carbon dioxide (Zheng, Lin, & Tsao, 1998). However, some surface damages resulting from energetic electron beam were observed especially in the processed cellulose samples under $atmCO_2$ that is a main obstacle to surface morphological analysis. Figure 4.5 shows FE-SEM images of the cellulose sample after processing under $ScCO_2$ for 60 min. There was no significant change in the morphology and fibril size of the cellulose after processing at the pressure of 8, 15, 20 MPa and the temperature of 313.15, 333.15, 353.15 K. The cellulose samples were fibrillated with average 26 nm in diameter. Similar to the cellulose samples after processing for 120 min, the average diameter of the fibril was 25 nm (Figure 4.6).
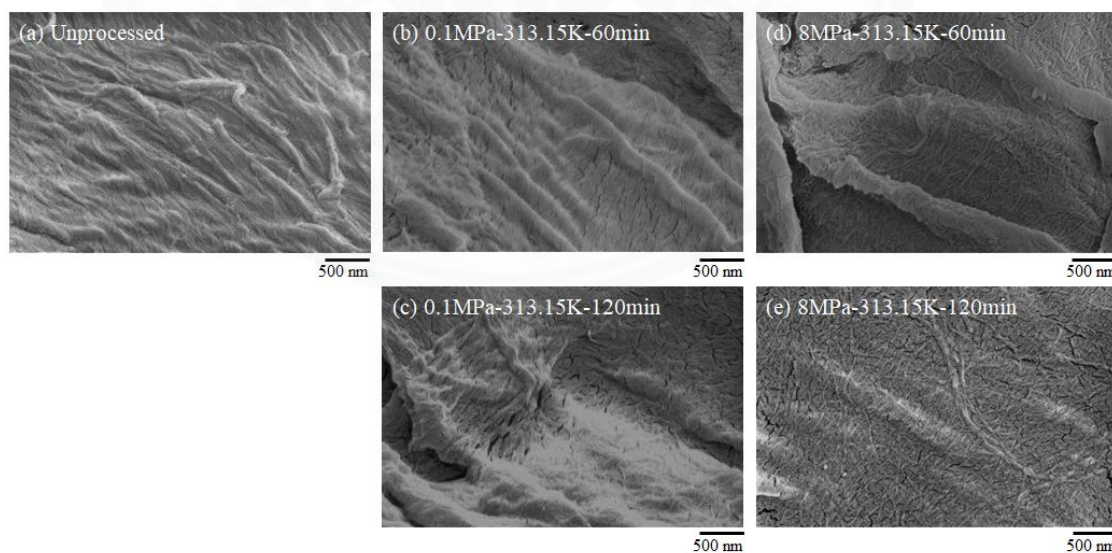
Figure 4.4 Field emission scanning electron microscopy (FE-SEM) of unprocessed cellulose and processed cellulose samples at 313.15 K under CO_2 processing at 0.1 MPa and $ScCO_2$ processing at 8 MPa for 60 and 120 min.
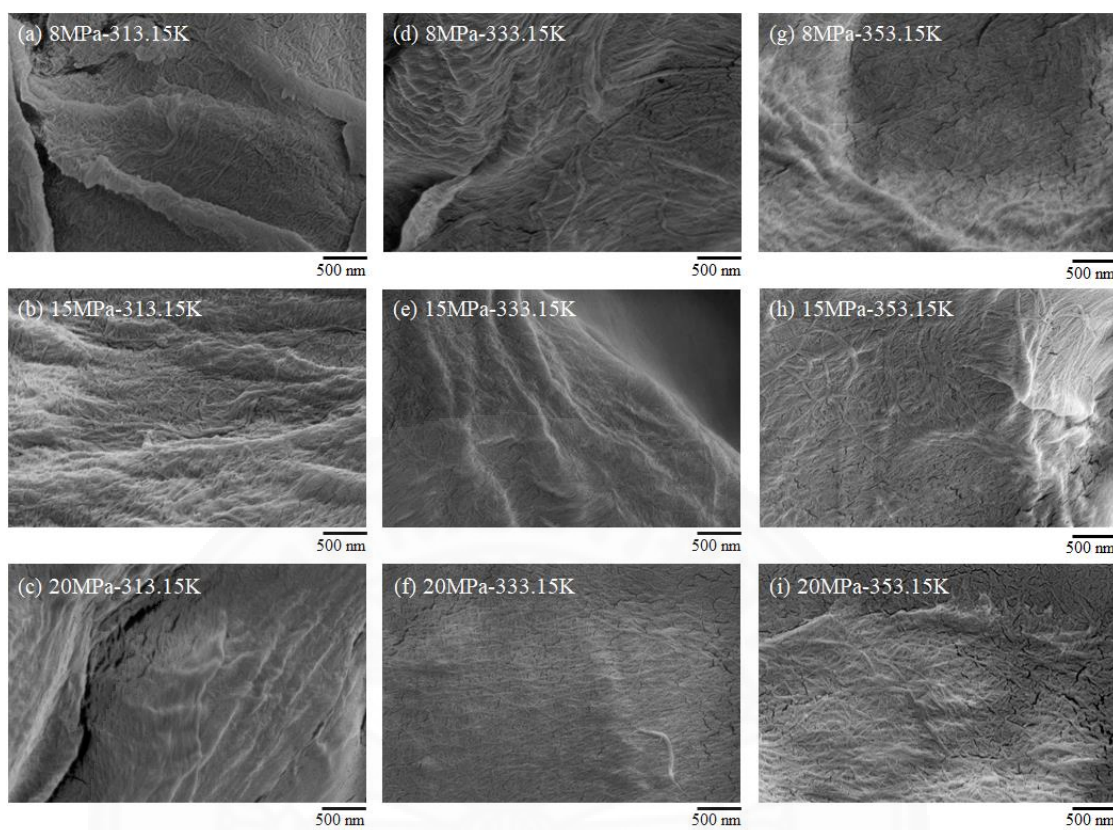
Figure 4.5 Field emission scanning electron microscopy (FE-SEM) of processed cellulose samples under $ScCO_2$ processing at temperature of 313.15, 333.15, and 353.15 K and pressure of 8, 15, and 20 MPa for 60 min.

The fibril sizes of unprocessed and processed cellulose sample are shown in Table 4.6; however, the fibril size of the cellulose after processing under $atmCO_2$ could not be evaluated due to interruption caused by surface damages as aforementioned. The statistical analysis reveals the significant difference in the size of the fibril between unprocessed and $ScCO_2$-processed cellulose sample (p-value 0.001). This indicates that $ScCO_2$ processing could dissociate the cellulose chains resulting decreasing in fibril size of the cellulose.
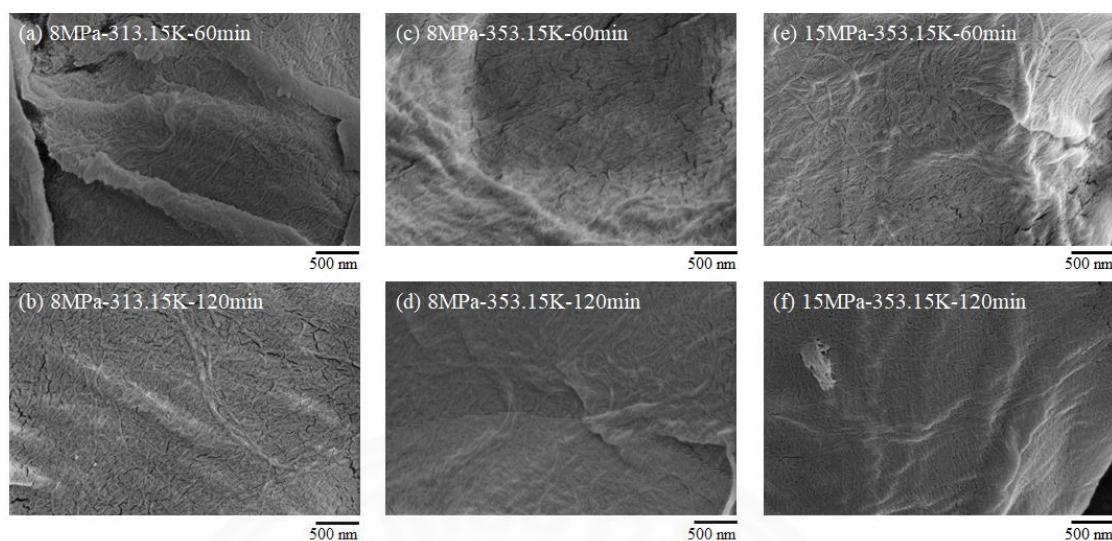
Figure 4.6 Field emission scanning electron microscopy (FE-SEM) of processed cellulose samples under $ScCO_2$ processing for 60 and 120 min.

Table 4.6 Fibril size of unprocessed and processed cellulose under $ScCO_2$.

Processing condition			Average	Processing condition			Average
p	T	t	fibril size	p	T	t	fibril size
(MPa)	(K)	(min)	(nm)	(MPa)	(K)	(min)	(nm)
Unprocessed			50.93±25.41	20	313.15	60	23.36±7.83
8	313.15	60	29.03±8.94	20	333.15	60	26.38±10.31
8	333.15	60	29.08±11.87	20	353.15	60	32.55±16.00
8	353.15	60	37.09±35.98	8	313.15	120	28.70±14.42
15	313.15	60	20.43±5.99	8	353.15	120	24.68±8.97
15	333.15	60	19.16±6.57	15	353.15	120	16.96±4.12
15	353.15	60	20.23±6.69	20	333.15	120	28.38±13.57

$AtmCO_2$ existing in subcritical state at 313.15 K and $ScCO_2$ processing changed the thermal properties of cellulose without losing its crystalline nature. Compared with TGA results of unprocessed cellulose, the thermal degradation temperature of processed cellulose shifted to higher temperature. It suggests that thermal stability of processed cellulose is superior to that of unprocessed sample. In

the meantime, the reduction of percent loss in cellulose weight was observed for processed cellulose samples. This may be attributed that the alteration in cellulose compositions occurs during processing which cannot be measured with TGA technique. Evidently, CO_2 at high-pressure conditions (sub- and supercritical) could penetrate inside the structure of cellulose. The observation of the cellulose chains dissociation after processing was verified by FE-SEM images as shown in Figures 4.4 - 4.5.

The results support the hypothesis that employing sub- and supercritical carbon dioxide in CO_2-SWS enhance penetrability of solvent molecules in cellulose matrix as discussed in section 4.3.

4.3 Dissolution of cellulose with CO_2-SWS

Variations of the switchable solvent conditions such as pressure and temperature were studied to achieve dissolving cellulose for its further processing. To understand the effect of CO_2-SWS conditions on solubility of cellulose, the phase behavior and mechanism of cellulose during dissolution in CO_2-SWS were studied.

4.3.1 Phase behavior of cellulose during dissolution in CO_2-SWS

The dynamic of the phase behavior during the cellulose dissolution in CO_2-SWS are shown in Figure 4.7. At 313.15 and 333.15 K, the cellulose in the solution was dissolved by introducing carbon dioxide with a pressure of 5.8 MPa. The transparent and homogeneous solution was then formed and stabilized in 20 min as shown in Figure 4.7 (b) and (c), respectively whereas at low-temperature condition 298.15 K, cellulose could not get to dissolving form as shown in Figure 4.7 (a). Interestingly, the cellulose in the solution was precipitated after forming the homogeneous phase at 10.0 MPa and 313.15 K as shown in Figure 4.7 (d). It is found that the phase behavior of the cellulose dissolution in CO_2-SWS depend on the pressure (p) and temperature (T).
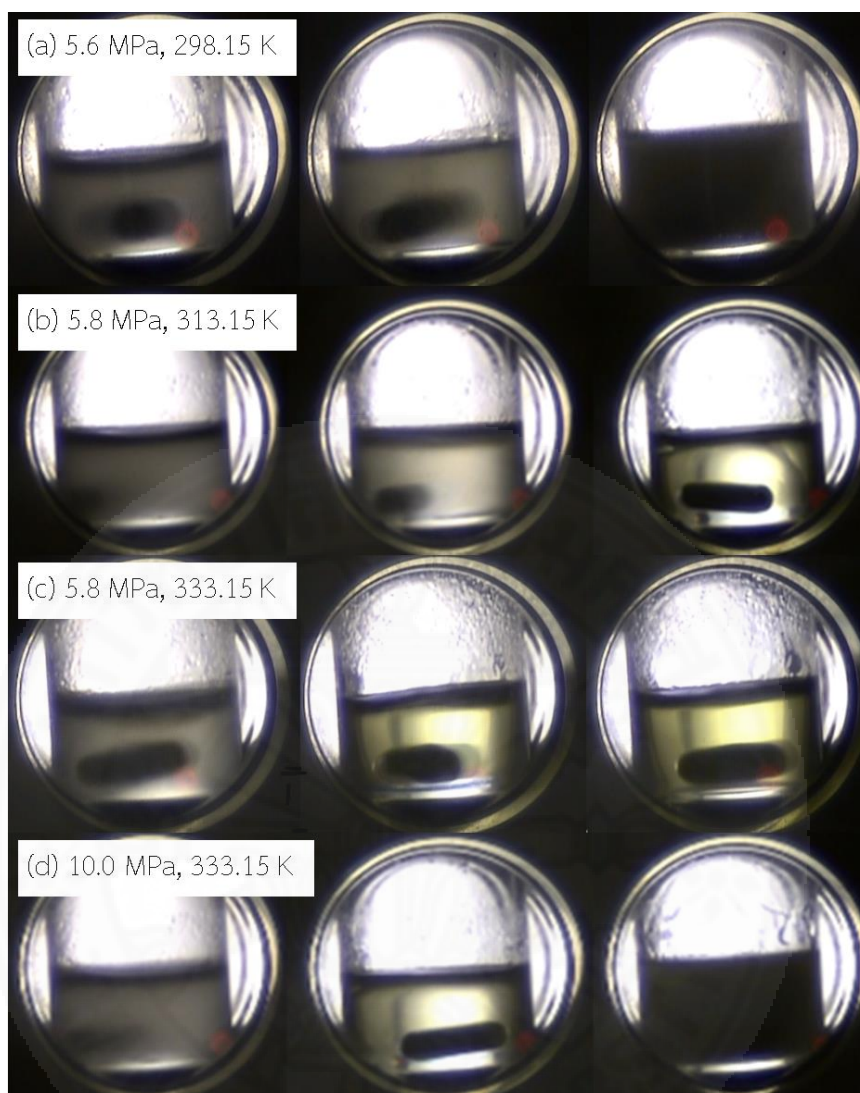
Figure 4.7 Phase behavior during dissolving cellulose in CO_2-SWS.

Figure 4.8 illustrates the phase diagram on the dissolution of the cellulose in the CO_2-SWS and that phase diagram in the projection of density of CO_2 (Figure 4.8 (b)). This phase diagram contains the dissolution or precipitation at various p and T and the boundary conditions for the cellulose dissolution in the CO_2-SWS. The boundary conditions on the cellulose dissolution are also listed in Table 4.7. Figure 4.8 (b) also shows the preferable physical state of CO_2 at any pressures and temperatures. The results reveal the cellulose could be dissolved into the CO_2-SWS at the conditions that are triggered by CO_2 existing in its sub- and supercritical state. Conversely, we can see the precipitation of the cellulose in the switchable solution when the system was

performed at the conditions using gaseous CO_2 as a trigger. The precipitation as shown in Figure 4.7 (d) could be resulted from the cellulose modification in the switchable solution as described in the following section. It has been suggested that sub- or supercritical CO_2 are capable of enhancing the penetrability of the CO_2-SWS into the cellulose structure and consequently, the strong hydrogen bonds were deconstructed. It also found that the processing temperature required for cellulose dissolving in CO_2-SWS began at 303.15 K which is lower than typical range optimal temperature of 353.15 - 403.15 K for cellulose dissolving in common solvents. However, it was evident that the solubility of cassava-based cellulose in the CO_2-SWS was density dependent as shown in Figures 4.8 (a) and (b).

Table 4.7 Phase boundary on dissolution of cellulose in CO_2-SWS.

p (MPa)	T (K)
0.1	303.15
5.3	304.65
6.3	313.15
7.2	322.15
8.2	333.15
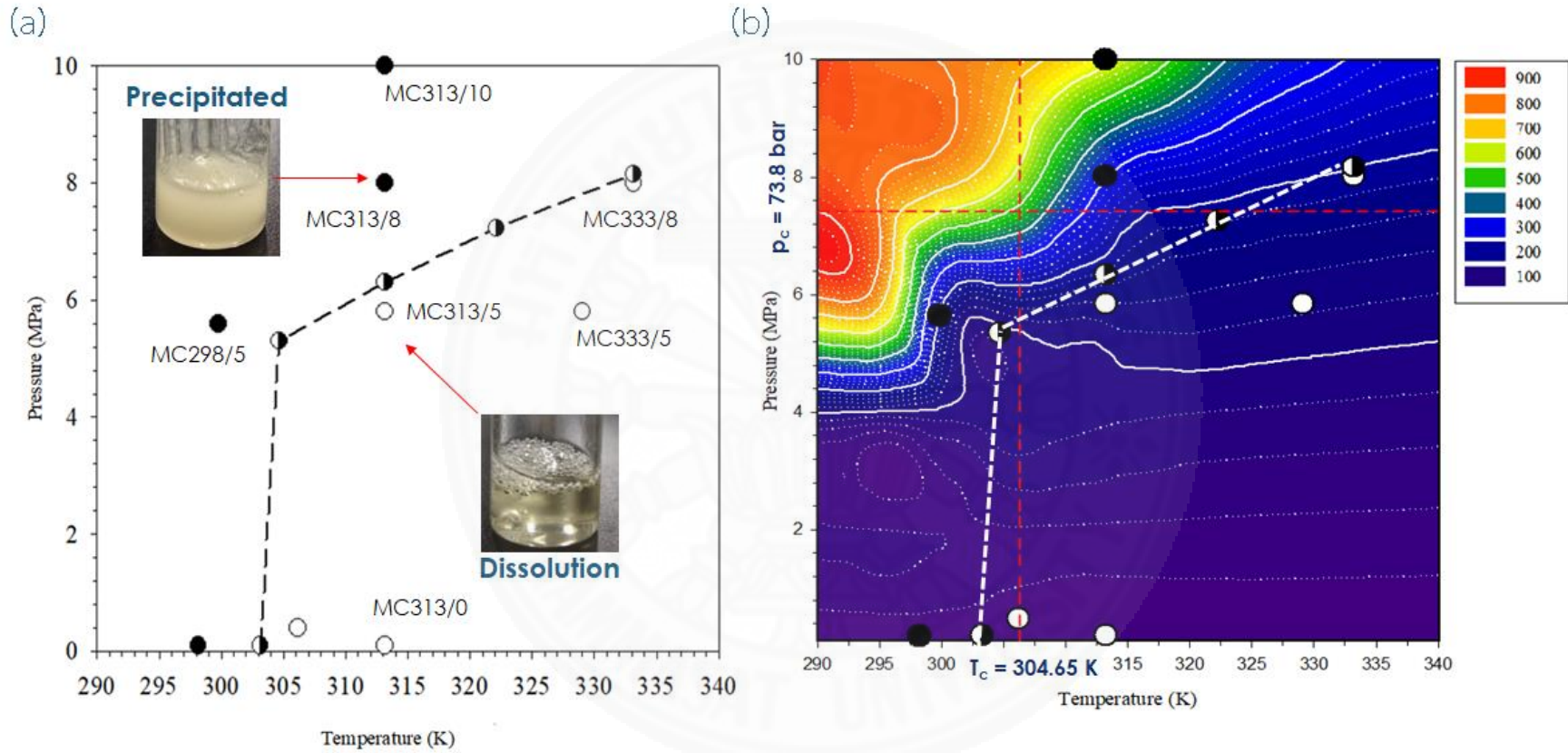
Figure 4.8 (a) Phase diagram on dissolution of cellulose in CO_2-SWS and (b) that diagram in the projection of density of CO_2; ◐ phase boundary,●; precipitation,○; dissolution.

4.3.2 Reaction occurring in CO$_2$-SWS prediction using Fourier Transform Infrared Spectroscopy (FTIR)

The switchable polarity solvent containing cationic of DBU ([DBUH]$^+$) and anionic of ethylenedicarbonate ([O$_2$COCH$_2$CH$_2$OCO$_2$]$^{2-}$) were produced in the mixture of DBU and EG with carbon dioxide. Similar to the ionization of TMG and EG mixture under carbon dioxide exposure (Xie et al., 2014), the mixture of DBU and alcohol was switched to the ionic forms with [DBUH]$^+$ and alkylcarbonate by carbon dioxide (Phan, Chiu, et al., 2008)
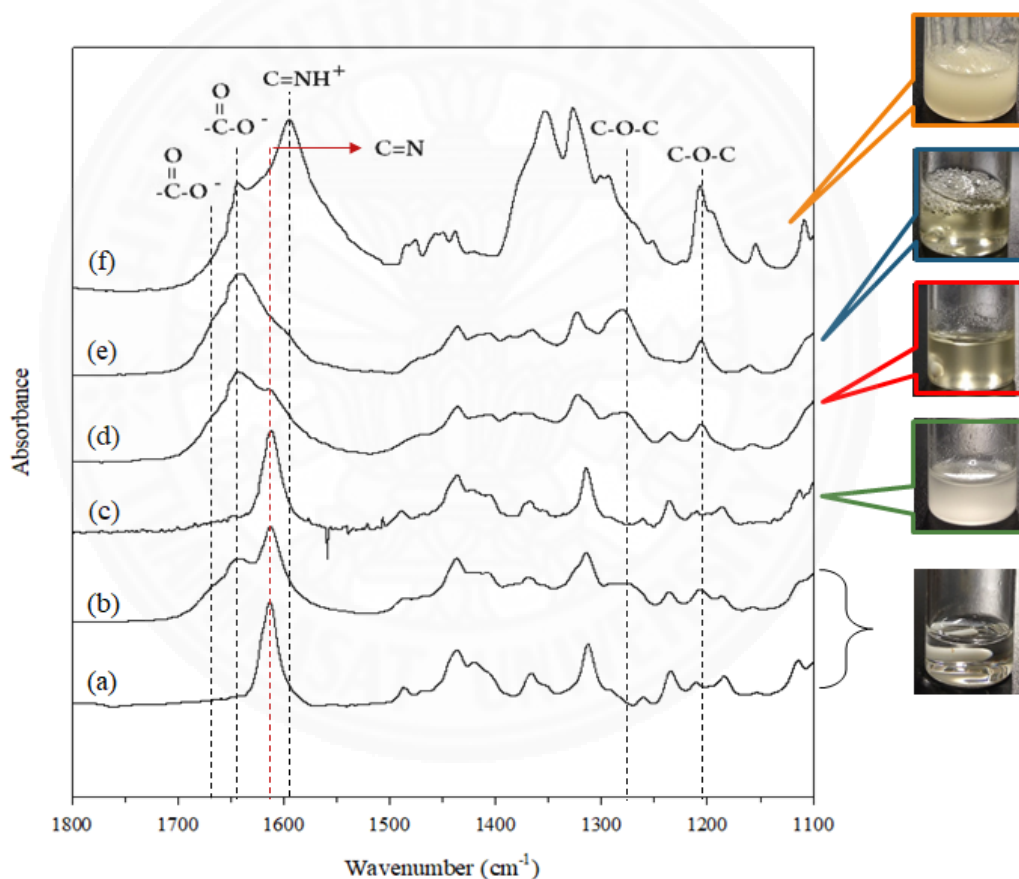
Figure 4.9 FTIR spectra of (a) the mixture of DBU + EG + DMSO before CO$_2$ switchable, (b) the mixture of DBU + EG + DMSO after CO$_2$ switchable (CO$_2$-SWS) prepared at 5.8 MPa and 313.15 K, (c) the mixture of DBU + EG + DMSO containing cellulose before CO$_2$ switchable, (d) the CO$_2$-SWS containing cellulose prepared at 0.1 MPa and 313.15 K, (e) the CO$_2$-SWS containing cellulose prepared at 5.8 MPa and 313.15 K and (f) the CO$_2$-SWS containing cellulose prepared at 10.0 MPa and 313.15 K.

The IR spectra of the mixture of DBU + EG + DMSO without cellulose before and after the CO_2 treatment are given inFigure 4.9 (a) and (b). We can see the peak of C=N stretching vibration of DBU at 1612 cm^{-1} in the IR spectra before the CO_2 treatment as given in Figure 4.9 (a). After the CO_2 treatment at 5.8 MPa and 313.15 K, the carbonyl group (COO^-) can be formed by the ionization of the DBU in the switchable solution as the peaks around 1668 and 1639 cm^{-1} of the IR spectra in Figure 4.9 (b). Additionally, the finding of asymmetric and symmetric C-O stretching vibration around 1280 and 1200 cm^{-1} in Figure 4.9 (b) also represents the production of $[O_2COCH_2CH_2OCO_2]^{2-}$. Phan et al. have reported that the mixture of DBU and alcohol can be the switchable solvent by carbon dioxide and form the ionized cationic $[DBUH]^+$ and anionic alkylcarbonate (Phan, Chiu, et al., 2008). The mixture containing $[DBUH]^+$ and $[O_2COCH_2CH_2OCO_2]^{2-}$ could be used to dissolve the cellulose by breaking the hydrogen bonding between the cellulose chains and dissembling its structure by competitive hydrogen bonding with those ionized ions as given in Figure 4.10 (a) (Olsson & Westman, 2013; Xie et al., 2014; Y. Yang et al., 2015).

The IR spectra of cellulose in the mixture of DBU + EG + DMSO showed a peak of C=N stretching vibration of DBU at 1612 cm^{-1} before CO_2 treatment (Figure 4.9 (c)) that was similar to the observed peak found in the mixture of DBU + EG + DMSO without addition of cellulose (Figure 4.9 (a)). It can be confirmed that the mixture of DBU + EG + DMSO could not affect to cellulose in the absence of CO_2.

Figure 4.9 (d) - (f) give the IR spectra of the CO_2-SWS containing the cellulose after the treatment at 313.15 K, 0.1, 5.8 and 10.0 MPa. As discussed before, dissolving cellulose and cellulose precipitation observation depends on the p and T of the SWS. Expectedly, the IR spectra obtained from both cellulose forms are different in shape. Figure 4.9 (d) and (e) correspond to the IR spectra of dissolving cellulose form gave at 0.1 and 5.8 MPa, respectively. The vibration of C=N, COO^- and $C=NH^+$ groups were found at the same positions as the CO_2-SWS without cellulose (Figure 4.9 (b)) unless the intensity ratio of the C=N to COO^- was contrasting. The peak intensity of the C=N stretching vibration was weaker than the COO^- vibration for the dissolving cellulose form. This observation suggests the consuming of DBU in the reaction with

hydroxyl groups of cellulose as proposed in Figure 4.10 (b). Carbon dioxide in DBU solution allows for the derivative dissolution of cellulose as reported by the literatures (Song et al., 2015; Y. Yang et al., 2015).
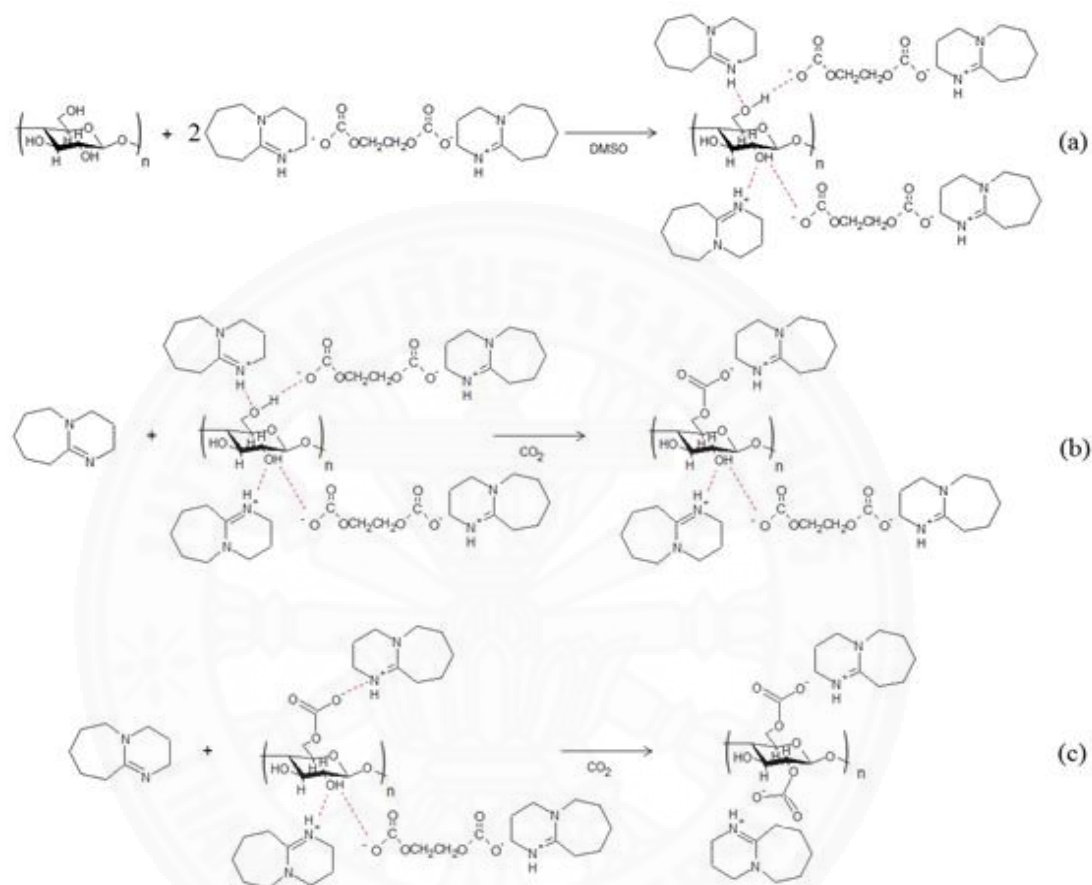
Figure 4.10 Proposed reactions for cellulose in a CO_2-SWS. (a) Cellulose dissolving by ionized cationic DBUH$^+$ and anionic carbonate modified from Y. Yang et al. (2015a), (b) Formation of anionic cellulose carbonate in dissolution, (c) Formation of anionic cellulose carbonate in precipitation.

Figure 4.9 (f) shows the IR spectra of precipitated cellulose form yielded at 10.0 MPa. The stretching vibration of C=NH$^+$ in [DBUH]$^+$ was detected at 1595 cm^{-1}. Interestingly, the C=NH$^+$ vibration is obviously stronger than that at 5.8 MPa. This might be resulted from the formation of derivative cellulose by the reaction between carbon dioxide and hydroxyl groups of the cellulose in the presence of DBU. The carbonate

anion group on the cellulose unit links to the cationic DBU via ionic bonding to yield the cellulose carbonate salt formation as proposed in Figure 4.10 (c). At higher pressure (density), carbon dioxide can react with hydroxyl groups of the cellulose more than those in the case of the lower pressure. Consequently, the hydrogen bonds between cellulose and ionized DBU and EG are reduced so that the dissolved cellulose in the solution is precipitated as shown in the phase behavior in Figure 4.7 (d). Heldebrant and co-workers reported that the carbonate salts of DBU result in the formation of a white solid precipitating out of solution (Heldebrant et al., 2005).

4.3.3 Shrinking particle modeling for cellulose dissolution in CO_2-SWS

The diffusion-limited shrinking particle model (SPM) was developed based on the successful cellulose dissolution conditions. The results show that cassava-based cellulose can be completely dissolved in the CO_2-SWS under sub- and supercritical CO_2-triggered SWS. After complete cellulose dissolution, the diffusivity of CO_2-SWS in liquid boundary (Step 2 of Figure 3.9) (D), completed cellulose dissolution time (τ), and cellulose dissolution conversion (X_c) were determined by the developed SPM. To calculate these model-predicted parameters, initial CO_2 concentration had to be estimated by correlation and regression analysis among initial CO_2 concentration, dissolving pressure and temperature.

4.3.3.1 Calculation of a diffusion coefficient

The dissolution behavior of cellulose in the CO_2-SWS showing in Figure 4.8 is also listed in Table 4.8. The results show that cellulose can be dissolved in the CO_2-SWS (excepted in the cases termed MC298/0, MC298/5, and MC313/8 where precipitation of cellulose was observed). It can be seen that cellulose could not be dissolved at ambient or low temperature where CO_2 exists in a gas state, and sufficient heat might also be required to dissolve the cellulose under higher-pressure conditions. In this work, the SPM was developed based on successful cellulose dissolution under the studied conditions.

Table 4.8 CO_2 state and behavior of dissolving cellulose under various conditions in the CO_2-SWS.

Condition	p (MPa)	T (K)	CO_2 state	Dissolving of cellulose
MC298/0	0.1	298.15	Gaseous	Precipitated
MC313/0	0.1	313.15	Subcritical	Dissolved
MC298/5	5.6	298.15	Gaseous	Precipitated
MC313/5	5.8	313.15	Subcritical	Dissolved
MC333/5	5.8	329.05	Subcritical	Dissolved
MC313/8	8.0	313.15	Supercritical	Precipitated
MC333/8	8.0	333.15	Supercritical	Dissolved

The diffusion coefficient of the CO_2-SWS (D) was solved using Eq. (3-28) to minimize the normalized error of estimated τ compared with measured τ. The estimated values of D, together with the measured and estimated values of τ are listed in Table 4.9 for the various pressure and temperature conditions. The results show that the diffusion coefficients of CO_2-SWS in the liquid film boundary are in the range 10^{-20} to 10^{-17} m^2 s^{-1} depending on the system conditions.

Table 4.9 Estimated D, measured and estimated τ, and X_C values under various conditions in the CO_2-SWS.

Condition	p (MPa)	T (K)	$C_{CO_2,l}$ (kg m^{-3})	Measured τ (s)	Predictive τ [a] (s)	Estimated $D \times 10^{20}$ (m^2 s^{-1})	Predictive X_C [b] at 120 s
MC313/0	0.1	313.15	1.70	1620	16131.02	1765	0.011
MC313/5	5.8	313.15	142.34	960	947.31	5.05	0.18
MC333/5	5.8	329.05[*]	123.63	180	163.21	72.14	0.86
MC333/8	8.0	333.15	192.01	120	121.97	67.22	1.00

[*]Actual temperature reading from the temperature controller (setting temperature: 333.15 K). [a] Using Eq. (4-6) and [b] Eq. (3-30).

The Jordaan group studied the gas–solid system of nitrogen and molybdenum, and they reported calculated diffusion coefficients of 10^{-21} for molybdenum and 10^{-14} for nitrogen at temperatures around 800–900 K (Jordaan, Terblans, & Swart, 2008).

4.3.3.2 Effects of system conditions on diffusion coefficient

The calculated D values in Table 4.9 show the drastic decrease when the pressure of CO_2 reaches a high-pressure subcritical and supercritical (SC) state. The statistical correlation coefficients in Table 4.10 indicate that the negative relationship between p and D possesses a strong r_s value (–0.632) similarly to that relationship between $C_{CO_2,l}$ and D (-0.800). At higher pressure, an increase in CO_2-SWS molecules causes self-hindrance between CO_2-SWS molecules, which then decrease the movement of CO_2-SWS molecules. On the other hand, the correlation between T and D, as reported in Table 4.10, is very weak, indicating that the temperature dependence is negligible. This evidence suggests that the development of the dissolution process by increasing the pressure from atmospheric to high, causes the decrease in the diffusion coefficient.

Table 4.11 shows the correlation test results considering at high-pressure conditions. The r_s value between T and D is 0.966 indicating a strong positive correlation; thus, the D value estimated at the pressure of 5.8 MPa in Table 4.9 was increased when the temperature was increased from 313.15 to 329.05 K.

Table 4.10 Pearson and Spearman correlation coefficients among the responses and processing conditions.

			p	T	$C_{CO_2,l}$	D
Spearman's rho	D	Correlation coefficient	-0.632	-0.105	-0.800	1.000*
		Sig (2-tailed)	0.368	0.895	0.200	.
	$\tau_{predicted}$	Correlation coefficient	-0.949*	-0.949*	-0.800	0.400
		Sig (2-tailed)	0.051	0.051	0.200	0.600
Pearson's	X_C	Correlation coefficient	0.791	0.989*	0.743	-0.657
		Sig (2-tailed)	0.209	0.011	0.257	0.343
	$C_{CO_2,l}$	Correlation coefficient	0.995*	0.660	1.000*	-0.931*
		Sig (2-tailed)	0.005	0.340	.	0.069

* Correlation is significant at the 0.1 level (2-tailed).

Table 4.11 Pearson correlation coefficients among the responses and processing conditions considering only high-pressure conditions.

			p	T	$C_{CO_2,l}$	D
Pearson's	D	Correlation coefficient	0.442	0.966	0.189	1.000*
		Sig (2-tailed)	0.709	0.166	0.879	.
	$\tau_{predicted}$	Correlation coefficient	-0.538	-0.989	0.296	-0.994
		Sig (2-tailed)	0.638	0.096*	0.809	0.070*
	X_C	Correlation coefficient	0.632	0.999	0.404	0.975
		Sig (2-tailed)	0.565	0.022*	0.735	0.144
	$C_{CO_2,l}$	Correlation coefficient	0.964	0.436	1.000*	0.189
		Sig (2-tailed)	0.171	0.713	.	0.879

* Correlation is significant at the 0.1 level (2-tailed).

4.3.3.3 Prediction of τ and X_c

A multiple regression model expressing the relationship among the system conditions, i.e., pressure, temperature, and the initial CO_2 concentration is shown in Eq. (4-3):

$$C_{CO_2,l} = 211.66 + 25.29p - 0.6874T \qquad \text{4-3}$$

where $C_{CO_2,l}$ is the initial CO_2 concentration (kg m^{-3}), p is the operating pressure (MPa), and T is the operating temperature (K).

The coefficient of determination and analysis of variance (ANOVA) gave an R^2 value of 99.3% at the 90% confidence level, as shown in Table H.1. Because the p-value of T is greater than 0.10, T has a statistically insignificant effect on CO_2 concentration. Thus, T can be removed from Eq. (4-3) to yield the simplified model expressed in Eq. (4-4):

$$C_{CO_2,l} = -2.21 + 23.78p \qquad \text{4-4}$$

The R^2 value (0.989) of Eq. (4-4) (Table H.2) indicates that the model can accurately explain 98.9% of the data variation and that only 1.1% of the total variation (low operating pressure) was not explained by the model. The adjusted R^2 value of 0.984 confirmed the good agreement between the observed and predicted initial CO_2 concentrations.

The model in Eq. (4-4) was substituted into Eq. (3-27) gives

$$t = \frac{R_0^2 \rho_C}{(-2.21 + 23.8P)(D + 0.3D(\mathbf{Re})^{1/2}(\mathbf{Sc})^{1/3})} \left[1 - \left(\frac{R}{R_0} \right)^2 \right] \qquad \text{4-5}$$

Eq. (4-5) was then reduced to Eq. (4-6) to predict t and τ from the system conditions:

$$\tau = \frac{R_0^2 \rho_C}{(-2.21 + 23.8P)(D + 0.3D(\mathbf{Re})^{1/2}(\mathbf{Sc})^{1/3})} \qquad \text{4-6}$$

Substitution of the estimated D value into Eq. (4-5) was performed with the aims of defining the model dissolution time (t) at any progressive reduction in cellulose particle

radius (R). On the basis of the experimental results, the most rapid complete dissolution time was 120 s, as shown in Table 4.9. Experimental X_c values at 120 s of dissolution time were calculated by Eq. (3-30), where R was calculated by Eq. (3-27) according to measured τ values for each dissolution condition. The predictive X_c values at the same dissolution time were estimated by the same equations (Eq. (3-30)), where R was calculated by Eq. (4-5) in accordance with predictive τ obtained by Eq. (4-6), as shown in Table 4.9. The predictive t values calculated by Eq. (4-5) were then transformed into a dimensionless form by dividing by Eq. (4-6) and plotting against $1 - X_c$ as shown in Figure 4.11. Figure 4.11 shows good agreement between the predictive X_c values and the corresponding observed values.
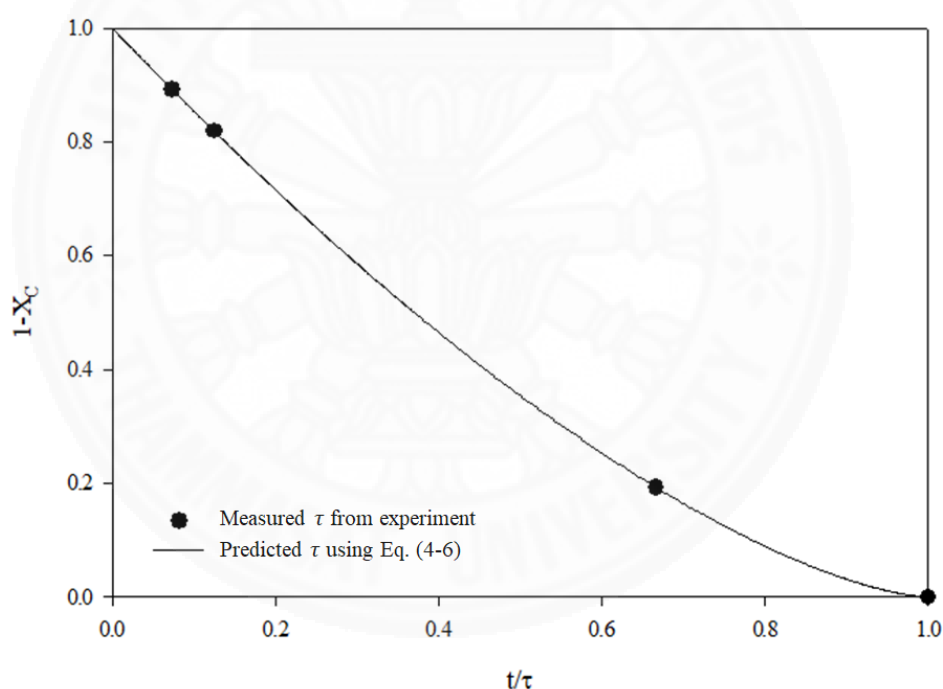
Figure 4.11 Comparision of the predicted and observed dissolution conversion of cellulose particles in the CO_2-SWS as a function of dimensionless time expressed in Eq. (4-6) when t = 120 s.

4.3.3.4 Effects of system conditions on τ and X_c

The predicted τ and X_c results in Table 4.9 change according to variation in the CO_2-SWS conditions. This shows that the cellulose was rapidly

dissolved, and high cellulose conversion was achieved under the high pressure and temperature of the system. The r_s values in Table 4.10 reveal a very strong inverse relationship and indicate that at increased p and T values, the complete dissolution time (τ) decreases. This can be explained by the fact that increasing CO_2 concentration (reactant) with increasing pressure typically caused rapid cellulose dissolution in the CO_2-SWS. Because temperature and CO_2 pressure are closely related properties (as shown by their correlations in Table 4.10), the temperature, T, term is not included in the developed model in Eq. (4-6). In other words, the pressure, p, term, takes the temperature effect into account. Among high-pressure conditions, the r_s values in Table 4.11 reveal that T influences τ by the development of CO_2-SWS molecules diffusion.

The complete dissolution time (τ) and cellulose dissolution conversion (X_c) values were plotted against the model-estimated dissolution times, as shown in Figure 4.12 (a) and (b). The results were compared across the different CO_2-SWS conditions. It can be seen that the model could successfully predict τ and X_c values for cellulose dissolution in CO_2-SWS under high-pressure conditions; however, these values under low pressure condition (0.1 MPa) show a large discrepancy between the measurement and model predictive data. The model inaccuracy may be caused by bias in designed experiments due to in sufficient at low pressure dissolution condition. The results of cellulose dissolution conversion show that the condition MC333/8 reached the complete conversion in a dissolution time of 120 s, whereas conditions MC313/0, MC313/5, and MC333/5 reached 1%, 18%, and 86% conversion, respectively. However, under low pressure condition (MC313/0), the cellulose conversion reached 0.1% in accordance with the model predictive τ. The statistical correlation coefficients in Table 4.10 reveal a strong and very strong positive effect of p and T on X_c (X_c increases with increasing p and T), respectively. However, for the high-pressure regions, the positive r_s value between p and X_c decreases, whereas the positive r_s value between T and X_c increases (Table 4.11).
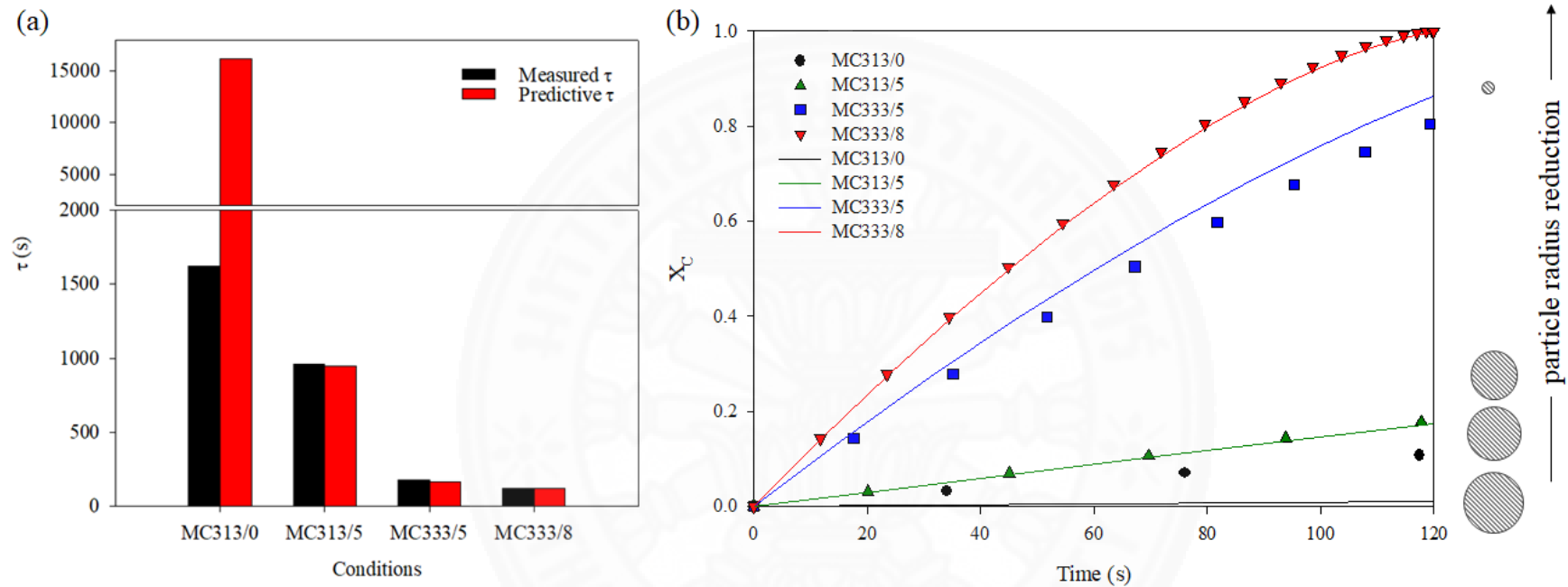
Figure 4.12 Comparison between the experimental and predicted (a) complete dissolution time (τ) and (b) conversion of cellulose achieving at the time of CO_2-SWS dissolution between 0 to 120 s. Symbols represent experimental X_c values using Eq. (3-30) by substituting R obtained from Eq. (3-37) and lines represent predicted X_c values using Eq. (3-30) by substituting R obtained from Eq. (4-5).

4.4 Transparent cellulose film fabrication using cellulose processing in CO_2-SWS

4.4.1 The cellulose film appearance and surface morphology

The cellulose films were fabricated by casting the solution containing the cellulose treated in CO_2-SWS. Table 4.12 lists the fabrication condition of the cellulose modified in the CO_2-SWS solution. The appearance of the solution containing modified celluloses and the fabricated films are shown in Figure 4.13 andFigure 4.14, respectively. It appears that the films fabricated from homogeneous cellulose/CO_2-SWS show more stable in shape after drying than that fabricated from precipitated form. Additionally, the homogeneous cellulose/CO_2-SWS was prepared at high p and T produced the film with high optical transparency, especially at supercritical condition. Figure 4.15 shows SEM images of the film surface from the modified cellulose. The non-porous surface was observed for all the modified cellulose films. The large particles of the cellulose were observed for the films MC313/0, MC313/5 and MC298/5, which are fabricated from the cellulose modification at low temperatures and pressures.
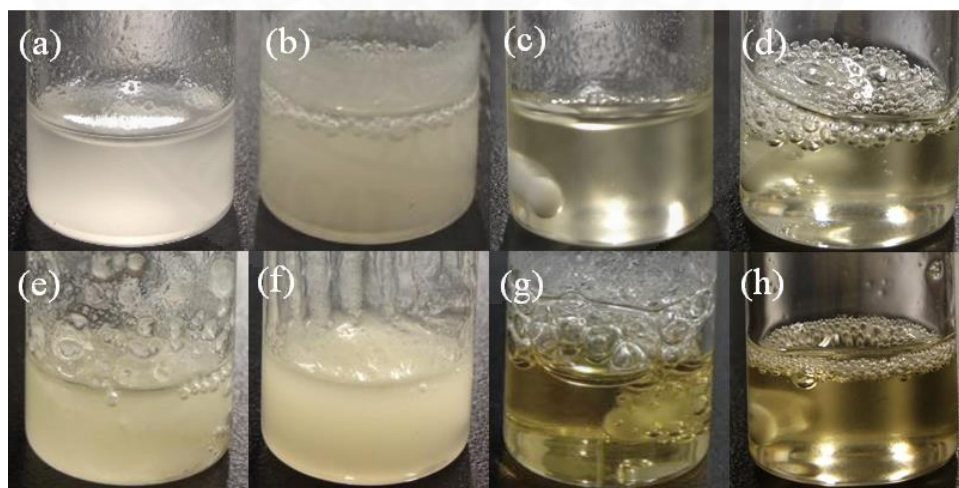
Figure 4.13 The appearance of modified cellulose solution; (a) cellulose in low polarity solvent, (b) MC298/5, (c) MC313/0, (d) MC313/5, (e) MC313/8, (f) MC313/10, (g) MC333/5, and (h) MC333/8.

NOTE.   The definition of sample name MCx/y; MC = modified cellulose, x = operating temperature of CO_2 switchable solution, and y = operating pressure of CO_2 switchable solution
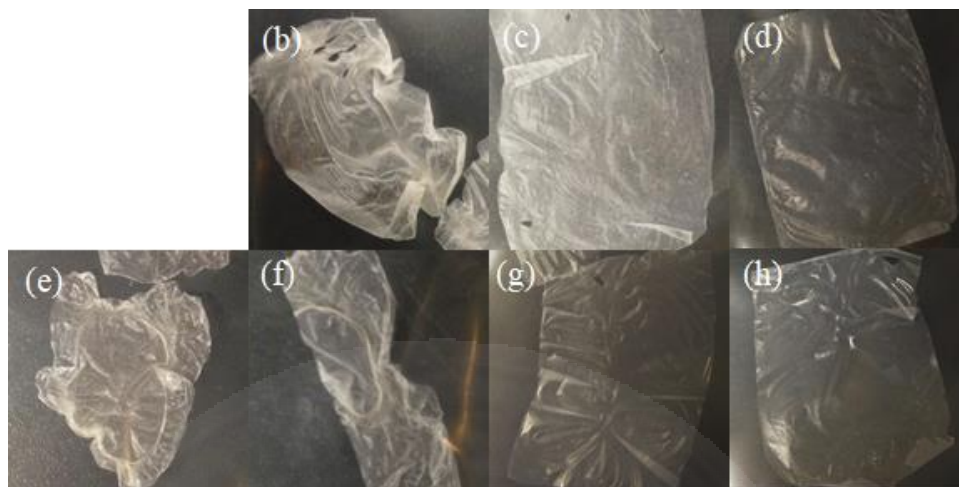
Figure 4.14 The appearance of fabricaated cellulose film; (b) MC298/5, (c) MC313/0, (d) MC313/5, (e) MC313/8, (f) MC313/10, (g) MC333/5, and (h) MC333/8.

NOTE.   The definition of sample name MCx/y; MC = modified cellulose, x = operating temperature of CO_2 switchable solution, and y = operating pressure of CO_2 switchable solution
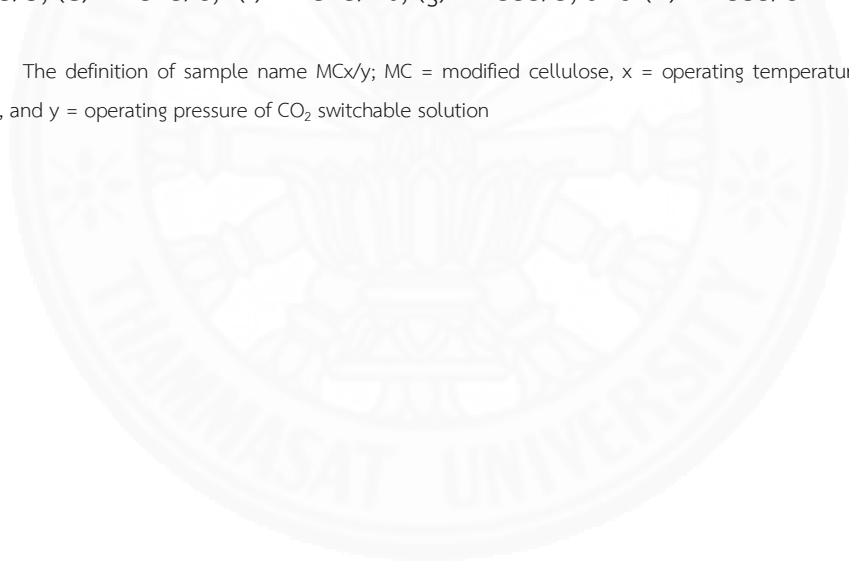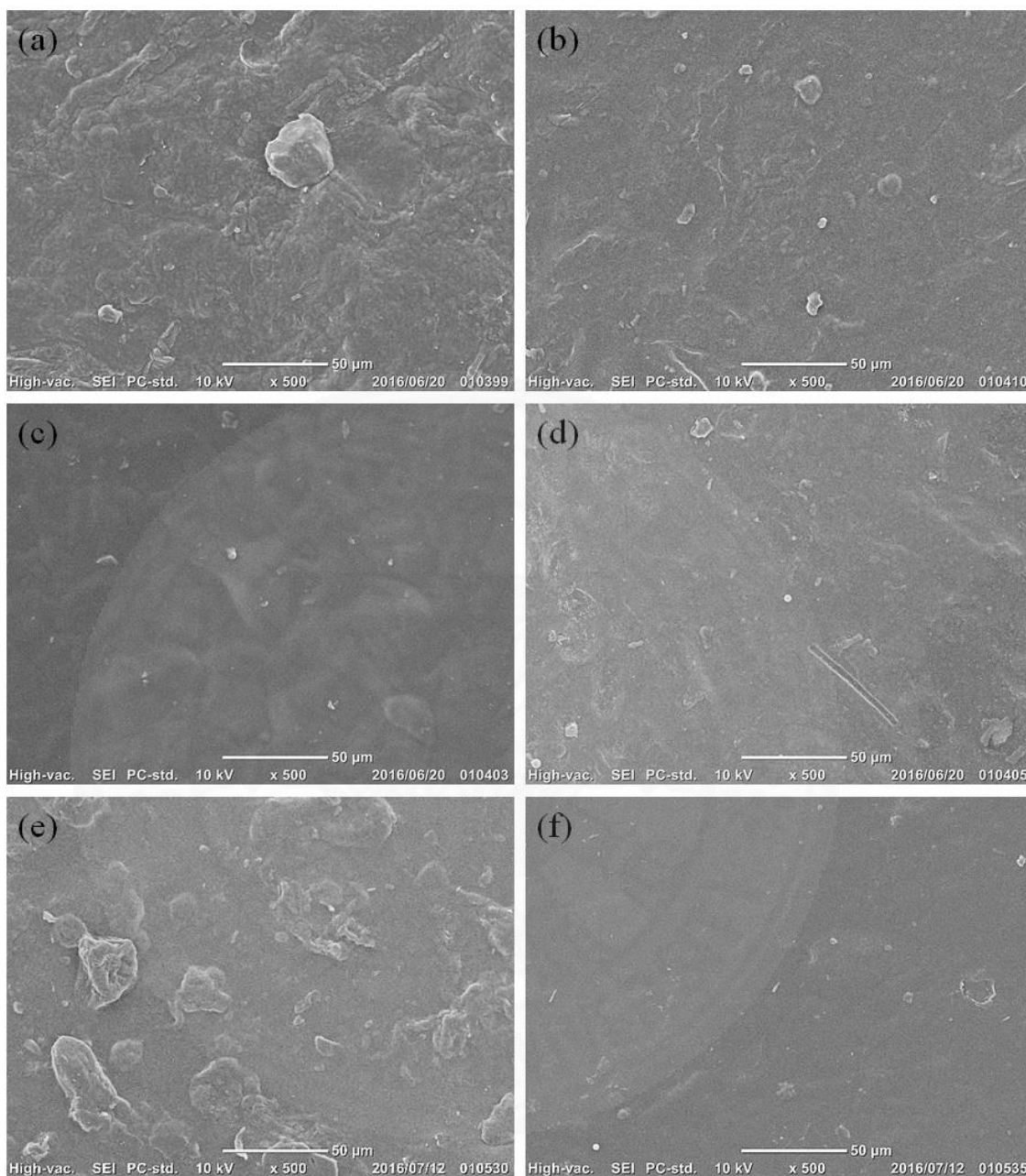
Figure 4.15 SEM images of the fabricated cellulose film (a) MC313/0, (b) MC313/5, (c) MC313/8, (d) MC313/10, (e) MC298/5 and (f) MC333/5.

NOTE.   The definition of sample name MCx/y; MC = modified cellulose, x = operating temperature of CO_2 switchable solution, and y = operating pressure of CO_2 switchable solution

Table 4.12 Fabrication conditions and characterization results of cellulose film

	Fabrication condition		The state of CO_2	Polymorphs type	T_d (K)	Weight loss (%)
	T (K)	p (MPa)				
Unprocessed				*I*	597.61	63.80
MC298/5	298.15	5.6	Gaseous	*II*	596.46	52.08
MC313/0	313.15	0.1	Subcritical	*I* (amorphous)	597.41	55.58
MC313/5	313.15	5.8	Subcritical	*II*	580.00	50.52
MC313/8	313.15	8.0	Supercritical	*II*	596.71	56.28
MC313/10	313.15	10.0	Supercritical	*II*	596.00	47.40
MC333/5	329.05	5.8	Subcritical	*II*	592.23	55.93
MC333/8	333.15	8.0	Supercritical	*II*	n/a	n/a

NOTE.   The definition of sample name MCx/y; MC = modified cellulose, x = operating temperature of CO_2 switchable solution, and y = operating pressure of CO_2 switchable solution

4.4.2 The chemical structural characteristic of the cellulose film

FTIR spectra of fabricated cellulose films prepared from the cellulose/CO_2-SWS under various conditions are shown in Figure 4.16. The spectrum of unprocessed (control) cellulose as shown in Figure 4.16 (a) was similar to those of cellulose prepared at different processing conditions as shown in Figures 4.16 (b) to (g). It was pronounced that the major common peaks found in cellulose were observed. The absorption band around 3360 cm^{-1} and the band around 2900 cm^{-1} are assigned to OH stretching of hydroxyl groups and CH stretching in glucose unit, respectively. The absorption groups around 1200-920 cm^{-1} are assigned to CO group of secondary alcohols and ether functional group found in the cellulose.
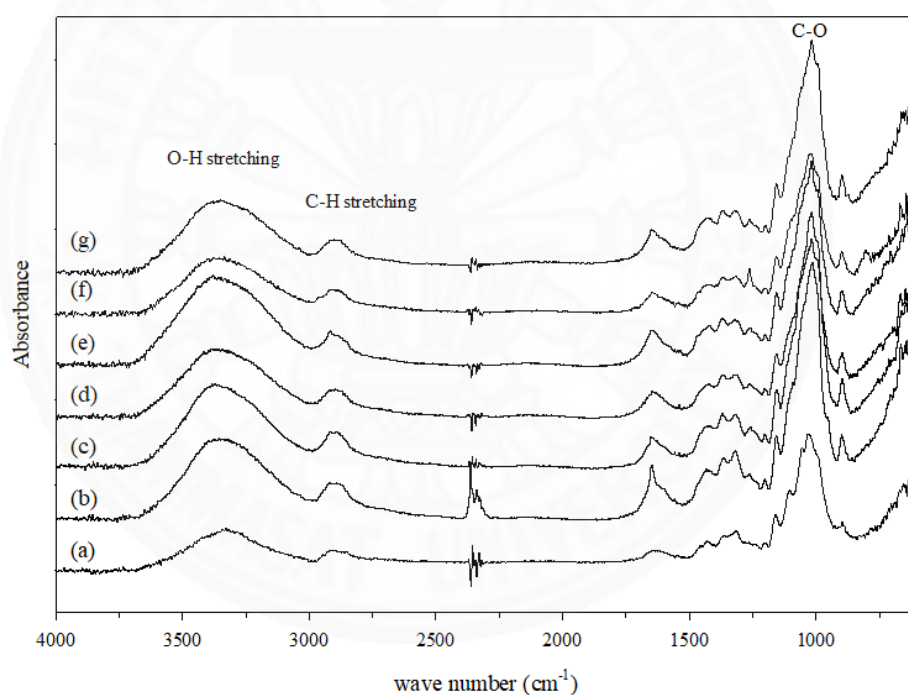
Figure 4.16 FTIR spectra of (a) unprocessed cellulose, (b) MC313/0, (c) MC313/5, (d) MC313/8, (e) MC313/10, (f) MC298/5 and (g) MC333/5.

NOTE.   The definition of sample name MCx/y; MC = modified cellulose, x = operating temperature of CO_2 switchable solution, and y = operating pressure of CO_2 switchable solution

Representative spectra for all fabricated films in the range of 2000-600 cm^{-1} are shown in Figure 4.17. The characteristic band to CO groups appearing at 1160,

1104, 1028, 989 cm^{-1} are assigned to the stretching vibration of C-O-C, deformation vibration of C-OH, the symmetric stretching of C-O-C and the stretching vibration of C-O, respectively. A broad band centered around 1620 cm^{-1} is attributed to the OH bending mode of adsorbed water. In addition, the vibration at 897 cm^{-1} corresponds to β-glycosidic linkage between glucose molecules.
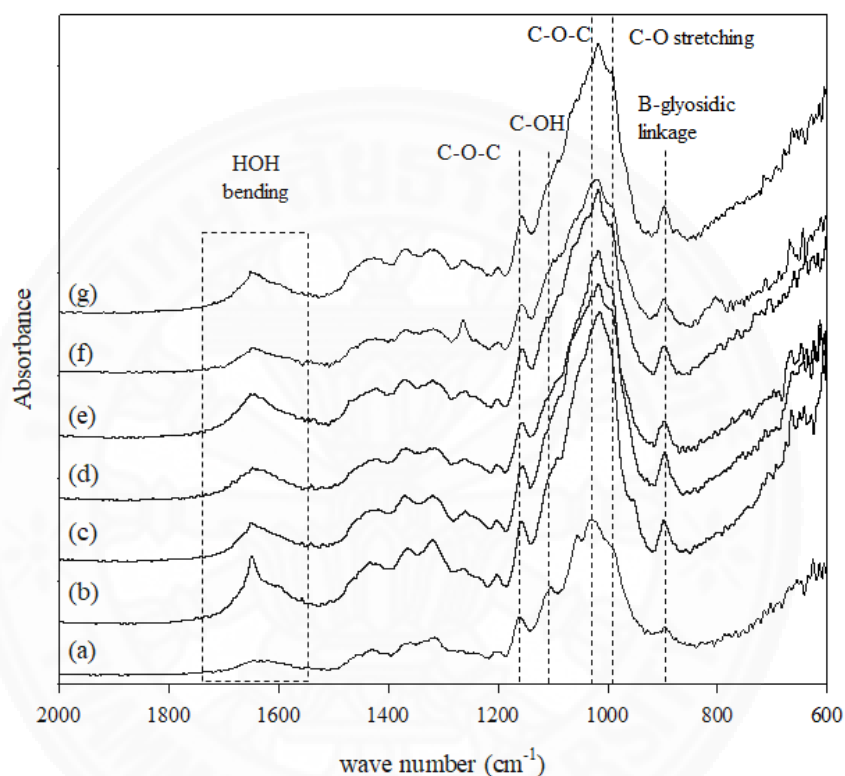
Figure 4.17 FTIR spectra (2000-600 cm^{-1}) of (a) unprocessed cellulose, (b) MC313/0, (c) MC313/5, (d) MC313/8, (e) MC313/10, (f) MC298/5 and (g) MC333/5.

NOTE.   The definition of sample name MCx/y; MC = modified cellulose, x = operating temperature of CO_2 switchable solution, and y = operating pressure of CO_2 switchable solution

4.4.3 The cellulose crystalline structure transformation

XRD was used to analyze the crystalline structure type of cellulose. The classification of crystalline structure of cellulose was based on its differences in conformation and packing arrangement of the cellulose chains. The conversion from nature occurring cellulose (type I) to cellulose type II was the irreversible

rearrangement of chain polarity from parallel to antiparallel chain. Figure 4.18 gives the XRD results of the film from the modified cellulose. The unprocessed cellulose in Figure 4.18 (a) had the two main peaks around 16 and 22° that corresponds to the structure of cellulose I (Dumitriu, 2004; Tang et al., 2012). The modified cellulose MC313/0 (Figure 4.18 (c)) exhibited the one broad peak around 22° for the formation of amorphous cellulose as well as the regenerated cellulose in the literature (Tang et al., 2012). From the modifications of MC298/5, MC313/5 to 10, MC333/5, and MC333/8 the structure of cellulose II was formed as the main peaks around 20° (Dumitriu, 2004; Tang et al., 2012). The crystal structure change as the modification using the switchable solution as shown in Figure 4.18 is the valuable and promising technique on the upgrading process of the cellulose.
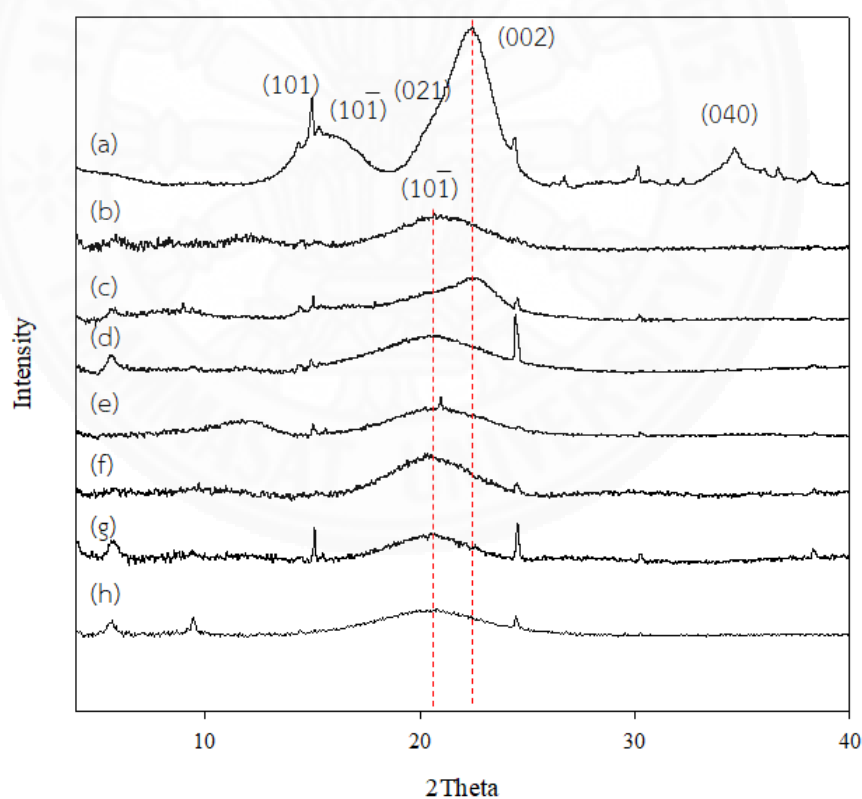
Figure 4.18 XRD diffraction peaks of (a) unprocessed cellulose, (b) MC298/5, (c) MC313/0, (d) MC313/5, (e) MC313/8, (f) MC313/10, (g) MC333/5, and (h) MC333/8.

NOTE. The definition of sample name MCx/y; MC = modified cellulose, x = operating temperature of CO_2 switchable solution, and y = operating pressure of CO_2 switchable solution

4.4.4 Thermal property of cellulose film

The decomposition temperature (T_d) and weight loss (%) of the modified cellulose film from TG analysis were listed in Table 4.12. The results revealed that T_d of the modified cellulose film was quite lower than that of unprocessed cellulose; however, the statistical analysis suggests no difference between T_d of unprocessed cellulose and that of modified cellulose films (p-value 0.462). Considering the weight loss results, the weight loss of unprocessed cellulose was 63.80% whereas that of modified celluloses ranged from 47.40 to 56.28% depending on the treatment conditions. The statistical analysis suggests that there is a statistically significant difference between the weight loss (%) of unprocessed cellulose and modified cellulose films (p-value 0.038). It was indicated that the thermal stability of the modified cellulose was higher than that of unprocessed cellulose. It was consistent with the XRD result that the crystalline polymorph of modified cellulose was transformed to cellulose II type which is the most thermal stable form of cellulose (Gubitosi et al., 2017).

4.5 Fabrication of cellulose/carbon electrode for lithium-air battery

A preliminary application of the homogeneous cellulose solution and precipitated cellulose processed in CO_2-SWS as a sustainable candidate binder solution used in preparing hybrid composite cellulose/carbon black electrode for lithium-air rechargable battery was studied.

4.5.1 Cellulose/carbon electrode characteristics

The fabrication of cellulose/carbon electrode were prepared using two methods such as supercritical carbon dioxide ($ScCO_2$) drying and solvent evporation. The homogeneous cellulose solution and precipitated cellulose processed in CO_2-SWS were compared regarding relationship of electrode characteristics-properties.

4.5.1.1 The electrode appearances and surface morphology

The cellulose binder electrode was prepared by supercritical carbon dioxide ($ScCO_2$) drying technique as shown in Figure 4.19. Figure 4.19 (a) - (c) show the electrodes fabricated from the homogenous modified cellulose which were prepared using CO_2-SWS at 5.8 MPa, whereas the electrode prepared using CO_2-SWS at 10.0 MPa are shown in Figure 4.19 (d) and (e). The cracks on the surface of cellulose binder electrodes were detected for the electrode prepared using the high pressure CO_2-SWS due to the CB particle aggregation.
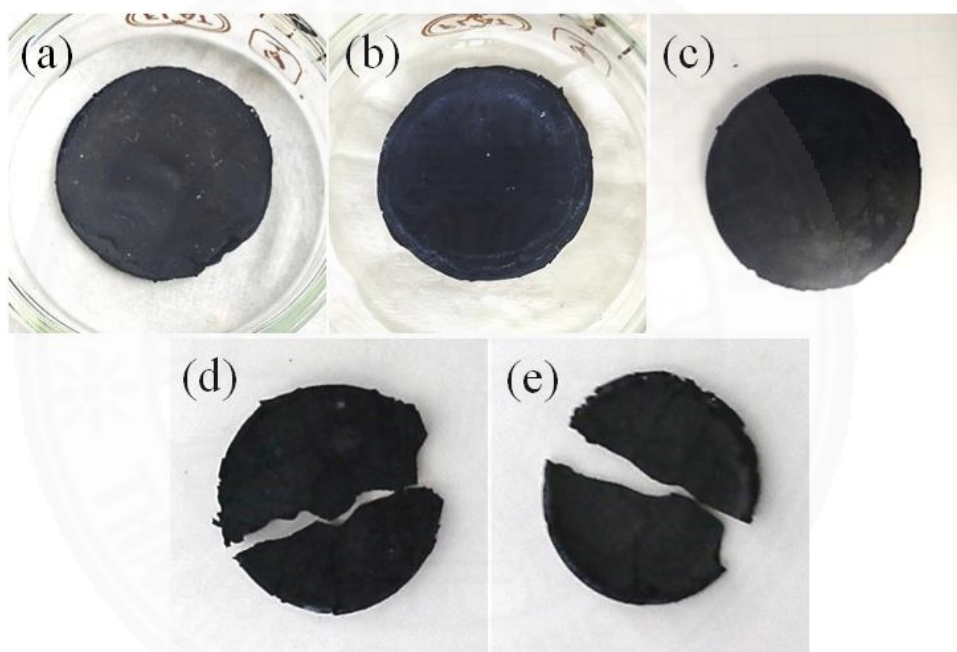
Figure 4.19 Appearance of cellulose binder electrode prepared using supercritical drying technique; (a) 1/1SACD, (b) 1/1SBCD, (c) 2/1SBCD, (d) 2/1PACD, and 2/1PBCD.

The surface morphology of the cellulose binder electrodes characterized by SEM are given in Figure 4.20 - Figure 4.22. Figure 4.20 presents the surface and cross-section morphologies of the cellulose binder electrode after solvent evaporation at the atmospheric pressure (1/1SAOD). As shown in Figure 4.20, the CB particle aggregation and packed layer between CB and cellulose were observed. The supercritical drying prevents the collapse of cellulose binder electrode structure by eliminating surface tension between solvent and the electrode (Weibel & Ober, 2002)

resulting in the porous structure of the cellulose binder electrode as given in Figure 4.21 and 4.22. Consequently, it enhances oxygen permeability in the porous electrode.
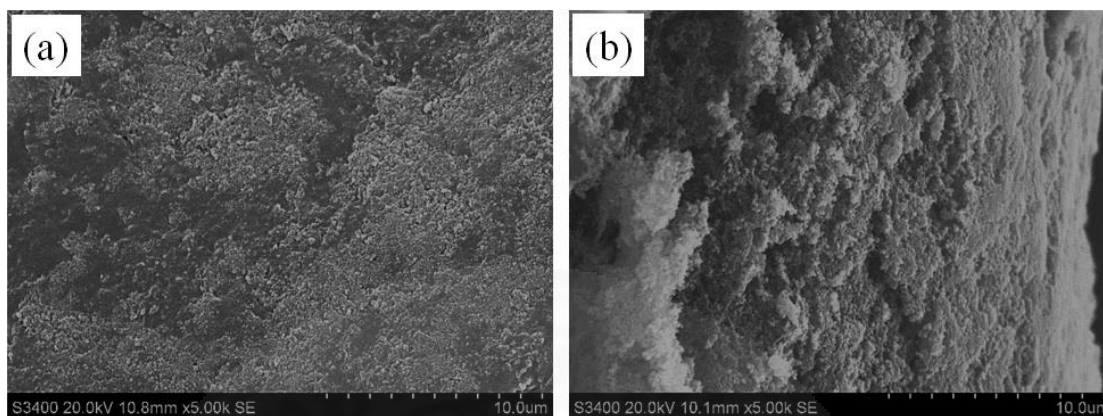
Figure 4.20 E-SEM images show (a) surfaces and (b) cross-sections of cellulose binder electrode (1/1SAOD) prepared using solvent evaporation.

Figure 4.21 represents the surface and cross-section morphology of the cellulose binder electrode fabricating from homogeneous dissolving cellulose modified in CO_2-SWS under 5.8 MPa, 313 K. The results illustrate combination of isolated and interconnected (pore spaces connected to one another) nano-pores with narrow outer pore walls of the prepared 1/1SBCD and 1/1SACD composites. However, the 1/1SACD showed more connected nano-pores network than that observed in the 1/1SBCD. After adjusting the mass ratio of CB/cellulose to 2:1, the dense pores on the electrode surface apparently decreased due to the pore blocking by CB particles.

Figure 4.22 represents the surface and cross-section morphology of the cellulose binder electrode fabricating from precipitated cellulose modified in CO_2-SWS under 10.0 MPa, 313 K. Non-porous surface was observed for the 2/1PACD electrode as shown in Figure 4.22 (a), while the aggregation of CB particles onto the cellulose structure can be seen in the 2/1PBCD electrode as shown in Figure 4.22 (c).
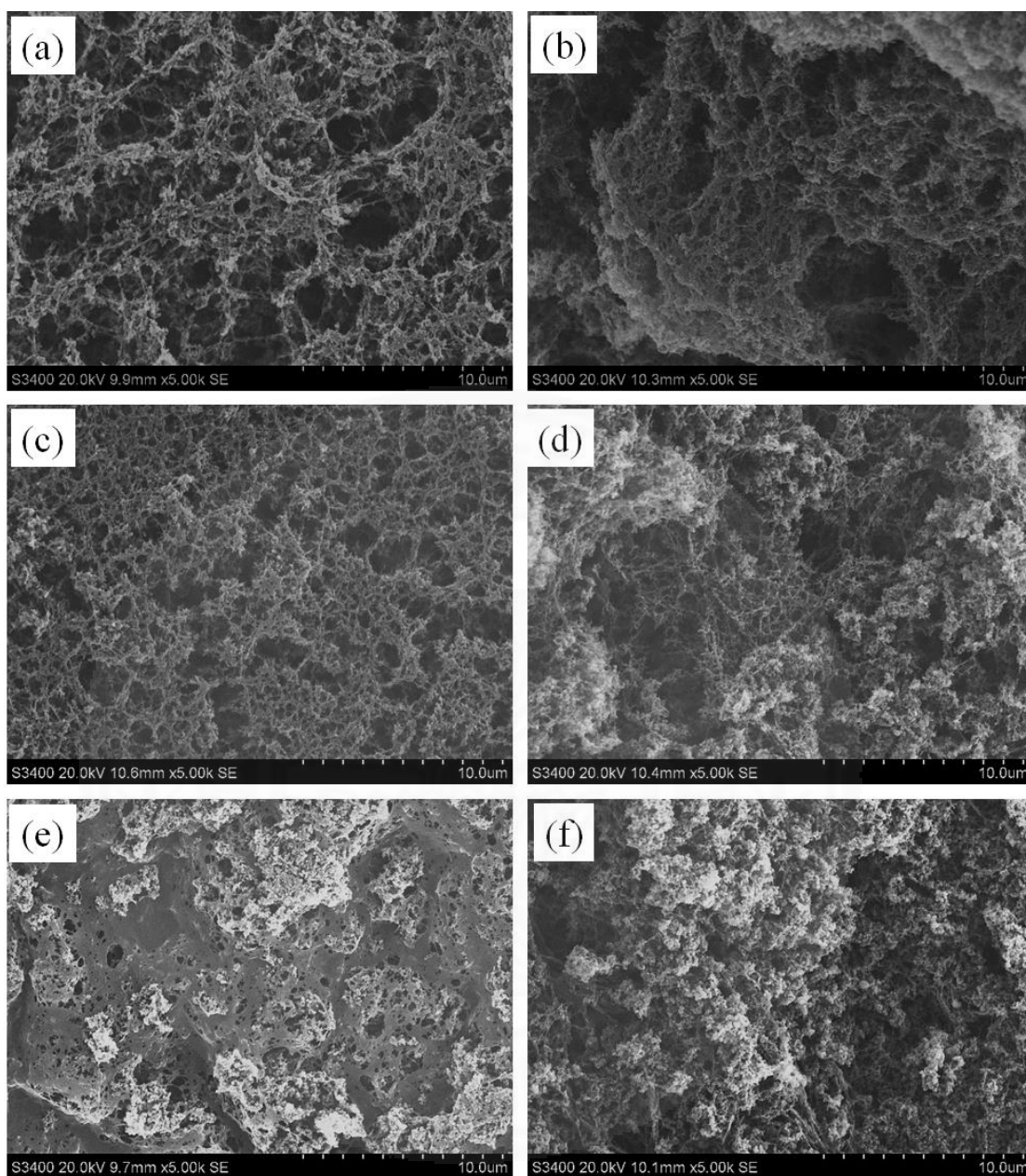
Figure 4.21 E-SEM images show surfaces and cross-sections of cellulose binder electrode prepared using supercritical drying technique; (a) Surface and (b) cross-section of the 1/1SACD, (c) surface and (d) cross-section of the 1/1SBCD, (e) surface and (f) cross-section of the 2/1SBCD. The electrodes were prepared from homogeneous dissolving cellulose modified in CO_2-SWS under 5.8 MPa, 313 K.
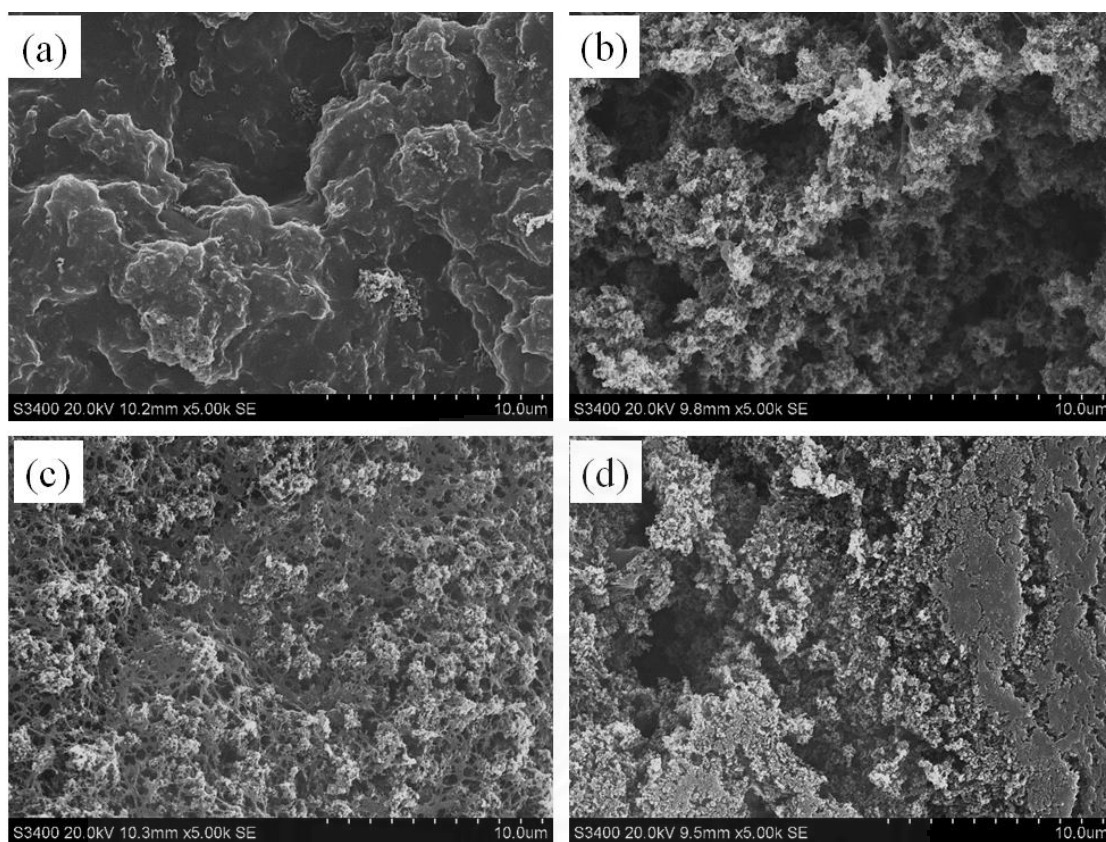
Figure 4.22 E-SEM images show surfaces and cross-sections of cellulose binder electrode prepared using supercritical drying; (a) Surface and (b) cross-section of the 2/1PACD and (c) surface and (d) cross-section of the 2/1PBCD. The electrodes were prepared from precipitated cellulose modified in CO_2-SWS under 10.0 MPa, 313 K.

Table 4.13 Calculated radial shrinkage, porosity and conductivity values of cellulose binder electrodes.

Sample code	Mass ratio CB:MC	Method for CO_2 removal	CO_2-SWS pressure (MPa)	Drying method	radial shrinkage (%)	Porosity (%)	Conductivity (S m^{-1})
1/1SAOD	1:1	A	5.8	Evaporation	60	8.09	NA
1/1SACD	1:1	A	5.8	Supercritical	33	91.25	0.038
1/1SBCD	1:1	B	5.8	Supercritical	33	91.33	0.0087
2/1SBCD	2:1	B	5.8	Supercritical	26	91.70	0.18
2/1PACD	2:1	A	10.0	Supercritical	33	76.25	2.82
2/1PBCD	2:1	B	10.0	Supercritical	40	78.47	1.69

4.5.1.2 Porosity and electric conductivity

The homogeneous cellulose solution and precipitated cellulose was immersed in ethanol to form alcogel, and then it was dried using either $ScCO_2$ drying or solvent evaporation technique. The results of radial shrinkage, porosity and conductivities of the cellulose binder electrode are listed in Table 4.13. The $ScCO_2$ drying gave the radial shrinkage ratio of the cellulose binder electrode ranging from 26 to 40 % while solvent evaporation at the atmospheric pressure gave radial shrinkage ratio of the cellulose binder electrode of 60 %. Figure 4.23 shows a radial shrinkage of the alcogel form of cellulose binder electrode after solvent evaporation and $ScCO_2$ drying. The phase interfacial tension of homogeneous mixture of $ScCO_2$ and ethanol prepared using the $ScCO_2$ drying is lower than using the solvent evaporation (Scherer, 1992). As a results, the degree of shrinkage of the cellulose binder electrode after the $ScCO_2$ drying was reduce. The porous structure of the cellulose binder electrode is given in Figure 4.20 - Figure 4.22. The porosities of the cellulose binder electrode obtained after $ScCO_2$ drying are approximately 76 – 92 % which are higher than that electrode obtained after solvent evaporation (8.09 %). Among the electrode drying with $ScCO_2$, the porosities of the electrodes prepared from the homogeneous dissolving cellulose in CO_2-SWS at 5.8 MPa are higher than those prepared from precipitated cellulose given at 10.0 MPa as shown in Table 4.13. As previously discussed in section 4.3, the dissolution and modification in CO_2-SWS at the pressure of 5.8 MPa gave the homogeneous solution of cellulose, while the precipitation of modified cellulose were formed under modification in CO_2-SWS at the pressure of 10.0 MPa. This precipitation may cause insufficient mixing of CB and the modified cellulose during the suspension preparation, consequently some parts of the fabricated electrode were aggregated and packed.
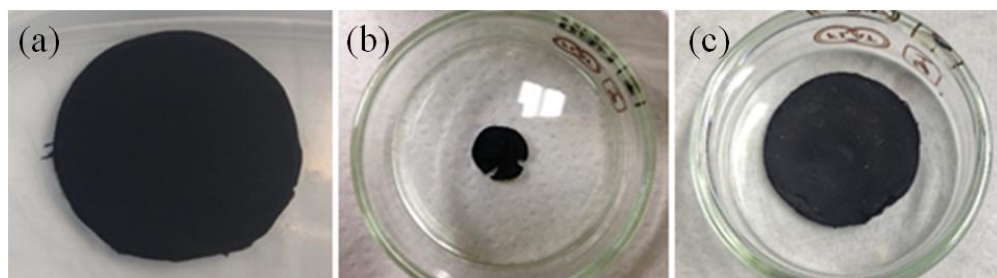
Figure 4.23 The cellulose binder electrode; (a) its alcogel form before drying, (b) after solvent evaporation and (c) after ScCO$_2$ drying.

The aggregation of the fabricated electrode caused increasing electric conductivity of the electrode. The conductivity results showing in Table 4.13 reveal that the electric conductivity of the electrodes prepared from homogeneous dissolving cellulose are lower than those prepared from precipitated cellulose. However, the electrode prepared from precipitated cellulose cracked after drying. Interestingly, the CO$_2$ removal operation before electrode casting caused increasing electrode conductivity.

4.5.2 Electric capacity of lithium-air battery

The cellulose binder electrode from 2/1SBCD was used as the cathode of lithium-air battery. The discharge-charge profile and cycleability of lithium-air battery with 2/1SBCD are given in Figure 4.24 (a) and (b), respectively. At the fist cycle the 2/1SBCD electrode with the cellulose binder gave high discharge capacity of 801.40 mAh g^{-1} that was used to calculate the specific energy density of the lithium-air battery yielding 2,404.2 Wh kg^{-1}. The calculated specific energy density of the prepared lithium-air battery which is approximately ten-fold higher than that of typical small lithium-ion batteries of 266 Wh kg^{-1} (Imanishi et al., 2014). However, its cycleability was poor, as shown in Figure 4.24 (b). The capacity dramatically decreases to 290.62 mAh g^{-1} and 147.64 mAh g^{-1} in the first charge and second discharge period, respectively.
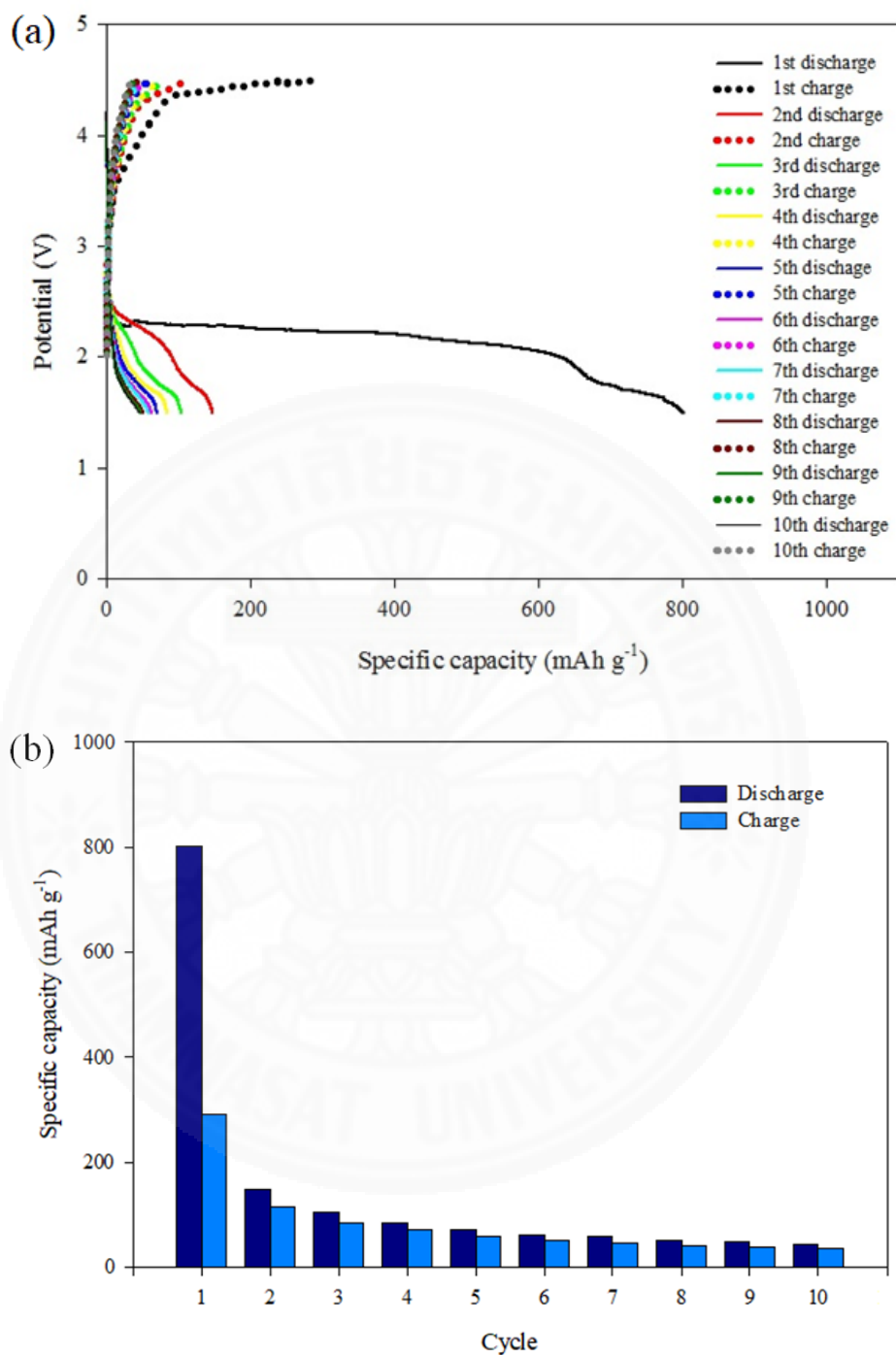
Figure 4.24 Results of lithium-air battery test using cellulose binder electrode 2/1SBCD;

(a) discharge-charge profile and (b) cycleability.

CHAPTER 5

CONCLUSIONS, ORIGINAL CONTRIBUTION AND
RECOMMENDATIONS

This chapter contains a summary of our finding, unique research contributions and further work recommendations.

5.1 Conclusions

1. Based on the proposed phase behavior of the cellulose/CO_2-SWS at various p and T, dissolving ability of CO_2-SWS depends on the state of the triggered CO_2. The transparent cellulose solution was achieved under the conditions of CO_2 existing in sub- and supercritical states whereas the cellulose carbonate salts were formed and precipitated out of the CO_2-SWS under the conditions of CO_2 existing in gaseous state.

2. The diffusion-limited SPM was useful for predicting time required to achieve complete cellulose dissolution under various operating conditions of CO_2-SWS.

3. In determination of the values of D, τ and X_C under various operating conditions, the diffusion-limited SPM describing dissolution behavior of cellulose in sub- and supercritical CO_2-SWS was successfully developed and verified with experimental data. The model suggests that complete cassava-based cellulose dissolution is achieved much more rapidly in CO_2-SWS comprising supercritical CO_2 than that comprising subcritical CO_2.

4. On the basis of ANOVA analysis, the operating pressure (p) had a significant effect on the initial concentration of CO_2 ($C_{CO_2 l}$). p showed adverse effect on the calculated D and τ values, whereas X_C showed a very strong positive relationship with p. The pressure dependence of these variables was attributable to the pressure dependence of T.

5. The sub-optimum condition of the cellulose dissolving in CO_2-SWS was under the pressure of 8 MPa and temperature of 333.15 K to obtain complete dissolution in a shortest time.

6. In a view point of applications of the modified cellulose in CO_2-SWS it was applied to fabricate transparent cassava-based cellulose film that consisted of the cellulose II crystalline polymorph which is the most theoretical thermodynamic stable crystalline form.

7. Modified cellulose in sub- and supercritical CO_2-SWS was successfully assembled with CB and subsequently fabricated a porous cathode for lithium-air battery. The properties of the electrode depend on the phase of cellulose/CO_2-SWS, preparing method and drying techniques. After charge/discharge cycle performance testing, the battery provides the high discharge capacity at the first cycle 801.4 mAhg^{-1} which is of great improvement for conventional lithium-ion battery by a factor of ten.

5.2 Original contributions

1. Applying sub- and supercritical CO_2 states played an important role in solvation of cellulose by sorption and swelling resulting in reduction in viscosity and dissolution temperature of the CO_2-SWS.

2. The phase behavior diagram and mechanism of dissolution cellulose in CO_2 switchable solution were proposed.

3. The strength of relationships among cassava cellulose dissolution conditions in the switchable solution at CO_2 sub- and supercritical were analyzed using Pearson and Spearman correlations.

4. The theoretical study of cellulose dissolution conditions in the switchable solution was carried out by developing a diffusion-controlled shrinking particle model.

5. An innovative approach in the value addition to cassava was achieved by fabricating cellulose transparent film for further development and application of commercial flexible electronic devices.

6. The synthesis of novel cellulose-based conductive hybrid composite consisting of dissolved cellulose fiber and a carbon black was developed as a porous carbon electrode lithium-air battery as green electronically polymeric material.

5.3 Recommendations

1. The developed diffusion-limited SPM is suitable for only high-pressure CO_2-SWS. A large difference of the model-predicted diffusion coefficient at low pressure (0.1 MPa) is found even though the predicted τ and X_C values were in good agreement with the observed results. It is suggested that the diffusion-limited SPM under low pressure should be developed for further study.

2. The radius of cellulose at any times t should be measured using particle size analyzer throughout the dissolution process for further improving the model accuracy.

3. The effect of cellulose loading on its solubility in CO_2-SWS should be studied.

4. The measurement of prepared film properties, i.e., brittleness, stiffness, young modulus, thermal conductivity should be performed.

5. The lithium-air battery assembled from cellulose/CB cathode provides the high discharge capacity at the first cycle; however, there is still the drawback of the low recyclability of the porous cathode. Further studies should focus on the recyclability improvement by increasing electrode strength.

REFERENCES

Books and Book Articles

Chen, H. (2014). Chemical composition and structure of natural lignocellulose. In *Biotechnology of Lignocellulose: Theory and Practice* (pp. 1–511).

Dumitriu, Severian. 2004. CRC Press *Polysaccharides: Structural Diversity and Functional Versatility, Second Edition*.

Freemantle, M. (2010). *An Introduction to Ionic Liquids*. *The Royal Society of Chemistry*.

Frössling, N. (1938). *The evaporation of falling drops. Gerlands Beitr. Geophys.* (Vol. 52).

Gilbert, M. (2017). Chapter 1 - Plastics Materials: Introduction and Historical Development. In *Brydson's Plastics Materials (Eighth Edition)* (pp. 1–18).

Johnson, D. C., Nicholson, M. D., & Haigh, F. C. (1976). *Dimethyl sulfoxide/paraformaldehyde: a nondegrading solvent for cellulose. Applied Polymer Symposium* (Vol. 28). NY: Wiley and Sons.

Imanishi, N., Luntz, A. C., & Bruce, P. (2014). *The lithium air battery: Fundamentals. The Lithium Air Battery: Fundamentals*.

Levenspiel, O. (1972). *Chemical Reaction Engineering* (2nd ed.). New York: Wiley.

Liebert, T. (2010). Cellulose Solvents – Remarkable History, Bright Future. In *Cellulose Solvents: For Analysis, Shaping and Chemical Modification* (pp. 3–54).

Mallakpour, S., & Dinari, M. (2012). Ionic liquids as green solvents: Progress and prospects. In *Green Solvents II: Properties and Applications of Ionic Liquids* (pp. 1–32).

McHugh, M. A., Mandel, F. S., & Wang, J. D. (2002). Supercritical Fluid Processing of Polymeric Materials. In Y.-P. Sun (Ed.), *Supercritical Fluid Technology in Materials Science and Engineering: Synthesis, properties, and applications*. Marcel Dekker, Inc.

Olsson, C., & Westman, G. (2013). Direct Dissolution of Cellulose: Background, Means and Applications. In *Cellulose–Fundamental Aspects* (pp. 143–178). InTech.

Quiroz-Castañeda, R. E., & Folch-Mallol, J. L. (2013). Hydrolysis of Biomass Mediated by Cellulases for the Production of Sugars. In A. K. Chandel & S. S. da Silva (Eds.), *Sustainable Degradation of Lignocellulosic Biomass - Techniques, Applications and Commercialization*. Rijeka: InTech.

Schweiger, R. G. (1978). Sodium Cellulose Sulfate via Cellulose Nitrite. In *Carbohydrate Sulfates* (pp. 163–172).

Sengers, J. M. H. L. (2000). Supercritical Fluids: Their properties and applications. In E. Kiran, P. G. Debenedetti, & C. J. Peters (Eds.), *Supercritical Fluids: Fundamentals and Applications*. Springer Netherlands.

Wertz, J.-L., Deleu, M., Coppée, S., & Richel, A. (2017). *Hemicelluloses and Lignin in Biorefineries*. CRC Press.

Zugenmaier, P. (2008). *Crystalline cellulose and cellulose derivatives: Characterization and structures*. (T. E. Timell & R. Wimmer, Eds.). Springer.

Articles

Abraham, K. M., & Jiang, Z. (1996). A Polymer Electrolyte-Based Rechargeable lithium / Oxygen Battery. *Electrochemical Science and Technology*, *143*(1), 1–5.

Armand, M., Endres, F., MacFarlane, D. R., Ohno, H., & Scrosati, B. (2009). Ionic-liquid materials for the electrochemical challenges of the future. *Nature Materials*, *8*(8), 621–629.

Arns, B., Bartz, J., Radunz, M., Evangelho, J. A. do, Pinto, V. Z., Zavareze, E. da R., & Dias, A. R. G. (2015). Impact of heat-moisture treatment on rice starch, applied directly in grain paddy rice or in isolated starch. *LWT - Food Science and Technology*, *60*(2), 708–713.

Ass, B. A. P., Frollini, E., & Heinze, T. (2004). Studies on the Homogeneous Acetylation of Cellulose in the Novel Solvent Dimethyl Sulfoxide/Tetrabutylammonium Fluoride Trihydrate. *Macromolecular Bioscience, 4*(11), 1008–1013.

Attard, T. M., Bainier, C., Reinaud, M., Lanot, A., McQueen-Mason, S. J., & Hunt, A. J. (2018). Utilisation of supercritical fluids for the effective extraction of waxes and Cannabidiol (CBD) from hemp wastes. *Industrial Crops and Products*, *112*, 38–46.

Barbara, I., Flourat, A. L., & Allais, F. (2015). Renewable polymers derived from ferulic acid and biobased diols via ADMET. *European Polymer Journal*, *62*, 236–243.

Beckman, E. J. (2004). Supercritical and near-critical CO_2 in green chemical synthesis and processing. *The Journal of Supercritical Fluids*, *28*(2–3), 121–191.

Blasucci, V. M., Hart, R., Pollet, P., Liotta, C. L., & Eckert, C. A. (2010). Reversible ionic liquids designed for facile separations. *Fluid Phase Equilibria*, *294*(1–2), 1–6.

Brandt, A., Grasvik, J., Hallett, J. P., & Welton, T. (2013). Deconstruction of lignocellulosic biomass with ionic liquids. *Green Chem.*, *15*(3), 550–583.

Buranov, A. U., & Mazza, G. (2010). Extraction and characterization of hemicelluloses from flax shives by different methods. *Carbohydrate Polymers*, *79*(1), 17–25.

Casarano, R., Nawaz, H., Possidonio, S., da Silva, V. C., & Seoud, O. A. El. (2011). A convenient solvent system for cellulose dissolution and derivatization: Mechanistic aspects of the acylation of the biopolymer in tetraallylammonium fluoride/dimethyl sulfoxide. *Carbohydrate Polymers*, *86*(3), 1395–1402.

Chen, L., Yang, X., Li, G., Wen, C., Li, X., & Snape, C. (2017). An Improved Form of Shrinking Core Model for Prediction of the Conversion during Reduction Process in Chemical Looping Combustion. *Energy and Fuels*, *31*(2), 1993–2006.

Ciacco, G. T., Liebert, T. F., Frollini, E., & Heinze, T. J. (2003). Application of the solvent dimethyl sulfoxide/tetrabutyl-ammonium fluoride trihydrate as reaction medium for the homogeneous acylation of Sisal cellulose. *Cellulose*, *10*(2), 125–132.

Ciolacu, D., Ciolacu, F., & Popa, V. I. (2011). Amorphous Cellulose – Structure and Characterization. *Cellulose Chemistry and Technology*, *45*(1–2), 13–21.

DeSimone, J. M. (2002). Practical Approaches to Green Solvents. *Science*, *297*(5582), 799–803.

Dogan, H., & Hilmioglu, N. D. (2009). Dissolution of cellulose with NMMO by microwave heating. *Carbohydrate Polymers*, *75*(1), 90–94.

Dokoumetzidis, A., Papadopoulou, V., Valsami, G., & Macheras, P. (2008). Development of a reaction-limited model of dissolution: Application to official dissolution tests experiments. *International Journal of Pharmaceutics*, *355*(1–2), 114–125.

Durelle, J., Vanderveen, J. R., & Jessop, P. G. (2014). Modelling the behaviour of

switchable-hydrophilicity solvents. *Phys. Chem. Chem. Phys.*, *16*(11), 5270–5275.

Feng, L., & Chen, Z. lan. (2008). Research progress on dissolution and functional modification of cellulose in ionic liquids. *Journal of Molecular Liquids*, *142*(1–3), 1–5.

Fink, H. P., Weigel, P., Purz, H. J., & Ganster, J. (2001). Structure formation of regenerated cellulose materials from NMMO-solutions. *Progress in Polymer Science (Oxford)*, *26*(9), 1473–1524.

Ford, Z. M., Stevens, E. D., Johnson, G. P., & French, A. D. (2005). Determining the crystal structure of cellulose IIII by modeling. *Carbohydrate Research*, *340*(5), 827–833.

Garcia-Gonzalez, L., Geeraerd, A. H., Spilimbergo, S., Elst, K., Van Ginneken, L., Debevere, J., … Devlieghere, F. (2007). High pressure carbon dioxide inactivation of microorganisms in foods: The past, the present and the future. *International Journal of Food Microbiology*, *117*(1), 1–28.

Gardiner, E. S., & Sarko, A. (1985). Packing analysis of carbohydrates and polysaccharides. 16. The crystal structures of celluloses IV $_I$ and IV $_{II}$. *Canadian Journal of Chemistry*, *63*(1), 173–180.

Gericke, M., Fardim, P., & Heinze, T. (2012). Ionic liquids - Promising but challenging solvents for homogeneous derivatization of cellulose. *Molecules*, *17*(6), 7458–7502.

Gubitosi, M., Nosrati, P., Hamid, M. K., Kuczera, S., Behrens, M. A., Johansson, E. G., & Gubitosi, M. (2017). Stable , metastable and unstable cellulose solutions. *Royal Society Open Science*, *4*, 170487.

Hammer, R. B., O'Shaughnessy, M. E., Strauch, E. R., & Turbak, A. F. (1979). Process and fiber spinning studies for the cellulose/paraformaldehyde/dimethyl sulfoxide system. *Journal of Applied Polymer Science*, *23*(2), 485–494.

Hasegawa, M., Isogai, A., Onabe, F., & Usuda, M. (1992). Dissolving states of cellulose and chitosan in trifluoroacetic acid. *Journal of Applied Polymer Science*, *45*(10), 1857–1863.

He, L., Zhang, X., Xu, H., Xu, C., Yuan, F., Knez, Ž., … Gao, Y. (2012). Subcritical water extraction of phenolic compounds from pomegranate (Punica granatum L.) seed

residues and investigation into their antioxidant activities with HPLC-ABTS + assay. *Food and Bioproducts Processing*, *90*(2), 215–223.

Heldebrant, D. J., Jessop, P. G., Thomas, C. A., Eckert, C. A., & Liotta, C. L. (2005). The reaction of 1,8-diazabicyclo[5.4.0]undec-7-ene (DBU) with carbon dioxide. *Journal of Organic Chemistry*, *70*(13), 5335–5338.

Hermans, P. H., & Weidinger, A. (1948). Quantitative x-ray investigations on the crystallinity of cellulose fibers. A background analysis. *Journal of Applied Physics*, *19*(5), 491–506.

Ibañez, E., Kubátová, A., Señoráns, F. J., Cavero, S., Reglero, U., & Hawthorne, S. B. (2003). Subcritical water extraction of antioxidant compounds from rosemary plants. *Journal of Agricultural and Food Chemistry*, *51*(2), 375–382.

Isogai, a, Atalla, R. H., & Service, F. (1998). Dissolution of cellulose in aqueous NaOH solutions. *Solutions*, *5*(4), 309–319.

Iwai, Y., Koujina, Y., Arai, Y., Watanabe, I., Mochida, I., & Sakanishi, K. (2002). Low temperature drying of low rank coal by supercritical carbon dioxide with methanol as entrainer. *Journal of Supercritical Fluids*, *23*(3), 251–255.

Jahirul, M. I., Rasul, M. G., Chowdhury, A. A., & Ashwath, N. (2012). Biofuels production through biomass pyrolysis- A technological review. *Energies*, *5*(12), 4952–5001.

Jedvert, K., & Heinze, T. (2017). Cellulose modification and shaping - A review. *Journal of Polymer Engineering*, *37*(9), 845–860.

Jessop, P. G., Heldebrant, D. J., Li, X., Eckertt, C. A., Liotta, C. L., Eckert, C. A., & Liotta, C. L. (2005). Green chemistry: Reversible nonpolar-to-polar solvent. *Nature*, *436*(7054), 1102–1102.

Jessop, P. G., Mercer, S. M., & Heldebrant, D. J. (2012). CO_2-triggered switchable solvents, surfactants, and other materials. *Energy & Environmental Science*, *5*(6), 7240.

Jin, H., Zha, C., & Gu, L. (2007). Direct dissolution of cellulose in NaOH/thiourea/urea aqueous solution. *Carbohydrate Research*, *342*(6), 851–858.

Jordaan, W. A., Terblans, J. J., & Swart, H. C. (2008). The effect of nitrogen on the co-segregation with molybdenum in a Fe–3.5wt%Mo–N(100) single crystal. *South African Journal of Science*, *104*, 393–397.

Kazarian, S. G. (2000). Polymer Processing with Supercritical Fluids. *Polymer Science*, *42*(1), 78–101.

Kelly, C. a., Howdle, S. M., Shakesheff, K. M., Jenkins, M. J., & Leeke, G. a. (2012). Viscosity studies of poly(DL-lactic acid) in supercritical CO$_2$. *Journal of Polymer Science Part B: Polymer Physics*, *50*(19), 1383–1393.

Kinoshita, M., & Shimoyama, Y. (2016). Dynamic phase behavior during sol-gel reaction in supercritical carbon dioxide for morphological design of nanostructured titania. *Journal of Supercritical Fluids*, *116*, 190–197.

Kitzberger, C. S. G., Lomonaco, R. H., Michielin, E. M. Z., Danielski, L., Correia, J., & Ferreira, S. R. S. (2009). Supercritical fluid extraction of shiitake oil: Curve modeling and extract composition. *Journal of Food Engineering*, *90*(1), 35–43.

Kleinebudde, P., Jumaa, M., & El Saleh, F. (2000). Influence of degree of polymerization on behavior of cellulose during homogenization and extrusion/spheronization. *AAPS PharmSci*, *2*(3), 18–27.

Kosan, B., Michels, C., & Meister, F. (2008). Dissolution and forming of cellulose with ionic liquids. *Cellulose*, *15*(1), 59–66.

Krawczyk, H., Persson, T., Andersson, A., & Jönsson, A. S. (2008). Isolation of hemicelluloses from barley husks. *Food and Bioproducts Processing*, *86*(1), 31–36.

Kroon-Batenburg, L. M. J., Bouma, B., & Kroon, J. (1996). Stability of cellulose structures studied by MD simulations. Could mercerized cellulose II be parallel? *Macromolecules*, *29*(17), 5695–5699.

Kumar, S. P. J., Prasad, S. R., Banerjee, R., Agarwal, D. K., Kulkarni, K. S., & Ramesh, K. V. (2017). Green solvents and technologies for oil extraction from oilseeds. *Chemistry Central Journal*, *11*(1).

Kunanusont, N., & Shimoyama, Y. (2018). Porous carbon electrode for Li-air battery fabricated from solvent expansion during supercritical drying. *Journal of Supercritical Fluids*, *133*, 77–85.

Langan, P., Nishiyama, Y., & Chanzy, H. (1999). A revised structure and hydrogen-bonding system in cellulose II from a neutron fiber diffraction analysis. *Journal of*

the American Chemical Society, *121*(43), 9940–9946.

Langan, P., Nishiyama, Y., & Chanzy, H. (2001). X-ray structure of mercerized cellulose II at 1 Å resolution. *Biomacromolecules*, *2*(2), 410–416.

Langan, P., Sukumar, N., Nishiyama, Y., & Chanzy, H. (2005). Synchrotron X-ray structures of cellulose Iβ and regenerated cellulose II at ambient temperature and 100 K. *Cellulose*, *12*(6), 551–562.

Li, B., Xu, W., Kronlund, D., Määttänen, A., Liu, J., Smått, J. H., … Xu, C. (2015). Cellulose nanocrystals prepared via formic acid hydrolysis followed by TEMPO-mediated oxidation. *Carbohydrate Polymers*, *133*, 605–612.

Li, H. J., Cao, Y. M., Qin, J. J., Jie, X. M., Wang, T. H., Liu, J. H., & Yuan, Q. (2006). Development and characterization of anti-fouling cellulose hollow fiber UF membranes for oil-water separation. *Journal of Membrane Science*, *279*(1–2), 328–335.

Lian, Z., Epstein, S. A., Blenk, C. W., & Shine, A. D. (2006). Carbon dioxide-induced melting point depression of biodegradable semicrystalline polymers. *Journal of Supercritical Fluids*, *39*(1), 107–117.

Lin, Y., Cho, J., Davis, J. M., & Huber, G. W. (2012). Reaction-transport model for the pyrolysis of shrinking cellulose particles. *Chemical Engineering Science*, *74*, 160–171.

Luchese, C. L., Spada, J. C., & Tessaro, I. C. (2017). Starch content affects physicochemical properties of corn and cassava starch-based films. *Industrial Crops and Products*, *109*, 619–626.

Ma, X. J., Yang, X. F., Zheng, X., Lin, L., Chen, L. H., Huang, L. L., & Cao, S. L. (2014). Degradation and dissolution of hemicelluloses during bamboo hydrothermal pretreatment. *Bioresource Technology*, *161*, 215–220.

Ma, X., Long, Y., Duan, C., Lin, X., Cao, S., Chen, L., … Ni, Y. (2017). Facilitate hemicelluloses separation from chemical pulp in ionic liquid/water by xylanase pretreatment. *Industrial Crops and Products*, *109*, 459–463.

McCormick, C. L., Callais, P. A., & Hutchinson, B. H. (1985). Solution studies of cellulose in lithium chloride and N,N-dimethylacetamide. *Macromolecules*, *18*(12), 2394–

2401.

Mehra, A. (1996). Gas absorption in reactive slurries: Particle dissolution near gas-liquid interface. *Chemical Engineering Science*, *51*(3), 461–477.

Memon, Z. M., Yilmaz, E., & Soylak, M. (2017). Switchable solvent based green liquid phase microextraction method for cobalt in tobacco and food samples prior to flame atomic absorption spectrometric determination. *Journal of Molecular Liquids*, *229*, 459–464.

Morgan, N. K., & Choct, M. (2016). Cassava: Nutrient composition and nutritive value in poultry diets. *Animal Nutrition*, *2*(4), 253–261.

Morgenstern, B., Kammer, H. W., Berger, W., & Skrabal, P. (1992). 7Li-NMR study on cellulose/LiCl/N.N-dimethylacetamide solutions. *Acta Polymerica*, *43*(6), 356–357.

Newman, R. H., & Hemmingson, J. A. (1990). Determination of the degree of cellulose crystallinity in wood by carbon-13 nuclear magnetic resonance spectroscopy. *Holzforschung*, *44*, 351–355.

Ngo, M. T., Dickmann, J. S., Hassler, J. C., & Kiran, E. (2016). A new experimental system for combinatorial exploration of foaming of polymers in carbon dioxide: The gradient foaming of PMMA. *Journal of Supercritical Fluids*, *109*, 1–19.

Nishiyama, Y., Langan, P., & Chanzy, H. (2002). Crystal structure and hydrogen-bonding system in cellulose Iβ from synchrotron X-ray and neutron fiber diffraction. *Journal of the American Chemical Society*, *124*(31), 9074–9082.

Nishiyama, Y., Sugiyama, J., Chanzy, H., & Langan, P. (2003). Crystal structure and hydrogen bonding system in cellulose Iα from synchrotron x-ray and neutron fiber diffraction. *Journal of the American Chemical Society*, *125*(47), 14300–14306.

Öztürk, M. Ç., Ume, C. S., & Alper, E. (2012). Reaction Mechanism and Kinetics of 1,8-Diazabicyclo[5.4.0]undec-7-ene and Carbon Dioxide in Alkanol Solutions. *Chemical Engineering and Technology*, *35*(12), 2093–2098.

Parida, C., Dash, S. K., & Pradhan, C. (2015). FTIR and Raman Studies of Cellulose Fibers of Luffa cylindrica. *Open Journal of Composite Materials*, *5*(January), 5–10.

Park, S., Baker, J. O., Himmel, M. E., Parilla, P. A., & Johnson, D. K. (2010). Cellulose

crystallinity index: measurement techniques and their impact on interpreting cellulase performance. *Biotechnology for Biofuels*, *3*(1), 10.

Park, S. J., Lee, J. I., & Park, J. (2002). Effects of a Combined Process of High-Pressure Carbon Dioxide and High Hydrostatic Pressure on the Quality of Carrot Juice. *Journal of Food Science*, *67*(5), 1827–1834.

Pasquini, D., Teixeira, E. de M., Curvelo, A. A. da S., Belgacem, M. N., & Dufresne, A. (2010). Extraction of cellulose whiskers from cassava bagasse and their applications as reinforcing agent in natural rubber. *Industrial Crops and Products*, *32*(3), 486–490.

Peng, Z., Freunberger, S. a, Chen, Y., Bruce, P. G., & Battery, L. (2012). A Reversible and Higher-Rate Li-O $_2$ Battery. *Science*, *337*(6094), 563–566.

Phan, L., Andreatta, J. R., Horvey, L. K., Edie, C. F., Luco, A. L., Mirchandani, A., … Jessop, P. G. (2008). Switchable-polarity solvents prepared with a single liquid component. *Journal of Organic Chemistry*, *73*(1), 127–132.

Phan, L., Brown, H., White, J., Hodgson, A., & Jessop, P. G. (2009). Soybean oil extraction and separation using switchable or expanded solvents. *Green Chemistry*, *11*(1), 53–59.

Phan, L., Chiu, D., Heldebrant, D. J., Huttenhower, H., John, E., Li, X., … Jessop, P. G. (2008). Switchable solvents consisting of amidine/alcohol or guanidine/alcohol mixtures. *Industrial and Engineering Chemistry Research*, *47*(3), 539–545.

Pinkert, A., Marsh, K. N., Pang, S., & Staiger, M. P. (2009). Ionic liquids and their interaction with cellulose. *Chemical Reviews*, *109*(12), 6712–6728.

Piyachomkwan, K., & Tanticharoen, M. (2011). Cassava Industry in Thailand: Prospects. *The Journal of the Royal Institute of Thailand*, *3*.

Rai, A., Mohanty, B., & Bhargava, R. (2016). Supercritical extraction of sunflower oil: A central composite design for extraction variables. *Food Chemistry*, *192*, 647–659.

Ruan, D., Zhang, L., Zhou, J., Jin, H., & Chen, H. (2004). Structure and properties of novel fibers spun from cellulose in NaOH/thiourea aqueous solution. *Macromolecular Bioscience*, *4*(12), 1105–1112.

Rubio-Rodríguez, N., De Diego, S. M., Beltrán, S., Jaime, I., Sanz, M. T., & Rovira, J. (2012).

Supercritical fluid extraction of fish oil from fish by-products: A comparison with other extraction methods. *Journal of Food Engineering*, *109*(2), 238–248.

Saalwächter, K., Burchard, W., Klüfers, P., Kettenbach, G., Mayer, P., Klemm, D., & Dugarmaa, S. (2000). Cellulose solutions in water containing metal complexes. *Macromolecules*, *33*(11), 4094–4107.

Safari, V., Arzpeyma, G., Rashchi, F., & Mostoufi, N. (2009). A shrinking particle-shrinking core model for leaching of a zinc ore containing silica. *International Journal of Mineral Processing*, *93*(1), 79–83.

Scherer, G. W. (1992). Stress development during supercritical drying. *Journal of Non-Crystalline Solids*, *145*(C), 33–40.

Schnabelrauch, M., Vogt, S., Klemm, D., Nehls, I., & Philipp, B. (1992). Readily hydrolyzable cellulose esters as intermediates for the regioselective derivatization of cellulose, 1. Synthesis and characterization of soluble, low‑substituted cellulose formates. *Die Angewandte Makromolekulare Chemie*, *198*(1), 155–164.

Schweiger, R. G. (1979). New cellulose sulfate derivatives and applications. *Carbohydrate Research*, *70*(2), 185–198.

Segal, L., Creely, J. J., Martin, A. E., & Conrad, C. M. (1959). An Empirical Method for Estimating the Degree of Crystallinity of Native Cellulose Using the X-Ray Diffractometer. *Textile Research Journal*, *29*(10), 786–794.

Sen, S., Martin, J. D., & Argyropoulos, D. S. (2013). Review of cellulose non-derivatizing solvent interactions with emphasis on activity in inorganic molten salt hydrates. *ACS Sustainable Chemistry and Engineering*, *1*(8), 858–870.

Shaarani, F. W., & Bou, J. J. (2017). Synthesis of vegetable-oil based polymer by terpolymerization of epoxidized soybean oil, propylene oxide and carbon dioxide. *Science of the Total Environment*, *598*, 931–936.

Shen, Z., Xu, J., Liu, H., & Liang, Q. (2016). Modeling study for the effect of particle size on char gasification with CO_2. *AIChE Journal*, *63*(2), 716–724.

Shieh, Y. T., & Liu, K. H. (2002). Solubility of CO_2 in glassy PMMA and PS over a wide pressure range: The effect of carbonyl groups. *Journal of Polymer Research*, *9*(2), 107–113.

Singh, B. R., & Singh, O. (2012). Global Trends of Fossil Fuel Reserves and Climate Change in the 21st Century. *Fossil Fuel and the Environment*, 167–192.

Song, L., Yang, Y., Xie, H., & Liu, E. (2015). Cellulose Dissolution and in Situ Grafting in a Reversible System using an Organocatalyst and Carbon Dioxide. *ChemSusChem*, *8*(19), 3217–3221.

Suetsugu, T., Tanaka, M., Iwai, H., Matsubara, T., Kawamoto, Y., Saito, C., … Goto, M. (2013). Supercritical CO_2 extraction of essential oil from Kabosu (Citrus sphaerocarpa Tanaka) peel. *Flavour*, *2*(1), 18.

Sun, Y., Lin, L., Pang, C., Deng, H., Peng, H., Li, J., … Liu, S. (2007). Hydrolysis of cotton fiber cellulose in formic acid. *Energy and Fuels*, *21*(4), 2386–2389.

Swatloski, R. P., Spear, S. K., Holbrey, J. D., & Rogers, R. D. (2002). Dissolution of cellulose with ionic liquids. *Journal of the American Chemical Society*, *124*(18), 4974–4975.

Tan, H. T., & Lee, K. T. (2012). Understanding the impact of ionic liquid pretreatment on biomass and enzymatic hydrolysis. *Chemical Engineering Journal*, *183*, 448–458.

Tan, P., Jiang, H. R., Zhu, X. B., An, L., Jung, C. Y., Wu, M. C., … Zhao, T. S. (2017). Advances and challenges in lithium-air batteries. *Applied Energy*.

Tang, S., Baker, G. A., Ravula, S., Jones, J. E., & Zhao, H. (2012). PEG-functionalized ionic liquids for cellulose dissolution and saccharification. *Green Chemistry*, *14*(10), 2922.

TAPPI T 203 cm-99. (1999). Alpha- , beta- and gamma-cellulose in pulp. *TAPPI TEST METHODS. Technical Association of Pulp an Paper Industry. Atlanta, GA. Tappi Press.*, 1–5.

Tewari, P. H., Hunt, A. J., & Lofftus, K. D. (1985). Ambient-temperature supercritical drying of transparent silica aerogels. *Materials Letters*, *3*(9–10), 363–367.

Tsotsas, E., & Mujumdar, A. S. (2014). *Modern Drying Technology*. *Modern Drying Technology* (Vol. 1–4).

Van Soest, P. J., Robertson, J. B., & Lewis, B. A. (1991). Methods for Dietary Fiber, Neutral Detergent Fiber, and Nonstarch Polysaccharides in Relation to Animal Nutrition. *Journal of Dairy Science*, *74*(10), 3583–3597.

Vanderveen, J. R., Durelle, J., & Jessop, P. G. (2014). Design and evaluation of switchable-hydrophilicity solvents. *Green Chem.*, *16*(3), 1187–1197.

Vieira De Melo, S. A. B., Costa, G. M. N., Garau, R., Casula, A., & Pittau, B. (2000). Supercritical CO_2 extraction of essential oils from Thymus vulgaris. *Brazilian Journal of Chemical Engineering*, *17*(3), 238–243.

Wada, M., Chanzy, H., Nishiyama, Y., & Langan, P. (2004). Cellulose III I crystal structure and hydrogen bonding by synchrotron X-ray and neutron fiber diffraction. *Macromolecules*, *37*(23), 8548–8555.

Wang, H.-D., Jessop, P., Bouchard, J., Champagne, P., & Cunningham, M. (2015). Cellulose Nanocrystals with CO_2-Switchable Aggregation and Redispersion Properties. *Cellulose*, *22*(5), 3105–3116.

Wang, Y., & Zhou, H. (2010). A lithium-air battery with a potential to continuously reduce O2 from air for delivering energy. *Journal of Power Sources*, *195*(1), 358–361.

Weibel, G. L., & Ober, C. K. (2002). An overview of supercritical CO_2 applications in microelectronics processing. *Microelectronic Engineering*, *65*(1–2), 145–152.

Wojdyr, M. (2010). Fityk: A general-purpose peak fitting program. *Journal of Applied Crystallography*, *43*(5 PART 1), 1126–1128.

Xie, H., Yu, X., Yang, Y., & Zhao, Z. K. (2014). Capturing CO_2 for cellulose dissolution. *Green Chemistry*, *16*(5), 2422–2427.

Yagi, S., & Kunii, D. (1955). Studies on combustion of carbon particles in flames and fluidized beds. In *Symposium (International) on Combustion* (Vol. 5, pp. 231–244).

Yang, H., Yan, R., Chen, H., Lee, D. H., & Zheng, C. (2007). Characteristics of hemicellulose, cellulose and lignin pyrolysis. *Fuel*, *86*(12–13), 1781–1788.

Yang, Y. J., Shin, J. M., Kang, T. H., Kimura, S., Wada, M., & Kim, U. J. (2014). Cellulose dissolution in aqueous lithium bromide solutions. *Cellulose*, *21*(3), 1175–1181.

Yang, Y., Song, L., Peng, C., Liu, E., & Xie, H. (2015). Activating cellulose via its reversible reaction with CO 2 in the presence of 1,8-diazabicyclo[5.4.0]undec-7-ene for the efficient synthesis of cellulose acetate. *Green Chem.*, *17*(5), 2758–2763.

Yao, Y., Wu, X.-H., Geng, M.-T., Li, R.-M., Liu, J., Hu, X.-W., & Guo, J.-C. (2014). Cloning,

3D Modeling and Expression Analysis of Three Vacuolar Invertase Genes from Cassava (Manihot Esculenta Crantz). *Molecules, 19*(5), 6228–6245.

Zhang, C., Liu, R., Xiang, J., Kang, H., Liu, Z., & Huang, Y. (2014). Dissolution mechanism of cellulose in N,N-dimethylacetamide/lithium chloride: Revisiting through molecular interactions. *Journal of Physical Chemistry B, 118*(31), 9507–9514.

Zhang, H., Wu, J., Zhang, J., & He, J. (2005). 1-allyl-3-methylimidazolium chloride room temperature ionic liquid: A new and powerful nonderivatizing solvent for cellulose. *Macromolecules, 38*(20), 8272–8277.

Zhang, Q., Oztekin, N. S., Barrault, J., De Oliveira Vigier, K., & Jérôme, F. (2013). Activation of microcrystalline cellulose in a CO_2-based switchable system. *ChemSusChem, 6*(4), 593–596.

Zhang, S., Li, F., Yu, J., & Gu, L. (2009). Novel fibers prepared from cellulose in NaOH/thiourea/urea aqueous solution. *Fibers and Polymers, 10*(1), 34–39.

Zhang, S., Wang, W., Li, F., Yu, J., & Zhang, S. (2013). Swelling and Dissolution of cellulsoe in NaOH Aqueous Solvent System. *Cellulose Chemistry and Technology, 47*, 671–679.

Zheng, Y., Lin, H. M., & Tsao, G. T. (1998). Pretreatment for cellulose hydrolysis by carbon dioxide explosion. *Biotechnology Progress, 14*(6), 890–896.

Zhu, Y., Romain, C., & Williams, C. K. (2016). Sustainable polymers from renewable resources. *Nature, 540*(7633), 354–362.

Zugenmaier, P. (2001). Conformation and packing of various crystalline cellulose fibers. *Progress in Polymer Science (Oxford), 26*(9), 1341–1417.

Patent

Graenacher, C. (1934). Cellulose Solution. *US Patent*.

Report

AOAC. (1995). *Official methods of analysis of AOAC International*. *Association of Official Analysis Chemists International*.

Conference proceeding

Chen, C., Luo, J., Qin, W., & Tong, Z. (2014). Elemental analysis, chemical composition, cellulose crystallinity, and FT-IR spectra of Toona sinensis wood. In *Monatshefte fur Chemie* (Vol. 145, pp. 175–185).

Perepelkin, K. E. (2007). Lyocell fibres based on direct dissolution of cellulose in N-methylmorpholine N-oxide: Development and prospects. In *Fibre Chemistry* (Vol. 39, pp. 163–172). https://doi.org/10.1007/s10692-007-0032-9

Sriroth, K. (2000). Cassava industry in Thailand: The status of technology and utilization. In *International Symposium on Cassava, Starch and Starch Derivatives* (pp. 169–180).

Thesis

Kunanusont, N. (2017). *Development of porous carbon electrode for Li-air battery fabricated from supercritical carbon dioxide drying*. Tokyo Institute of Technology.

Punyanunt, S. (2017). *Isolation and characterization of microfibrillated cellulose and microcrystalline cellulose from destarched cassava pulp*. Kasetsart University.

Website

AKR. (2016). Cellulosic Technology Overview. Retrieved from http://akrcorp.kr/en/cellulosic-technology/cellulosic-technology-overview/

Casey, T. (2017). Toyota (still) banks on lithium-air energy storage for next -gen EV batteries. Retrieved from https://cleantechnica.com/2017/08/21/toyota-still-banks-lithium-air-energy-storage-next-gen-ev-batteries/

Ecotricity. (n.d.). The end of fossil fuels. Retrieved December 17, 2017, from https://www.ecotricity.co.uk/our-green-energy/energy-independence/the-end-of-fossil-fuels

FAO. (1977). Cassava processing. Retrieved from http://www.fao.org/docrep/x5032e/x5032E02.htm#Supply of cassava roots

FAO. (2016). Thailand: Cassava quantity (tons). Retrieved from

http://www.factfish.com/statistic-country/thailand/cassava%2C production quantity

Gilroy, J. (2017). Shifting conventional plastic into the renewable resource arena. Retrieved from http://innovate.bunzlcatering.co.uk/shifting-conventional-plastics-renewable-resource-arena/

Wikipedia. (n.d.). Nitrocellulose. Retrieved from https://en.wikipedia.org/wiki/Nitrocellulose

APPENDICES

APPENDIX A

PROXIMATE ANALYSIS

Table A.1 Data for moisture content calculation.

Sample	Sample weight/m_{wet} (g)	Crucible weight/m_C (g)	Crucible + dried sample weight/m_T (g)	$m_{dried} = m_T - m_C$	% Moisture	Average	std.
DCP1	2.034	53.274	55.066	1.792	11.90		
DCP2	2.047	54.303	56.105	1.802	11.97	11.87	0.1099
DCP3	2.025	53.472	55.259	1.787	11.75		
ATP1	2.005	54.074	55.814	1.740	13.22		
ATP2	2.009	54.526	56.271	1.745	13.14	13.14	0.0771
ATP3	2.021	52.960	54.717	1.757	13.06		
Cellulose1	2.021	54.420	56.193	1.773	12.27		
Cellulose2	2.003	54.553	56.310	1.757	12.28	12.29	0.0192
Cellulose3	2.023	53.358	55.132	1.774	12.31		

Table A.2 Data for crude protein calculation.

Sample	% N from CHNS	% CP	Average	std.
DCP1	0.5208	3.25		
DCP2	0.5396	3.37	3.20	0.2023
DCP3	0.4766	2.98		
ATP1	0.2909	1.82		
ATP2	0.3138	1.96	1.85	0.0998
ATP3	0.2830	1.77		
Cellulose1	0.1184	0.74		
Cellulose2	0.1117	0.70	0.72	0.0218
Cellulose3	0.1134	0.71		

Table A.3 Data for ash content calculation.

Sample	Sample weight/m_{sample} (g)	Cucible weight/m_1 (g)	Cucible+burned sample weight/m_2 (g)	% Ash	Average	std.
DCP1	2.034	53.274	53.335	2.9990		
DCP2	2.047	54.303	54.363	2.9311	3.014	0.09090
DCP3	2.025	53.472	53.535	3.1111		
ATP1	2.005	54.074	54.121	2.3441		
ATP2	2.040	54.526	54.573	2.3039	2.355	0.05775
ATP3	2.068	52.960	53.010	2.4178		
Cellulose1	2.021	54.420	54.463	2.1277		
Cellulose2	2.003	54.553	54.595	2.0969	2.117	0.01721
Cellulose3	2.023	53.358	53.401	2.1256		

APPENDIX B

FIBER COMPOSITE ANALYSIS
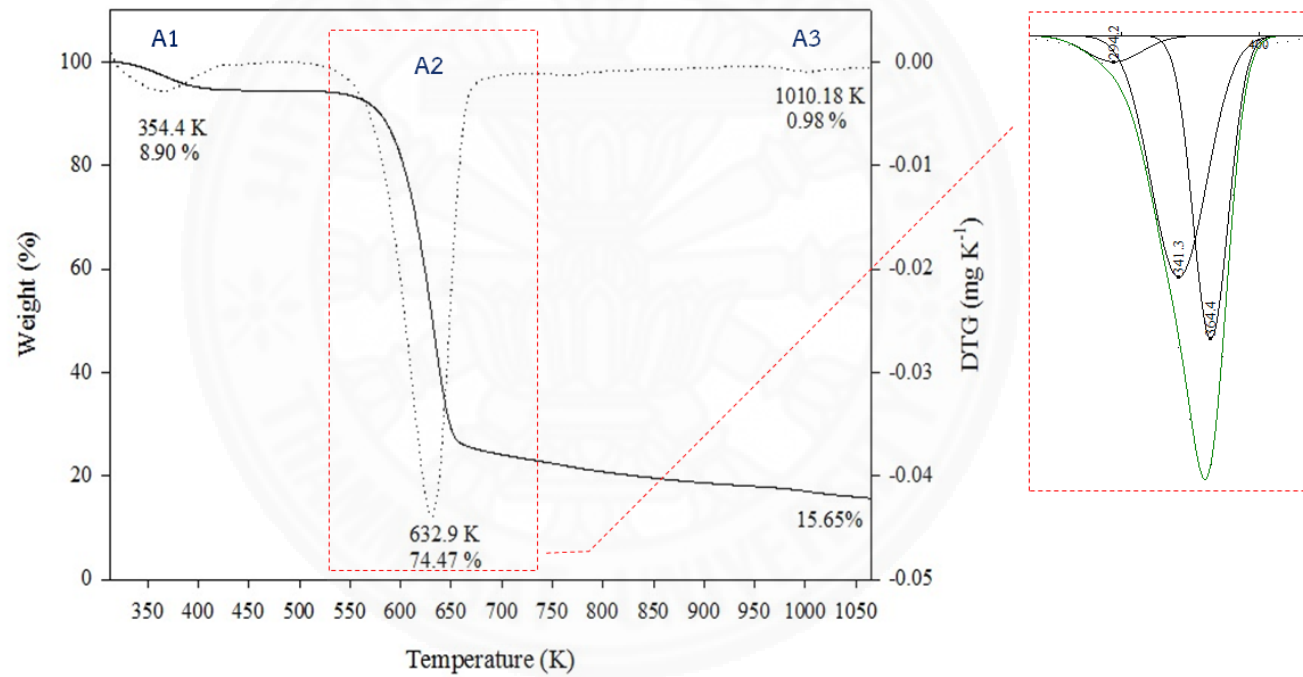
Figure B.1 TGA thermogram of cellulose derived from cassava pulp.

Table B.1 Cellulose composition calculated from peak area.

A1	A2			A3	Sum	%				
	1	2	3			Ash	Moisture	Hemicellulose	Cellulose	Lignin
0.667314	0.319212	2.93878	2.32799	0.073522	6.326818	15.65	8.90	4.26	70.22	0.98

Table B.2 Cellulose compositions analysis using T203 cm-99 method.

Sample	Sample weight (g)	Titrate volume V_1, V_2 (mL)			Avg (mL)	V_2-V_1 (mL)	Alpha (%)	std.	Titrate volume V_3, V_4 (mL)		Avg (mL)	V_4-V_3 (mL)	Gamma (%)	std.	Beta (%)	std.
		1	2	3					1	2						
B1	0.0000	N/A	47.20	47.30	47.50	0.00			23.40	22.70	23.05	0.00				
B2	0.0000	47.90	47.60	N/A					N/A	N/A						
C1	1.3679	31.00	30.70	30.50	30.73	16.77	71.92		11.00	11.20	11.10	11.95	4.79		21.18	
C2	1.3743	30.90	30.60	31.35	30.95	16.55	72.21	0.36	11.10	11.20	11.15	11.90	4.75	0.11	20.92	0.26
C3	1.3679	31.25	32.40	30.70	31.45	16.05	72.64		11.40	11.80	11.60	11.45	4.59		20.66	

B = Blank (no cellulose sample), C = derived cellulose

Alpha-, Beta-, and gamma-cellulose calculations

$$\%\text{Alpha cellulose} = 100 - \frac{6.85(V_2 - V_1) \times N \times 20}{10 \times W}$$

B-1

where

V_1 is titration of the pulp filtrate (mL)

V_2 is titration of blank (mL)

N is exact normality of the ferrous ammonium sulfate solution,

10 is the volume of the pulp filtrate (mL)

W is dried weight of pulp sample (g)

$$\%\text{Gamma cellulose} = \frac{6.85(V_4 - V_3) \times N \times 20}{25 \times W}$$

B-2

where

V_3 is titration of the solution after beta-cellulose precipitation (mL)

V_4 is titration of blank (mL)

$$\%\text{Beta cellulose} = 100 - (\%\text{alpha} + \%\text{gamma})$$

B-3

Calculation of alpha-, beta-, and gamma-cellulose for C1 sample

$$\%\text{Alpha cellulose} = 100 - \frac{6.85(47.5 - 30.73) \times 0.1 \times 20}{10 \times 1.3679} = 71.92$$

$$\%\text{Gamma cellulose} = \frac{6.85(23.05 - 11.1) \times 0.1 \times 20}{25 \times 1.3679} = 4.79$$

$$\%\text{Beta cellulose} = (100 - 2.12) - 71.92 - 4.79 = 21.18$$

APPENDIX C

FE-SEM IMAGES OF CELLULOSE PROCESSING IN SCCO$_2$
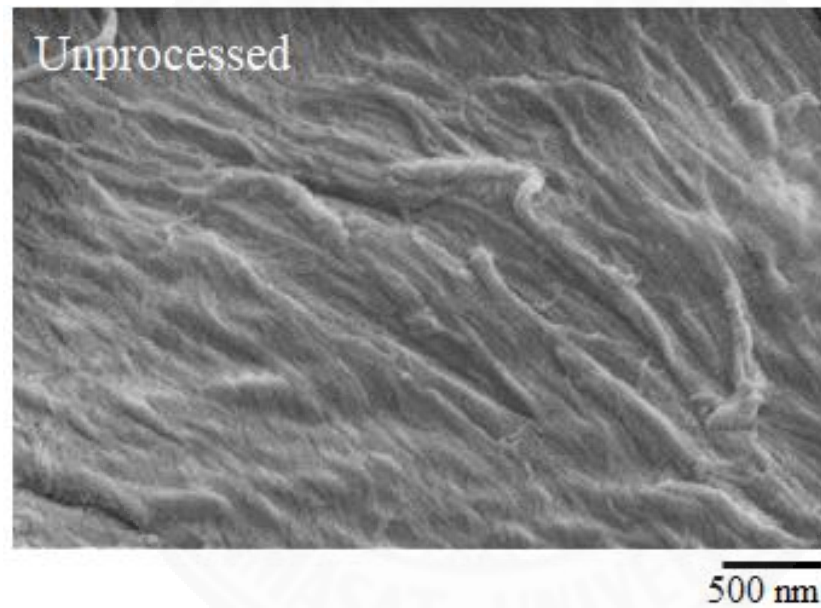
Figure C.1 FE-SEM of unprocessed.
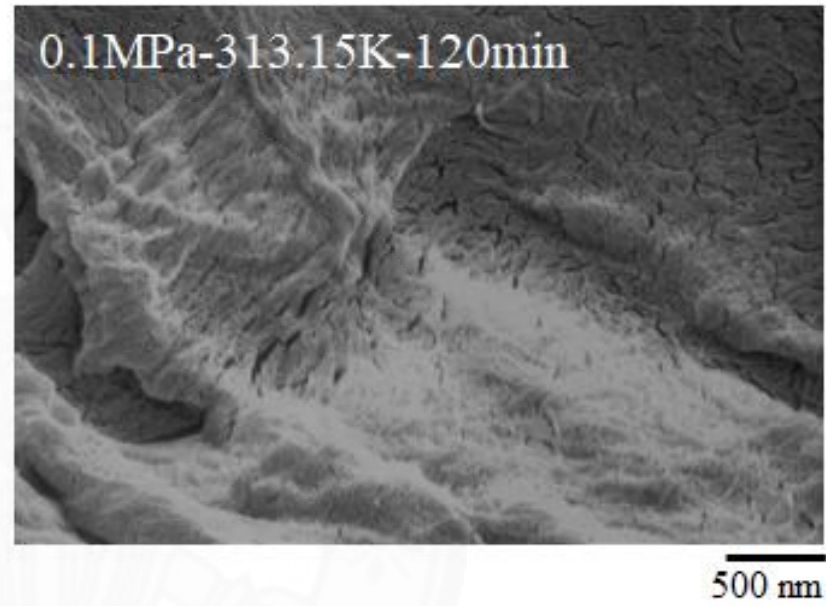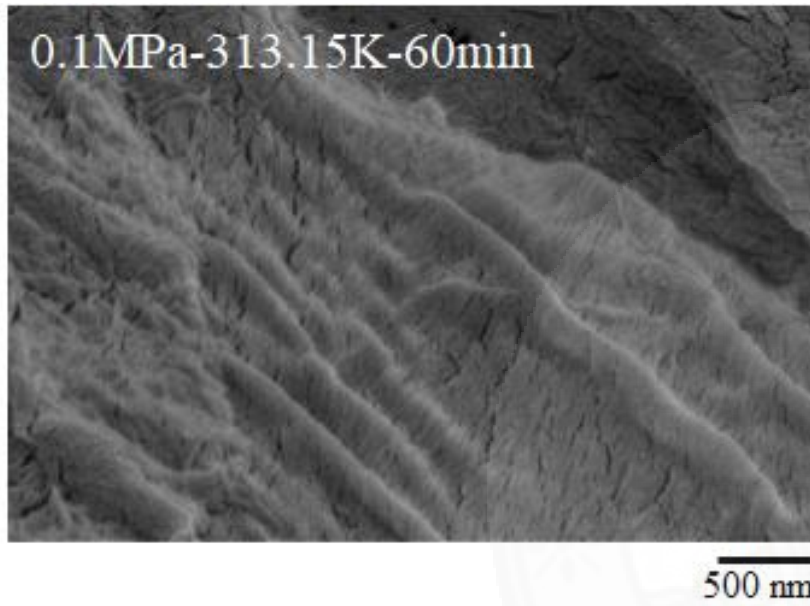
Figure C.2 FE-SEM of processed cellulose samples at 313.15 K under CO_2 processing at 0.1 MPa for 60 and 120 min.
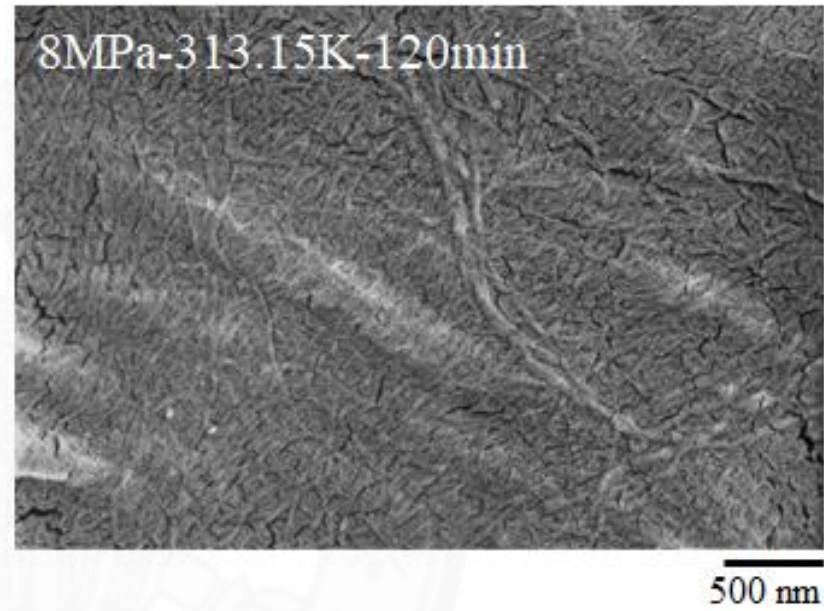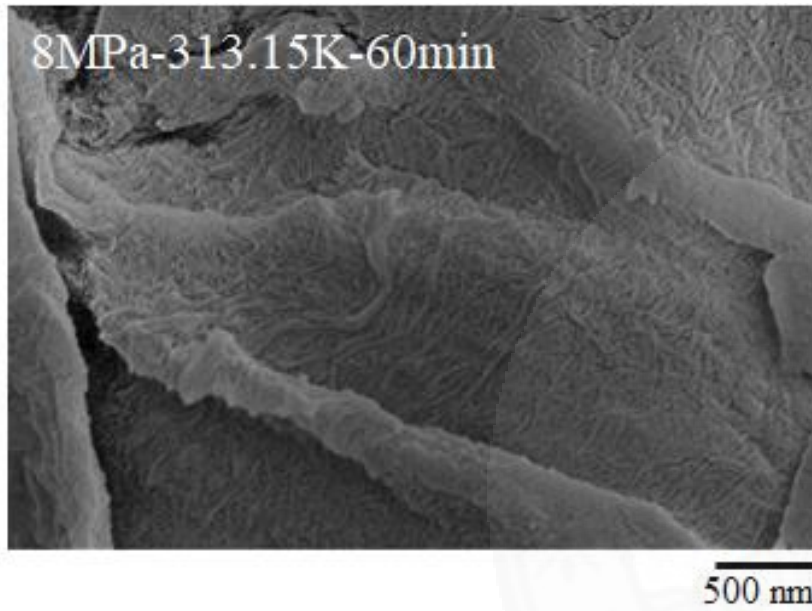
Figure C.3 FE-SEM of processed cellulose samples at 313.15 K under ScCO$_2$ processing at 8 MPa for 60 and 120 min.
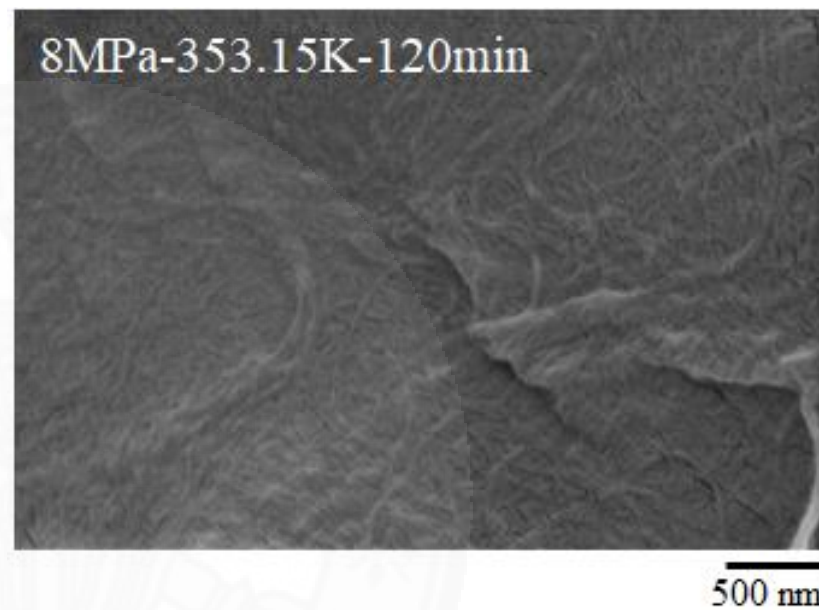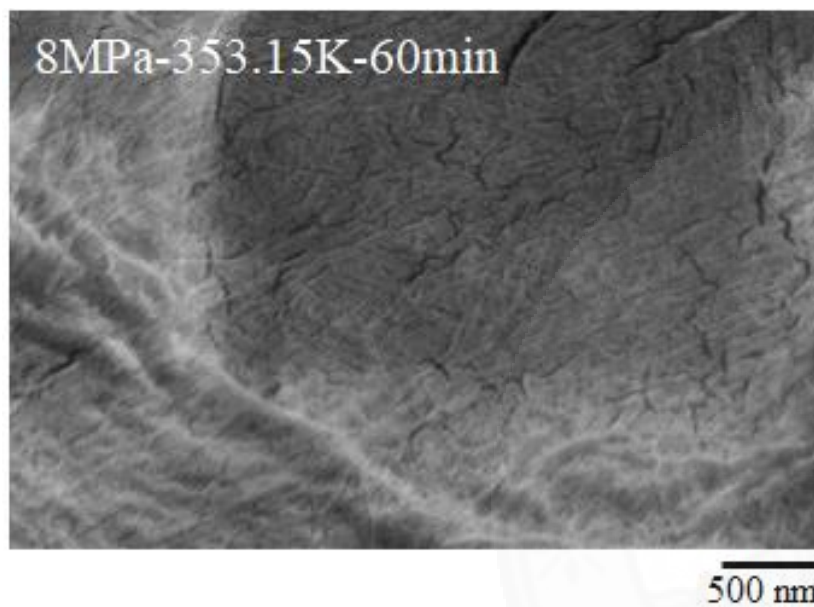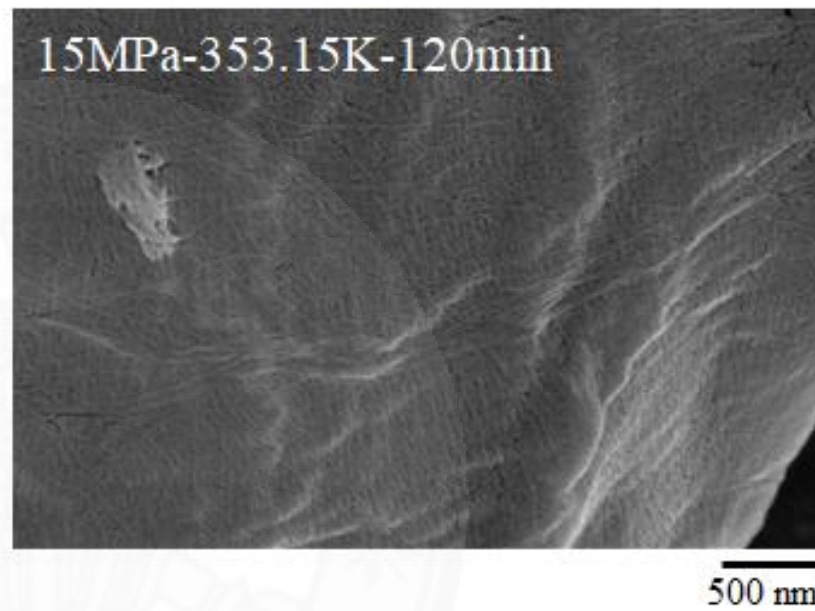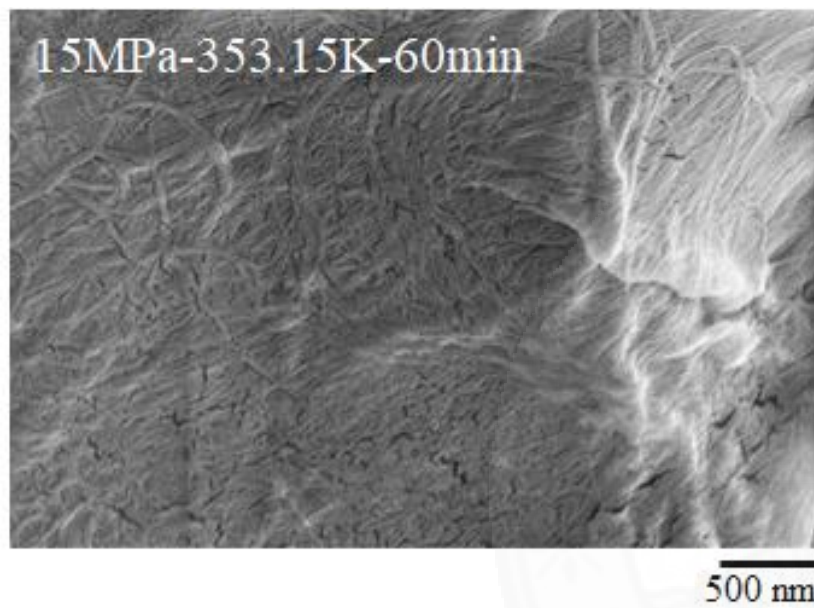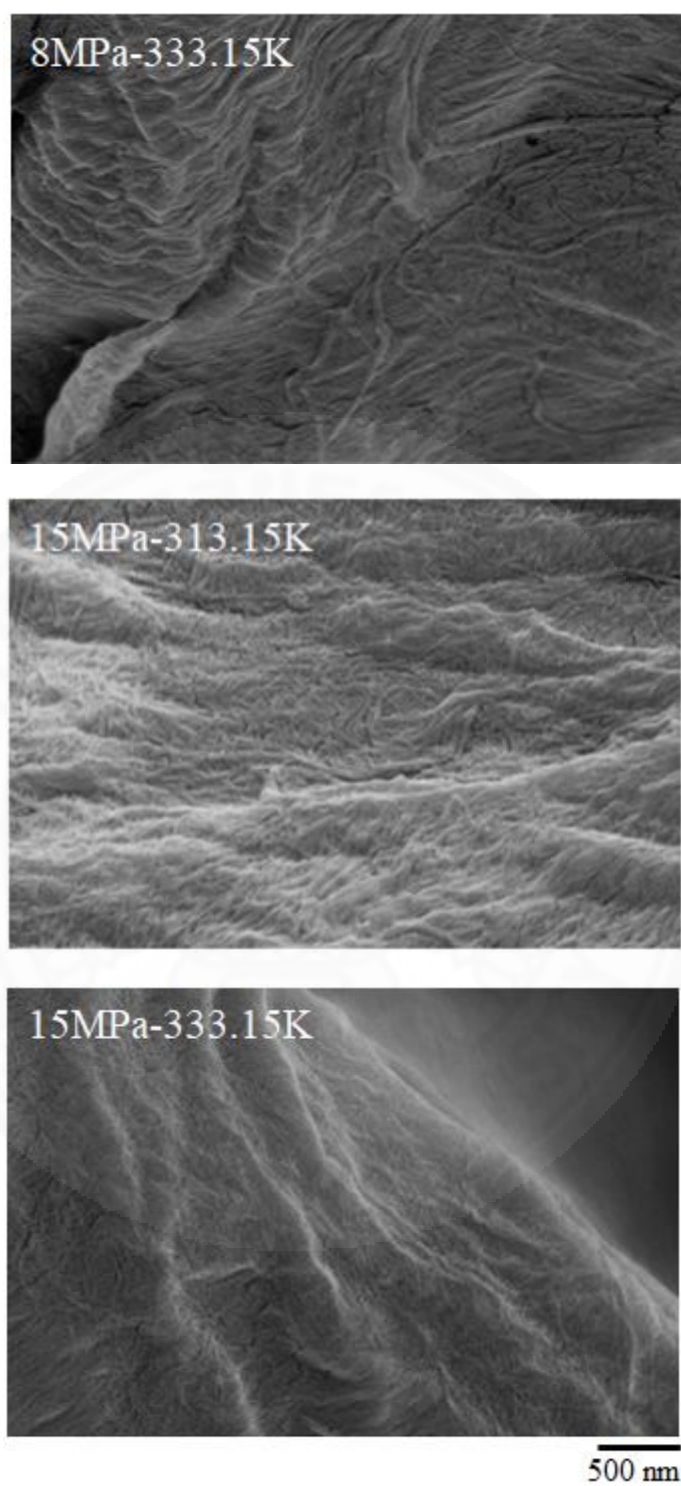
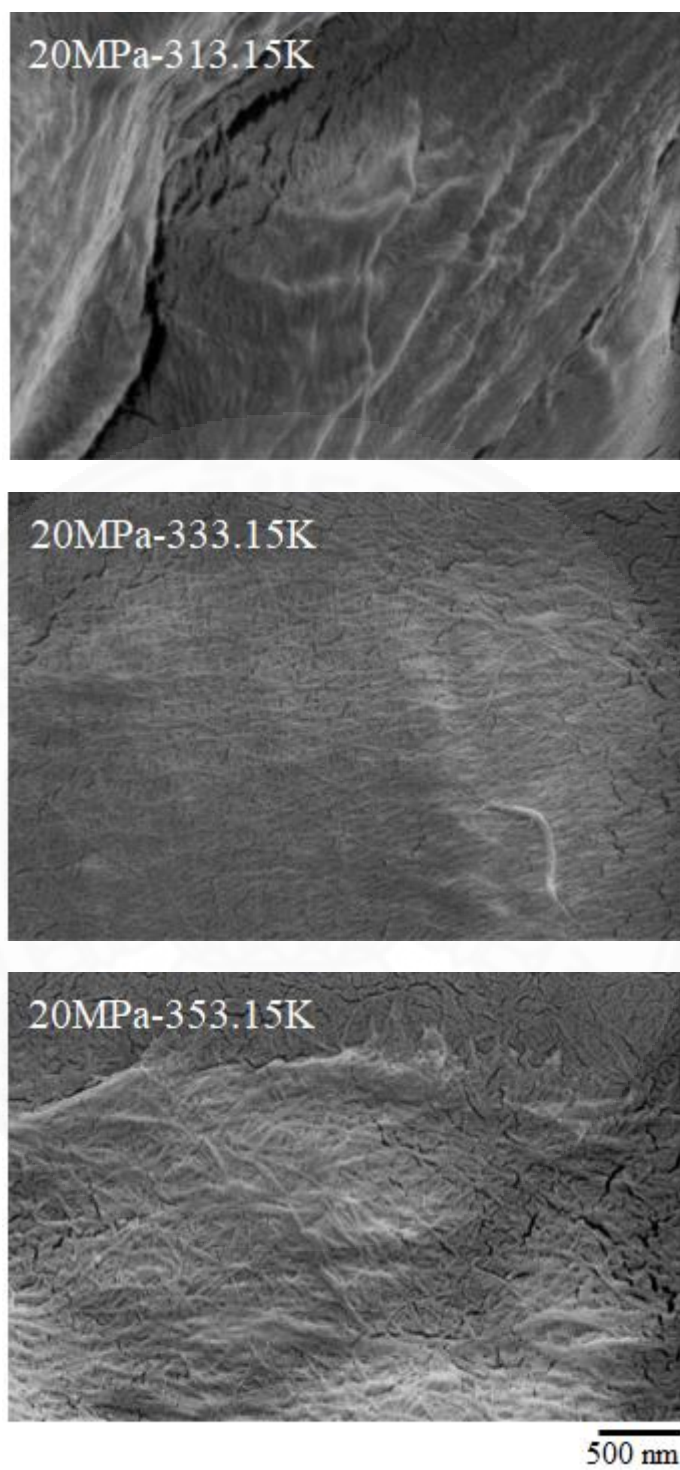Figure C.4 FE-SEM of processed cellulose samples at 353.15 K under $ScCO_2$ processing at 8 MPa for 60 and 120 min.

Figure C.5 FE-SEM of processed cellulose samples at 353.15 K under $ScCO_2$ processing at 15 MPa for 60 and 120 min.

Figure C.6 FE-SEM of processed cellulose samples under ScCO$_2$ processing for 60.

Figure C.7 FE-SEM of processed cellulose samples under ScCO$_2$ processing at 20 MPa for 60.

APPENDIX D

CRYSTALLINE PATTERN OF CELLULOSE PROCESSING IN SCCO$_2$ FROM XRD
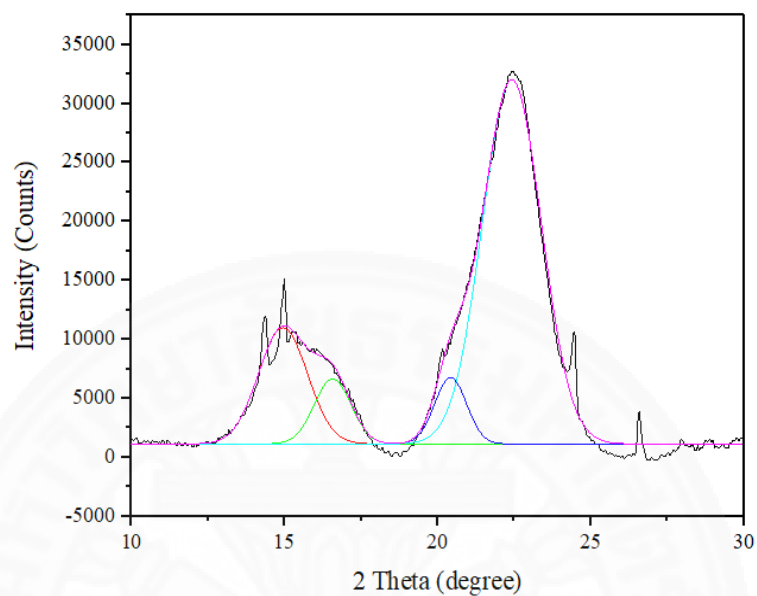
Figure D.1 X-ray diffraction of unprocessed cellulose.
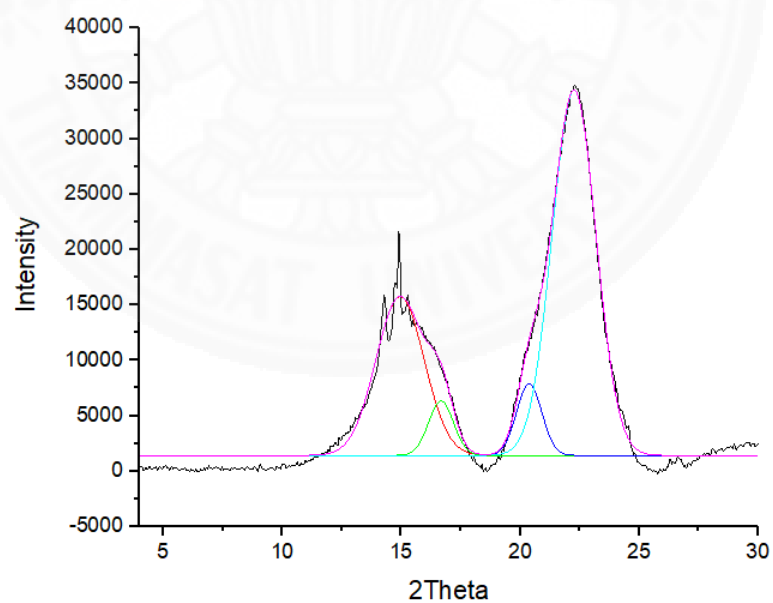
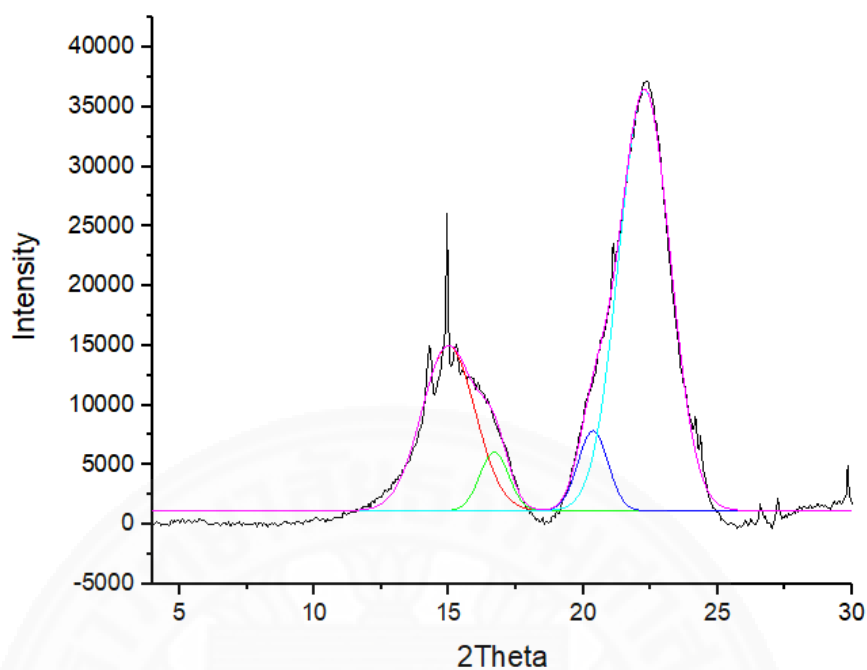Figure D.2 X-ray diffraction of processed cellulose at 0.1 MPa, 313.15 K for 60 min

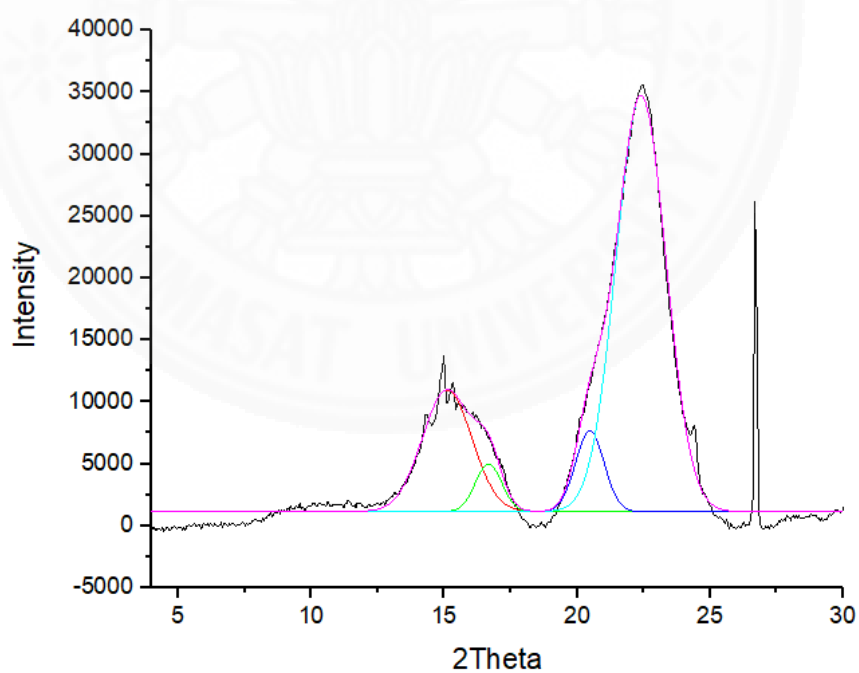Figure D.3 X-ray diffraction of processed cellulose at 0.1 MPa, 313.15 K for 120 min

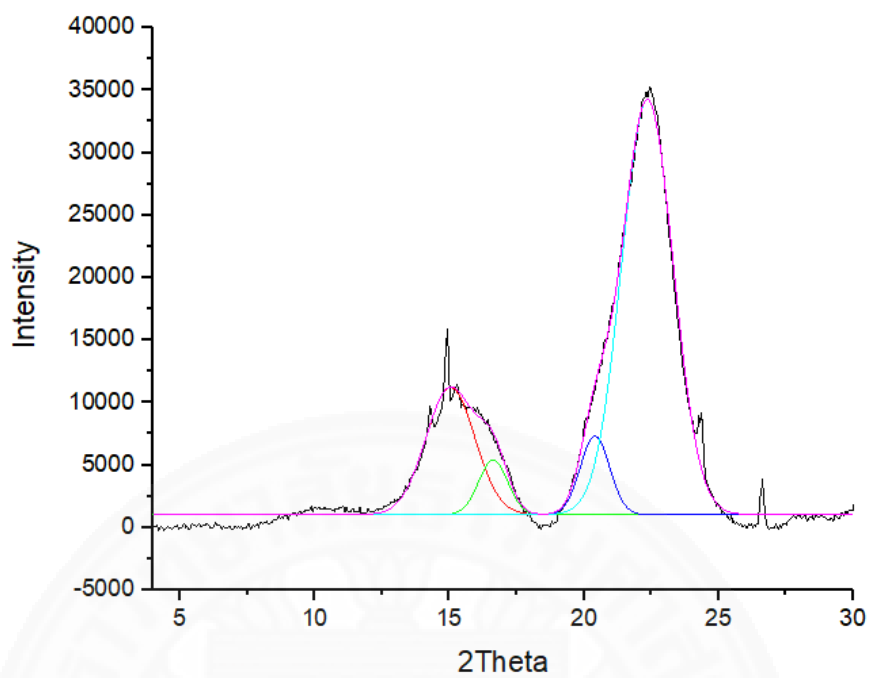Figure D.4 X-ray diffraction of processed cellulose at 8 MPa, 313.15 K for 60 min

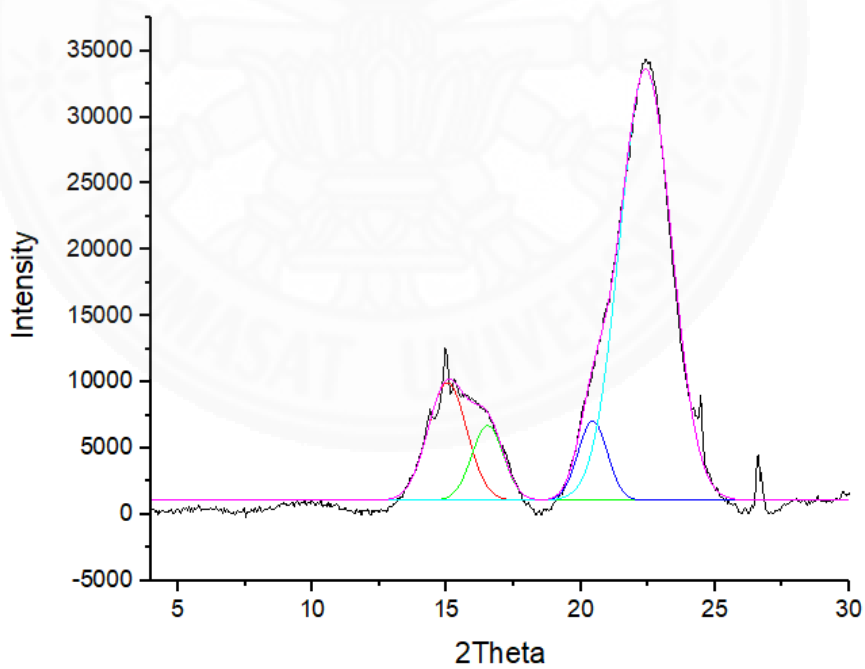Figure D.5 X-ray diffraction of processed cellulose at 8 MPa, 313.15 K for 120 min

Figure D.6 X-ray diffraction of processed cellulose at 8 MPa, 333.15 K for 60 min
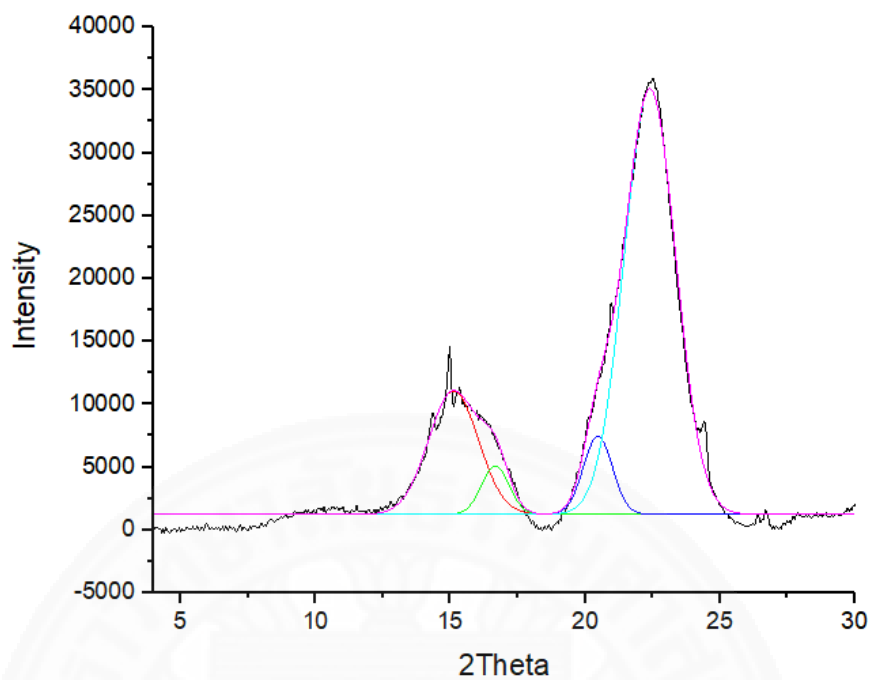
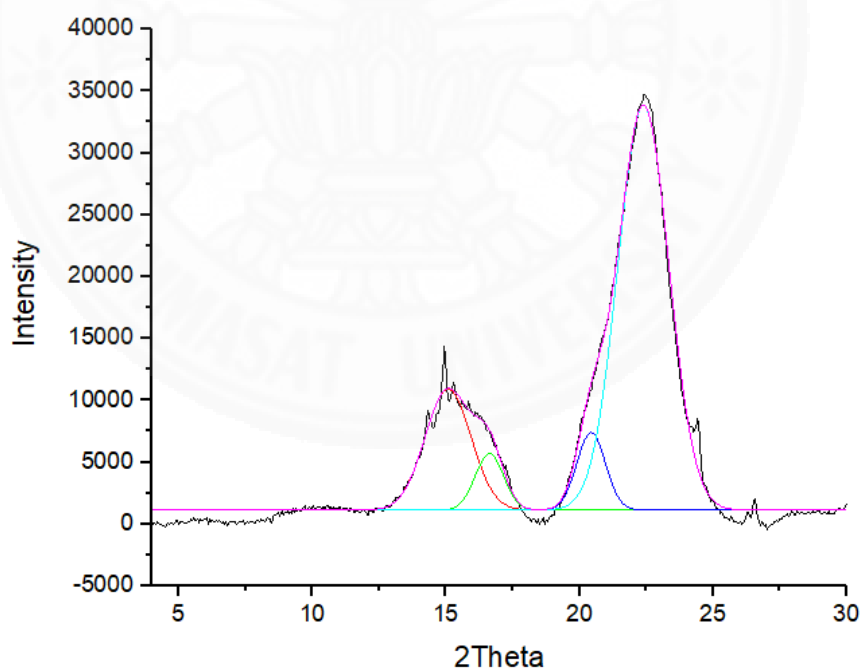Figure D.7 X-ray diffraction of processed cellulose at 8 MPa, 353.15 K for 60 min

Figure D.8 X-ray diffraction of processed cellulose at 8 MPa, 353.15 K for 120 min

Figure D.9 X-ray diffraction of processed cellulose at 15 MPa, 313.15 K for 60 min

Figure D.10 X-ray diffraction of processed cellulose at 15 MPa, 333.15 K for 60 min
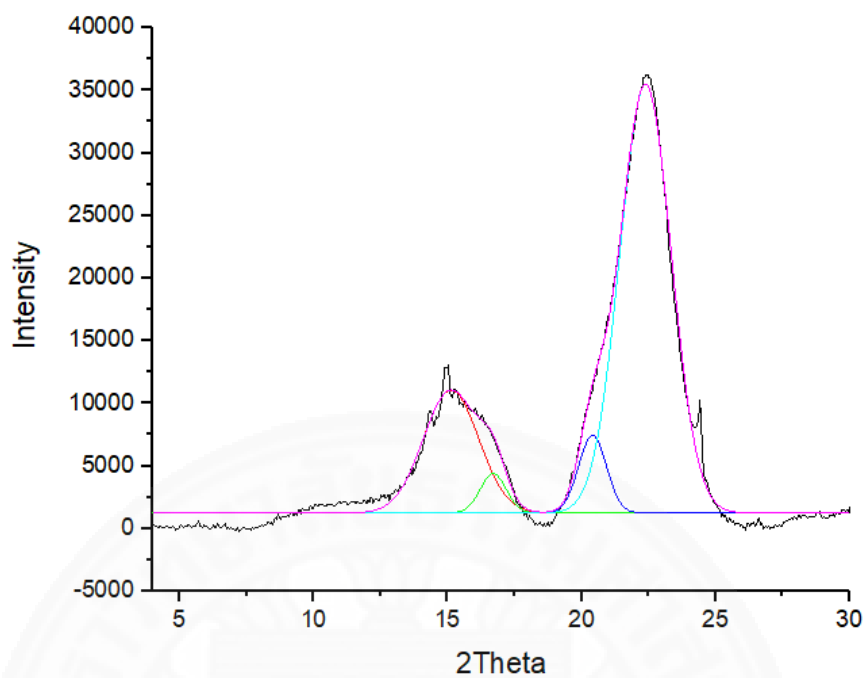
Figure D.11 X-ray diffraction of processed cellulose at 15 MPa, 353.15 K for 60 min

Figure D.12 X-ray diffraction of processed cellulose at 15 MPa, 353.15 K for 120 min

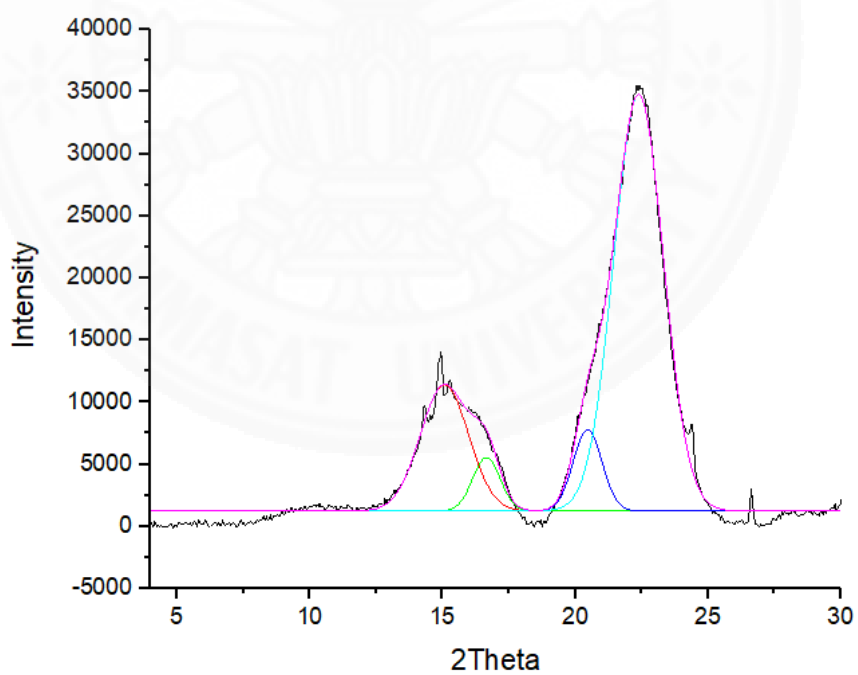Figure D.13 X-ray diffraction of processed cellulose at 20 MPa, 313.15 K for 60 min
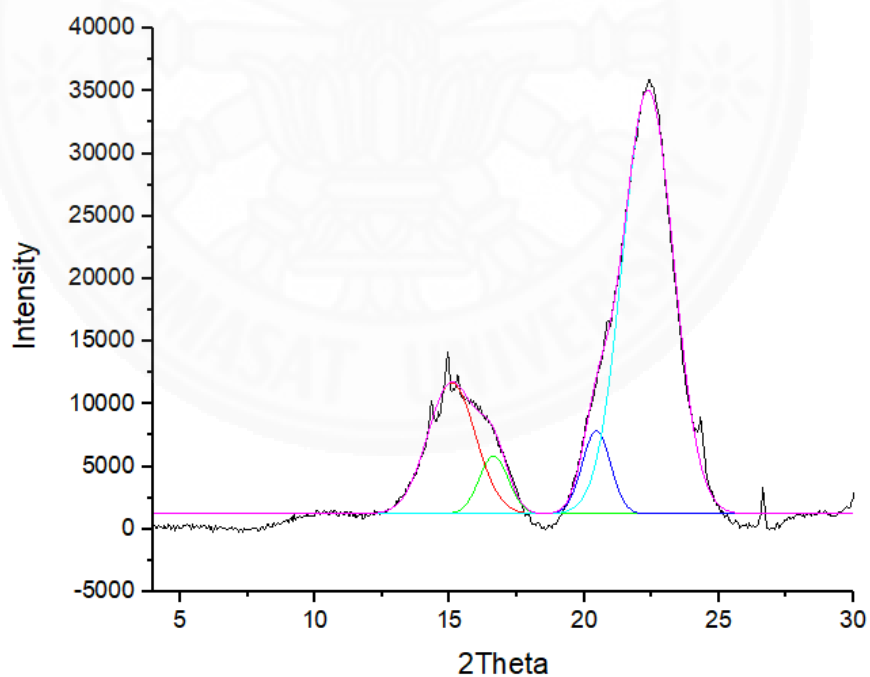
Figure D.14 X-ray diffraction of processed cellulose at 20 MPa, 333.15 K for 60 min
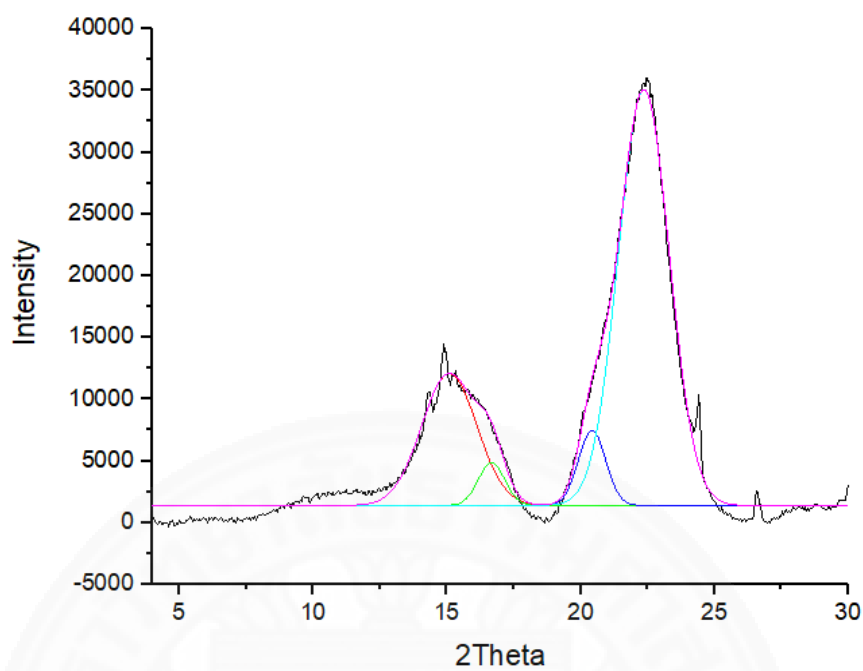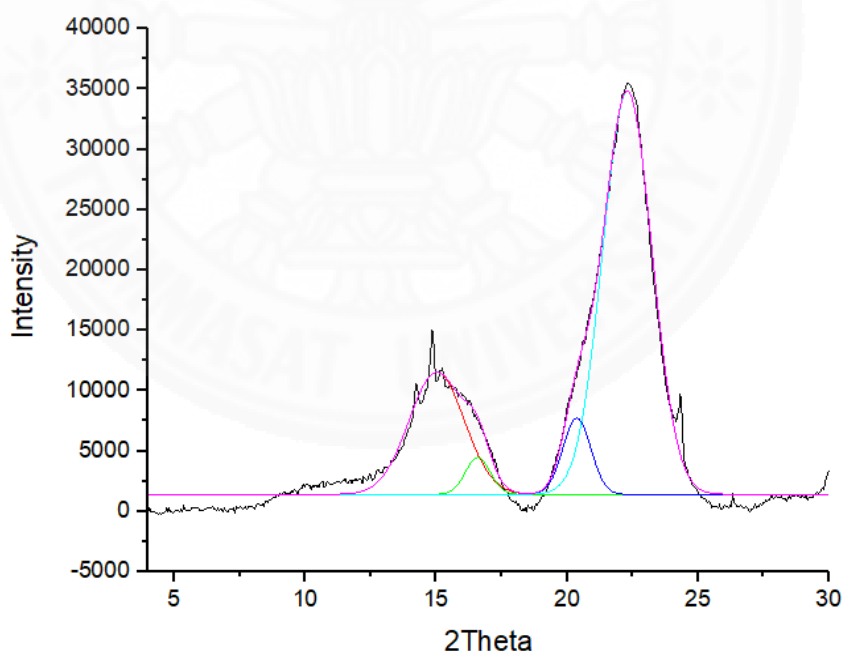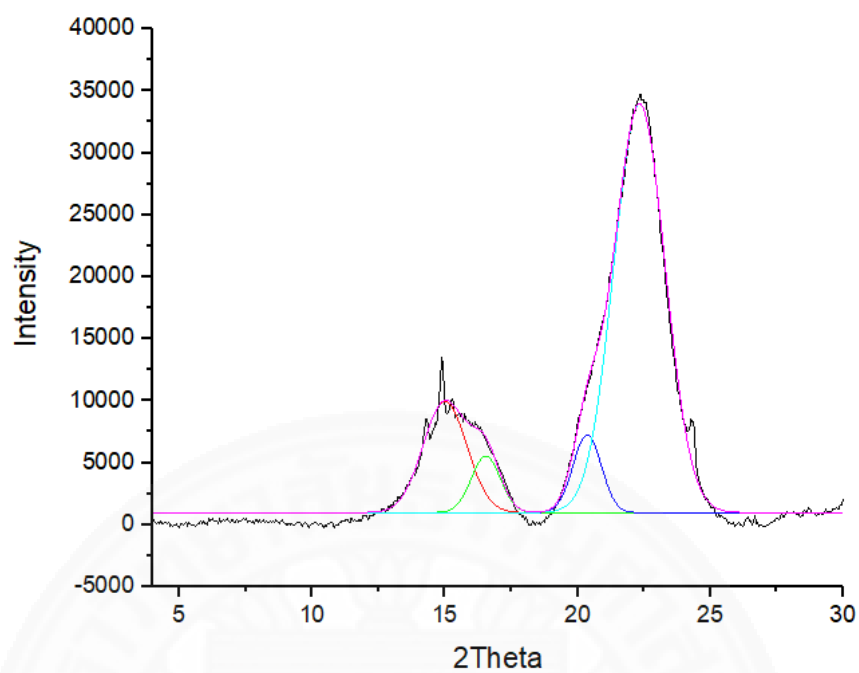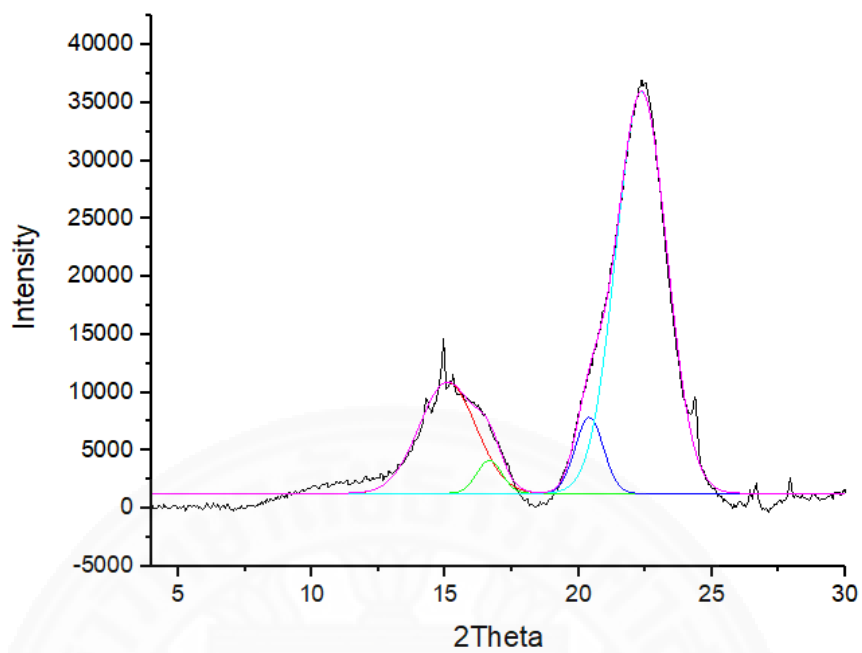
Figure D.15 X-ray diffraction of processed cellulose at 20 MPa, 333.15 K for 120 min
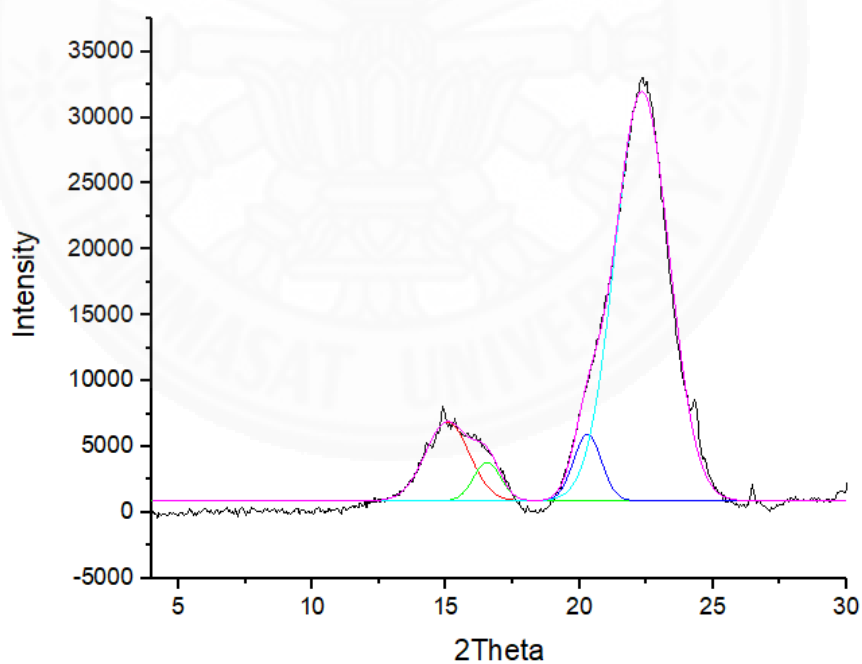
Figure D.16 X-ray diffraction of processed cellulose at 20 MPa, 353.15 K for 60 min

APPENDIX E

CRYSTALLINITY CALCULATIONS FOR CELLULOSE PROCESSING IN SCCO$_2$

Amorphous subtraction and peak deconvolution method (Herman's equation) from XRD

Model	Gaussian
Equation	y = y0 + A/(w*sqrt(pi/(4*ln(2)))) * exp(-4*ln(2)*(x-xc)^2/
Plot	Baseline_Data Y1
y0	-328.60423 ± 10.46554
xc	18.90067 ± 0.00909
A	111484.11386 ± 336.90823
w	12.69471 ± 0.03054
Reduced Chi-Sqr	18386.97369
R-Square(COD)	0.99786
Adj. R-Square	0.99785
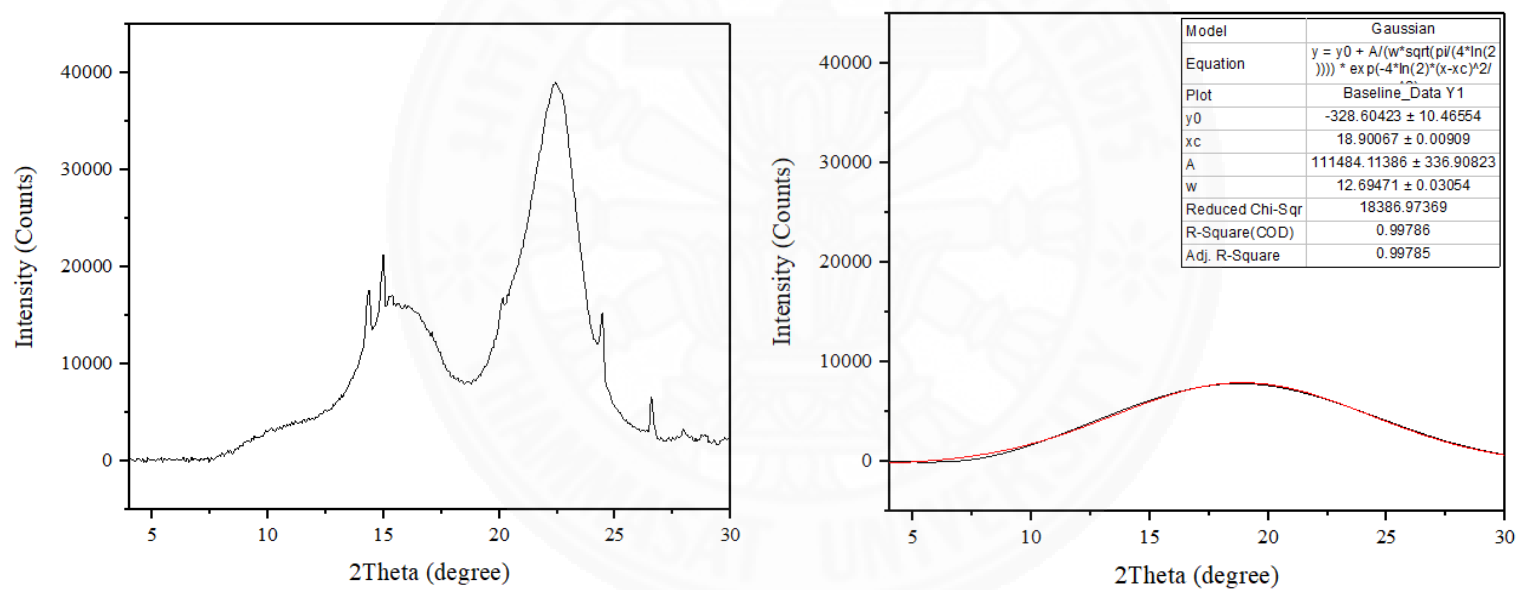
Figure E.1 X-ray diffraction pattern for unprocessed cellulose and its amorphous region fitted using Gaussian function.
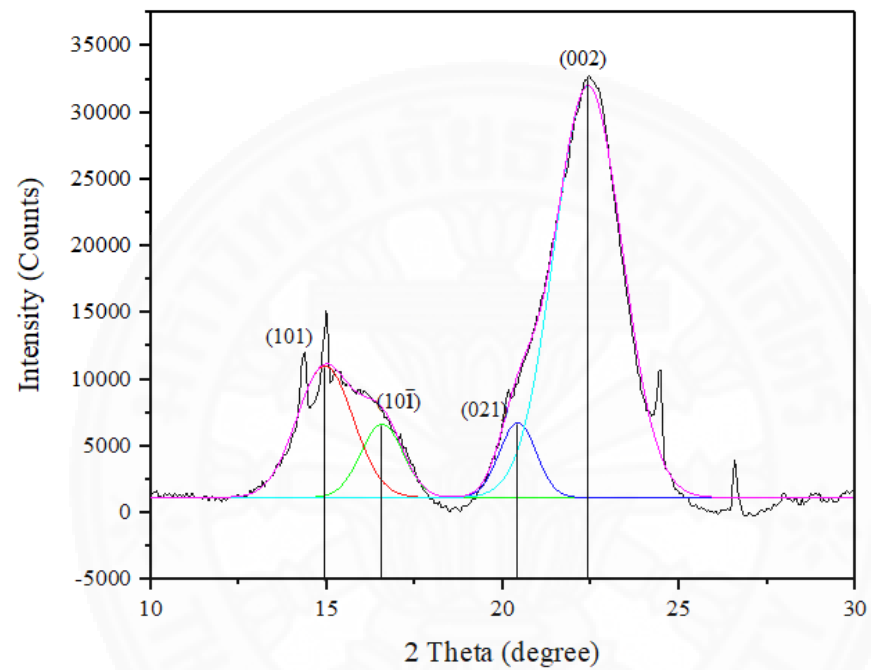
Figure E.2 Crystalline region of unprocessed cellulose and its deconvolution peaks fitted using Gaussian function.

$$Cr = A_{crystalline} / A_{total}$$

E-1

Peak height method (Segal's equation) from XRD
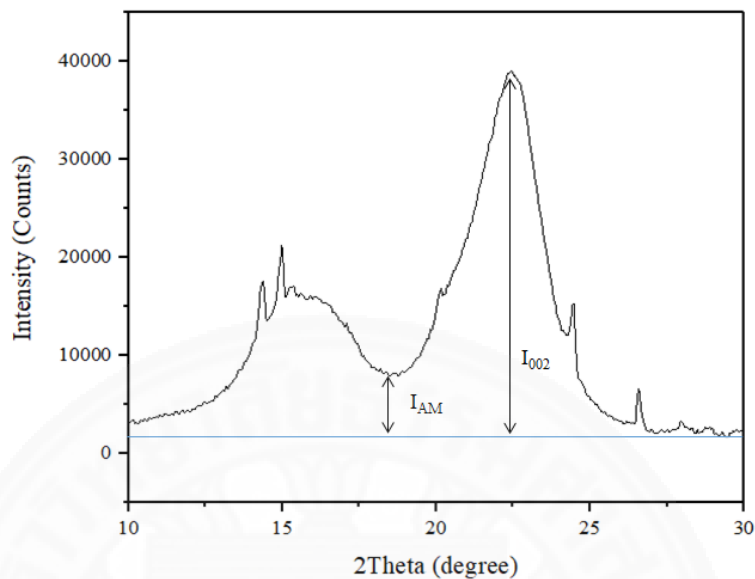
Figure E.3 X-ray diffraction pattern for unprocessed cellulose and peak height positions.

$$C.I. = (I_{002} - I_{AM}) / I_{002} = 1 - (I_{AM} / I_{002})$$ E-2

FTIR method
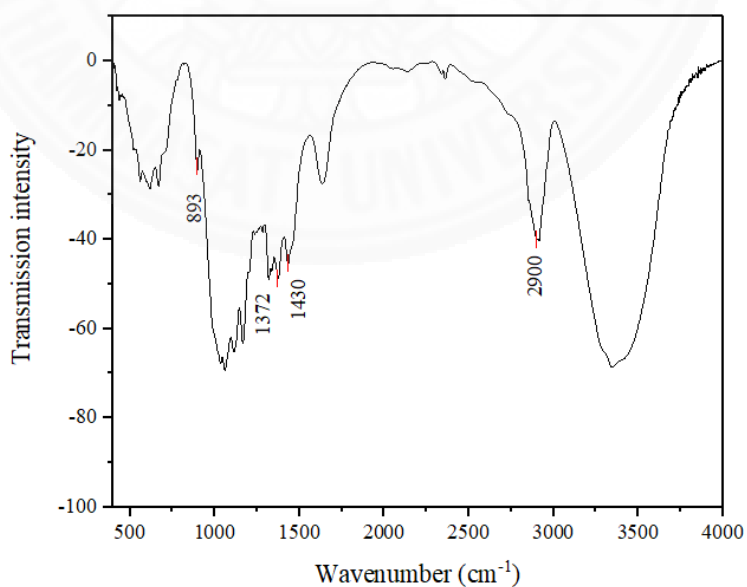
Figure E.4 FTIR pattern for unprocessed cellulose.

$$C.I. = I_{1372} / I_{2900} \qquad \text{E-3}$$

$$C.I. = I_{1430} / I_{893} \qquad \text{E-4}$$

Solid-state ^{13}C NMR method (Newman method)

Figure E.5 Solid state ^{13}C NMR of unprocessed cellulose.

Figure E.6 Solid state ^{13}C NMR of processed cellulose under $ScCO_2$ at 20 MPa and 333.15 K for 120 min.

Table E.1 Area and intensity of X-ray diffraction peaks for Herman's and Segal's calculations.

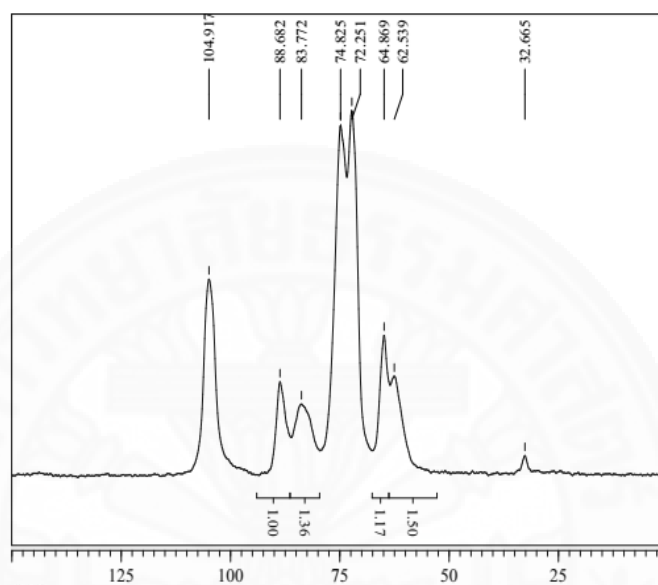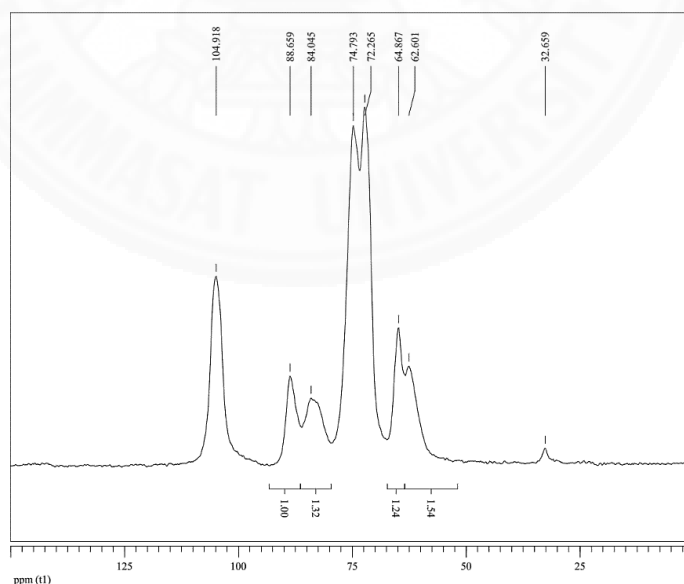| p (MPa)	T (K)	t (min)	Herman's equation						Segal's equation		
			Amorphous region	Crystal region				Cr.	I_{AM}	I_{002}	C.I
				101	10$\bar{1}$	210	002				
Unprocessed		0	111484.11	19701.44	8300.56	7317.87	74658.65	0.4966	8020	39000	0.7944
0.1	313.15	60	130613.21	36356.74	6479.22	8577.92	76239.96	0.4943	8520	40530	0.7898
0.1	313.15	60	159210.42	40389.73	4219.16	9099.20	74139.71	0.4454	10870	42370	0.7435
8	313.15	60	114797.63	22865.23	4767.70	8765.71	79163.82	0.5017	8730	42370	0.7940
8	333.15	60	95190.93	16033.22	8325.67	8151.32	78916.82	0.5393	7180	39690	0.8191
8	353.15	60	115224.96	22755.85	4922.43	8393.54	81438.77	0.5049	8800	39700	0.7783
15	313.15	60	116949.29	25420.39	3797.00	8066.66	82512.01	0.5060	8790	42740	0.7943
15	333.15	60	110873.33	23119.52	5585.12	8887.57	78950.52	0.5125	8300	42050	0.8026
15	353.15	60	125036.41	27661.86	4274.78	7776.82	80440.42	0.4900	9080	43060	0.7891
20	313.15	60	127531.30	18456.01	6242.70	8366.36	79854.33	0.4696	9080	41140	0.7793

Table E.1 (Cont.)

p (MPa)	T (K)	t (min)	Herman's equation							Segal's equation		
			Amorphous region	Crystal region				Cr.	I_{AM}	I_{002}	C.I
				101	10$\bar{1}$	210	002				
20	333.15	60	128248.11	23239.93	6212.33	8704.58	80309.09	0.4802	9080	42810	0.7879
20	353.15	60	92022.34	12282.28	3713.03	6598.04	79193.66	0.5252	6830	37400	0.8174
0.1	313.15	120	129815.38	34282.16	6570.23	9320.28	84488.35	0.5092	9520	43750	0.7824
0.1	313.15	120	113666.80	39055.61	5623.15	7141.95	80794.21	0.5385	8050	40840	0.8029
8	313.15	120	107882.93	23153.16	5875.28	8554.30	79712.20	0.5209	8360	41360	0.7979
8	353.15	120	107143.10	21065.80	6079.20	8403.66	78373.62	0.5153	8040	40680	0.8024
15	353.15	120	108129.27	26804.20	3631.32	8475.63	78981.20	0.5216	8010	41440	0.8067
20	333.15	120	107772.87	25575.61	3371.36	8673.10	83044.98	0.5282	8000	42800	0.8131

Table E.2 Crystallinity index (C.I.) calculated using FTIR method.

p (MPa)	T (K)	t (min)	weight (mg)		I1372	I2900	I1430	I893	C.I.1	C.I.2	average	SD
			KBr	Sample								
KBr			149.8	0								
Unprocessed		0	148.78	2.16	0.5159	0.5942	0.5489	0.7674	0.8681	0.7153	0.7917	0.1080
0.1	313.15	60	148.70	1.44	0.5127	0.7512	0.5409	0.7938	0.6824	0.6814	0.6819	0.0007
0.1	313.15	60	148.27	1.76	0.4560	0.6312	0.4920	0.7242	0.7225	0.6794	0.7010	0.0305
8	313.15	60	148.23	1.81	0.5034	0.6986	0.5382	0.7450	0.7206	0.7224	0.7215	0.0012
8	333.15	60	148.19	1.97	0.4924	0.6091	0.5272	0.7532	0.8084	0.6999	0.7542	0.0767
8	353.15	60	147.98	2.24	0.4994	0.7078	0.5350	0.7321	0.7056	0.7308	0.7182	0.0178
15	313.15	60	148.40	1.71	0.4963	0.6579	0.5320	0.7593	0.7543	0.7006	0.7274	0.0380
15	333.15	60	148.20	2.06	0.4427	0.5833	0.4778	0.7205	0.7591	0.6631	0.7111	0.0678
15	353.15	60	148.01	2.40	0.4149	0.5823	0.4485	0.6983	0.7125	0.6422	0.6774	0.0497
20	313.15	60	148.13	1.90	0.5676	0.7137	0.6012	0.7998	0.7952	0.7518	0.7735	0.0307

Table E.2 (Cont.)

p (MPa)	T (K)	t (min)	weight (mg)		I1372	I2900	I1430	I893	C.I.1	C.I.2	average	SD
			KBr	Sample								
20	333.15	60	147.99	2.11	0.5264	0.7318	0.5620	0.7488	0.7194	0.7506	0.7350	0.0221
20	353.15	60	148.79	1.24	0.6134	0.7581	0.6445	0.8188	0.8090	0.7871	0.7981	0.0155
0.1	313.15	120	148.55	1.49	0.5695	0.7412	0.6039	0.7931	0.7684	0.7615	0.7650	0.0049
0.1	313.15	120	147.96	2.27	0.4125	0.5404	0.4473	0.7040	0.7633	0.6353	0.6993	0.0905
8	313.15	120	148.37	2.05	0.5487	0.7435	0.5829	0.7701	0.7380	0.7569	0.7475	0.0134
8	353.15	120	147.98	2.17	0.5419	0.7410	0.5772	0.7642	0.7313	0.7553	0.7433	0.0170
15	353.15	120	148.21	1.82	0.5535	0.7060	0.5877	0.7975	0.7840	0.7370	0.7605	0.0333
20	333.15	120	148.03	2.07	0.4511	0.6374	0.4868	0.7232	0.7077	0.6731	0.6904	0.0245

Table E.3 Degree of crystallinity (Cr) calculated using ^{13}C NMR method.

Unprocessed			ScCO$_2$ treated		
crystalline	amorphous	crystallinity	crystalline	amorphous	crystallinity
1.00	1.36	0.4237	1.00	1.32	0.4310
1.17	1.50	0.4382	1.24	1.54	0.4460
Average		0.43097	Average		0.43854
SD		0.01023	SD		0.01061

APPENDIX F

STATISTICAL ANALYSIS FOR CELLULOSE PROCESSING IN SC-CO$_2$

Normality test

Figure F.1 Probability plot of fiber size.

Figure F.2 Probability plot of Cp_DSC.

Figure F.3 Probability plot of ΔH_DSC.

Figure F.4 Probability plot of %loss_TGA.

Figure F.5 Probability plot of To_TGA.

Figure F.6 Probability plot of Cr_XRD.
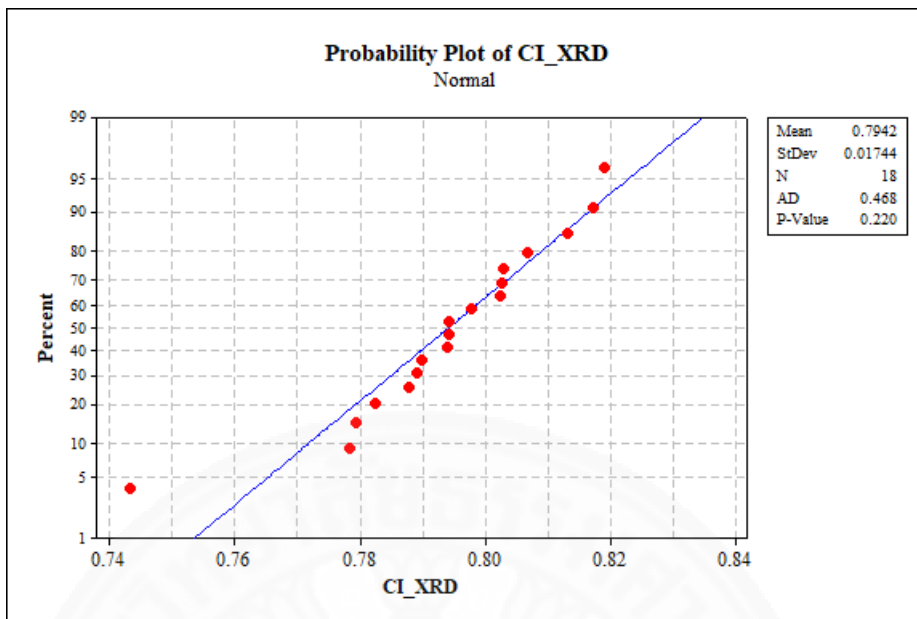
Figure F.7 Probability plot of C.I._XRD.

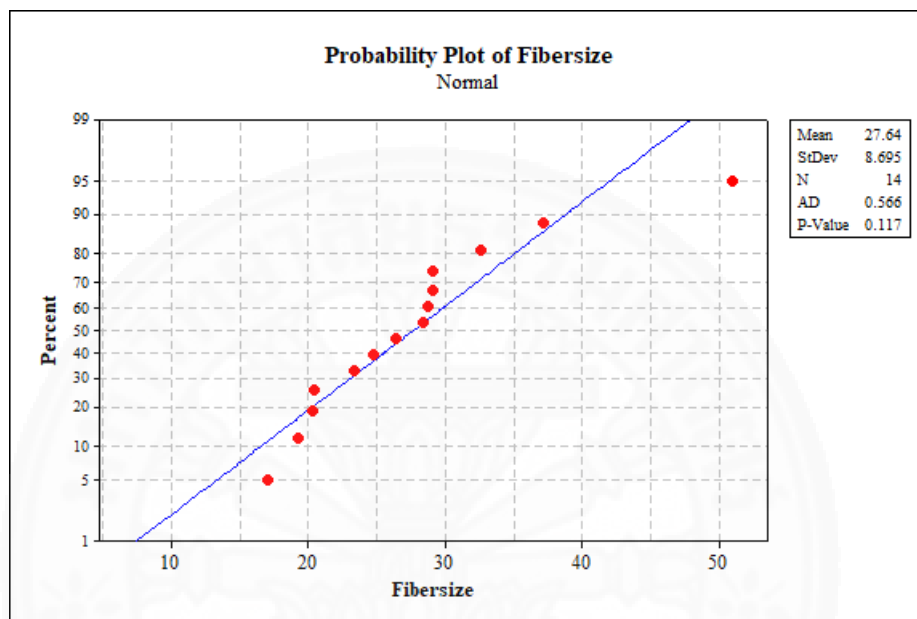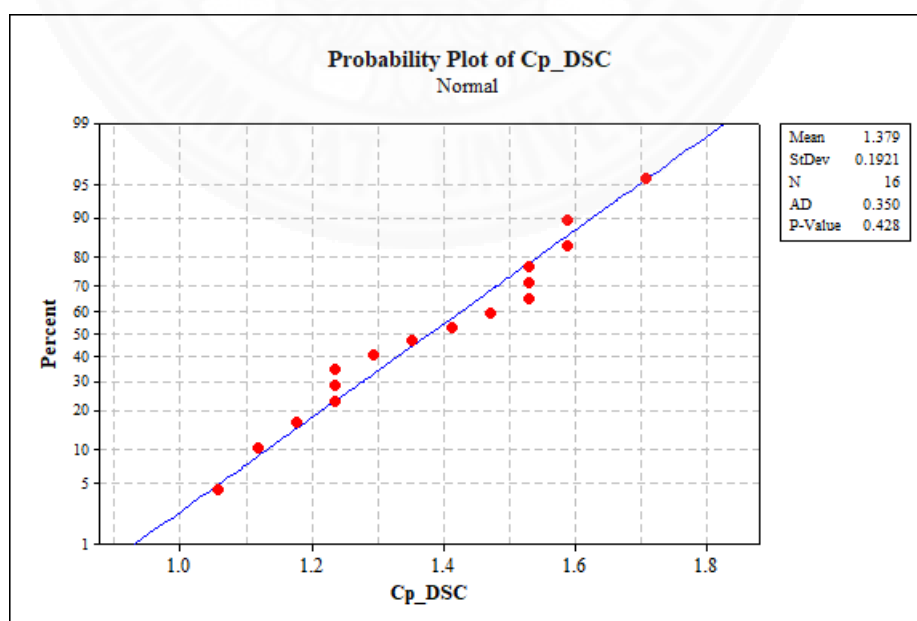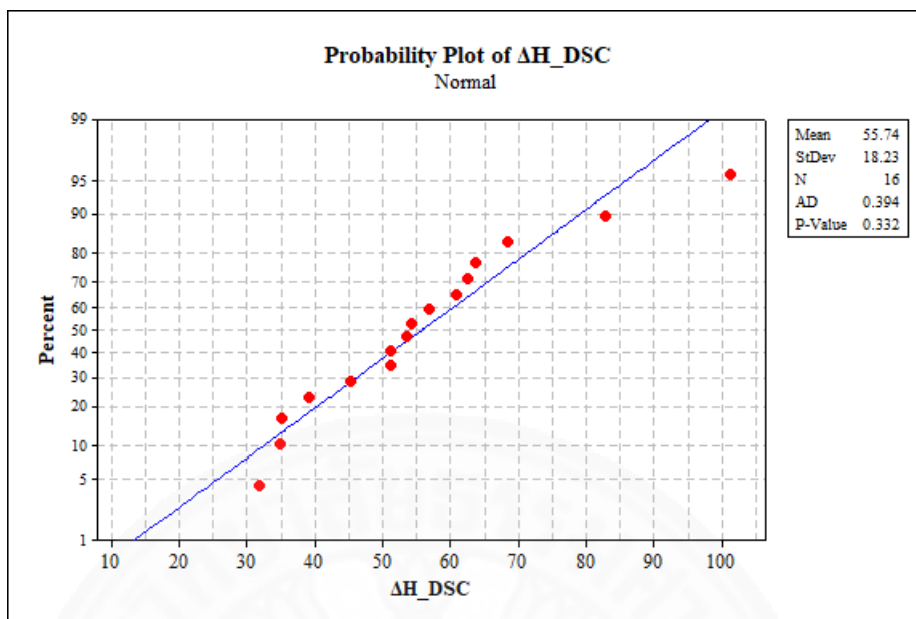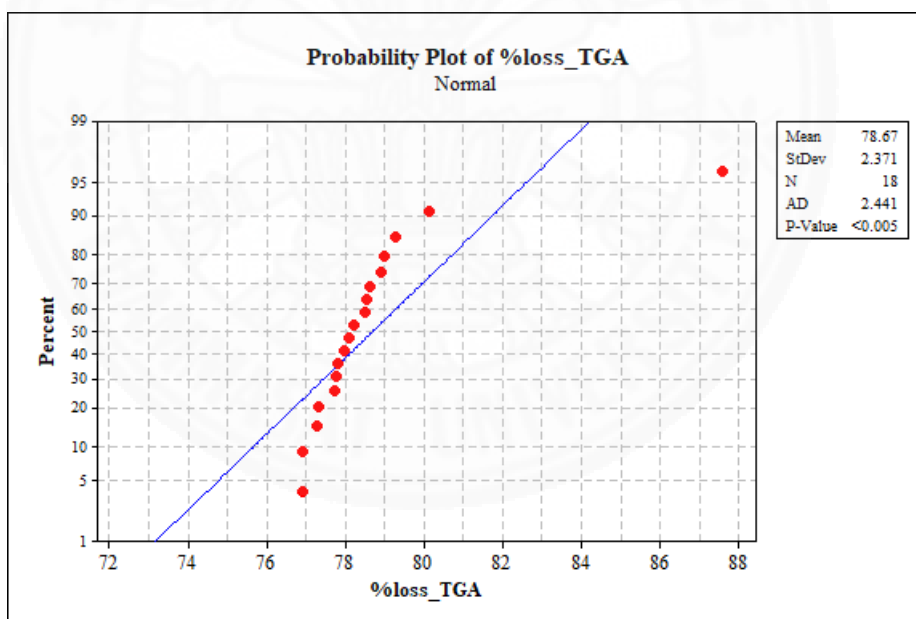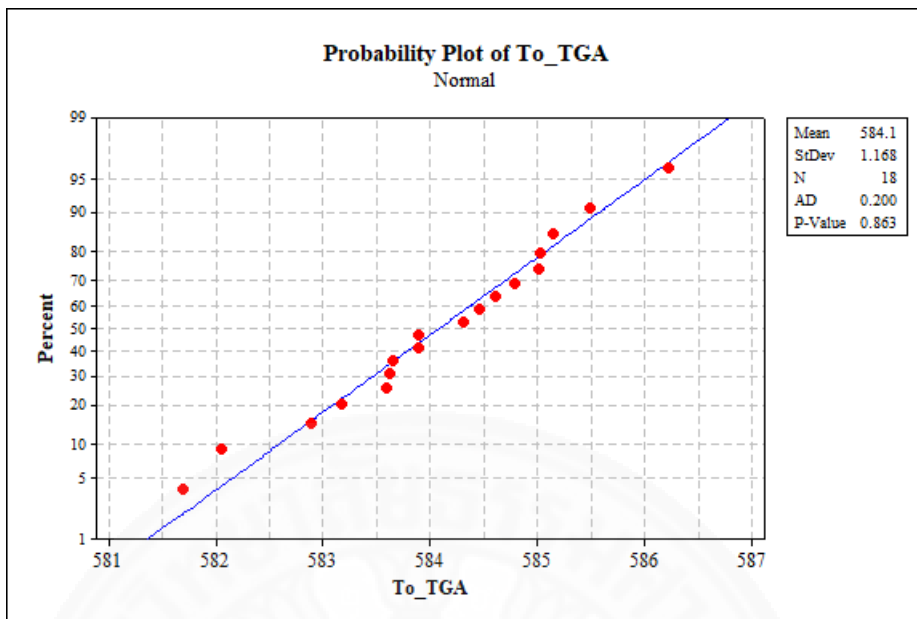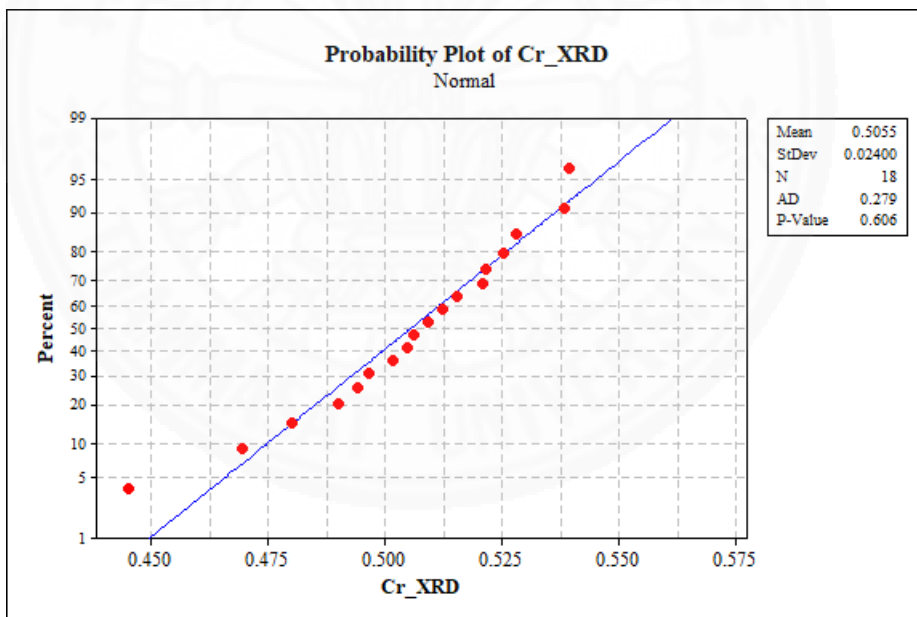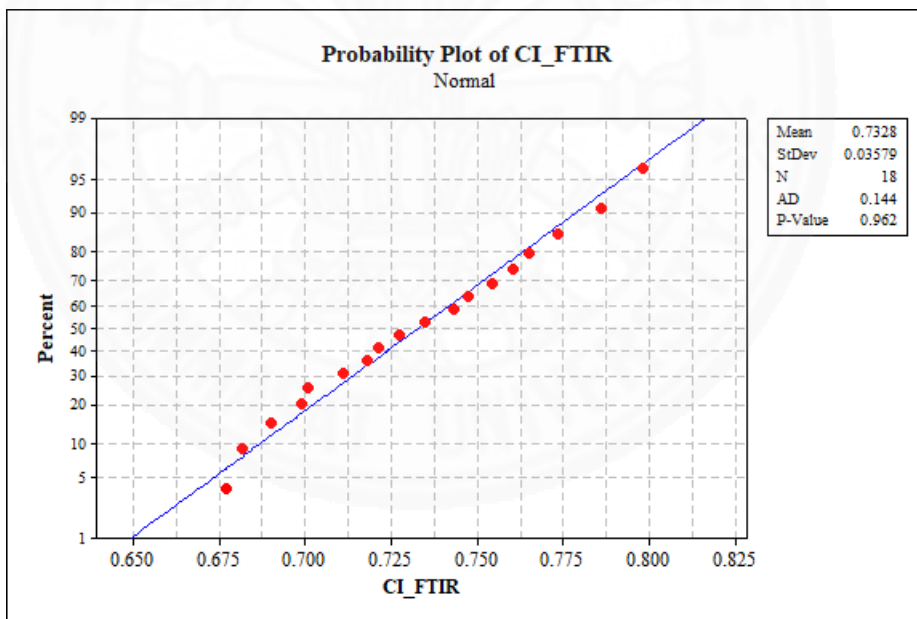Figure F.8 Probability plot of C.I._FTIR.
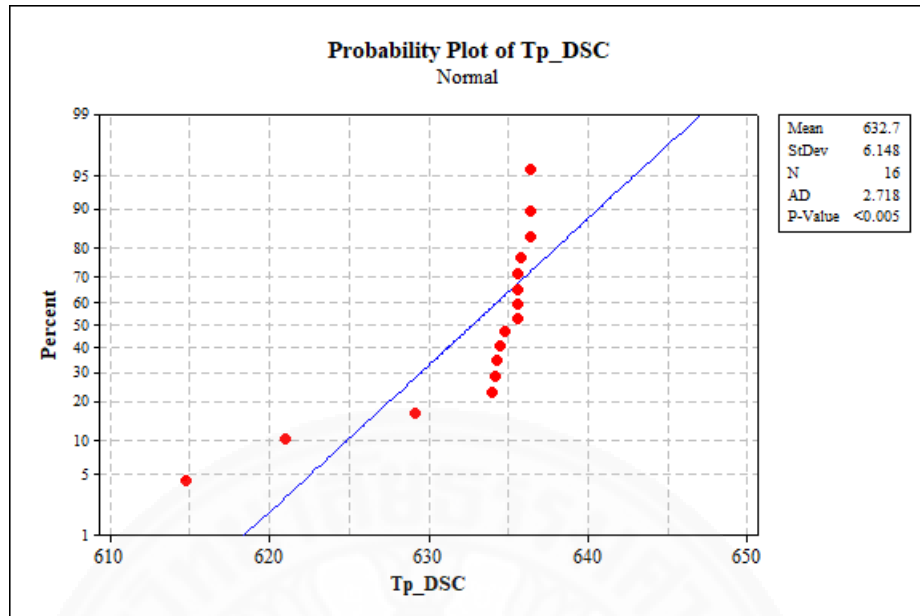
Figure F.9 Probability plot of Tp_DSC.
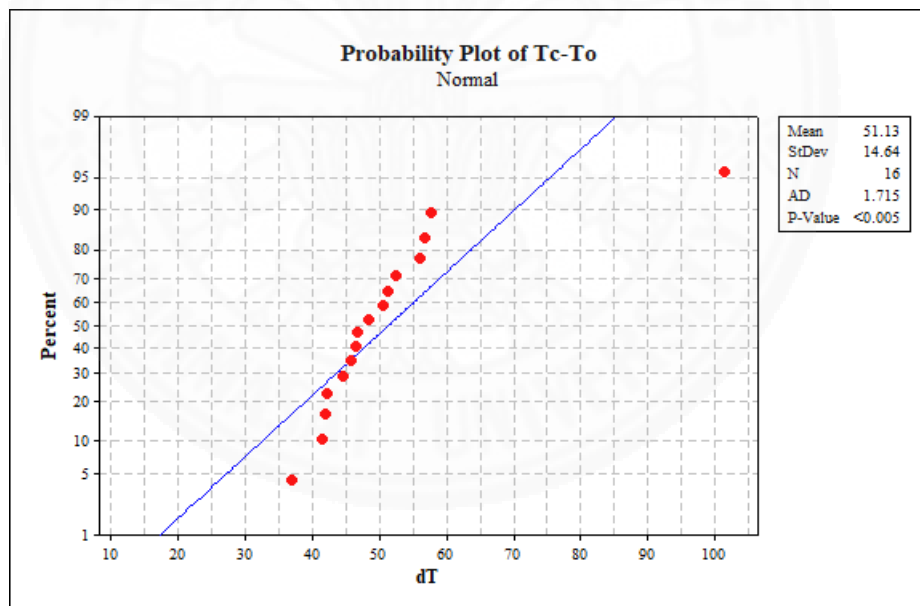
Figure F.10 Probability plot of Tc-To_DSC.

One-way ANOVA and Kruskal-Wallis

Table F.1 One-way ANOVA: Fiber size versus variable.

```
Source   DF    SS     MS     F     P
Variable  1  584.1  584.1  17.57  0.001
Error    12  398.8   33.2
Total    13  982.9
```

```
S = 5.765   R-Sq = 59.42%   R-Sq(adj) = 56.04%
```

```
                    Individual 95% CIs For Mean Based on
                    Pooled StDev
Level  N   Mean   StDev  -+---------+---------+---------+--------
1      1  50.928    *            (---------*----------)
3     13  25.848  5.765  (--*-)
                          -+---------+---------+---------+--------
                          24        36        48        60
```
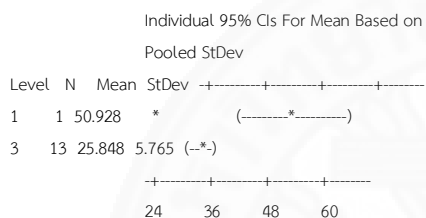
```
Pooled StDev = 5.765
```

Table F.2 One-way ANOVA: Cp_DSC versus variable.

```
Source   DF    SS      MS     F     P
Variable  2  0.1338  0.0669  2.07  0.165
Error    13  0.4196  0.0323
Total    15  0.5534
```

```
S = 0.1797   R-Sq = 24.18%   R-Sq(adj) = 12.51%
```

```
                    Individual 95% CIs For Mean Based on
                    Pooled StDev
Level  N   Mean    StDev  -------+---------+---------+---------+--
1      1  1.7059     *             (------------*------------)
2      2  1.2647  0.0416    (--------*--------)
3     13  1.3710  0.1866        (---*--)
                           -------+---------+---------+---------+--
                                 1.20      1.50      1.80      2.10
```
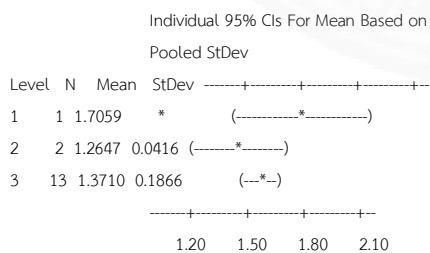
```
Pooled StDev = 0.1797
```

Table F.3 One-way ANOVA: ΔH_DSC versus variable.

```
Source   DF   SS   MS    F     P
Variable  2  391  196  0.55  0.588
Error    13 4596  354
Total    15 4987
```

S = 18.80   R-Sq = 7.84%   R-Sq(adj) = 0.00%

```
                        Individual 95% CIs For Mean Based on
                        Pooled StDev
Level  N  Mean  StDev  -----+---------+---------+---------+----
1      1  53.52     *   (---------------*---------------)
2      2  42.95  11.50  (---------*----------)
3     13  57.87  19.29             (---*----)
                       -----+---------+---------+---------+----
                          25        50        75       100
```
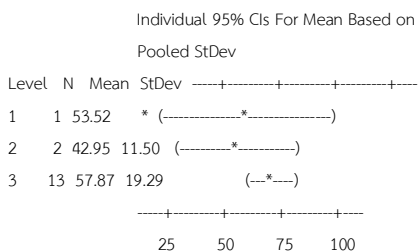
Pooled StDev = 18.80

Table F.4 One-way ANOVA: To_TGA versus variable.

```
Source    DF    SS      MS     F     P
Variable   2  12.256  6.128  8.41  0.004
Error     15  10.933  0.729
Total     17  23.189
```

S = 0.8537   R-Sq = 52.85%   R-Sq(adj) = 46.57%

```
                         Individual 95% CIs For Mean Based on
                         Pooled StDev
Level  N    Mean    StDev  ---+---------+---------+---------+------
1      1  583.880     *    (--------------*--------------)
2      4  582.563  0.866   (-------*------)
3     13  584.561  0.851                (---*----)
                          ---+---------+---------+---------+------
                          582.0     583.2     584.4     585.6
```
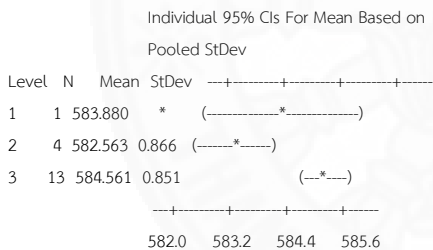
Pooled StDev = 0.854

Table F.5 One-way ANOVA: Td_TGA versus variable.

```
Source    DF    SS     MS     F     P
Variable   2  28.88  14.44  11.70  0.001
Error     15  18.52  1.23
Total     17  47.39
```

S = 1.111   R-Sq = 60.93%   R-Sq(adj) = 55.72%

```
                         Individual 95% CIs For Mean Based on Pooled StDev
Level  N   Mean   StDev    +---------+---------+---------+--------
1      1  612.33     *     (----------*----------)
2      4  614.41  1.13               (-----*-----)
3     13  616.65  1.11                     (--*---)
                          +---------+---------+---------+--------
```
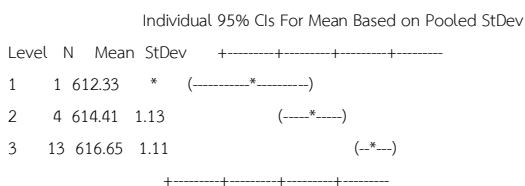
```
                    610.0    612.0    614.0    616.0
```

Pooled StDev = 1.11

Table F.6 One-way ANOVA: Cr_XRD versus variable.

```
Source   DF      SS        MS     F     P
Variable  2  0.000529  0.000265  0.43  0.659
Error    15  0.009262  0.000617
Total    17  0.009791
```

S = 0.02485   R-Sq = 5.40%   R-Sq(adj) = 0.00%

```
                         Individual 95% CIs For Mean Based on
                         Pooled StDev
Level  N    Mean    StDev  --+---------+---------+---------+-------
1      1  0.49660      *    (----------------*----------------)
2      4  0.49682  0.03890        (--------*-------)
3     13  0.50888  0.01984              (----*----)
                           --+---------+---------+---------+-------
                           0.450    0.480    0.510    0.540
```
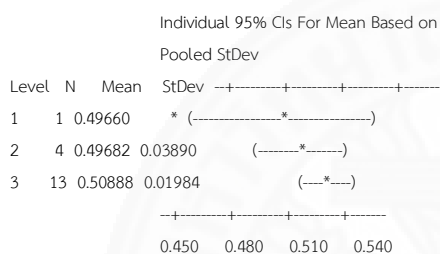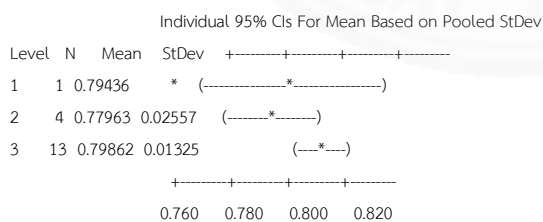
Pooled StDev = 0.02485

Table F.7 One-way ANOVA: C.I._XRD versus variable.

```
Source   DF      SS        MS     F     P
Variable  2  0.001103  0.000552  2.03  0.165
Error    15  0.004067  0.000271
Total    17  0.005170
```

S = 0.01647   R-Sq = 21.33%   R-Sq(adj) = 10.85%

```
                         Individual 95% CIs For Mean Based on Pooled StDev
Level  N    Mean    StDev   +---------+---------+---------+---------
1      1  0.79436      *    (----------------*----------------)
2      4  0.77963  0.02557  (--------*-------)
3     13  0.79862  0.01325              (----*----)
                            +---------+---------+---------+---------
                            0.760    0.780    0.800    0.820
```

Pooled StDev = 0.01647

Table F.8 One-way ANOVA: C.I._FTIR versus variable.

```
Source   DF     SS       MS     F     P
Variable  2  0.00468  0.00234  2.05  0.163
Error    15  0.01710  0.00114
Total    17  0.02178
```

S = 0.03377 R-Sq = 21.48% R-Sq(adj) = 11.02%

```
                     Individual 95% CIs For Mean Based on
                     Pooled StDev
Level   N   Mean    StDev  -----+---------+---------+---------+----
1       1  0.78604    *         (-------------*-------------)
2       4  0.71177  0.03649  (------*-------)
3      13  0.73523  0.03305        (---*---)
                            -----+---------+---------+---------+----
                              0.700     0.750     0.800     0.850
```
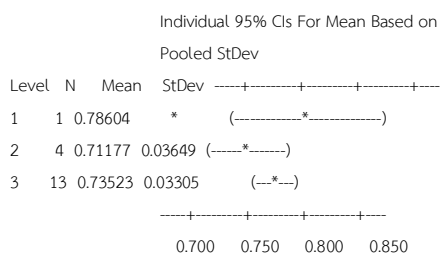
Pooled StDev = 0.03377

Table F.9 Kruskal-Wallis test: Tp_DSC versus variable.

Kruskal-Wallis Test on Tp_DSC

```
                 Ave
Variable  N  Median  Rank    Z
1         1  614.8   1.0   -1.63
2         2  631.5   3.5   -1.59
3        13  635.6   9.8    2.35
Overall  16          8.5
```

H = 5.73 DF = 2 P = 0.057

Table F.10 Kruskal-Wallis test: Tc-To_DSC versus variable.

Kruskal-Wallis Test on dT

```
                 Ave
Variable  N  Median  Rank    Z
1         1  36.83   1.0   -1.63
2         2  44.71   5.5   -0.95
3        13  50.35   9.5    1.82
Overall  16          8.5
```

H = 3.89 DF = 2 P = 0.143

Table F.11 Kruskal-Wallis test: Tp_DSC versus variable.

Kruskal-Wallis Test on C10

```
C1        N  Median  Ave Rank    Z
1         1  87.56    18.0   1.64
2         4  77.08     2.8  -2.87
3        13  78.47    10.9   1.82
Overall  18            9.5
```

H = 9.85 DF = 2 P = 0.007

* NOTE * One or more small samples

APPENDIX G

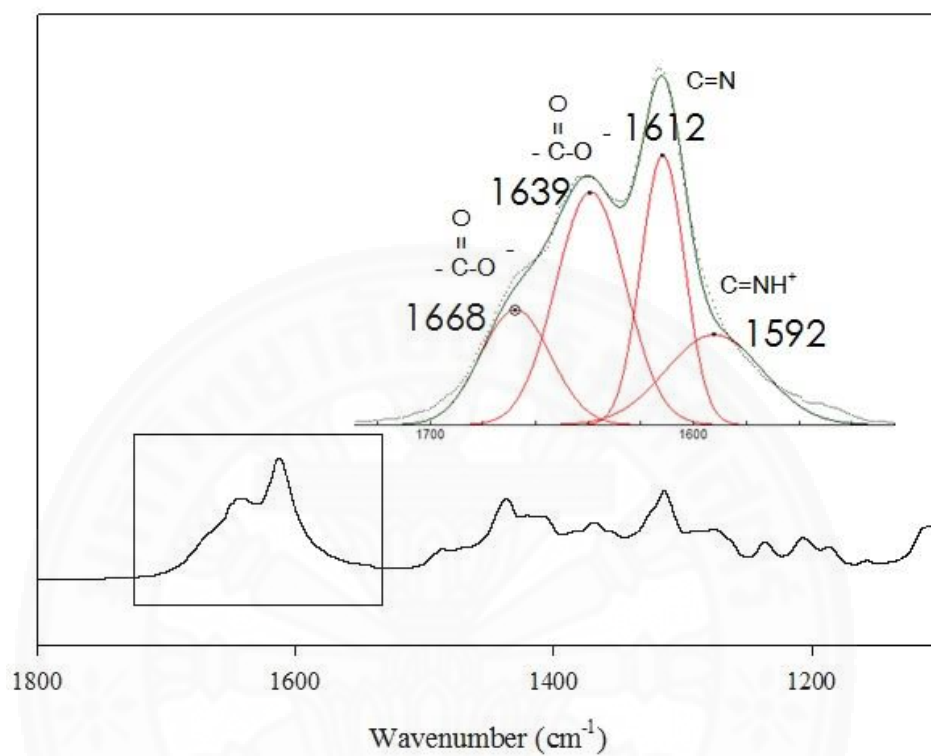## FTIR RESULTS OF CELLULOSE/CO$_2$-SWS

Figure G.1 The deconvolution of FTIR spectra of the CO$_2$-SWS (the mixture of DBU + EG + DMSO after carbon dioxide switchable).
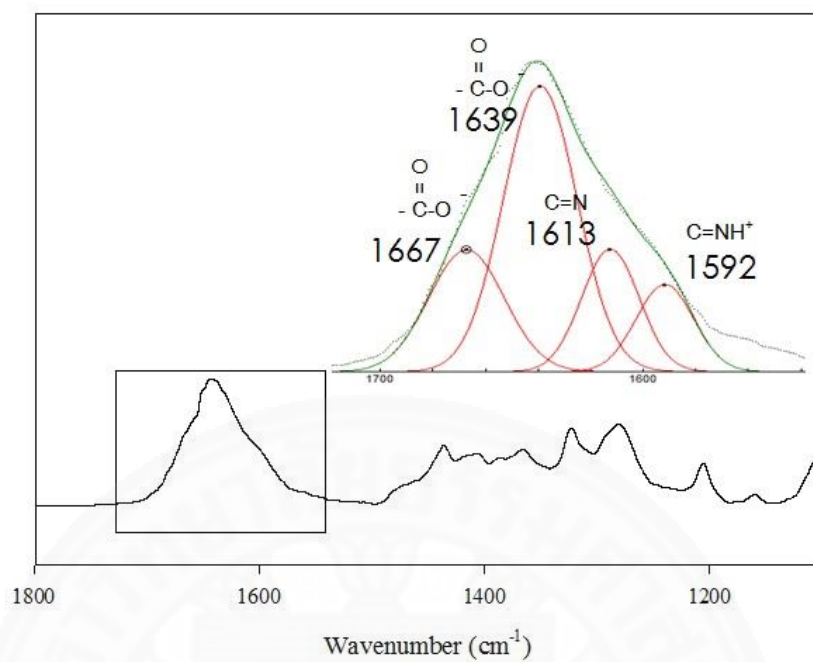
Figure G.2 The deconvolution of FTIR spectra of the CO_2-SWS containing the cellulose at 313.15 K and 5.8 MPa.
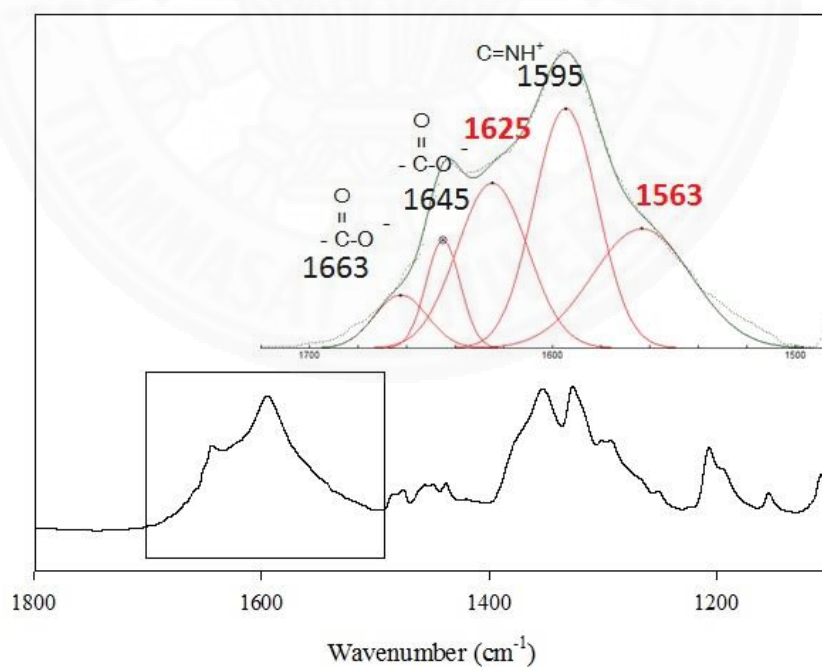

Figure G.3 The deconvolution of FTIR spectra of the CO_2-SWS containing the cellulose at 313 K and 10 MPa.

APPENDIX H

STATISTICAL ANALYSIS FOR CELLULOSE/CO_2-SWS

Table H.1 Analysis of variance for regression model of Eq. (4-3)

	Coefficient	F-value	p-value	R^2	Adjusted R^2
Regression equation 4-3		74.6600	0.081563	99.33	98.00
p	25.295	83.7882	0.069		
T	-0.687	0.5970	0.581		

Table H.2 Analysis of variance for regression model of Eq. (4-4)

	Coefficient	F-value	p-value	R^2	Adjusted R^2
Regression Eq. (4-4)		186.256	0.005326	98.94	98.41
p	23.787821	186.256	0.005326		

BIOGRAPHY

Name	Ms. Phawinee Nanta
Date of Birth	July28, 1987
Educational Attainment	2012: Master of Engineering (Chemical Engineering)
	2009: Bachelor of Science (Industrial Chemistry)
Scholarship	2012: The Royal Golden Jubilee (RGJ) Ph. D. program, Thailand Research Fund (TRF), grant number PHD/0265/2553
	2010: Thailand Graduate Institute of Science and Technology (TGIST), grant number TG-55-13-53-073M

Publications

Publication in Scopus and ISI database

Nanta, P., Kasemwong, K., Shimoyama, Y., Skolpap, W. (2018). Development of a diffusion-limited shrinking particle model of cellulose dissolution in a carbon dioxide switchable system. Chem. Eng. Sci. 179, pp 214-220.

Nanta, P., Skolpap, W., Kasemwong, K., Shimoyama, Y. (2017). Dissolution and modification of cellulose using high-pressure carbon dioxide switchable solution. J. Supercrit. Fluids. 130, pp 84-90.

Proceedings and conference works

Nanta P., Skolpap W., Shimoyama Y., Kasemwong K. "Development of modified-cellulose in carbon dioxide switchable system as an alternative matrix for hybrid carbon cathode in lithium-air battery." Poster presented at the Pure and Applied Chemistry International Conference 2018 (PACCON 2018), Hat Yai, Songkhla, Thailand, February 7-9, 2018.

Nanta P., Kasemwong K., Skolpap W., Shimoyama Y. "Transparent cassava-based cellulose film production using carbon dioxide switchable polarity

solvent." Poster presented at the 253rd American Chemical Society National Meeting & Exposition (ACS), San Francisco, CA, USA, April 2-6, 2017.

Nanta P., Skolpap W., Shimoyama Y. "Analysis of molecular interaction of Cassava-Based Cellulose treated in Ionic Liquid." Poster presented at The 11th Asian Thermophysical Properties Conference (ATCP2016), Yokohama, Japan, October 2-6, 2016.

Nanta P., Skolpap W., Shimoyama Y. "Chemical modification of cellulose in switchable solvent using high pressure carbon dioxide." Proceeding and oral presented at The Society of Chemical Engineering, Japan (SCEJ) 48th Autumn Meeting, Tokushima, Japan, September 6-8, 2016, F206.

Nanta P., Skolpap W., Shimoyama Y. "Development of transparent cellulose film using CO_2 switchable system." Poster presented at The 4th UK Japan Engineering Education League Workshop, Tokyo, Japan, August 5-8, 2016.

Work Experiences	Jan 2016 – Nov 2016: Research Student, Chemical Engineering
	Tokyo Institute of Technology, Tokyo, Japan
	Jul 2012 – Jul 2013: Research assistant
	NANOTEC, National Science and Technology Development Agency (NSTDA), Pathum Thani, Thailand